Evaluation of LS-DYNA Concrete Material Model 159

PUBLICATION NO. FHWA-HRT-05-063

MAY 2007

U.S. Department of Transportation
Federal Highway Administration

Research, Development, and Technology
Turner-Fairbank Highway Research Center
6300 Georgetown Pike
McLean, VA 22101-2296

Foreword

This report documents the evaluation of a concrete material model that has been implemented into the dynamic finite element code, LS-DYNA, beginning with version 971. This material model is in keyword format as MAT_CSCM for Continuous Surface Cap Model. This model was developed to predict the dynamic performance—both elastic deformation and failure—of concrete used in safety structures when involved in a collision with a motor vehicle. An example of a roadside safety structure is a concrete safety barrier that divides opposing lanes of traffic on a roadway. Default input parameters for concrete are stored in the model and can be accessed for use. This material model only replicates the concrete aggregate. Appropriate reinforcement bars or rods must be included in the structure model separately.

This report is the second of two that completely documents this material model. This report documents the testing performed to review the model's performance and accuracy of results. The first report is *Users Manual for LS-DYNA Concrete Material Model 159,* which documents the theoretical basis and required input format, and includes limited hypothetical problems for the user.

This report will be of interest to research engineers who are associated with the evaluation and crashworthy performance of roadside safety structures, particularly engineers responsible for predicting the crash response of such structures when using the finite element code, LS-DYNA.

Michael Trentacoste
Director, Office of Safety R&D

Notice

Quality Assurance Statement

The Federal Highway Administration (FHWA) provides high-quality information to serve Government, industry, and the public in a manner that promotes public understanding. Standards and policies are used to ensure and maximize the quality, objectivity, utility, and integrity of its information. FHWA periodically reviews quality issues and adjusts its programs and processes to ensure continuous quality improvement.

1. Report No. FHWA-HRT-05-063	2. Government Accession No.	3. Recipient's Catalog No.	
4. Title and Subtitle *Evaluation of LS-DYNA Concrete Material Model 159*		5. Report Date May 2007 6. Performing Organization Code	
7. Author(s) Yvonne D. Murray Akram Abu-Odeh and Roger Bligh		8. Performing Organization Report No.	
9. Performing Organization Name and Address APTEK, Inc. 1257 Lake Plaza Dr. Suite 100 Colorado Springs, CO 80906 Texas Transportation Institute Texas A&M University System 3135 TAMU College Station, TX 77843		10. Work Unit No. (TRAIS) 11. Contract or Grant No. DTFH61-98-C-00075	
12. Sponsoring Agency Name and Address Volpe National Transportation Systems Center 55 Broadway, Kendall Square Cambridge, MA 02142-1093 Federal Highway Administration 6300 Georgetown Pike McLean, VA 22101-2296		13. Type of Report and Period Covered Final Report September 27, 2001 through December 26, 2004 14. Sponsoring Agency Code	
15. Supplementary Notes The Contracting Officer's Technical Representative (COTR) for this project is Martin Hargrave, Office of Safety Research and Development, HRDS-04, Turner-Fairbank Highway Research Center.			
16. Abstract An elastoplastic damage model with rate effects was developed for concrete and implemented into LS-DYNA, a commercially available finite element code. This manual documents the evaluation of the concrete material model, including the selection of the concrete model input parameters. The model is evaluated through correlations with test data: drop tower impact of ⅓-scale beams (plain and reinforced), bogie vehicle impact of full-scale reinforced beams, pendulum impact of bridge rails, and quasi-static loading of a safety-shaped barrier. Although the model was developed and evaluated for roadside safety applications, it should also be applicable to many dynamic problems. The companion manual to this report is *Users Manual for LS-DYNA Concrete Material Model 159*, FHWA-HRT-05-062.			
17. Key Words concrete, LS-DYNA, material model, reinforced beam, New Jersey barrier, bridge rail, pendulum, bogie vehicle		18. Distribution Statement No restrictions. This document is available through the National Technical Information Service, Springfield, VA 22161.	
19. Security Classif. (of this report) Unclassified	20. Security Classif. (of this page) Unclassified	21. No. of Pages 206	22. Price N/A

Form DOT F 1700.7 (8-72) Reproduction of completed page authorized

SI* (MODERN METRIC) CONVERSION FACTORS

APPROXIMATE CONVERSIONS TO SI UNITS

Symbol	When You Know	Multiply By	To Find	Symbol
		LENGTH		
in	inches	25.4	millimeters	mm
ft	feet	0.305	meters	m
yd	yards	0.914	meters	m
mi	miles	1.61	kilometers	km
		AREA		
in^2	square inches	645.2	square millimeters	mm^2
ft^2	square feet	0.093	square meters	m^2
yd^2	square yard	0.836	square meters	m^2
ac	acres	0.405	hectares	ha
mi^2	square miles	2.59	square kilometers	km^2
		VOLUME		
fl oz	fluid ounces	29.57	milliliters	mL
gal	gallons	3.785	liters	L
ft^3	cubic feet	0.028	cubic meters	m^3
yd^3	cubic yards	0.765	cubic meters	m^3
	NOTE: volumes greater than 1000 L shall be shown in m^3			
		MASS		
oz	ounces	28.35	grams	g
lb	pounds	0.454	kilograms	kg
T	short tons (2000 lb)	0.907	megagrams (or "metric ton")	Mg (or "t")
		TEMPERATURE (exact degrees)		
^oF	Fahrenheit	5 (F-32)/9 or (F-32)/1.8	Celsius	^oC
		ILLUMINATION		
fc	foot-candles	10.76	lux	lx
fl	foot-Lamberts	3.426	candela/m^2	cd/m^2
		FORCE and PRESSURE or STRESS		
lbf	poundforce	4.45	newtons	N
lbf/in^2	poundforce per square inch	6.89	kilopascals	kPa

APPROXIMATE CONVERSIONS FROM SI UNITS

Symbol	When You Know	Multiply By	To Find	Symbol
		LENGTH		
mm	millimeters	0.039	inches	in
m	meters	3.28	feet	ft
m	meters	1.09	yards	yd
km	kilometers	0.621	miles	mi
		AREA		
mm^2	square millimeters	0.0016	square inches	in^2
m^2	square meters	10.764	square feet	ft^2
m^2	square meters	1.195	square yards	yd^2
ha	hectares	2.47	acres	ac
km^2	square kilometers	0.386	square miles	mi^2
		VOLUME		
mL	milliliters	0.034	fluid ounces	fl oz
L	liters	0.264	gallons	gal
m^3	cubic meters	35.314	cubic feet	ft^3
m^3	cubic meters	1.307	cubic yards	yd^3
		MASS		
g	grams	0.035	ounces	oz
kg	kilograms	2.202	pounds	lb
Mg (or "t")	megagrams (or "metric ton")	1.103	short tons (2000 lb)	T
		TEMPERATURE (exact degrees)		
^oC	Celsius	1.8C+32	Fahrenheit	^oF
		ILLUMINATION		
lx	lux	0.0929	foot-candles	fc
cd/m^2	candela/m^2	0.2919	foot-Lamberts	fl
		FORCE and PRESSURE or STRESS		
N	newtons	0.225	poundforce	lbf
kPa	kilopascals	0.145	poundforce per square inch	lbf/in^2

*SI is the symbol for the International System of Units. Appropriate rounding should be made to comply with Section 4 of ASTM E380.
(Revised March 2003)

TABLE OF CONTENTS

List of Figures

List of Tables

Acronyms and Abbreviations

CEB	Comite Euro-International Du Beton
COTR	Contracting Officer's Technical Representative
CSCM	continuous surface cap model
FHWA	Federal Highway Administration
FIP	Fédération Internationale de la Précontrainte
FOIL	Federal Outdoor Impact Laboratory
LSTC	Livermore Software Technology Corporation
NCAC	National Crash Analysis Center
NCHRP	National Cooperative Highway Research Program
SBP	spring-based pendulum
SGI	Silicon Graphics, Inc.

CHAPTER 1. INTRODUCTION

Three million human injuries and 42,000 premature deaths occur annually as a result of motor vehicle crashes.[1] To help reduce the toll of this problem, the Federal Highway Administration (FHWA) has set a strategic goal to improve the safety of our Nation's roadways. One way this is being accomplished is by expanding the use of the LS-DYNA finite element code to replicate three-dimensional motor vehicle crashes into roadside safety structures.[2] The objective is to protect the vehicle occupants from serious injury by making the structures more crashworthy. Roadside safety structures include bridge rails, barriers, and guardrails. One important bridge, barrier, and guardrail material is concrete (with reinforcement).

The roadside safety community supplements measured crash test data with LS-DYNA simulations performed on the computer. The accuracy of the simulations depends, in part, on the material models formulated to simulate the behavior of the roadside structures and vehicle materials. A comprehensive concrete material model was developed, implemented in the LS-DYNA finite element code, and evaluated for simulating the deformation and damage to reinforced concrete structures from dynamic impact. For ease of use, default material properties for standard concrete are incorporated into the model as a function of concrete compressive strength and maximum aggregate size. Correlations with drop tower, bogie vehicle, and pendulum impact tests are used to evaluate the model and finalize the default material properties.

The calculations of chapters 1 through 7, chapter 9, and appendix B of this evaluation report were conducted and documented by the developer of the concrete material model, referred to here as the "developer." The calculations of chapter 8, chapter 9, and appendix A were conducted and documented by a potential end user of the concrete material model, referred to here as the "user." Conclusions and recommendations from both the developer and user are discussed in chapter 10.

MODEL THEORY

The concrete model was primarily developed to simulate the deformation and failure of concrete in roadside safety structures impacted by vehicles. Examples are bridge rails and safety barriers. The concrete model is commonly referred to as a smooth or continuous surface cap model. Hence, model 159 is implemented in keyword format as MAT_CSCM for Continuous Surface Cap Model. A smooth and continuous intersection is formulated between the failure surface and hardening cap. The main features of the model are:

- Isotropic constitutive equations.
- Three stress invariant yield surface with translation for prepeak hardening.
- A hardening cap that expands and contracts.
- Damage-based softening with erosion and modulus reduction.
- Rate effects for increasing strength in high-strain rate applications.

General discussions of these types of formulations are given in references by Murray, Lewis, and Schwer.[3,4,5] Thorough details of the concrete model theory, a user's guide, and example input

are documented in the companion manual to this report titled FHWA HRT 05-062 *Users Manual for LS-DYNA Concrete Model 159*.[6]

Concrete structures typically contain steel reinforcement. Steel reinforcement exhibits rate effects, and yields in a ductile manner until it breaks at an ultimate strain greater than about 20 percent. The reinforcement model plays an important role in modeling reinforced concrete behavior. Our approach is to explicitly model the reinforcement (beam elements) separately from the concrete (hex elements) using an elastoplastic material model with yielding, hardening, rate effects, and plastic strain-based failure (such as MAT_PIECEWISE_LINEAR_PLASTICITY).

MODEL INPUT

There are two methods for setting up the model input. The traditional method is to supply all material parameters, such as moduli, strengths, hardening, softening, and rate effects parameters (MAT_CSCM). A more convenient method is to request default parameters (MAT_CSCM_CONCRETE). Default parameters are provided for the concrete model based on three input specifications: the unconfined compression strength (grade), the aggregate size, and the units. The parameters are fit to data for unconfined compression strengths between about 20 and 58 megapascals (MPa) (2,901 and 8,412 pounds per square inch (lbf/inch^2)), and aggregate sizes between 8 millimeters (mm) (0.3 inches) and 32 mm (1.26 inches). The unconfined compression strength affects all aspects of the fit, including stiffness, three-dimensional yield strength, hardening, and damage-based softening. The aggregate size affects only the softening behavior of the damage formulation.

The suite of material properties was primarily obtained through use of the Comite Euro-International Du Beton-Fédération Internationale de la Précontrainte Model (CEB-FIP) Code,[7] supplemented through correlations with the drop tower, bogie vehicle, and pendulum impact tests. This code is a synthesis of research findings and contains a thorough section on concrete classification and constitutive relations. Various material properties, such as compressive and tensile strengths, stiffness, and tensile fracture energy, are reported as a function of grade and aggregate size. A thorough discussion of the model input parameters is documented in the concrete model user's manual.[6]

LIMITATIONS OF MATERIAL PROPERTY DATA

Limitations of published laboratory test data for setting the default material properties include:

- No direct measurements of the softening behavior (fracture energy) in pure shear stress. The fracture energy is an area under the stress-displacement curve (from peak stress to zero stress).

- Limited information on rate effects for stress states other than uniaxial tensile stress and uniaxial compression stress. This includes the effect of rate on fracture energy as well as strength.

Our methodology is to estimate the missing material property values through LS-DYNA correlations with static and impact data provided by the user. Hence the LS-DYNA simulations discussed in this document serves not only to evaluate the material model but also to set default material property values.

EVALUATION PROCESS

Calculations were compared with a wide variety of test data to evaluate the performance of the concrete material model and the accuracy of the default material parameters. The evaluation of the concrete model proceeded in two steps. The first step was to evaluate the model as a user-defined material, which the developer accomplished. This means that the model was hooked up to the LS-DYNA code (version 970) as material model #42 via an interface. The developer retained access to the concrete model source code in order to enhance the formulation and adjust the default parameters during the evaluation process.

Once the evaluation was near completion and all default parameters were tentatively selected, the concrete model was forwarded to Livermore Software Technology Corporation (LSTC) for permanent implementation into the LS-DYNA code. LSTC and the developer implemented the model into a beta 971 version of LS-DYNA as material model 159.

The second step was to evaluate the concrete model as material model 159 in the LS-DYNA code. Both the developer and the user accomplished this step. One objective was to check the permanent implementation to make sure that material model 159 produced the same results as the user-defined material. Adjustments in the LSTC implementation were made until agreement was achieved. A second objective was to make sure that the model produced the same or similar results on different computer platforms. Generally, results agree by platform until erosion occurs, at which time they diverge slightly (see appendix A). A third objective was to allow a potential end user access to the model for independent evaluation. Calculations performed by the developer were conducted using LS-DYNA beta version 971 (revisions 1432 and 2582) on a PC using Microsoft® (MS) Windows® XP. Calculations performed by the user were conducted using LS-DYNA beta version 971 with MS-Windows (release 1612 single precision) and Linux™ Intel 32 bit architecture (release 1708 single precision). Minor adjustments in the model theory and default parameters were finalized with LSTC before documenting this effort. Results and conclusions from both the developer and user are included at the end of this document.

EVALUATION CALCULATIONS

Evaluation of the model requires two general types of test data: basic material property data of plain concrete for determining input parameters to the model and impact tests of reinforced concrete for evaluation of the model formulation. Most of the tests simulated are intended to produce failure conditions in the concrete that replicate the failure conditions in roadside safety applications. Evaluation simulations performed are:

- Single element simulations to check the implementation of the model via examination of the stress versus displacement behavior.

- Single material simulations (cylinders in tension and compression) to check simulation of the damage modes and to check convergence of the model with mesh refinement. Computed damage modes are compared with measured damage modes discussed in the general literature.

- Drop tower impact simulations of plain and reinforced concrete beams. Computed results are compared with test data on ⅓-scale beams in dynamic four-point bending. The test data were specifically generated for use on this project.

- Bogie vehicle impact simulations of full-scale reinforced concrete beams in dynamic four-point bending. Computed results are compared with test data specifically generated for this project.

- Pendulum impact simulations of the Texas T4 bridge rail parapet and deck section with two base-plate configurations (test 3-11 of *National Cooperative Highway Research Program (NCHRP) Report 350*). Computed results are compared with test data generated by the user on a separately funded project.[8]

- Quasi-static simulations of a New Jersey profile concrete safety-shaped barrier. Computed results are compared with test data generated by the user on a separately funded project.[9]

All calculations discussed in this report were performed with knowledge of the test results. This is because correlations with test results were used to set various default parameters and to help refine the model. Future calculations performed by roadside safety analysts will assess the predictive capability and provide a more thorough evaluation and validation of the concrete material model. Analysts include those at FHWA, National Highway Traffic Safety Administration, National Crash Analysis Center (NCAC), and FHWA-organized Centers of Excellence for Finite Element Crash Analysis. Accurate predictions, in which the analyst is unaware of the measured results before the simulation, build more confidence in a model than accurate correlations.

CHAPTER 2. SINGLE ELEMENT SIMULATIONS

Single element simulations were performed with LS-DYNA to verify the implementation of the concrete model and to display the basic stress-strain behavior of the model. All simulations were conducted with cubic hex elements, 38.1 mm (1.5 inches) in each dimension. Unless otherwise specified, approximate default material properties are used for 28 MPa (4,061 lbf/inch^2) concrete with 19 mm (0.75 inches) maximum aggregate size. Stresses and strains are plotted positive in tension unless otherwise noted.

UNIAXIAL AND TRIAXIAL STRESS

Typical behavior of the concrete model in uniaxial and triaxial stress is shown in Figures 1 and 2. In uniaxial tensile stress and pure shear stress, the stress-displacement behavior is modeled linear to peak, followed by brittle softening. Although not shown, the behavior of the model in biaxial and triaxial tensile stress is nearly identical to that shown for uniaxial tensile stress, with the same peak strength and softening response.

In uniaxial compressive stress, the stress-displacement behavior is also modeled linear to peak followed by gradual softening to near zero strength. The unconfined compressive strength is approximately 10 times the unconfined tensile strength, in agreement with typical test data for concrete. The fracture energy shown in unconfined compression is approximately 100 times greater than the fracture energy in unconfined tension. The energy is the area under the softening portion of the stress versus displacement curve. The developer recommends values between 50 and 100 for the compression to tension fracture energy ratio. A value of 100 was ultimately selected at the end of the program as the default value.

The concrete elements also soften when confined at moderate pressure, although they exhibit a residual strength (plateau) rather than softening to zero. Triaxial compression refers to tests or simulations in which the lateral confining pressure is held constant around the specimen (element) while the axial compression load is quasi-statically increased. The concrete strength increases with confining pressure in the simulations, in qualitative agreement with typical test data.

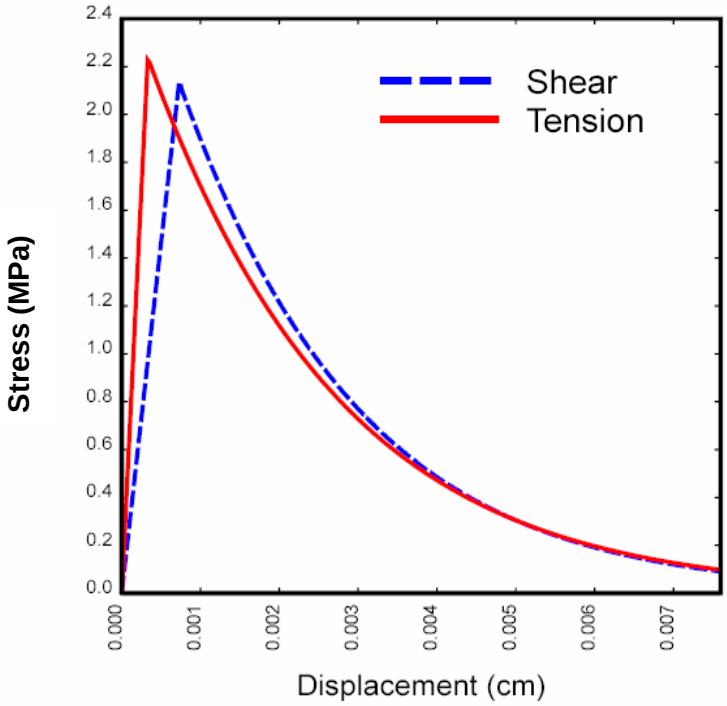

cm = 0.39 inch

Figure 1. The default behavior of the concrete model in uniaxial tensile stress and pure shear stress is linear to the peak, followed by brittle softening.

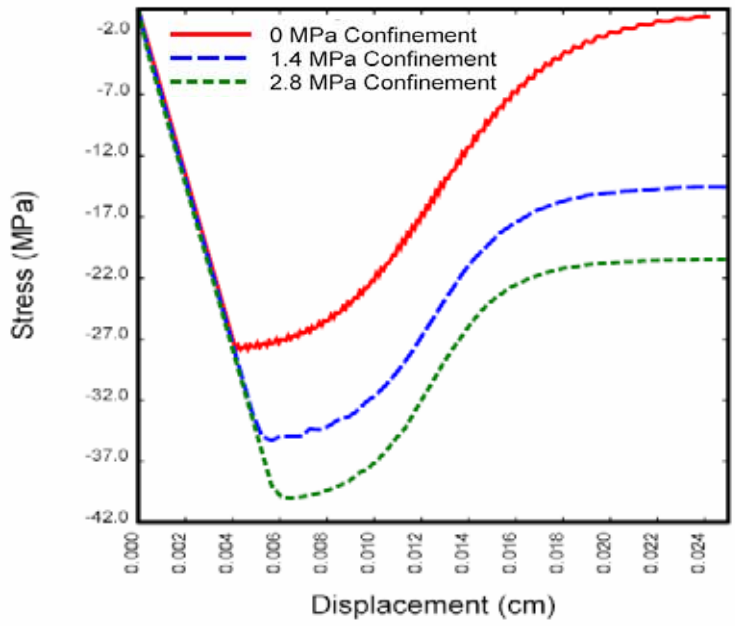

cm = 0.39 inch

Figure 2. Strength and ductility increase with confining pressure in these triaxial compression simulations.

VOLUME EXPANSION

Standard concrete exhibits volume expansion under compressive loading at low confining pressures less than about 100 MPa (14,504 lbf/inch^2). This volume expansion is called dilation and is calculated in the concrete model by the plasticity formulation. The volumetric behavior of the model is shown in Figure 3 for uniaxial compressive stress for 35 MPa (5,076 lbf/inch^2) concrete. The volume initially compacts during the elastic phase, because Poisson's ratio is less than 0.5. Volume expansion commences at peak strength and continues throughout the combined plasticity-softening phase. The effective Poisson's ratio during dilation may exceed 0.5

CYCLIC LOADING

As concrete softens, its stiffness also degrades. Stiffness degradation is shown in Figure 4 for uniaxial stress with cycling from tension to compression, and then back to tension for 45 MPa (6,527 lbf/inch^2) concrete. The unloading occurs along a different slope (degraded modulus), then the initial loading slope (undamaged modulus). In addition, when the state of stress transitions from tension to compression, the undamaged modulus is recovered (recovered modulus). This is the default option obtained with *recov* = 0. If *recov* = 1, the modulus remains fully degraded when transitioning from tension to compression. If *recov* is set between 0 and 1, the modulus remains partially degraded.

PRESSURE VERSUS VOLUMETRIC STRAIN

Concrete hardens due to pore compaction. Consider the pressure versus volumetric strain behavior of the model shown in Figure 5. One simulation was conducted for isotropic compression (also called hydrostatic compression), the other for uniaxial strain. Note that the pressure versus volumetric strain curves differ. This is because the amount of compaction depends upon the amount of shear stress present. Less pressure is required to compact concrete to a given volumetric strain when shear stress is present (the uniaxial strain simulation), than when shear stress is not present (the isotropic compression simulation). This behavior is known as shear enhanced compaction. It occurs in concrete and most geological materials. Slight shear enhanced compaction at low confining pressures is expected in roadside safety applications.

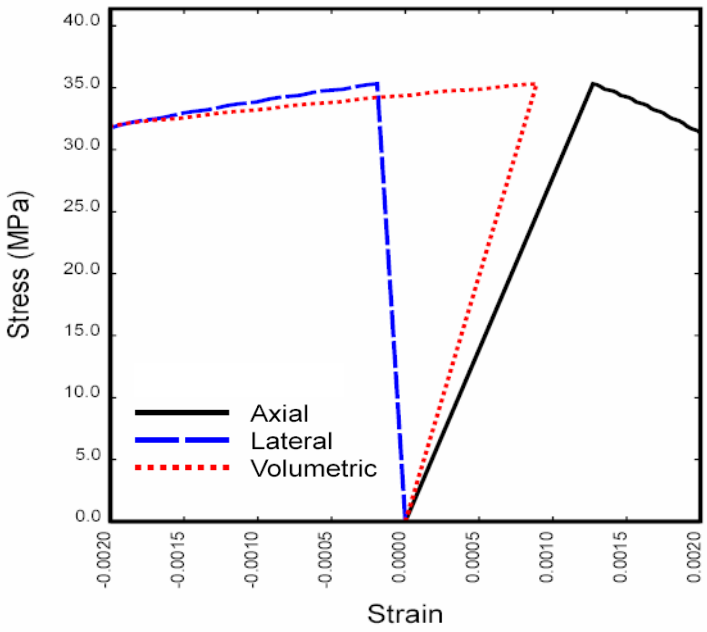

psi = 145.05 MPa

Figure 3. The concrete model simulates volume expansion in uniaxial compressive stress, in agreement with typical test data (strains and stress positive in compression).

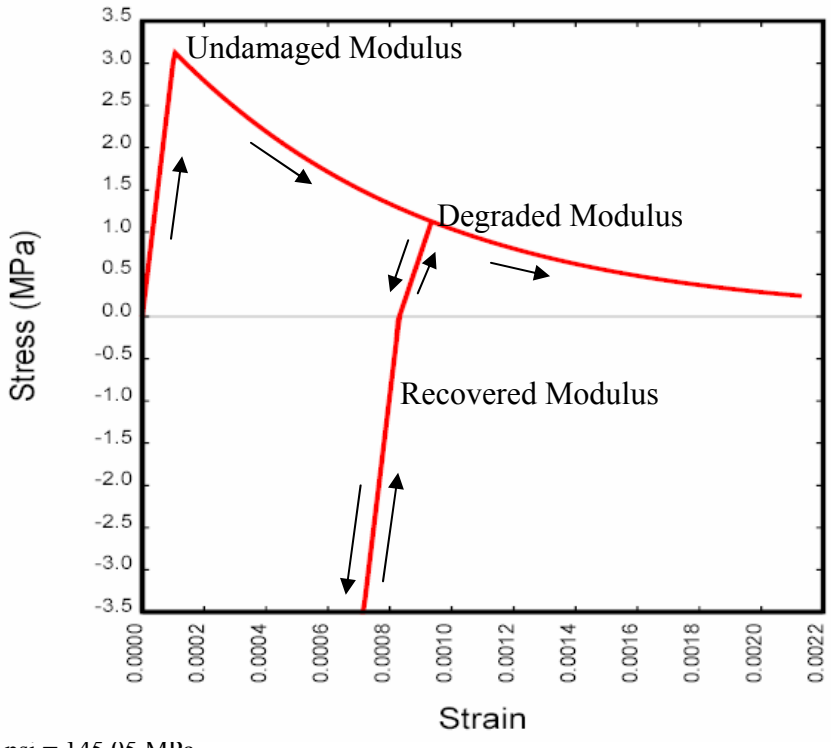

psi = 145.05 MPa

Figure 4. The modulus of concrete degrades with strength, as demonstrated by this cyclic loading simulation.

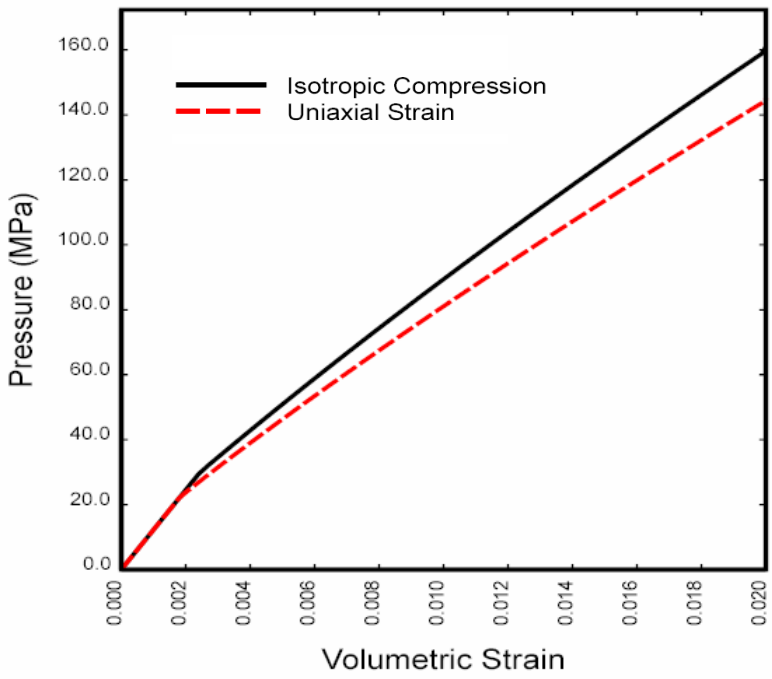

psi = 145.05 MPa

Figure 5. The difference in pressure at a given volumetric strain for these isotropic compression and uniaxial strain simulations is due to shear enhanced compaction.

RATE EFFECTS

The strength of concrete increases with increasing strain rate. For roadside safety applications, strain rates in the 1 to 10 per second (sec) range will produce peak strength increases of about 35 to 50 percent in compression and 150 to 300 percent in tension. The initial elastic modulus does not change significantly with strain rate.

Rate effects are computationally demonstrated in Figures 6–8 for simulations conducted in uniaxial tensile stress, pure shear stress, and uniaxial compression stress. The simulations were conducted at a high-strain rate of 100/sec. Note that the increase in strength in tension and shear is much greater than that in compression. Also note that the softening response depends on the value of *repow*. A value of *repow* = 0 minimizes the fracture energy. A value of *repow* = 1 increases the fracture energy in proportion to the increase in strength, and is the default value.

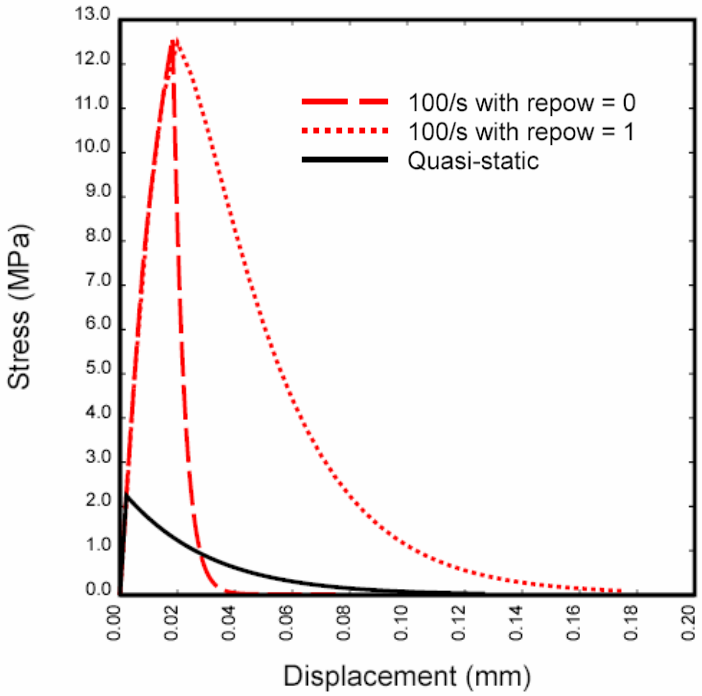

psi = 145.05 MPa, mm = 0.039 inch

Figure 6. The increase in strength with strain rate is significant in tension at a strain rate of 100 per second.

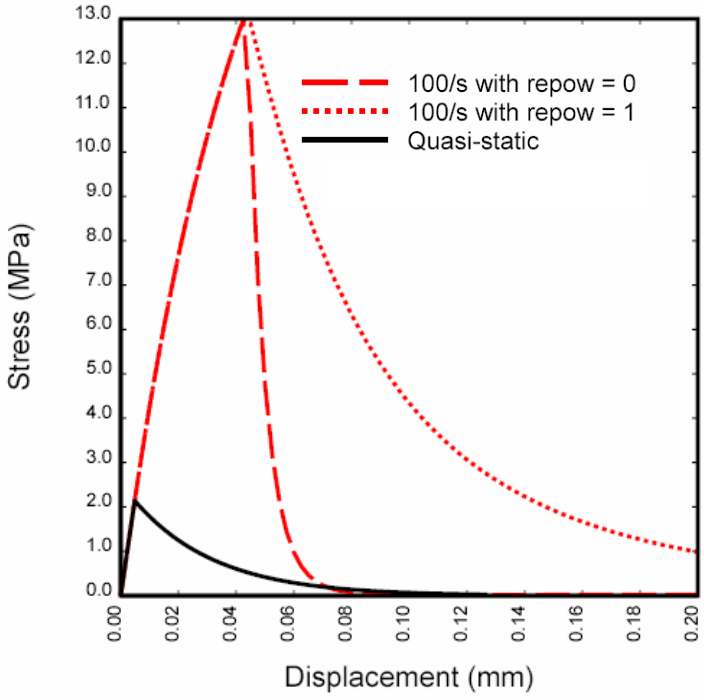

psi = 145.05 MPa, mm = 0.039 inch

Figure 7. The increase in strength with strain rate in pure shear stress is similar to that modeled in uniaxial tensile stress.

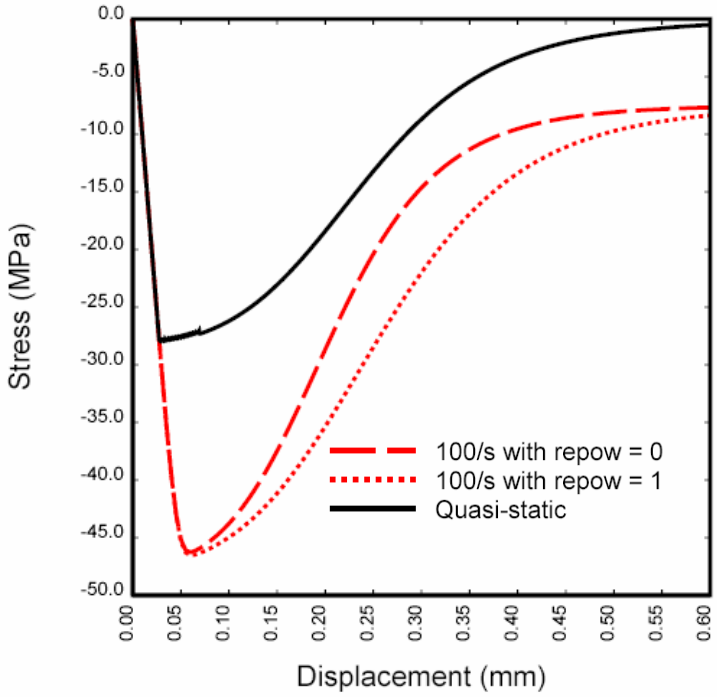

psi = 145.05 MPa, mm = 0.039 inch

Figure 8. The increase in strength with strain rate in uniaxial compression stress is less pronounced than in uniaxial tensile stress or pure shear stress.

KINEMATIC HARDENING

One optional variation on the behavior previously shown in Figure 2 is the addition of prepeak nonlinearity simulated with the kinematic hardening formulation. Such behavior is shown in Figure 9 for uniaxial stress in compression. Dilation initiates when hardening initiates, just prior to peak strength. Prepeak nonlinearity is more pronounced in compression than in tension or shear. This formulation is optional and not default because it is not essential to good performance of the model. The developer has found that accurate modeling of the damage fracture energies and rate effects are the key behaviors needed for good correlations with most dynamic roadside safety test data.

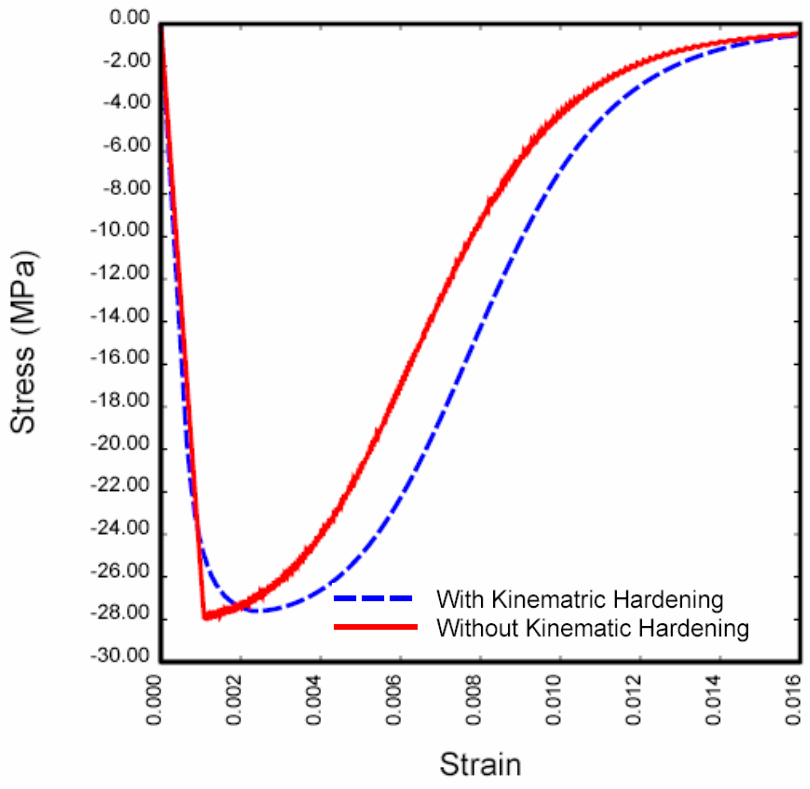

psi = 145.05 MPa

Figure 9. Application of kinematic hardening simulates prepeak nonlinearity accompanied by plastic volume expansion.

CHAPTER 3. SINGLE MATERIAL CYLINDER SIMULATIONS

Simulations of plain concrete allow us to evaluate the behavior of the concrete model without the complicating effects of the steel reinforcement. One such set of simulations performed were quasi-static loading of plain concrete cylinders in tension and compression. These simulations demonstrate that the concrete model simulates the basic damage modes observed in tests. These are splitting of the cylinder in tension, and diagonal failure in compression, as shown in Figure 10.

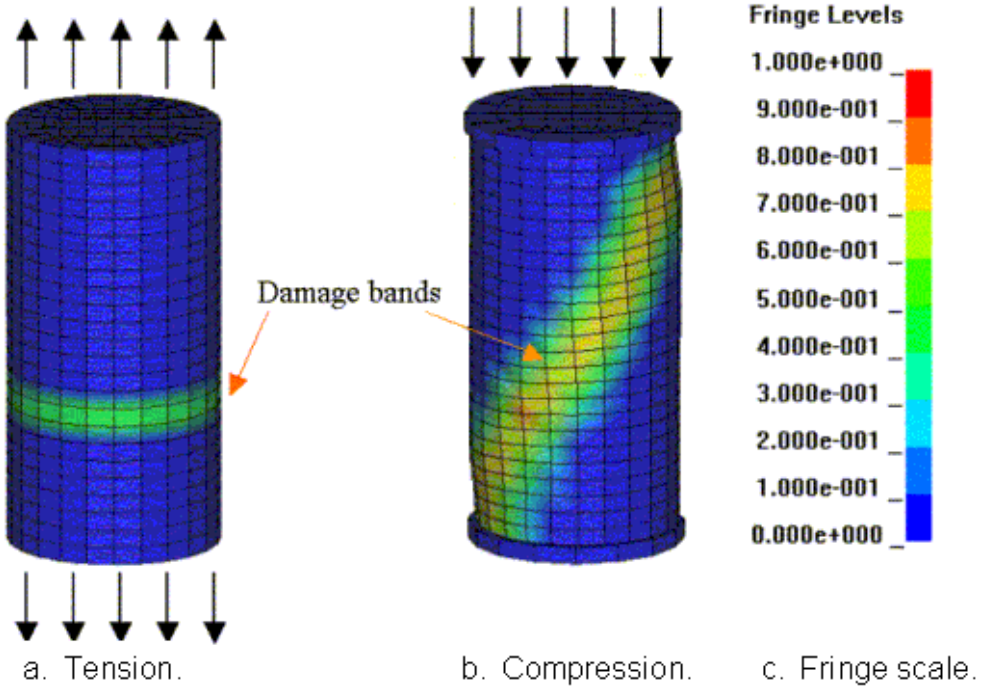

Figure 10. Realistic damage modes are simulated in concrete cylinders loaded in tension and compression.

CYLINDER GEOMETRY AND LOADING CONDITIONS

The cylinder analyzed is 304.8 mm (12 inches) long and 152.4 mm (6 inches) in diameter. Loading conditions are direct pull (uniaxial tensile stress) and unconfined compression (uniaxial compression stress). These are achieved by applying a uniform constant velocity to the nodes at one end of the cylinder (tension) or to the end caps (compression). Velocity is used to represent displacement control, rather than pressure or force conditions, in order to model softening following peak strength. Steel end caps, with slight friction between the cap and cylinder, are modeled in compression in order to simulate the diagonal failure observed in compression tests conducted as part of the bogie vehicle impact tests. Idealized end conditions in compression (applied nodal velocities without lateral constraint or friction) produce wedge-type failure, rather than diagonal failure. Laterally constrained ends produce two diagonal bands of damage (damage in an X-shape), as discussed in subsequent paragraphs.

The fringes shown in all deformed configuration plots of this paper range from 0 to 1 and indicate the level of damage calculated by the concrete model. A fringe value of 0 indicates no damage, so concrete strength and stiffness are those originally specified as input values. A fringe value of 1 indicates maximum damage, in which the concrete strength and stiffness are reduced to zero. Elements ERODE (are removed from the calculation and figure) when damage exceeds 0.99 and the maximum principal strain exceeds a user-specified value (typically between 0 and 0.10). An example fringe scale is given in Figure 10, which relates damage level to color. Alternatively, for those with difficulty distinguishing color, lighter fringes indicate higher levels of damage. Commentary is added to figures, where needed, to identify fringes of high damage.

CYLINDER TENSION RESPONSE

One boundary condition is analyzed for direct pull of the cylinders. The boundary condition is no lateral constraint on the ends of the cylinder so the cylinder is free to expand or contract laterally along its entire length. This idealized condition produces a realistic damage mode (breaking of the cylinder along one band of elements), as shown in Figure 11.

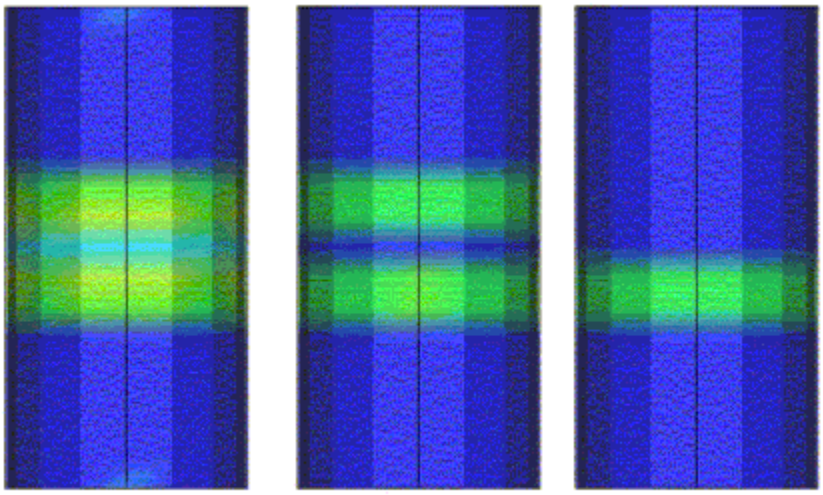

Figure 11. Two bands of damage initiate symmetrically about the axial midplane, then one band of damage rapidly dominates.

Initially, at very low damage levels, two bands of damage form, as shown at 13.598 milliseconds (msec). These bands are symmetrically located relative to the axial midplane of the cylinder. The location of the damage bands is thought to be dependent upon wave propagation within the cylinder, because the applied nodal velocities and damage bands are symmetric about the midplane. However, following initial formation, one of these bands becomes more dominant than the other band. Such asymmetric behavior probably results from numerical roundoff during brittle softening. This calculation demonstrates that a realistic damage mode is simulated by the concrete model in tension.

CYLINDER COMPRESSION RESPONSE

Damage Modes Observed in Tests

The damage mode observed in cylinder compression tests depends upon the end conditions of the test, as schematically shown in Figure 12. These figures are reproduced from a text by Bazant and Planas.[9] Cylinders with fixed ends exhibit two diagonal bands of damage. Cylinders with one fixed end and one sliding end (with negligible friction) exhibit a single diagonal band of damage. *Small* cylinders tested with two sliding ends with negligible friction (well lubricated platens or brushes) may split axially. Supposedly, these end conditions do not resist axial splitting. In practice, an axial split is difficult to achieve during testing.

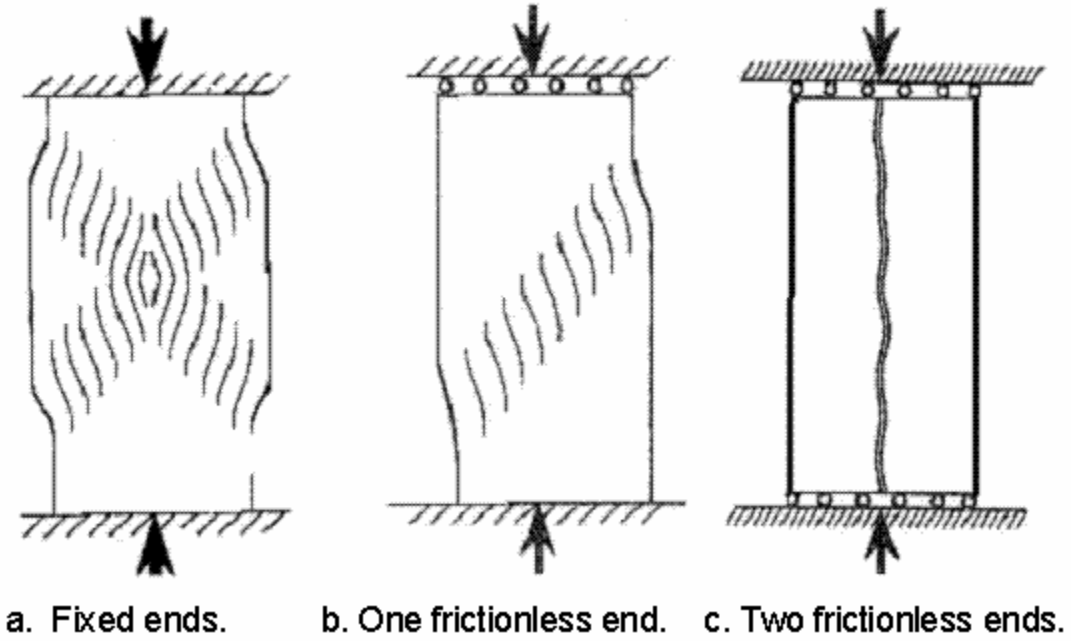

Figure 12. Damage modes observed in cylinder compression tests as a function of end conditions. Source: CRC Press.[9]

Fixed End Conditions

Cylinders with fixed ends (laterally constrained ends) were analyzed at three different mesh refinements, and all produced two diagonal bands of damage, consistent with schematic test results shown in Figure 12. Damage fringes from one refined mesh simulation are shown in Figure 13 at various simulation times and rotations. Note that the X-shaped damage bands appear as O-shaped bands when the cylinder is rotated 90 degrees along its axis. The calculation was run for 1.5 sec, during which time the 304.8-mm (12-inch) cylinder was compressed 3.81 mm (0.15 inches). Some views show damage on a slice through the midplane of the cylinder. Other views show damage on the outside of the cylinder.

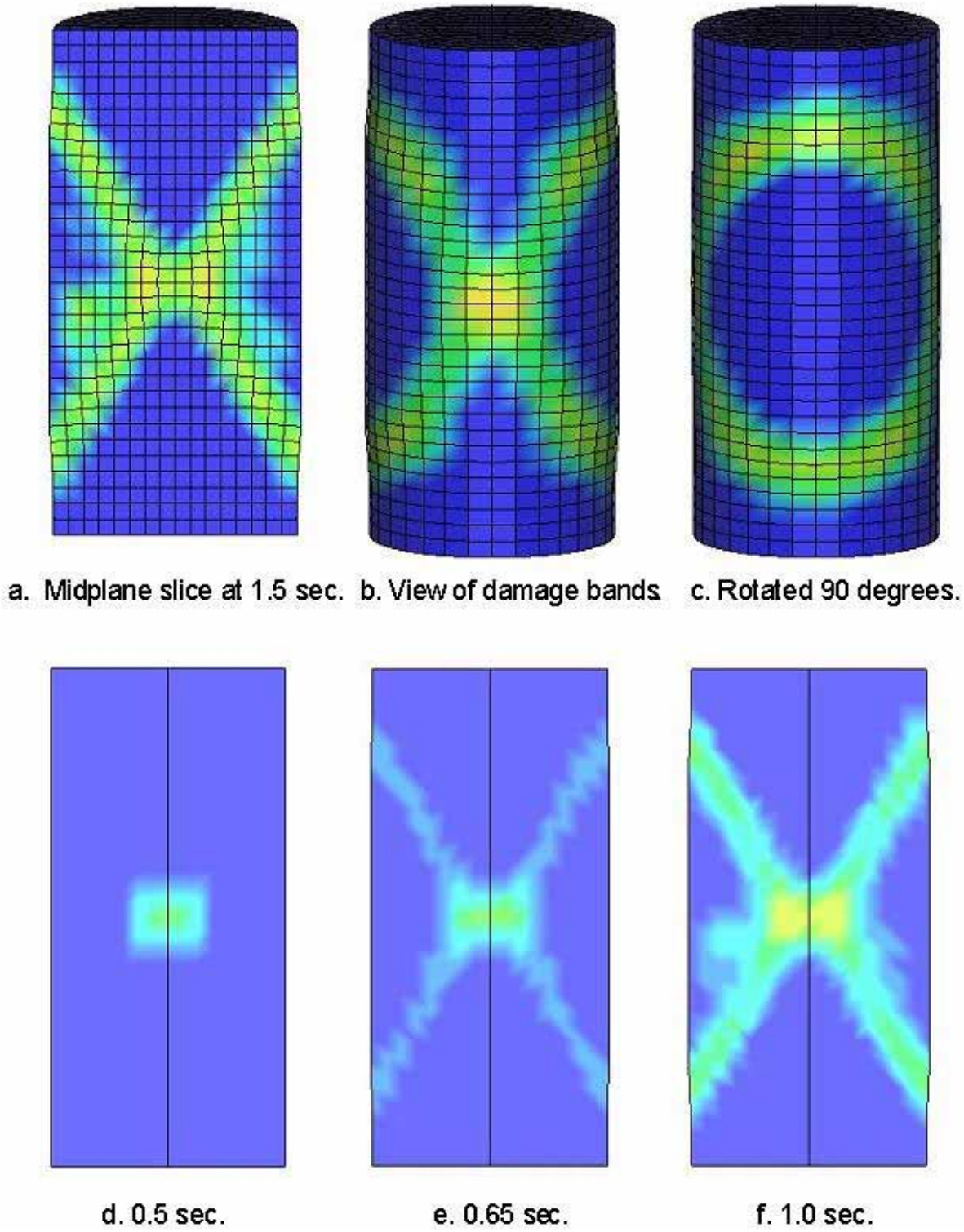

Figure 13. The damage mode calculated for compression cylinders with fixed ends agrees with the X-shaped damage bands observed in tests.

Capped End Conditions

Cylinders with steel end caps were also analyzed to determine the effect of frictional lateral end constraint on cylinder response. These calculations were performed because it is standard practice to cap cylinders during testing. Capping provides some lateral constraint. An example test cylinder, for the 46 MPa (6,672 lbf/inch^2) concrete used in the beams impacted by bogie vehicles, is shown Figure 14. Each idealized end cap is 165.1 mm (6.5 inches) in diameter (12.7 mm (0.5 inches) larger than the cylinders) and 12.7 mm (0.5 inches) in height. A contact surface is modeled between each end cap and the concrete cylinder using frictional coefficients ranging from 0.1 to 0.3. The contact surface type selected was *CONTACT_CONSTRAINT_NODES_TO_SURFACE using the soft contact option. The cylinder was loaded in compression by applying a constant axial velocity to the layer of nodes along the top of the top end cap. The bottom end cap was restrained from axial motion along the bottom layer of end cap nodes. A few sample calculations were performed to determine that compressing from one end of the capped cylinder gives approximately the same results as compressing from both ends.

Figure 14. Concrete cylinder tested as part of the bogie vehicle impact test series.

Five variations in boundary conditions were considered. They are:

1. No nodal constraints on the end caps to prevent them from sliding or rotating.
2. Constrain the bottom end cap from rotating and sliding.
3. Constrain the bottom and top end caps from rotating and sliding.
4. Constrain the bottom end cap from rotating and sliding and the top end cap from sliding.
5. Constrain the bottom and top end caps from sliding (rotation allowed).

Damage fringes from these five calculations are given in Figures 15–19. They indicate that the calculated damage mode depends on how the boundary conditions are modeled.

The first calculation without nodal constraints gives a distinct band of diagonal damage, as shown in Figure 15. However, further observation indicates that the capped cylinder is rotating about its longitudinal axis. To the eye, the rotation of the top cap is in sync with the rotation of the bottom cap (no relative rotation between the top and bottom caps). The top cap also slides laterally relative to the bottom cap.

The second calculation was conducted by laterally constraining some nodes of the bottom cap to prevent the bottom cap from rotating. This constraint also prevents the bottom end cap from sliding laterally. No nodal constraints were applied to the top cap, so it is free to slide and rotate relative to the bottom cap. Results of this calculation are shown in Figure 16. This calculation also gives a distinct band of diagonal damage. The diagonal band of damage forms prior to noticeable sliding of the top cap. Relative sliding of the top and bottom caps becomes apparent as the calculation progresses, as shown. Rotation of the top cap relative to the bottom cap is not apparent. These end constraints produce damage similar to that shown in Figure 12 for one frictionless end, because the frictionless end if free to slide relative to the fixed end.

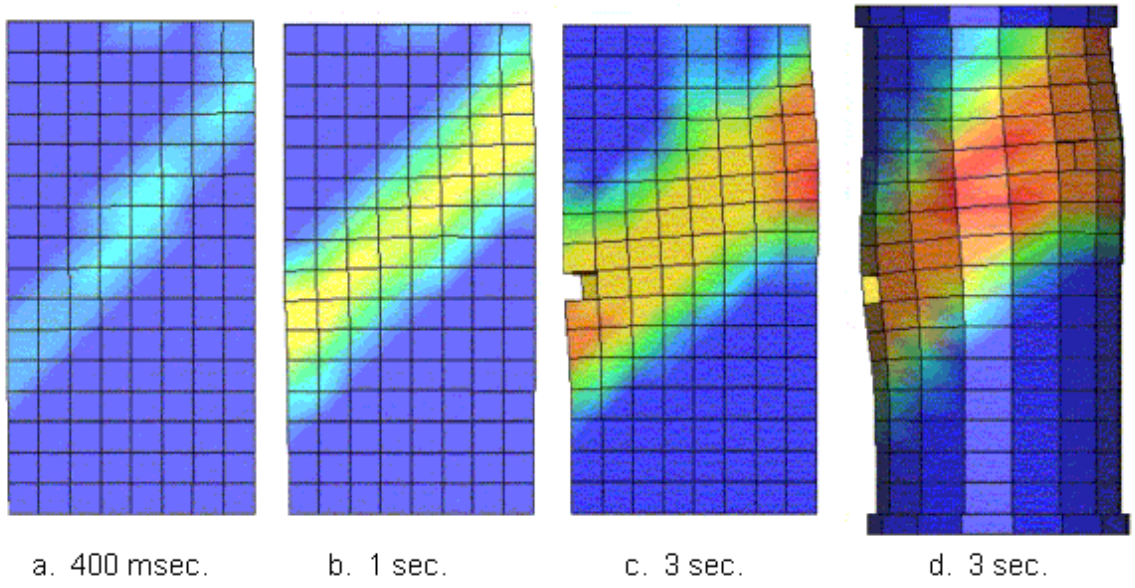

Figure 15. A diagonal band of damage is calculated with frictional end constraints if both end caps are allowed to rotate and slide (no end cap constraints).

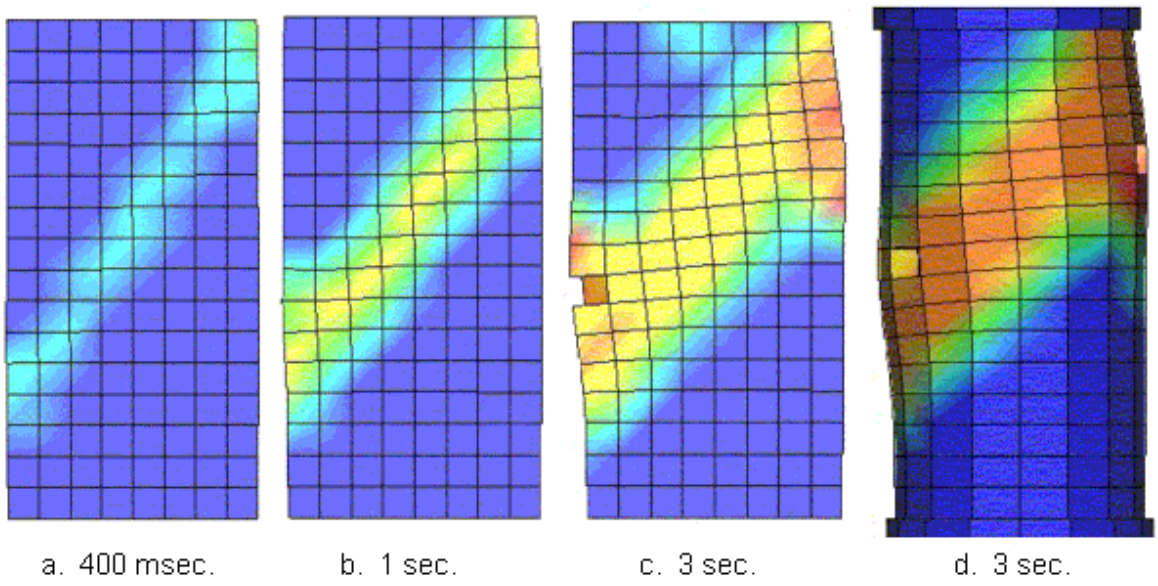

Figure 16. A diagonal band of damage is calculated with frictional end constraints if one end cap is allowed to rotate and slide relative to the other (bottom cap constrained from rotating and sliding).

The third calculation was conducted by preventing both the bottom and top end caps from rotating and sliding. This means that there is no relative rotation or relative sliding. This was accomplished by laterally constraining a few select nodes on each cap. Results of this calculation are shown in Figure 17. The damage mode calculated is initially two diagonal bands of damage, similar to the fixed end condition results. The difference between this calculation and the fixed end calculation is that this calculation allows for frictionally restricted lateral expansion at the cylinder ends, whereas the fixed end calculation allows no lateral expansion at the cylinder ends.

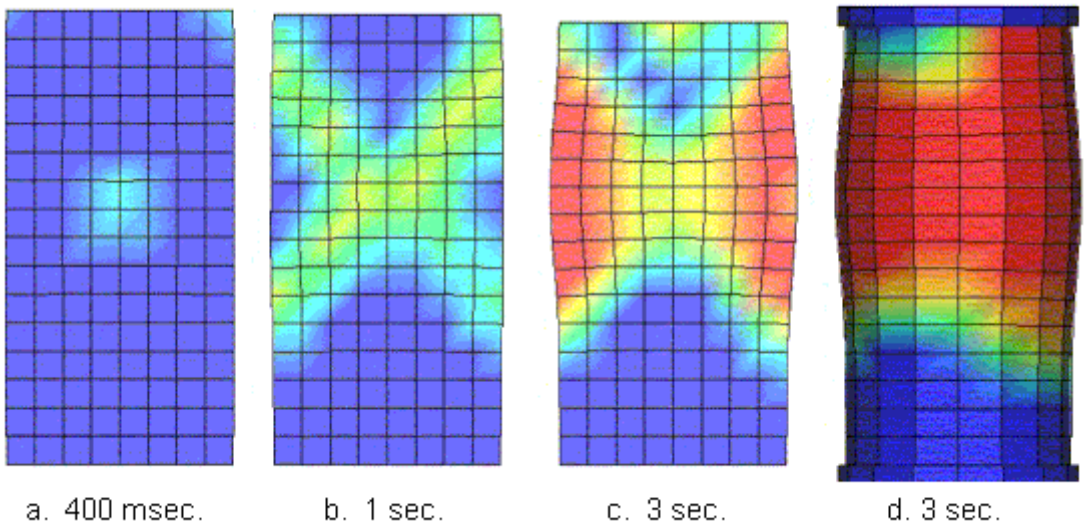

Figure 17. A double diagonal band of damage is initially calculated if both end caps are prevented from rotating and sliding (bottom and top caps constrained from rotating and sliding).

The fourth calculation was conducted by constraining the bottom cap from rotating and sliding laterally and the top cap from sliding laterally. The top cap is free to rotate relative to the bottom cap. Damage fringes from this calculation are shown in Figure 18. Again, two diagonal bands of damage form initially. Although the bands of damage are evident on an axial slice through the midplane, they are less distinct when viewed from the outside of the cylinder.

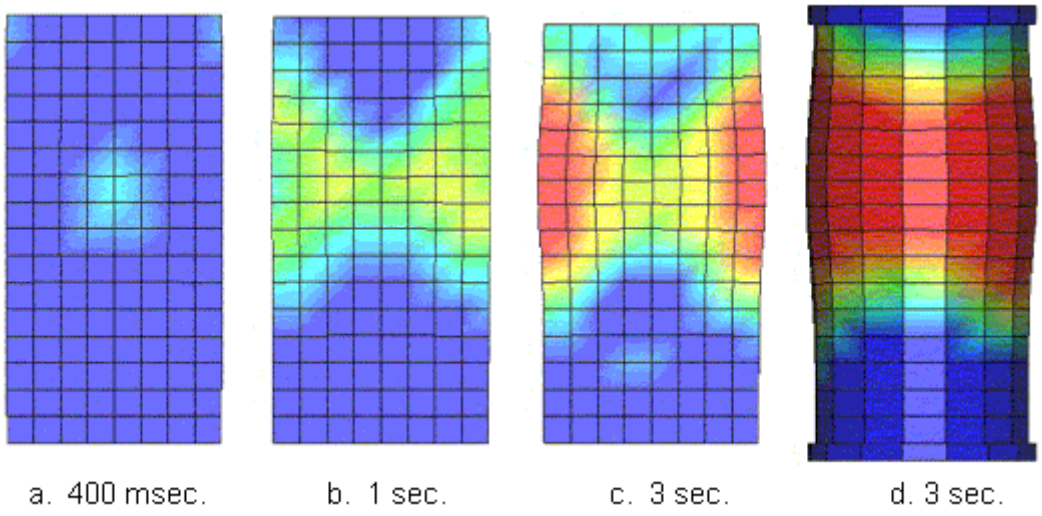

Figure 18. A double diagonal band of damage is initially calculated if one end cap is free to rotate (bottom cap restrained from rotating and sliding, top cap restrained from sliding).

The fifth calculation was conducted by constraining the bottom and top caps from sliding relative to one another, while allowing them to rotate. Initially, two diagonal bands of damage form, with one more prominent than the other, as shown in Figure 19.

The calculations just discussed indicate that one diagonal band of damage forms if the end caps are allowed to slide relative to one another, whether or not relative rotation of the end caps occurs. Otherwise, double bands of damage form initially, followed by severe bulging and damage towards the cylinder midheight. These calculations demonstrate that the concrete model accurately predicts a diagonal damage mode when the end conditions are modeled appropriately. They also indicate that slight variations in the boundary conditions affect the damage mode predicted.

The end caps calculations just discussed were all conducted with a 0.3 coefficient of friction (static and dynamic). Additional calculations conducted with a 0.1 coefficient of friction give similar results. Calculations conducted with a 0.01 coefficient of friction are discussed in the next section that reviews free or frictionless end conditions.

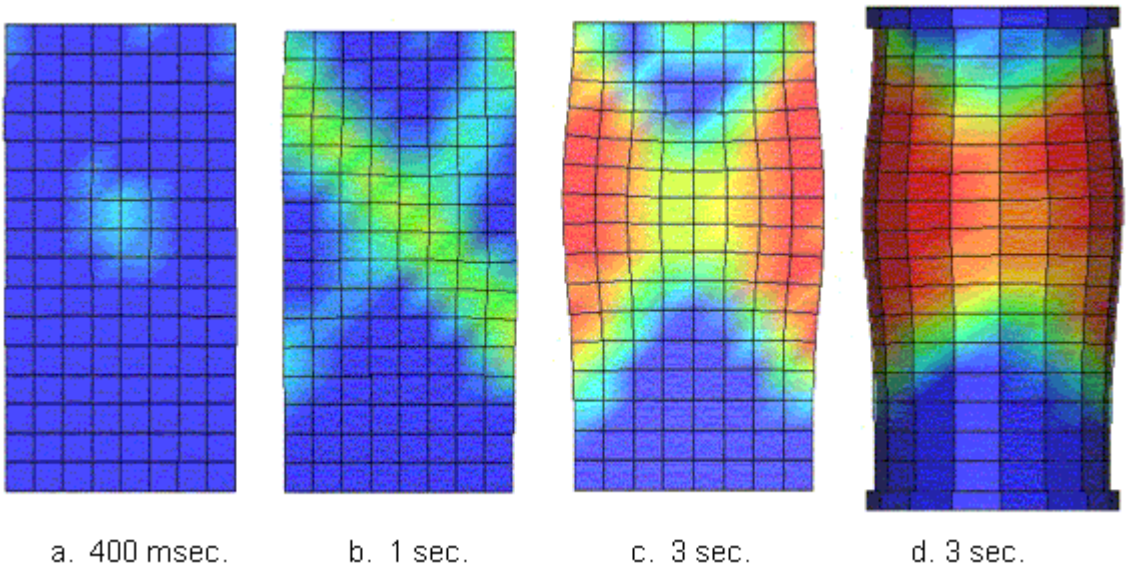

Figure 19. A single diagonal band of damage initiates, but is not retained, if the cylinder is over-constrained (bottom and top caps restrained from sliding).

Contact Surface Type

Use of additional contact surface types is discussed here to make users aware of issues surrounding the use of contact surfaces. Many of the previously discussed calculations with end caps were conducted with the *CONTACT_CONSTRAINT_NODES_TO_SURFACE interface. The CONSTRAINT option doesn't allow separation between the concrete cylinder and end caps. A few calculations were also conducted with the *CONTACT_NODES_TO_SURFACE and *CONTACT_SURFACE_TO_SURFACE interfaces. These options allow separation between the concrete cylinder and end caps.

The reason the *CONTACT_CONSTRAINT_NODES_TO_SURFACE interface was used in many calculations is because it did not result in any penetration between the concrete cylinder and end caps. Hence the axial displacement histories of the nodes on the end of the cylinder are the same as those on the caps. This makes post-processing easy, because the displacement history is readily calculated by scaling time by the applied nodal velocity. On the other hand, with most other contact surfaces and options selected, some penetration occurred between the cylinder and end caps, at least initially.

Consider two calculations conducted with the *CONTACT_SURFACE_TO_SURFACE interface. SURFACE_TO_SURFACE interfaces commonly are used because it is easier to call out a surface than to list all the nodes that define the surface. This particular interface also allows the concrete to separate from the end caps, as needed. Boundary conditions are one bottom end cap that is constrained from rotation and sliding, and a top end cap that is free to rotate and slide. In one calculation, default scale factors with a value of 1 were used for the slave and master surfaces (SFS = 1). In the other calculation, the slave surface scale factor was increased from 1 to 10 (SFS = 10). The diagonal damage band calculated with either of these scale factors (Figure 20) is the similar to that calculated with the *CONTACT_CONSTRAINT interface (previously shown as Figure 16).

Although the damage modes are similar, the stress-histories calculated with the SURFACE_ TO_SURFACE interface are different than that calculated with the CONSTRAINT option (Figure 21). One reason these stress-histories are different is because the end cap penetrates the concrete with the SURFACE_TO_SURFACE interface, but not with the CONSTRAINT interface, as shown in Figures 22 and 23. Nodes 1 and 8001 give the displacement histories at each end of the concrete cylinder. Nodes 9001 and 9501 give the displacement histories of the steel cap at the interface with the concrete cylinder. Nodes 18001 and 18501 give the displacement histories of the cap on the top and bottom free surfaces. The difference between the concrete displacements and end cap displacements is the amount of penetration present. Therefore, at a given time, the axial strain in the cylinder with penetration is less than that without penetration. The result is that the initial slopes of the stress histories are different, as previously shown in Figure 21. End cap penetration also occurs when the concrete material model is replaced with an elastic material model (Mat 1) of equivalent modulus (not shown).

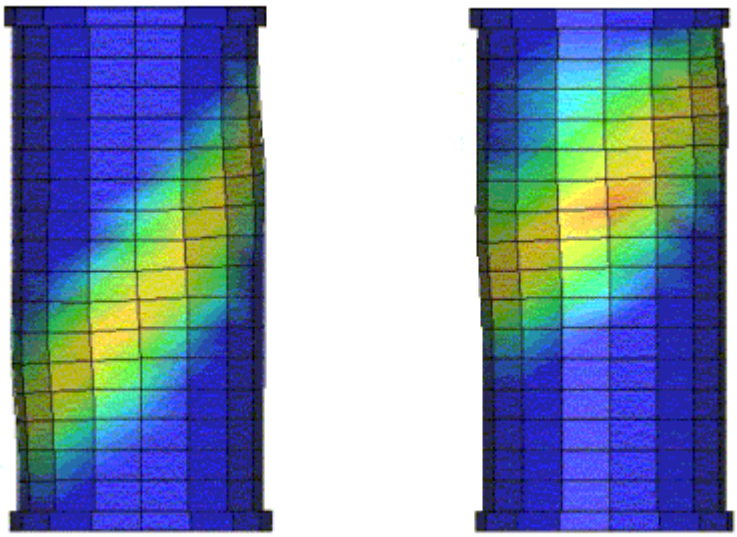

a. Slave surface scale factor = 1. b. Slave surface scale factor = 10

Figure 20. Diagonal damage bands are calculated using the *CONTACT_AUTOMATIC_SURFACE_TO_SURFACE option, although the diagonal band location varies with scale factor.

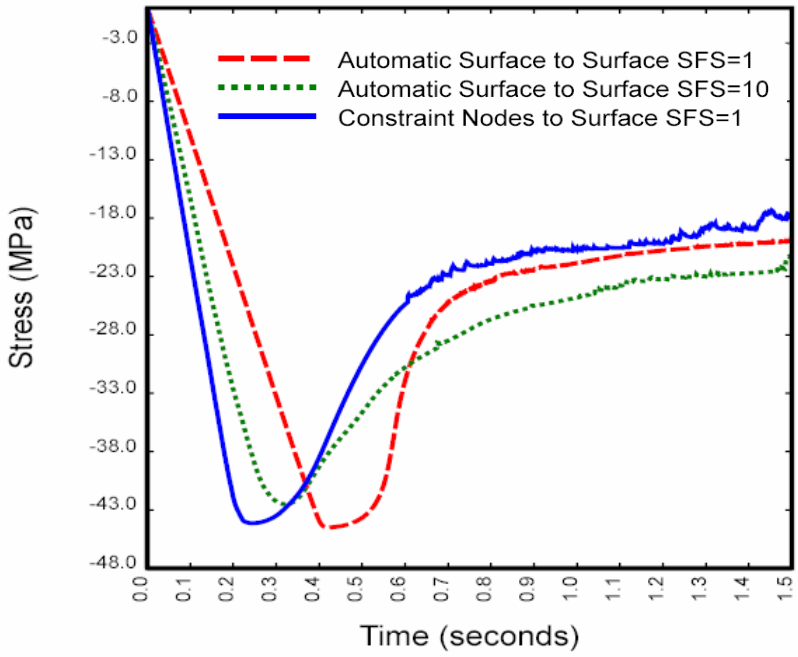

psi = 145.05 MPa

Figure 21. Differences in initial slope are primarily due to differing amounts of contact surface penetration between the concrete cylinder and end caps.

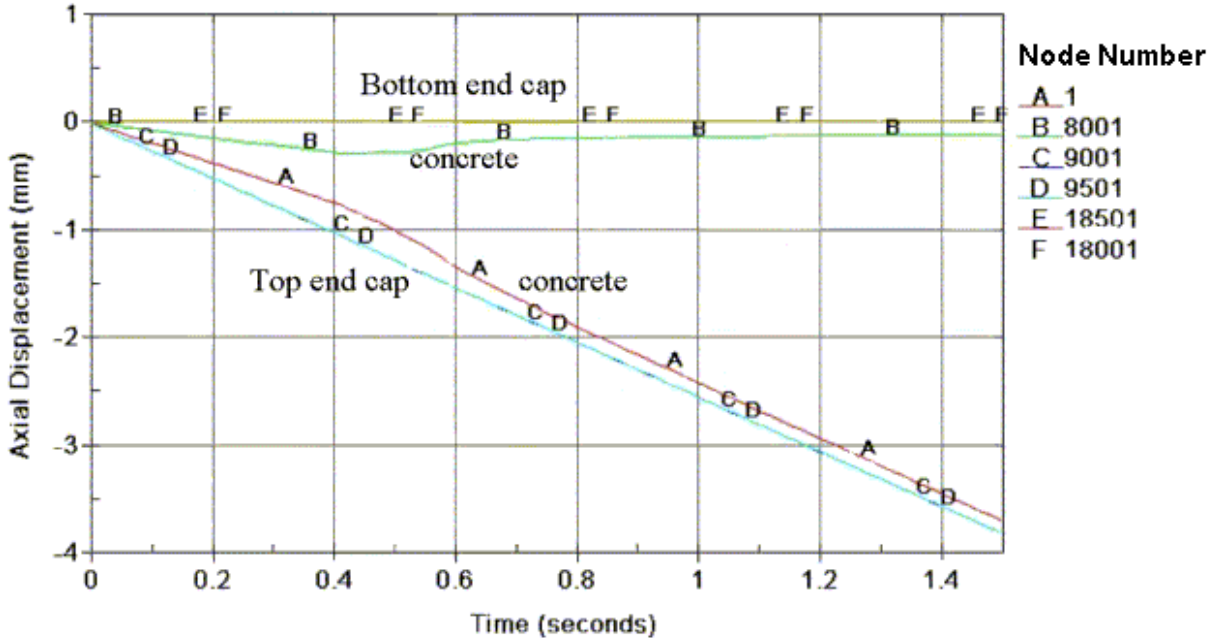

mm = 0.039 inch

Figure 22. End cap versus concrete displacement with penetration (SFS = 1).

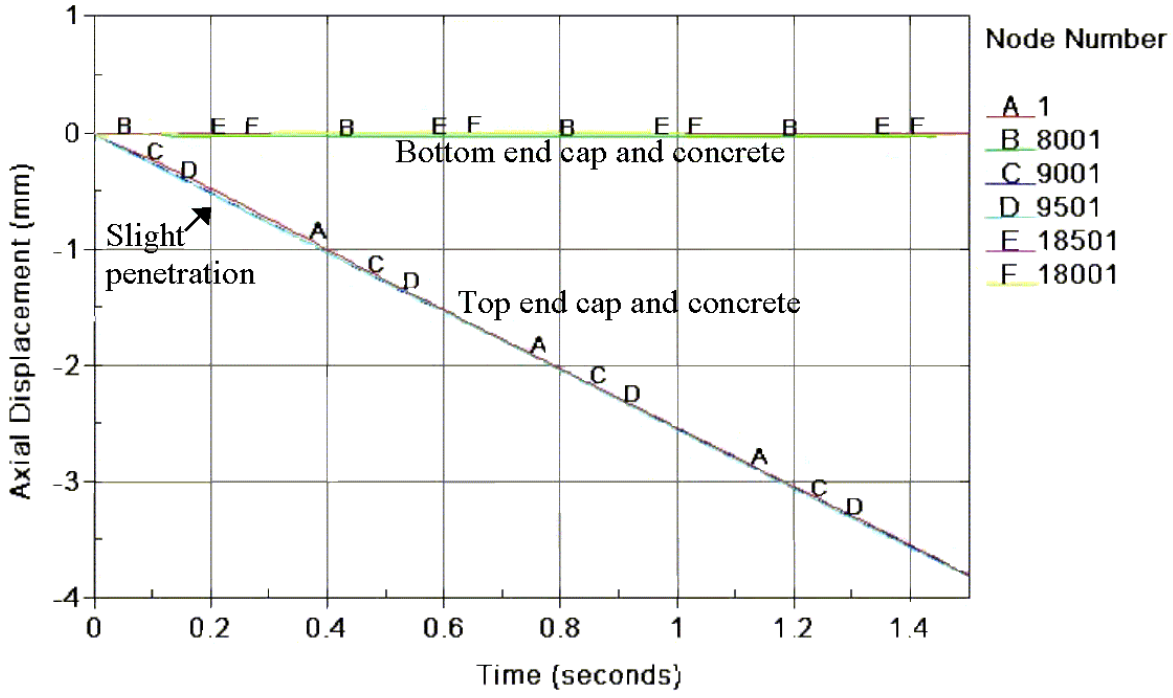

mm = 0.039 inch

Figure 23. End cap versus concrete displacement with little penetration (SFS = 10).

Stress versus displacement is obtained from a cross plot of the concrete stress history with the concrete displacement history. One must take special care in extracting the correct displacement history. If penetration occurs, use of the end cap displacement histories would overestimate the compression of the concrete. The result is that the concrete elastic modulus would appear to be lower than the user-supplied input value. This is easily corrected by using nodal displacement histories at the ends of the concrete cylinder, rather than on the end caps, as shown in Figure 24. The relative displacement plotted is the difference between the nodal displacements at the ends of the concrete cylinder. Note that at any given time, the relative displacement calculated with the SURFACE_TO_SURFACE interface with SFS = 1 is less than that calculated with the CONSTRAINT interface.

The corresponding stress versus displacement histories are shown in Figure 25. Note that with use of the correct concrete displacement history, two of the calculations are in good agreement. The exception is the calculation conducted with SFS = 10. The reason it is different is due to the presence of early time tensile damage, as discussed in the following paragraph.

Different options are available to relieve penetration. One is the soft constraint option. This option is recommended for use when the materials on each side of the interface have different stiffness, like steel and concrete. This option relieves some, but not all, of the penetration. Another option is to increase the scale factor of the concrete (slave) surface by a factor of 10. This option successfully prevents penetration of the end caps into the concrete (Figure 23). As desired, a diagonal damage band forms. The only concern is that slight tensile damage initiates near the contact surface very early in time at 20 msec, before the time of peak strength at 400 to 500 msec, as shown in Figure 26. This tensile damage is triggered by axial extension of the concrete in the vicinity of the contact surface. Such tensile damage has also been observed in some, but not all, of the calculations conducted with the *CONTACT_CONSTRAINT option. The early-time tensile damage lowers the stiffness of the concrete relative to that observed in calculations without early-time tensile damage, as previously shown in Figure 25.

In summary, the contact surface parameters and interface type affect damage initiation in these cylinder compression calculations. This effect appears to be due to the presence of early time tensile damage in the vicinity of the contact surface. In some calculations, this early time damage results in an accumulation of damage near one end of the cylinder. In other calculations, single and double bands of damage form, as desired. When creating stress-displacement curves, the displacement at the ends of the cylinder should be used to get the right modulus, if penetration between the end caps and concrete cylinder occurs.

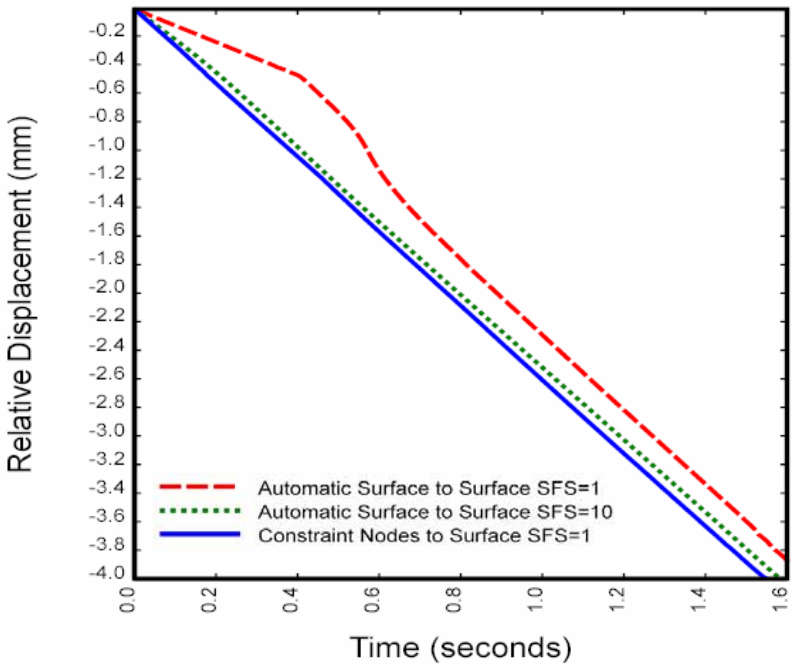

mm = 0.039 inch

Figure 24. The relative displacement between the ends of the concrete cylinder depends on the amount of interface penetration present.

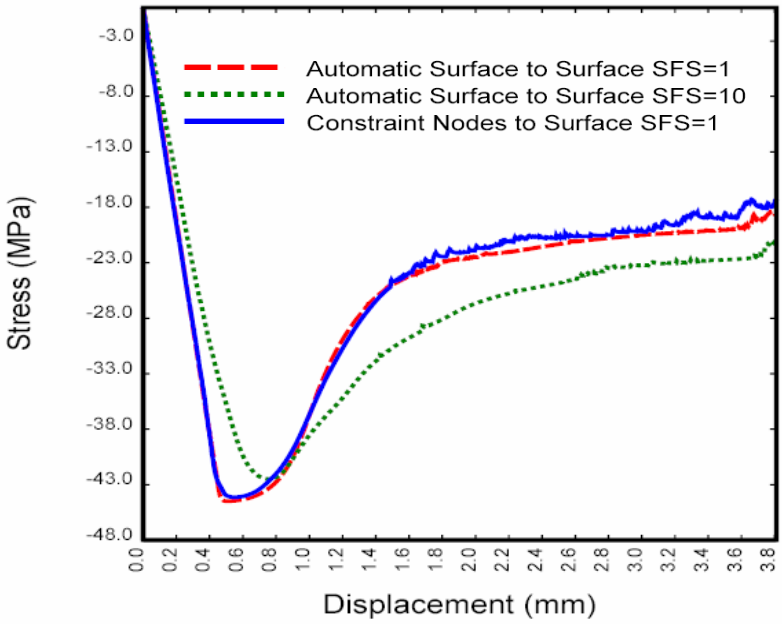

psi = 145.05 MPa, mm = 0.039 inch

Figure 25. The stress-displacement histories are in reasonable agreement if the relative displacement of the cylinder is used.

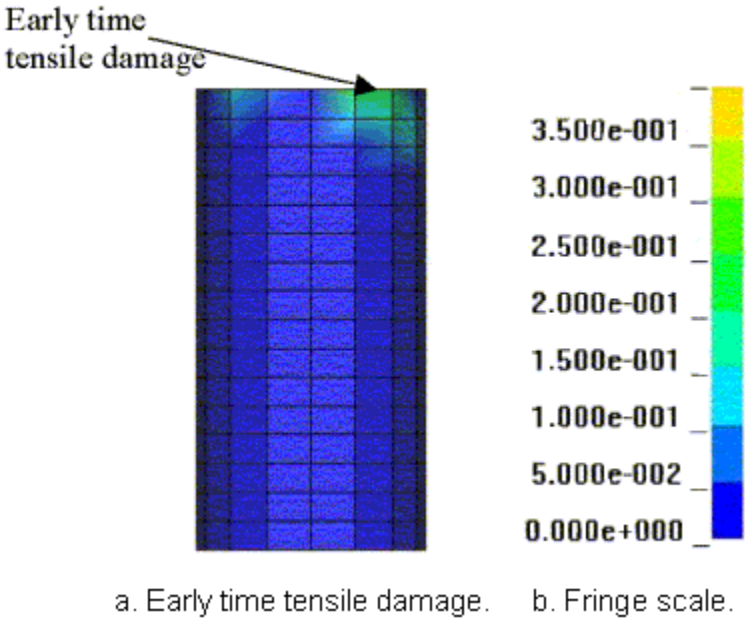

a. Early time tensile damage. b. Fringe scale.

Figure 26. Early time tensile damage occurs in some compressive cylinder calculations in the vicinity of the contact surface interface.

CHAPTER 4. REGULATION OF SOFTENING FORMULATION

One desirable attribute of the finite element method is convergence of the solution with reasonable mesh refinement. However, finite element solutions are known to have difficulty converging if the materials being modeled contain softening formulations. With softening formulations, there is a tendency for the greatest amount of damage to accumulate in the smallest elements. This is the result of modeling smaller fracture energy in the smaller elements. To overcome this tendency, a regulatory method was implemented to promote convergence by eliminating element-to-element variation in fracture energy. Refer to this report's companion Users Manual for a theoretical discussion of the regulatory technique implemented.[6] This chapter demonstrates convergence of results using the regulatory technique implemented for both single element and single material simulations.

SINGLE ELEMENTS IN TENSION AND COMPRESSION

Calculations were performed with single elements as a first step in evaluating mesh objectivity of the softening response. Calculations were performed for four cube sizes: 12.7 mm (0.5 inches), 38.1 mm (1.5 inches), 76.2 mm (3 inches), and 152.4 mm (6 inches) on each side. Each cube is modeled with quarter symmetry using nodal boundary conditions. Two loading conditions are analyzed. These are direct pull (uniaxial tensile stress) and unconfined compression (uniaxial compression stress). In each case, a uniform constant velocity is applied to the four nodes at one end of the element, while the four nodes at the other end are restrained from axial motion (lateral motion is not restrained). The velocity is 2.54 millimeters per second (mm/sec) (0.1 inch per second (inch/sec)) and is held constant for the duration of the simulations.

Stress-displacement curves for the direct pull simulations are shown in Figures 27 and 28. All elements exhibit linear elastic behavior to peak strength, followed by softening. The strength is independent of element size, although the displacement at peak strength increases with increasing element size. If stress-strain rather than stress-displacement were plotted (not shown), then all elements would peak at the same strain level (as expected).

Shifted stress-displacement results are shown in Figures 27 and 28. The curves are shifted by subtracting the displacement at peak stress from the displacement history. With such manipulation, the peak stress of each curve is plotted at a shifted displacement of 0. Plotted in this manner, the softening portion is identical for each curve, as desired. Hence the fracture energy (area under the softening portion of the stress-displacement curve) is constant from one element to another. These simulations demonstrate that the element-based softening theory is accurate and implemented without any coding errors.

Stress-displacement results for the unconfined compression simulations are shown in Figures 29 and 30. Once shifted, the softening portions of the four stress-displacement curves are close to, but not exactly equal to, each other. Careful checking of these results indicates that all four curves have the same fracture energy, but not the same shape. Note that all four curves have a point of agreement around 0.25 mm (0.01 inches) of displacement. For displacements less than

0.25 mm (0.01 inches), the smaller elements soften more rapidly than the larger elements. For displacements greater than 0.25 mm (0.01 inches), the smaller elements soften less rapidly than the larger elements. The overall result is consistent fracture energy from element to element.

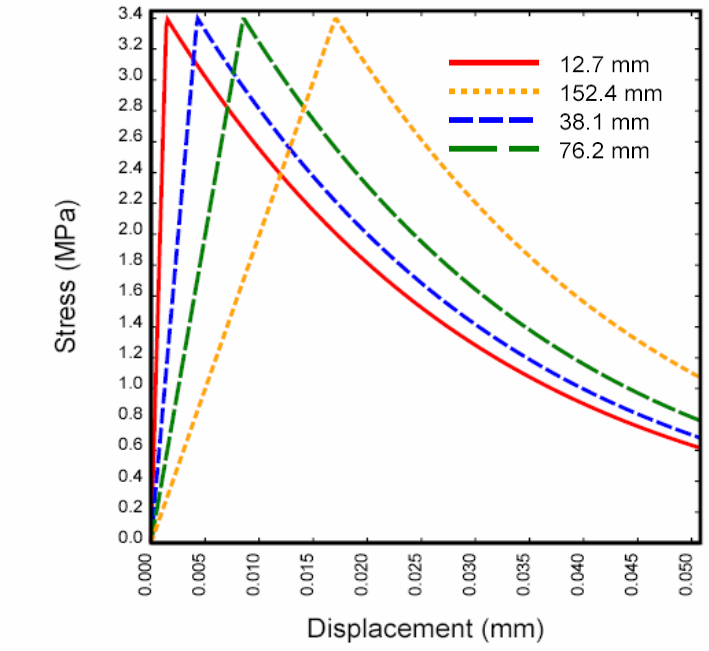

psi = 145.05 MPa, mm = 0.039 inch

Figure 27. The fracture energy, which is the area under the softening portion of the stress-displacement curve, is independent of element size in the direct pull simulations (not shifted).

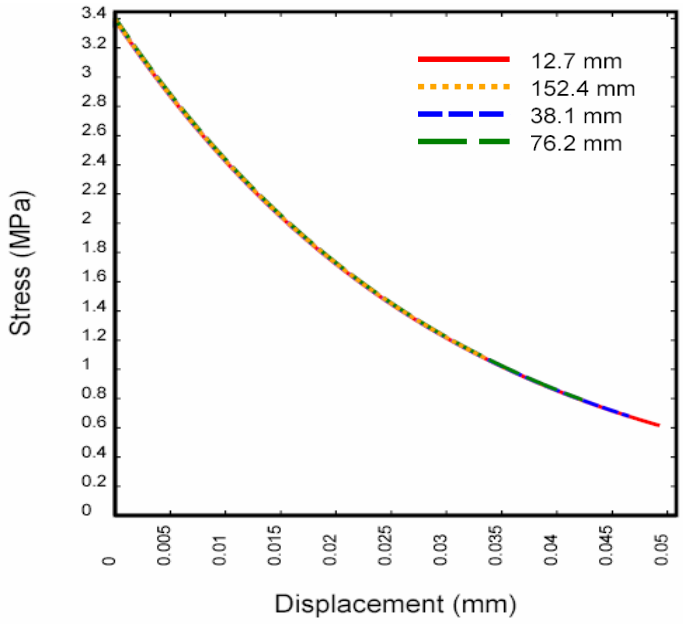

psi = 145.05 MPa, mm = 0.039 inch

Figure 28. The fracture energy, which is the area under the softening portion of the stress-displacement curve, is independent of element size in the direct pull simulations (shifted to displacement at peak stress).

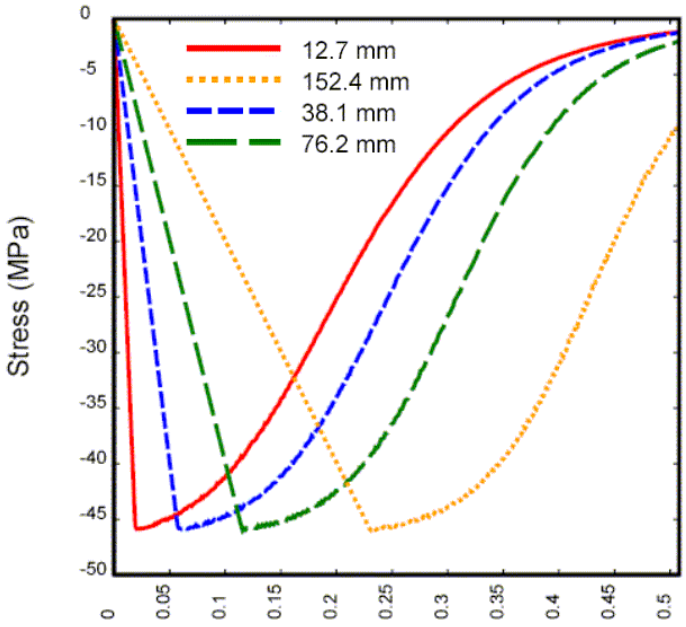

psi = 145.05 MPa, mm = 0.039 inch

Figure 29. Although the fracture energy is constant, the softening curves vary slightly with element size in the unconfined compression simulations (not shifted).

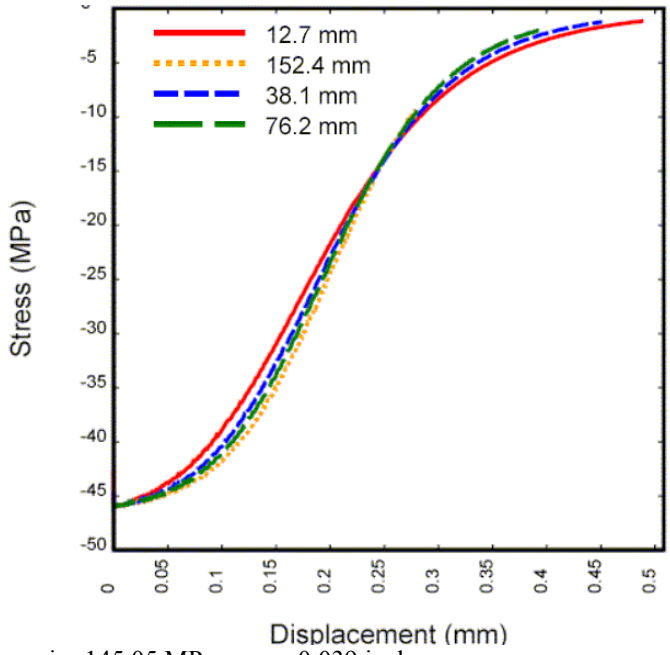

psi = 145.05 MPa, mm = 0.039 inch

Figure 30. Although the fracture energy is constant, the softening curves vary slightly with element size in the unconfined compression simulations (shifted to displacement at peak stress).

These results indicate that in compression, the regulatory method allows small differences in softening behavior to occur as a function of element size. However, the author suggests that the regulation is adequate despite these small differences. Figure 29 and 30 show that the largest and smallest elements vary in size by a factor of 12. This variation in element size is much larger than that typically meshed by most analysts. Within a region of interest, a factor of 2 variations in element size is typical. The 38.1-mm (1.5-inch) and 76.2-mm (3-inch) elements in Figures 29 and 30 vary in size by a factor of 2, and their difference in softening response is minimal.

CYLINDERS IN TENSION AND COMPRESSION

The objective of this chapter is to demonstrate mesh size sensitivity, and its regulation, for direct pull and unconfined compression of a concrete cylinder. This chapter begins with a description of each mesh used in the calculations, followed by results of calculations performed without regulation of the softening formulation. In general, these calculations do not converge to a unique solution and therefore demonstrate mesh size sensitivity, which is undesirable. This demonstration is followed by a theoretical discussion of softening formulations, with and without regulation. The chapter then discusses the results of calculations performed with regulation. The direct pull simulations demonstrate convergence to a unique solution with reasonable mesh refinement. The unconfined compression calculations tend toward convergence, but do not actually converge. Finally, conclusions are drawn concerning application of the technique implemented for regulating convergence of material models containing softening formulations.

Details of Each Cylinder Mesh

The specimen analyzed is a concrete cylinder that is 304.8 mm (12 inches) long and 152.4 mm (6 inches) in diameter. This simple structure is being analyzed because it isolates one softening material model of interest, without interaction with other materials or complications from detailed boundary conditions or contact surfaces.

Cylinders of two mesh refinements are analyzed, as shown in Figure 31. The basic mesh contains 768 solid elements. This mesh refinement is intended to be typical of what most users would generate to simulate a cylinder test. The more refined mesh contains 2,592 solid elements. This mesh is more refined than what most users would generate. In addition, one single element and a two element mesh are analyzed. The single element is 304.8 mm (12 inches) long and 135.1 mm (5.32 inches) along each edge of the square cross section, in such manner that the volume of the single element is equal to the volume of the cylinder. Each element of the two element mesh is 152.4 mm (6 inches) long, with a 135.1 mm (5.32 inches) by 135.1 mm (5.32 inches) cross section.

Two loading conditions are analyzed. These are direct pull (uniaxial tensile stress) and unconfined compression (uniaxial compression stress). In each case, a uniform constant velocity is applied to the nodes at both ends of the cylinder. The velocity is 1.27 mm/sec. It is held constant for the 40 msec duration of the direct pull simulations and for the 1,500 msec duration of the unconfined compression simulations.

One boundary condition is analyzed for direct pull of the cylinders. The boundary condition is no lateral constraint on the ends of the cylinder so that the cylinder is free to expand or contract laterally along its entire length. This idealized condition produces a realistic damage mode (breaking of the cylinder along one band of elements).

One boundary condition is analyzed for the unconfined compression cylinder. The boundary condition is a fixed end condition (no lateral motion of the nodes along the top and bottom of the cylinder). This condition produces a realistic double diagonal-type damage mode often seen in tests.

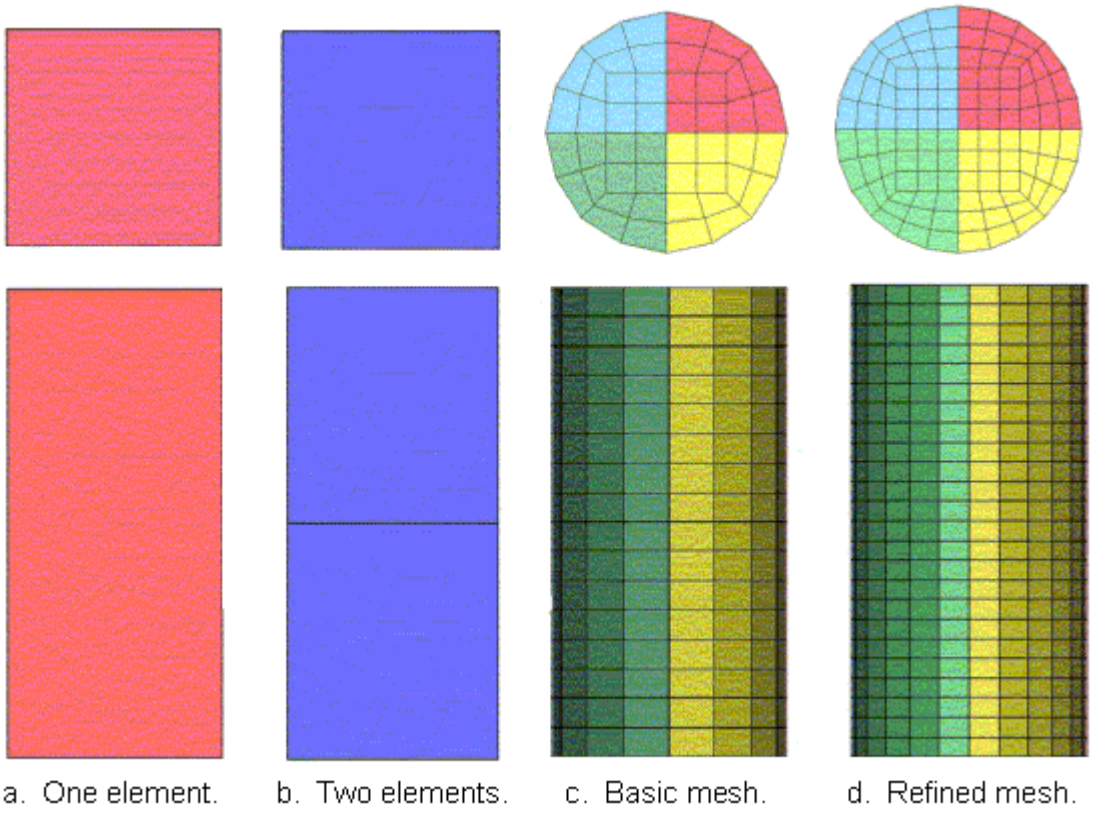

Figure 31. Refinement of each mesh used in sensitivity analyses.

Demonstration of Mesh Size Sensitivity

Direct Pull without Regulation. Stress-displacement curves and damage fringes for the direct pull simulations without regulation are given in Figures 32 and 33. The stress history for the single and double elements is output directly from LS-POST. The stress history for the cylinders is obtained from the cross-sectional force history that is output from LS-POST. The cross section is located at the axial midplane of the cylinder. The stress is calculated by dividing the force history by the initial cross-sectional area of the cylinder (which is 719.2 millimeters square (mm^2) (28.3 inches square ($inches^2$)). Each displacement history is output by LS-POST at the end nodes.

Figure 32 demonstrates that the softening response becomes more and more brittle as the mesh is refined. In particular, the stress-displacement behavior for the basic mesh does not converge to that of the refined mesh. This situation is undesirable. The damage modes for the basic mesh and refined mesh (see Figure 33) are similar, although they appear to be different at first glance. Damage is localized into a single row of elements that soften as they stretch. The row of elements is at one end of the refined mesh, but more toward the center of the basic mesh.

Parametric studies (not shown) indicate that the row of elements that damages is sensitive to the rate of loading. The rate of loading affects the uniformity of the stress distribution along the length of the cylinder. The rate of loading used in these calculations (quasi-static at 1.27 mm/sec (0.05 inch/sec) is slow enough that the stress distribution is uniform at peak strength to within about .001 of 1 percent. With a top-to-bottom uniform mesh, loading, and stress distribution, fracture is likely to occur anywhere along the length of the cylinder, and not necessarily at the center of the cylinder. However, the addition of friction at each end of the cylinder would probably push damage more toward the center of the cylinder.

For the single element mesh, the damage mode is softening of the entire element. For the double element mesh, very slight damage initiates simultaneously in both elements. But then damage in one of the two elements rapidly dominates, resulting in the softening and stretching of that one element, while the other remains effectively undamaged.

All direct pull calculations were conducted with the user-defined material model for concrete linked to version 970, using softening parameters of $A = 0.2467$ and $B = 0.1$ in tension ($P < 0$) and $A = 1.058$ and $B = 100$ in compression ($P > 0$). These parameters are more fully described in the next section.

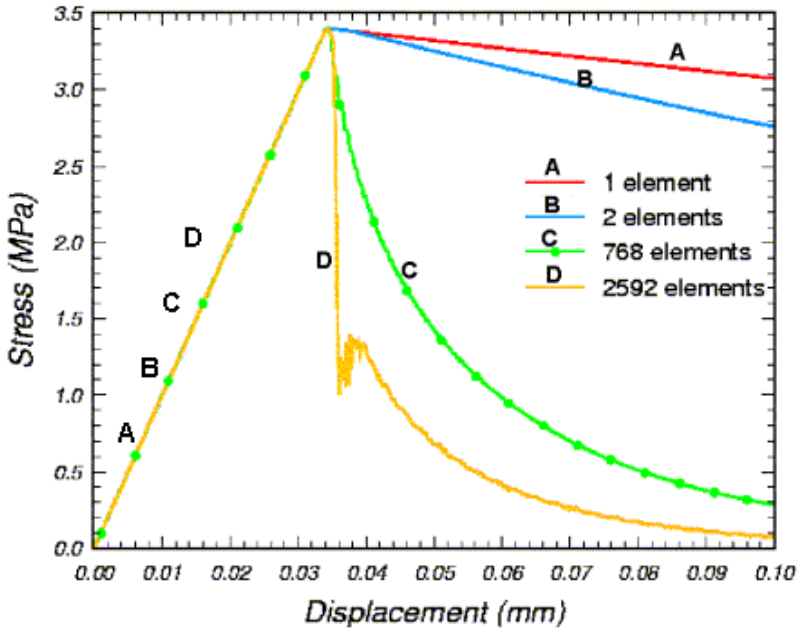

psi = 145.05 MPa, mm = 0.039 inch

Figure 32. The stress-displacement curves calculated in direct pull with an unregulated softening formulation do not converge as the mesh is refined.

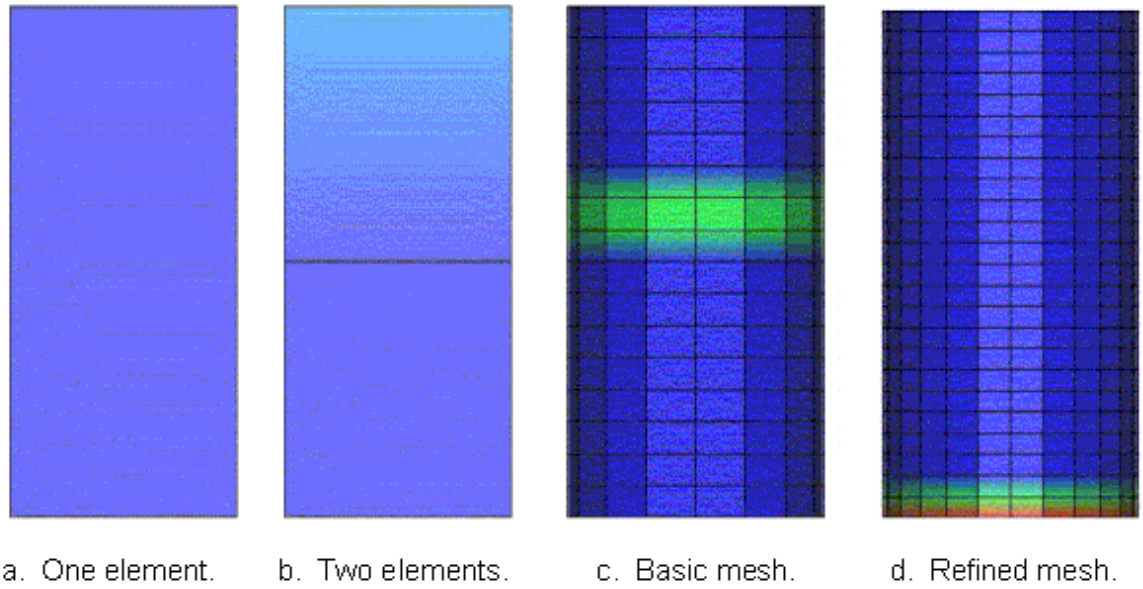

Figure 33. The damage mode calculated in direct pull with an unregulated softening formulation is damage within a single band of elements.

Unconfined Compression without Regulation. Stress-displacement curves and damage fringes for these fixed end unconfined compression simulations without regulation are given in Figures 34 and 35. The softening response tends to become more brittle as the mesh is refined. However, lack of convergence is not nearly as pronounced as previously demonstrated in Figure 32 for the direct pull simulations. In fact, the stress-displacement behavior for the basic mesh resembles that of the refined mesh. The author of this report considers the agreement between the basic and refined mesh curves as acceptable.

In addition, note that the single element does not damage. With fixed end conditions, the single element simulates uniaxial strain response, not uniaxial stress response. Therefore, this simulation displays hardening behavior (pushes the cap out without triggering damage) that is typically seen in tests of concrete under uniaxial strain conditions. The single element with fixed ends is a very poor representation of a cylinder with fixed ends.

As seen in Figure 35, the damage mode for the basic mesh and refined mesh is similar. Damage is primarily localized into two diagonals, forming an X-shape. This damage is in agreement with the double diagonal damage mode commonly observed in compression tests with fixed ends. For the double element mesh, both elements damage almost simultaneously and equally.

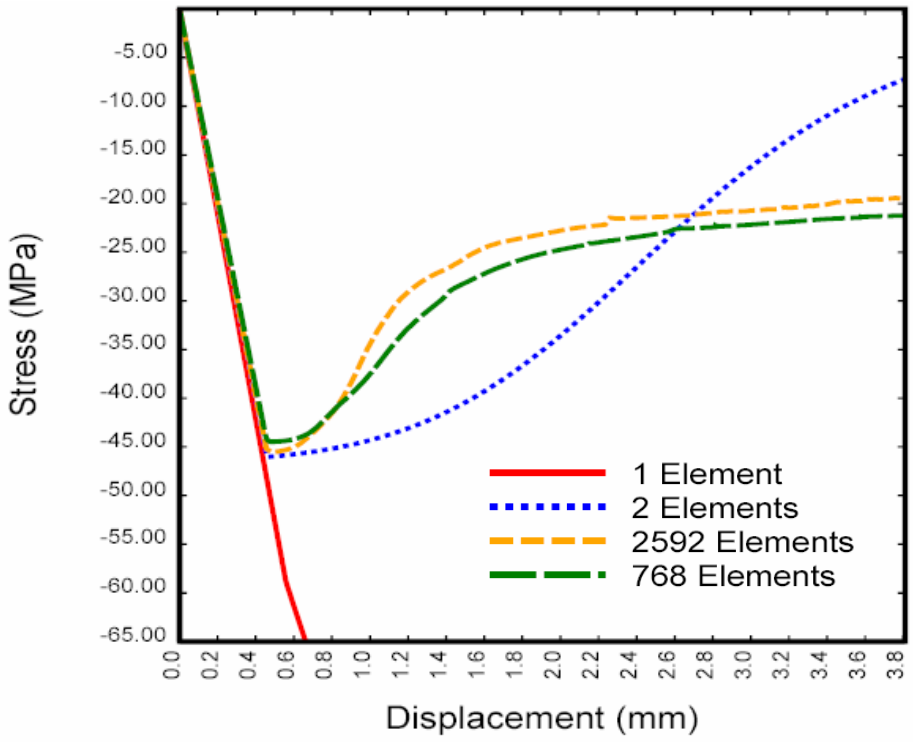

psi = 145.05 MPa, mm = 0.039 inch

Figure 34. The stress-displacement curves calculated in unconfined compression with an unregulated softening formulation are similar for the basic and refined meshes (fixed ends).

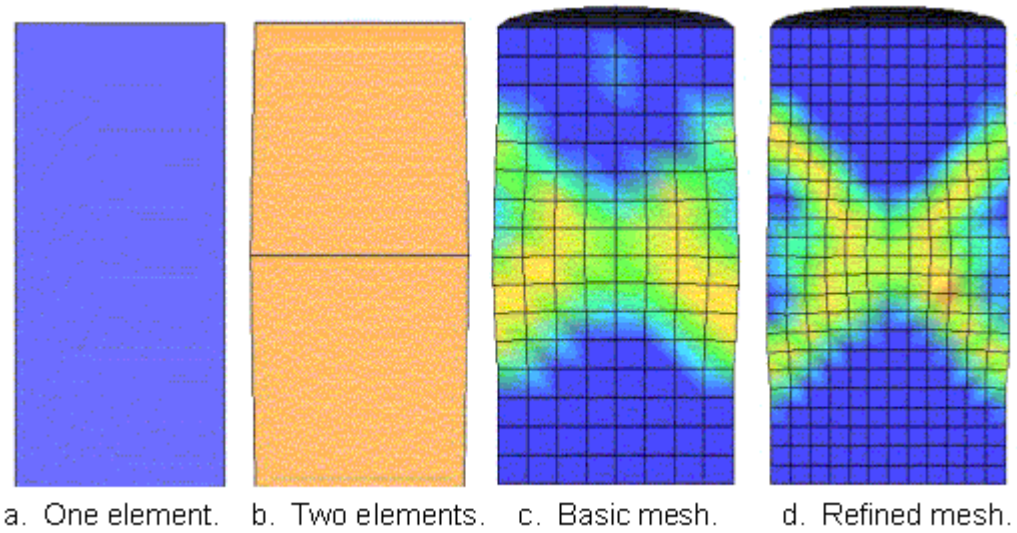

Figure 35. The damage mode calculated in unconfined compression with an unregulated softening formulation is a double diagonal (in the basic and refined meshes with fixed end conditions).

Description of Regulatory Technique

Softening is a reduction in strength with continued straining once a damage threshold is reached. Softening is modeled via a damage formulation. Without the damage formulation, most material models predict perfectly plastic behavior for laboratory test simulations like direct pull and unconfined compression. Such behavior is not realistic for materials like concrete, rock, soil, composites, and wood.

Softening is modeled with two parameters. Without regulation of mesh size dependency, these parameters are *A* and *B*, and are independent of element size. With regulation, these parameters are *B* and G_f rather than *A* and *B*. When the damage threshold is attained, the concrete material model internally solves for the value of *A* based upon the initial element size, the initial damage threshold, the fracture energy G_f, and a user-specified input value for *B*.

Evaluation of Regulatory Technique

Direct Pull with Regulation. Stress-displacement curves and damage fringes for the direct pull simulations with regulation are given in Figures 36 and 37. Although the softening response becomes more brittle as the mesh is refined, convergence is attained for the basic and refined meshes, as desired. In addition, the damage modes for the basic mesh and refined mesh are also in agreement: both calculate fracture along a single band of elements.

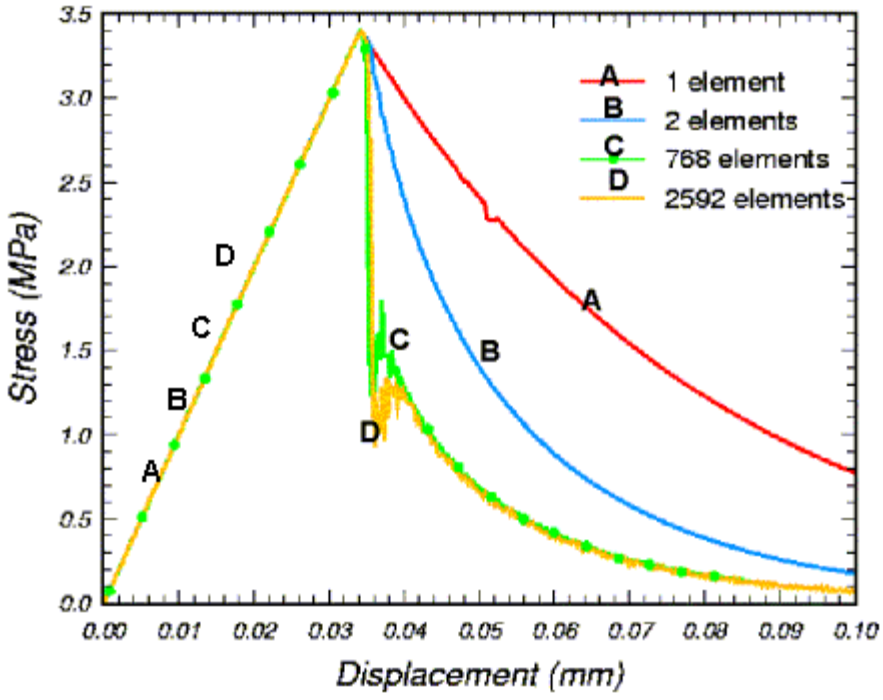

psi = 145.05 MPa, mm = 0.039 inch

Figure 36. The stress-displacement curves calculated in direct pull with a regulated softening formulation converge as the mesh is refined.

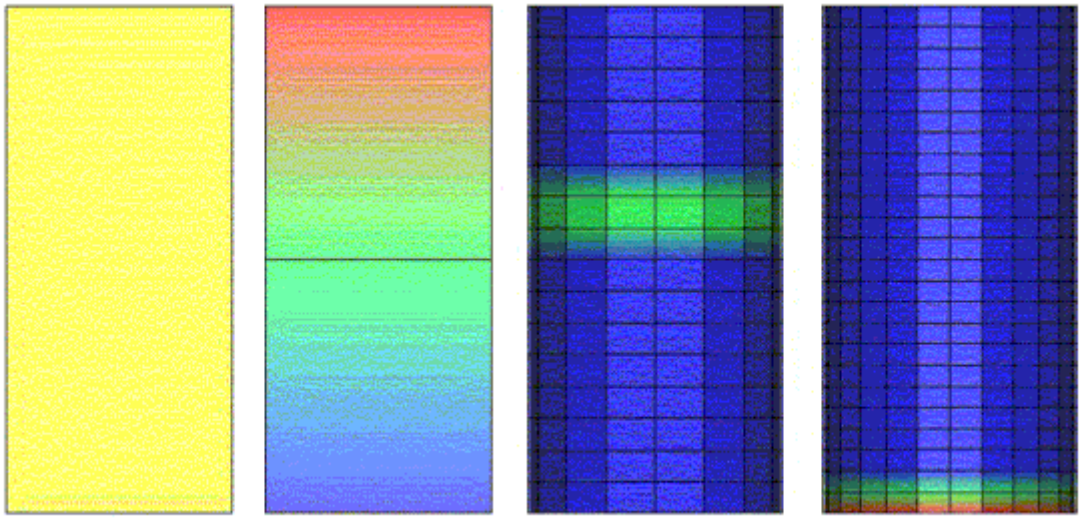

Figure 37. The damage modes calculated in direct pull with a regulated softening formulation are in agreement for the basic and refined mesh simulations.

All direct pull calculations were conducted with the user-defined material model for concrete linked to version 970, using softening parameters of G_f = 0.098 megapascal-millimeters (MPa-mm) (0.56 pounds per inch (lb/inch)) and B = 0.1 in tension ($P < 0$) with G_f = 9.81 MPa-mm (56 lb/inch) and B = 100 in compression ($P > 0$).

Unconfined Compression with Regulation. Stress-displacement curves and damage fringes for these fixed end unconfined compression simulations with regulation are given in Figures 38 and 39. The stress-displacement behavior for the refined mesh is nearly in agreement with that of the basic mesh, although the refined mesh is slightly more ductile. Greater ductility with mesh refinement is opposite the trend observed for the direct pull simulations.

The damage mode for the basic and refined meshes (see Figure 39) is similar. Damage is roughly localized into two diagonals, forming an X-shape. However, the damage is less diffuse (more localized), forming a sharper X, for the refined mesh than it is for the basic mesh. This situation suggests that a correlation may exist between diffusivity and softening response: the more diffuse the damage, the more brittle the softening behavior. These results also suggest that additional mesh refinement is needed to attain complete convergence.

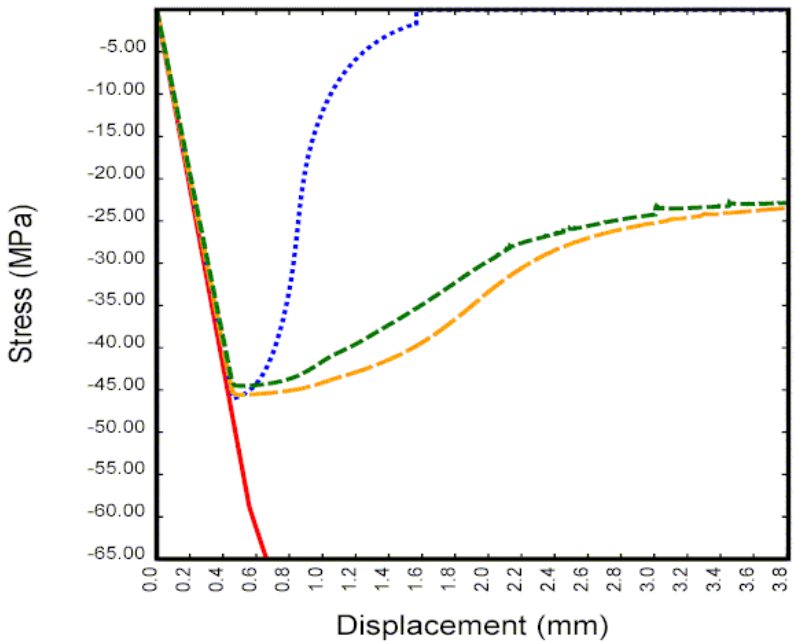

psi = 145.05 MPa, mm = 0.039 inch

Figure 38. The stress-displacement curves calculated in unconfined compression with a regulated softening formulation nearly converge as the mesh is refined (fixed ends).

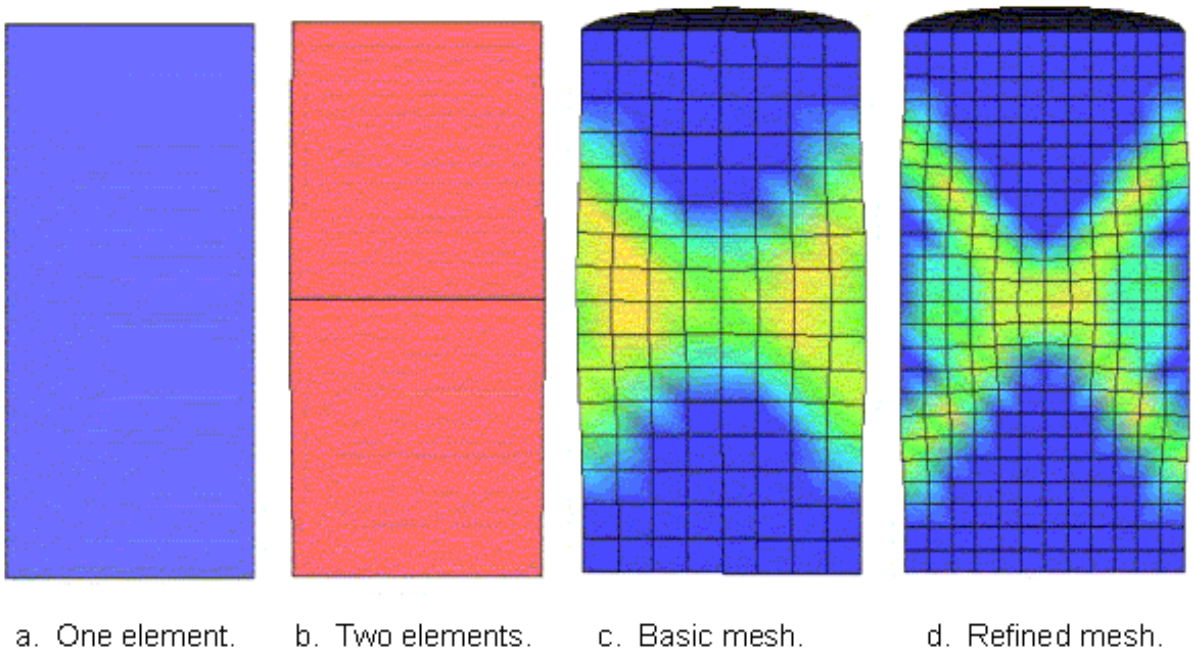

Figure 39. The X-shaped damage mode calculated in unconfined compression with a regulated softening formulation is similar for the basic and refined mesh simulations (fixed ends).

The argument could be made, however, that the basic and refined mesh simulations conducted without regulation (Figures 34 and 35) are in just as good agreement as those conducted with regulation (Figures 38 and 39). Hence, these simulations are inconclusive with regard to whether the proposed regulation scheme is necessary for the compressive response mode.

Note also that regulation has an opposite effect on the softening response in tension than it does in compression. In tension, regulation increases brittleness as the mesh is refined, at least until convergence is attained. In compression, regulation decreases brittleness (increases ductility) as the mesh is refined, hopefully until convergence is attained. Hence, if an analysis is conducted with a mesh that is too crude, there may be a tendency to underpredict tensile damage and overpredict compressive damage.

All unconfined compression calculations were conducted with concrete material model 159 in LS-DYNA version 971, using softening parameters of G_f = 0.098 MPa-mm (0.56 lb per inch (lb/inch)) and B = 0.1 in tension ($P < 0$) with G_f = 9.81 MPa-mm (56 lb/inch) and B = 100 in compression
($P > 0$).

Effect of Additional Mesh Refinement on Cylinder Response

A very refined mesh with 6,144 elements was created to further evaluate mesh size objectivity of the cylinder in compression. Refinement of this mesh is shown in Figure 40. Damage modes calculated with and without regulation are also shown in Figure 40. The calculations were conducted with fixed end conditions. Both calculations exhibit two diagonal bands of damage, forming an X. In the regulated calculation, these bands form simultaneously and about equally. In the unregulated calculation, one band forms prior to the other and exhibits greater damage. This X damage mode is the same as that previously calculated with less mesh refinement (768 and 2,592 elements), except now the damage is more localized so that the bands are more distinct.

Stress-displacement histories are shown in Figure 41 for all calculations without regulation and in Figure 42 for all calculations with regulation. Without regulation, the history calculated with the very refined mesh is more brittle than those calculated with less mesh refinement. With regulation, the history calculated with the very refined mesh is slightly more ductile than those calculated with less mesh refinement. Agreement is reasonable, but not exact.

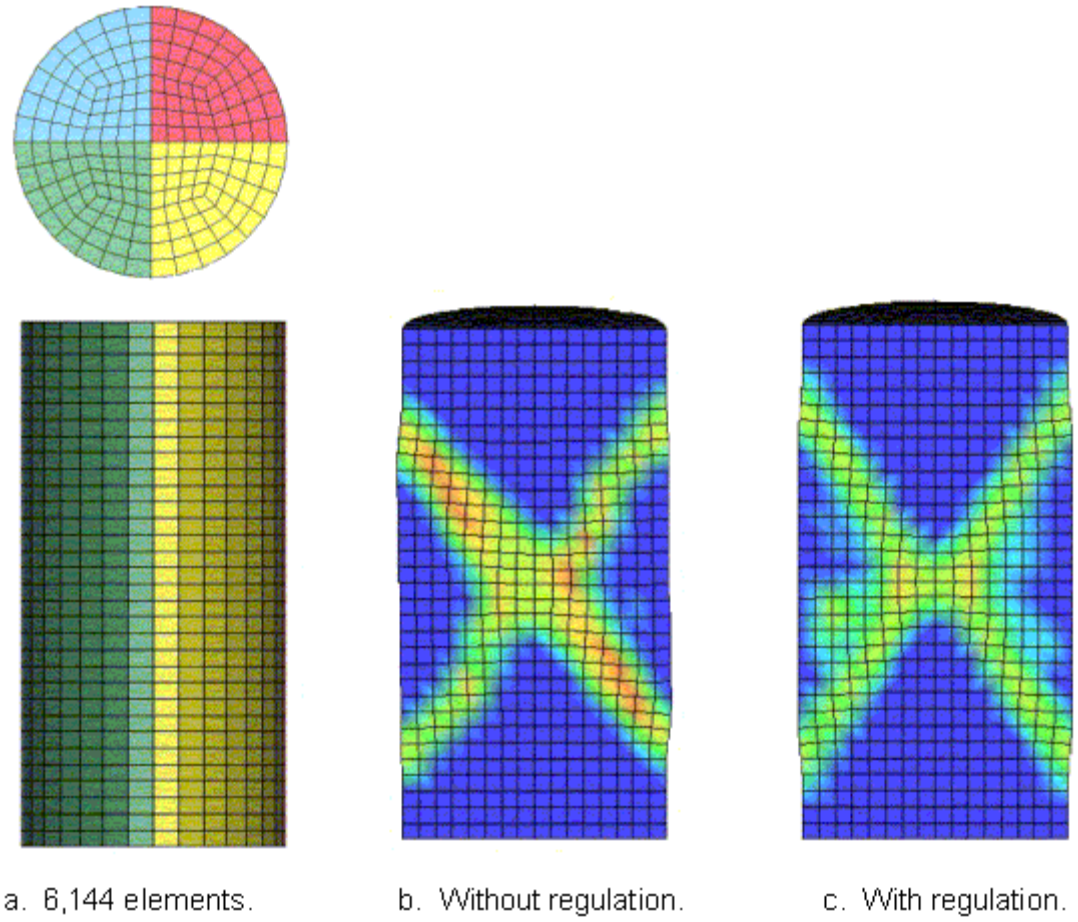

Figure 40. A crisp X-shaped band of damage is calculated for the very refined mesh, with or without regulation of the softening response.

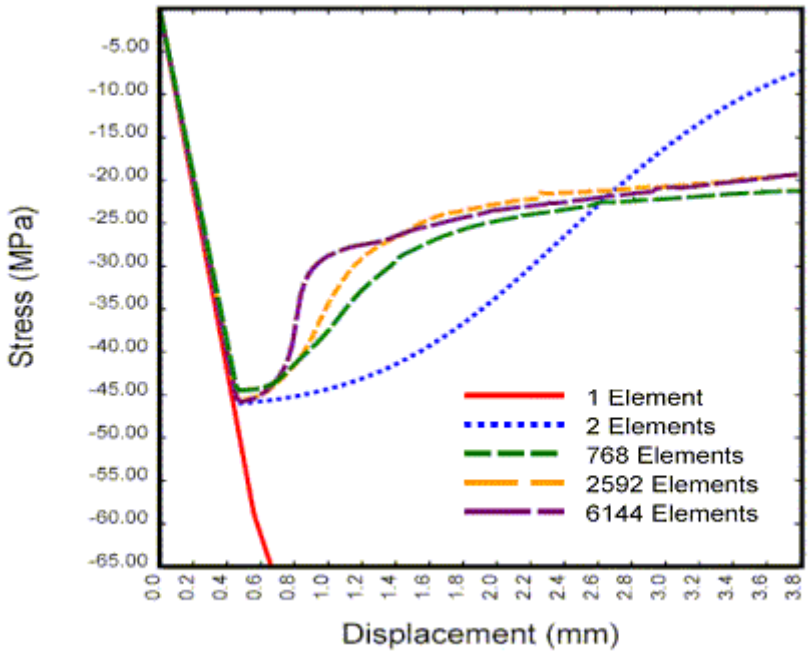

psi = 145.05 MPa, mm = 0.039 inch

Figure 41. The stress-displacement curves calculated in unconfined compression without a regulated softening formulation become more brittle as the mesh is refined (fixed ends).

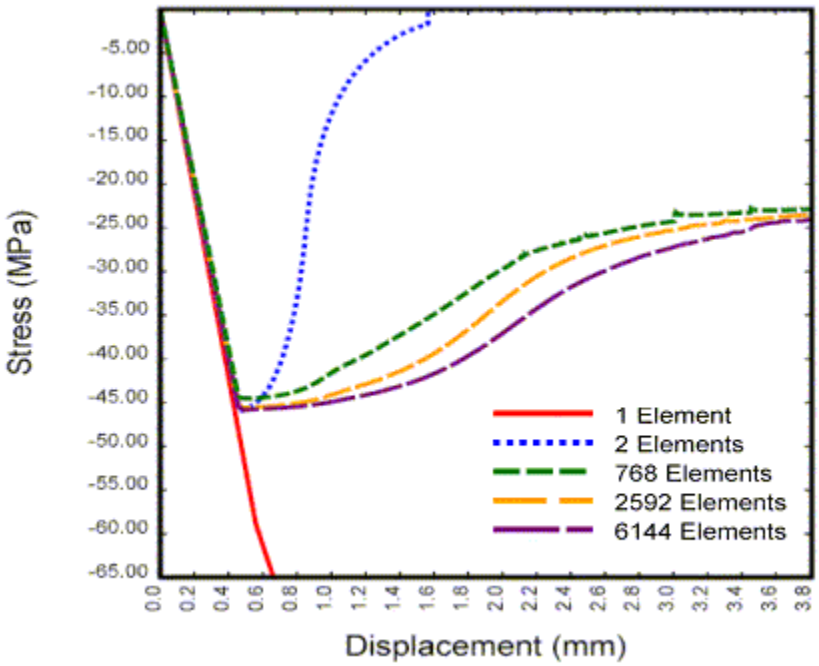

psi = 145.05 MPa, mm = 0.039 inch

Figure 42. The stress-displacement curves calculated in unconfined compression with a regulated softening formulation become more ductile as the mesh is refined (fixed ends).

SUMMARY REGARDING REGULATION

The direct pull calculations demonstrate that the technique implemented for regulating mesh size sensitivity achieves convergence of the solution with reasonable mesh refinement, as proposed. The direct pull calculations exercise the brittle damage mode only; therefore, this conclusion applies to the brittle damage mode only, and not the ductile damage mode.

The unconfined compression calculations support the application of the proposed regulation technique for the ductile damage mode, but do not indicate that it is absolutely necessary. Convergence is reasonable, but not exact. The fixed end calculations produce a double diagonal (X-shaped) damage mode that becomes more localized (less diffuse) with mesh refinement. This damage mode is similar to that seen in cylinder tests.

All calculations were performed for a single material without the use of contact surfaces or detailed boundary conditions. The appropriate element size to obtain convergence in more detailed applications may be problem dependent.

Finally, as previously noted, regulation in tension increases brittleness, whereas regulation in compression decreases brittleness (as the mesh is refined), until convergence is attained. Hence, if an analysis is conducted with a mesh that is too crude, there will be a tendency to underpredict tensile damage and overpredict compressive damage.

CHAPTER 5. SIZE EFFECT

Numerous articles in the literature, particularly those by Bazant, suggest that larger structures are softer than smaller structures.[9] This observation is schematically demonstrated in Figure 43. In general, a larger structure will be more brittle and have lower strength than a smaller, scaled-down structure. The larger structure will experience more damage than the smaller structure. The size effect is examined computationally by analyzing reinforced beams in four-point bending.

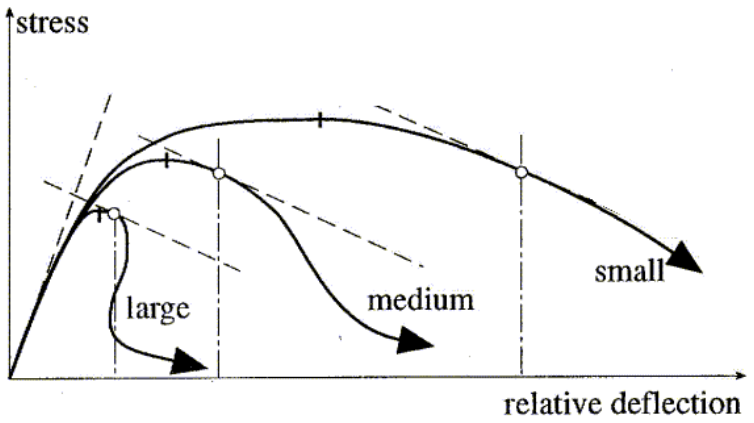

Figure 43. Schematic of the size effect, as suggested by Bazant and Planas.[9]

The effect of size on computed response was analyzed for two geometrically similar beams: one at full scale and the other at ⅓-scale. The full-scale beam is 4,572 mm (180 inches) long, with a cross section 457.2 mm (18 inches) deep and 342.9 mm (13.5 inches) wide. Two #3 longitudinal rebars are modeled on the tension side using beam elements with nodes common to the concrete hex elements. The rebars are located 228.6 mm (9 inches) apart and 276.2 mm (10.9 inches) deep (from the compression face of the beam). The concrete and rebar dimensions are reduced correspondingly in the ⅓-scale beam.

The beams are loaded in four-point bending, using nodal velocities to apply the load. The nodal velocity is 3,810 mm/sec (150 inches/sec) in the full-scale beam and 1,270 mm/sec (50 inches/sec) in the ⅓-scale beam. These velocities are intended to be slow enough to produce quasi-static conditions in the beam (no wave propagation effects). Pinned supports are modeled using nodal constraints. No contact surfaces are modeled. The concrete material was modeled with rate effects properties turned off. The steel reinforcement is modeled with elastic material properties.

The mesh of the concrete beam is shown in Figure 44. The full-scale and ⅓-scale beams are geometrically similar and are meshed with the same number of elements. The elements differ in length by a factor of 3. Only one mesh is shown, because the full-scale and ⅓-scale mesh refinements are identical.

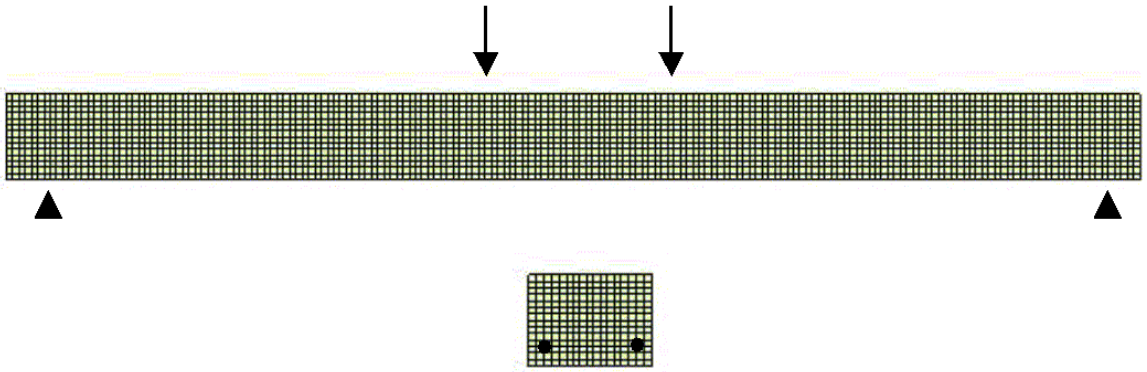

Figure 44. Refinement of the concrete beam mesh used in the size effect analyses.

Damage fringes and stress versus relative displacement curves, calculated with regulation of the softening formulation, are shown in Figures 45 and 46. The larger beam experiences substantially more damage, and softens with more brittleness, than the smaller beam. This result is consistent with the size effect. The nominal stress is the vertical reaction force divided by the beam cross-sectional area. The relative deflection is the midpoint beam deflection (u) divided by the beam depth (D).

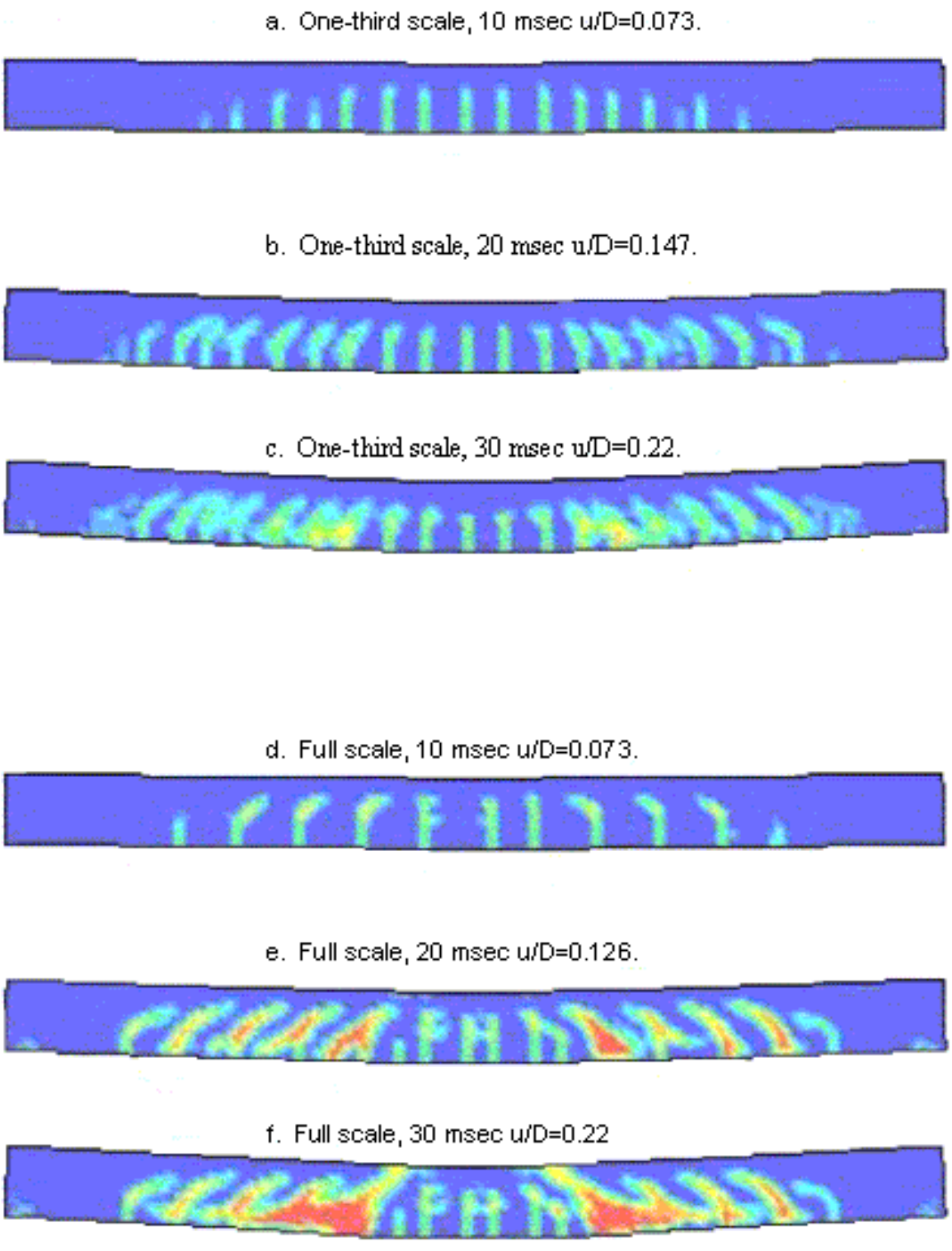

Figure 45. The damage simulated in the full-scale beam is more severe than that simulated in the ⅓-scale beam, which is consistent with the size effect.

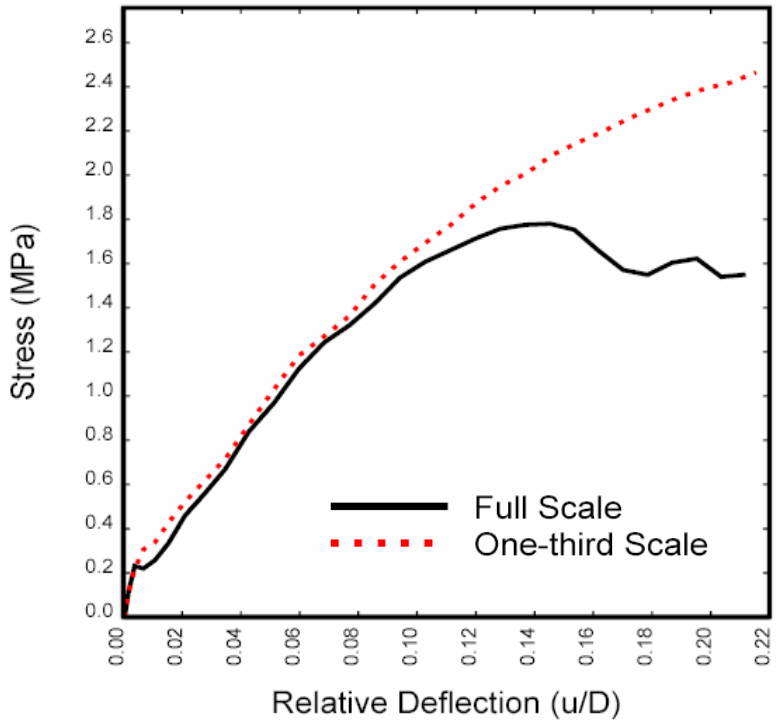

psi = 145.05 MPa

Figure 46. The stress-deflection behavior of the full-scale beam is softer than that of the ⅓-scale beam, which is consistent with the size effect.

It is interesting that the size effect is calculated when the softening response is regulated, but not when it is unregulated. Without regulation, the full and ⅓-scale beams exhibit the same amount of damage, as shown in Figure 47. In addition, the stress versus relative deflection behaviors are nearly the same. This similarity is because the strain distributions in the full and ⅓-scale beams are identical in the elastic regime and quite similar in the damage regime. The unregulated softening formulation keeps the softening stress versus strain consistent, regardless of size. Hence, damage is nearly equivalent because strain is nearly equivalent. But equivalent damage is not consistent with the size effect.

On the other hand, the regulated softening formulation keeps the softening stress versus displacement (crack opening) consistent. Displacements in the full-scale beam are 3 times as large as those in the ⅓-scale beam. Hence, damage is more pronounced in the full-scale beam (as shown in Figure 48).

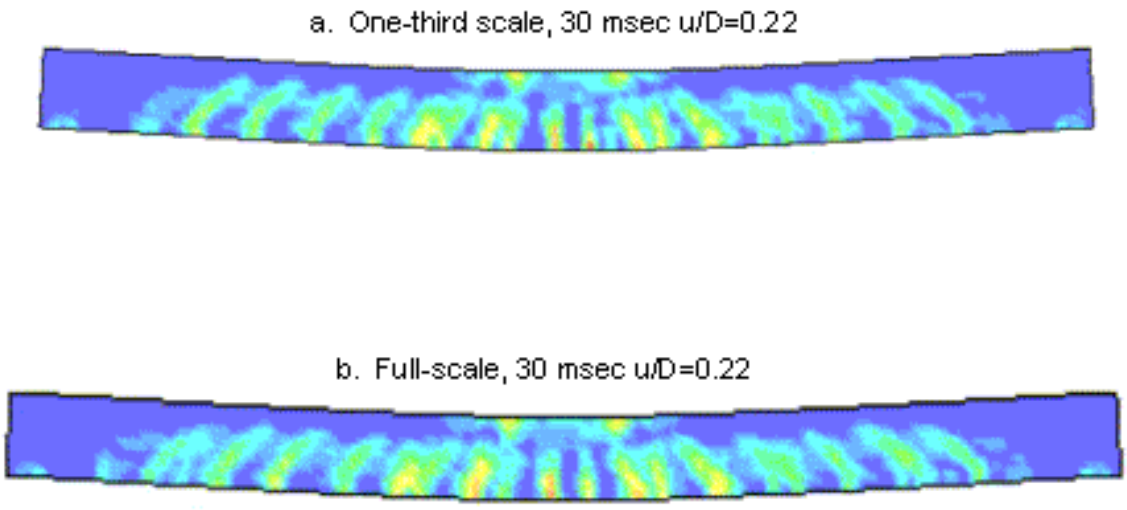

Figure 47. Without regulation of the softening formulation, the damage simulated in the full-scale and ⅓-scale beams is nearly the same, which is inconsistent with the size effect.

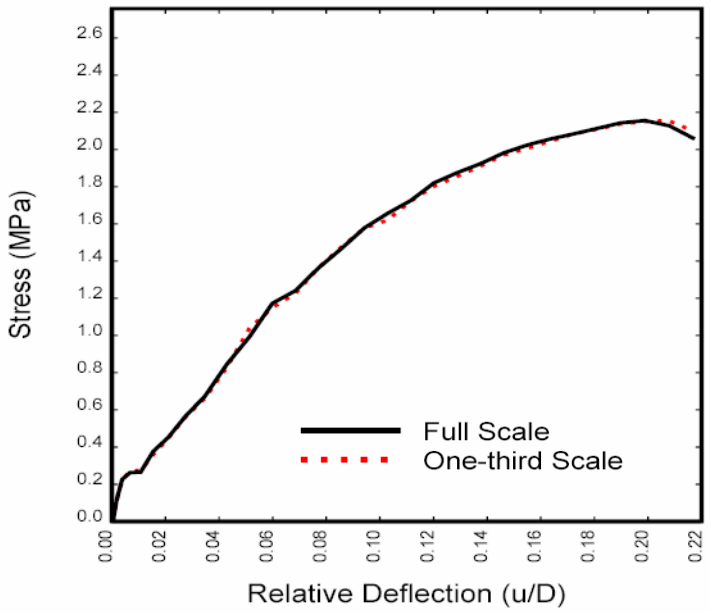

psi = 145.05 MPa

Figure 48. Without regulation of the softening formulation, the stress versus relative deflection curves of the full and ⅓-scale beams are nearly identical, which is inconsistent with the size effect.

CHAPTER 6. BEAM DROP TOWER IMPACT SIMULATIONS

TEST DATA

Forty-seven dynamic drop tower tests were conducted on ⅓-scale beams. Drop tower tests allow for dynamic testing of simple concrete structures in a controlled, well-documented environment. Scaling was necessary to perform the tests in the indoor drop tower facility. The beams are approximate scale models of typical bridge rails or posts. All testing procedures, tests results, and data reduction are documented in Oldani.[10] Figures of the test results and testing apparatus, shown in this section, are reproduced from that reference.

Three sets of beams were tested in dynamic, four-point bending: over-reinforced, under-reinforced, and plain concrete beams. Test matrices are given in Table 1–3. Calibration tests were conducted to determine the target impact kinetic energy at which the over-reinforced beams failed. Beam failure consisted of cracks running completely through the beam thickness, without pulverizing the beam. This target kinetic energy was held approximately constant throughout all tests while four combinations of impactor mass and velocity were tested. For all three types of tests, an increase in the impactor mass (with a corresponding reduction in impactor velocity) resulted in an increase in the beam deflection with deeper and wider cracks. The steel reinforcement did not break in any of the tests.

Table 1. Over-reinforced beam test matrix.

No. of Tests	Mass		Target Velocity		Target Impact Energy	
	kg	(lb)	m/sec	(ft/sec)	J	(ft-lb)
4	14.5	(32)	10.8	(35.4)	850	(627)
6	31.8	(70.1)	7.3	(24)	850	(627)
6	47.9	(105.6)	6.0	(19.7)	850	(627)
8	63.9	(140.9)	5.2	(17.1)	850	(627)

Table 2. Under-reinforced beam test matrix.

No. of Tests	Mass		Target Velocity		Target Impact Energy	
	kg	(lb)	m/sec	(ft/sec)	J	(ft-lb)
2	14.5	(32)	10.6	(34.8)	822	(606)
2	31.8	(70.1)	7.1	(23.3)	803	(592)
2	47.9	(105.6)	5.8	(19)	778	(574)
2	63.9	(140.9)	5.0	(16.4)	754	(556)

Table 3. Plain concrete beam test matrix.

No. of Tests	Mass		Target Velocity		Target Impact Energy	
	kg	(lb)	m/sec	(ft/sec)	J	(ft-lb)
2	14.5	(32)	10.6	(34.8)	822	(606)
2	31.8	(70.1)	7.1	(23.3)	803	(592)
2	47.9	(105.6)	5.8	(19)	778	(574)
2	63.9	(140.9)	5.0	(16.4)	754	(556)

The beams tested in these drop tower tests are intended to be approximate scale models of the beams tested in the bogie impact tests discussed in the next section. The 1,524-mm- (5-ft-) long beams are impacted by two steel 32-mm (0.10-ft) diameter cylinders spaced 203 mm (0.67 ft) apart, as schematically shown in Figure 49. The beams are supported on each end with 32-mm (0.10-ft) diameter cylinders. Tie-down straps are also placed around each beam at each end to prevent the beam from bouncing off the supports.

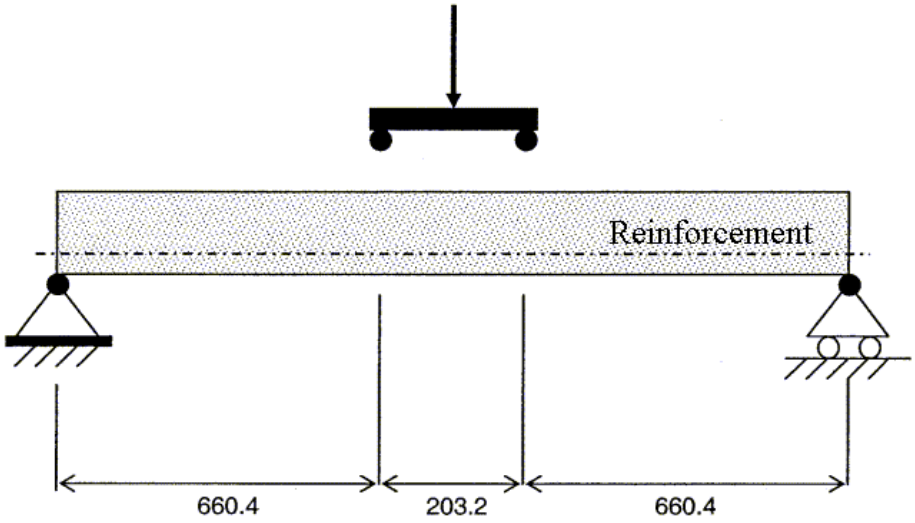

mm = 0.039 inch

Figure 49. Sketch of four-point bend tests, showing dimensions in millimeters.[10]

The cross section of the beam is 152.4 mm (6 inches) wide and 114.3 mm (4.5 inches) deep in the loading direction. Two bars of longitudinal reinforcement are located 76.2 mm (3 inches) apart and 92.08 mm (3.63 inches) deep from the loading face. No shear reinforcement is included. For the over-reinforced beams, the reinforcements are 9.525 mm (0.375 inches) in diameter (size #3 rebar). For the under-reinforced beams, the reinforcements are 3.2 mm (0.13 inches) in diameter (smooth cold-rolled steel rods).

To provide basic material property data for the analyses, the quasi-static compressive strength of the concrete was measured via cylinder compression tests. The nominal compressive concrete strength averages about 28 MPa (4,061 lbf/inch^2). The quasi-static tensile strength was measured using splitting tensile tests. The nominal tensile strength ranges from 1.82 to 2.7 MPa (264 to 392 lbf/inch^2). The stress-displacement behavior of the rebar was also measured. The initial yield

strength of the steel reinforcement averages about 457 MPa (66,282 lbf/inch^2), with an ultimate stress of about 614 MPa (89,053 lbf/inch^2).

LS-DYNA SIMULATIONS

All baseline calculations were conducted with default material properties for 28 MPa (4,061 lbf/inch^2) concrete with a 10-mm (0.39-inches) aggregate. The concrete is modeled with 170 hex elements along the length of the beam and 17 by 14 elements through the cross section. The reinforcement is modeled with beam elements with common nodes with the concrete hex elements. The steel impact and support cylinders are modeled with hex elements.

In some calculations, the tie-down straps are modeled with truss elements to prevent the concrete beam from bouncing off of the steel supports. The majority of calculations were conducted during development of the concrete model while it was interfaced with LS-DYNA as a user-defined material. A few calculations were performed with the final version of concrete material model as MAT 159.

Plain Beams

Multi-element simulations of the plain concrete beams were analyzed to ensure that the concrete model accurately predicts the damage mode observed in the tests, without the complicating effects of the steel reinforcement. A total of eight tests were conducted on plain beams, with two tests for each of the four combinations of mass and velocity. Six of the eight specimens initially failed with two major cracks beneath the impactor points, as shown in Figure 50. This initial failure mode occurred for all four combinations of mass and velocity tested. The remaining two specimens initially failed with one major crack beneath one impactor point, as shown in Figure 51. This initial failure mode occurred for one test conducted at 5 m/sec, (16.4 ft/sec) and another conducted at 5.8 m/sec (19.02 ft/sec). The beams do not rebound. They eventually hit the bottom of the test fixture. The final failure mode is breakage into three to five pieces, as shown in Figures 52 and 53. Four specimens broke into five pieces, three specimens broke into four pieces, and one specimen broke into three pieces. It is not clear to the developer whether the additional breakage occurs prior to, or because of, impact with the bottom of the text fixture.

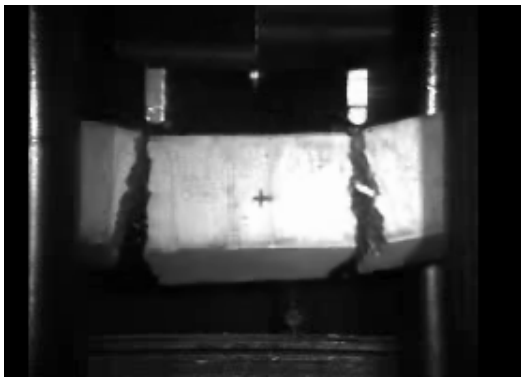

Figure 50. Six of the eight plain concrete specimens initially failed with two major cracks in the impact regime.

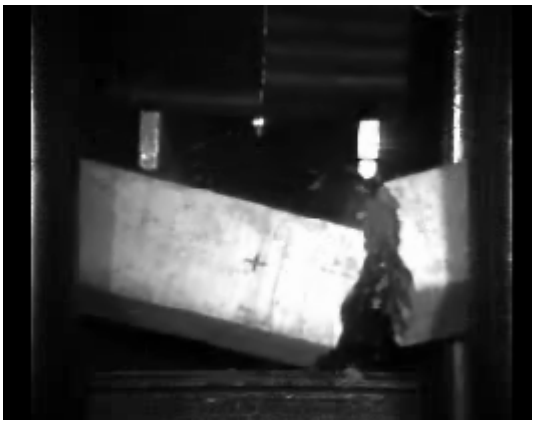

Figure 51. Two of the eight plain concrete specimens initially failed with one major crack in the impact regime.

Figure 52. All plain concrete specimens impact the bottom of the test fixture.

Figure 53. Four of the eight plain concrete specimens ultimately break into five pieces.

Four baseline calculations were conducted, one at each of the four mass-velocity combinations. The initial damage mode simulated in all four calculations is the formation of two major cracks on the tensile face of the beam. These cracks propagate toward the impactor points on the compressive face of the beam, ultimately splitting the beam into three distinct sections. The deformed configuration with damage fringes from one simulation is shown in Figure 54. The beam does not rebound. Additional breakage occurs as the calculations progress, as shown in Figures 55 and 56. In three of the four calculations, the beam broke into five pieces. In the other calculation, conducted at 5 m/sec (16.4 ft/sec), the beam broke into four pieces. Any additional damage that may have occurred due to impact with the bottom of the test fixture was not simulated, because the bottom of the test fixture was not modeled.

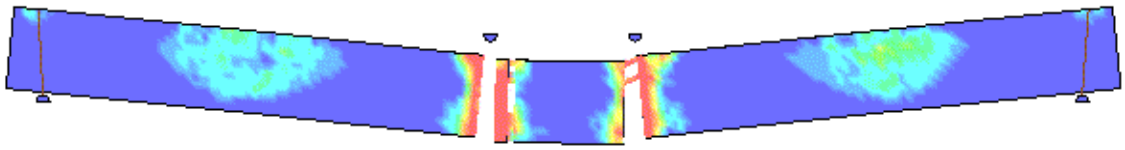

Figure 54. The plain concrete beam initially breaks into three large pieces in all baseline calculations performed (shown at 12 msec for impact at 5.8 m/sec (19.0 ft/sec)).

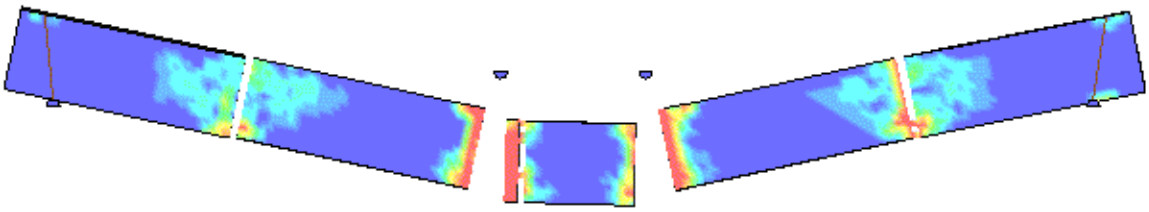

Figure 55. The plain concrete beam ultimately breaks into five pieces in three of four calculations performed (shown at 26 msec for impact at 5.8 m/sec (19.0 ft/sec)).

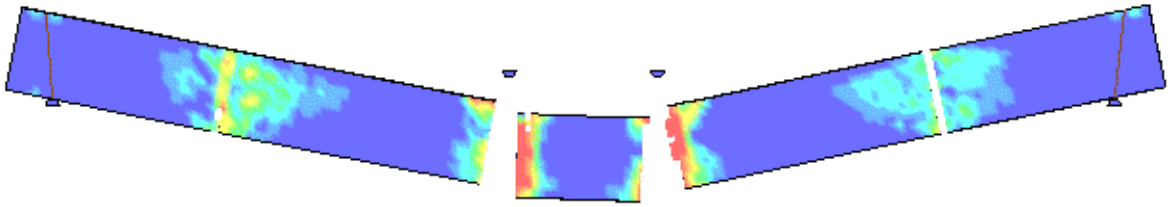

Figure 56. The plain concrete beam ultimately broke into four pieces in one of four calculations performed (shown at 26 msec for impact at 5.0 m/sec (16.4 ft/sec)).

Overall, there is good agreement between the computed and measured damage mode. The damage mode simulated is the primary damage model measured in the tests, i.e., the initial formation of two cracks beneath the impactor points, followed by additional breakage into five pieces. No accelerometer measurements were made for comparison with computed deflection histories.

Occasionally, in preliminary calculations conducted during model development and parameter selection, the damage mode simulated was the initial formation of one crack beneath one impactor point. One preliminary result, which was conducted before completing the model and selecting default properties, is shown in Figure 57. This damage mode does not occur using the final default properties implemented for 28 MPa (4,061 lbf/inch^2) concrete with 10-mm (0.4-inch) aggregate, but may be possible to obtain with user-specified properties.

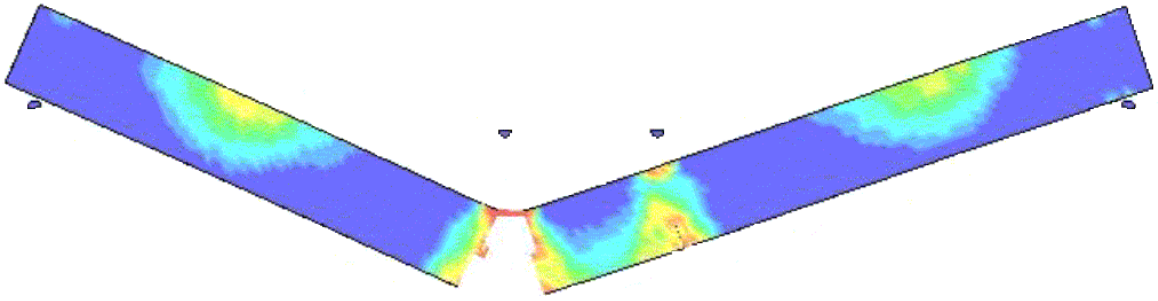

Figure 57. This preliminary calculation demonstrates the formation of one primary crack.

Reinforced Beams

Multi-element simulations of the over-reinforced and under-reinforced beams were also performed with LS-DYNA. Over-reinforced beams are statically designed to have the concrete crush before the steel reinforcement yields. Under-reinforced beams are statically designed to have the steel reinforcement yield before the concrete crushes. Over-reinforced beams are more brittle than under-reinforced beams; thus, each type of beam exhibits different response modes. The combined concrete and reinforcement models used in the analyses accurately simulate the different response modes.

Over-reinforced beam behavior is shown in Figure 58 for the post-test beam and in Figure 59 for the LS-DYNA simulation. Upon impact, in both the test and simulation, multiple cracks primarily initiate on the tensile face of the beam and propagate towards the compressive face. A listing of the primary cracks noted in the post-test specimen is given in Figure 59. Impact damage (crushing) is also visible beneath each impactor. The beam rebounds following peak deflection.

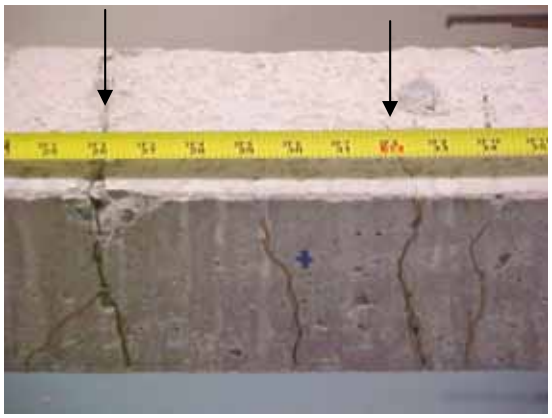

Figure 58. The over-reinforced concrete beam has localized tensile cracks and concrete crushing in the impactor regime (test 15 conducted at 5 m/sec (16.4 ft/sec)).

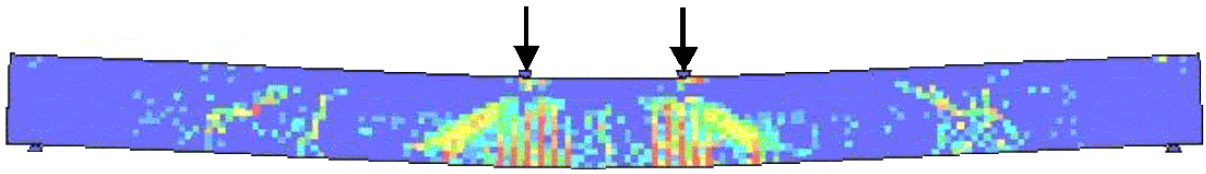

Figure 59. The damage mode of the over-reinforced concrete beam at peak deflection is localized tensile cracks and concrete crushing in the impactor regime (shown at 16 msec for impact at 5 m/sec (16.4 ft/sec)).

Table 4. Primary crack analysis of test 15 conducted at 5 m/sec (16.4 ft/sec).

Crack #	Position x (mm)	Depth Front (mm)	Depth Front percent	Depth back (mm)	Depth Back percent	Opening Top/Bottom
1	460.375	9.525	8.333	12.700	11.111	Bottom
2	673.100	114.300	100.000	114.300	100.000	Bottom
3	763.588	101.600	88.889	101.600	88.889	Bottom
4	835.025	114.300	100.000	114.300	100.000	Bottom
5	855.663	95.250	83.333	114.300	100.000	Bottom
6	949.325	95.250	83.333	88.900	77.778	Bottom
7	1009.650	34.925	30.556	88.900	77.778	Bottom
8	1168.400	63.500	55.556	50.800	44.444	Top

One measured trend is that the cracks become deeper and wider with an increase in impactor mass, or correspondingly with a decrease in impactor velocity. This trend is evident in the calculations, as shown in Figure 60. This figure shows the damage from the calculation conducted at the highest impact velocity of 10.6 m/sec (34.8 ft/sec). Note that fewer damage fringes are present in the impact regime at 10.6 m/sec (34.8 ft/sec) than previously shown in Figure 59 at 5.0 m/sec (16.4 ft/sec).

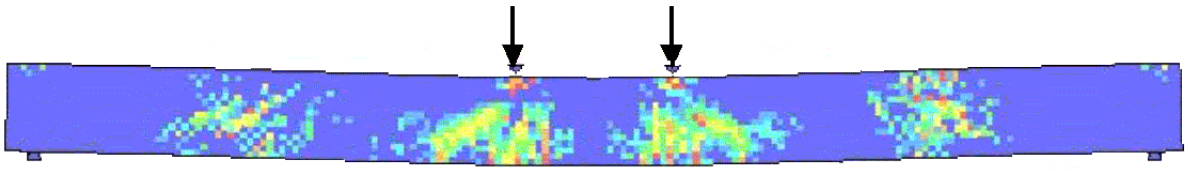

Figure 60. The simulated damage fringes for impact at 10.6 m/sec (34.8 ft/sec) are less extensive than those simulated at 5.0 m/sec (16.4 ft/sec).

In three sets of the over-reinforced beam tests, an accelerometer attached to the impactor measures acceleration that is integrated to produce velocity and displacement histories. The measured displacement histories are shown in Figure 61. Peak deflections attained from integration of the accelerometer readings agree with those attained from the videos to within about 5 percent accuracy. Peak deflections attained from the videos are given in Table 5. They indicate that as the impactor mass increases, the measured beam deflection increases. This trend is accurately simulated by the concrete material model. All four calculations are shown in Figure 61 for comparison with the test data. Good agreement is noted until just past peak deflection.

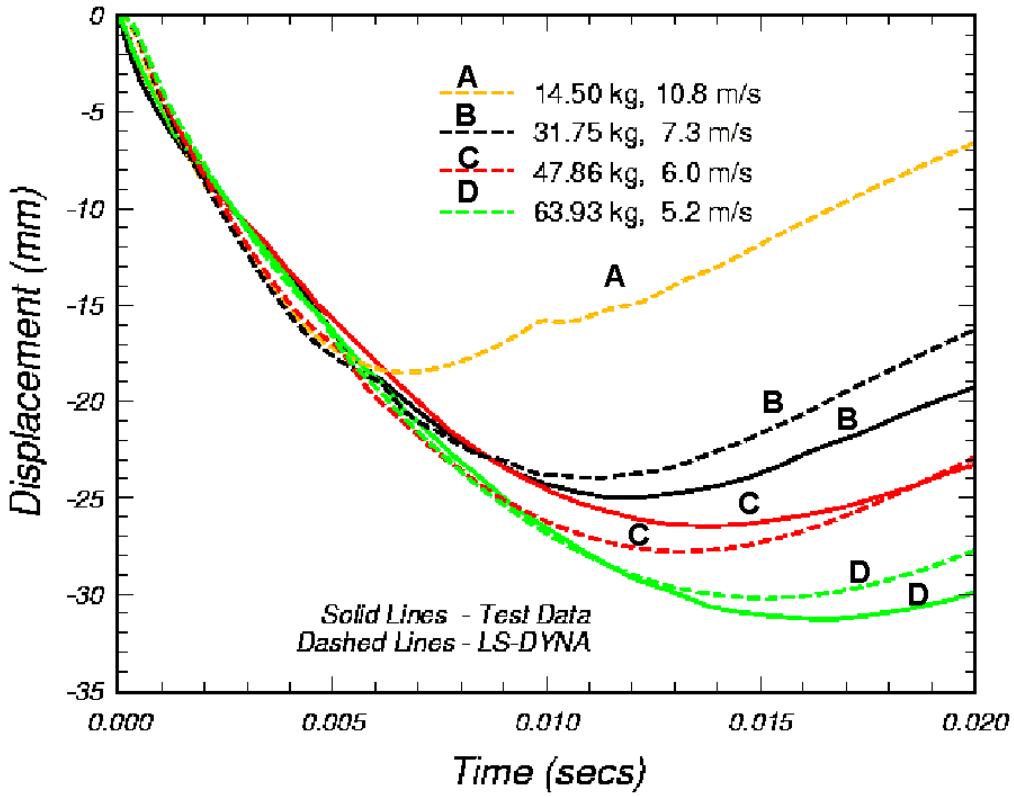

mm = 0.039 inch

Figure 61. The measured displacement histories are accurately simulated by LS-DYNA concrete material model MAT 159.

Table 5. Comparison of measured and computed deflections for the over-reinforced beams.

Specimen Mass		Velocity		Measured Displacement Range		Calculated Displacement	
kg	**(lb)**	**m/sec**	**(ft/sec)**	**mm**	**(inches)**	**mm**	**(inches)**
14.5	(32)	10.8	(35.4)	16	(0.63)	18	(0.71)
31.75	(70)	7.3	(24.0)	19–25	(0.75–0.98)	24	(0.94)
47.86	(105.5)	6.0	(19.7)	22–27	(0.87–1.06)	28	(1.10)
63.93	(141)	5.2	(17.1)	26–33	(1.02–1.3)	30	(1.18)

The measured and computed results previously shown in Figure 61 are not plotted past 20 msec, even though the accelerometer gage measurements continued to record past 20 msec. This happens because the deflection histories obtained from integrating the accelerometer readings begin to differ from the behavior shown in the videos once peak deflection is attained. This difference is attributed to a loss in the accelerometer's accuracy. Once peak deflection is attained, the impactor (upon which the accelerometer rests) separates from the beam. This separation greatly reduces the high amplitude, short duration acceleration experienced by the piezoelectric shock gage. Consequently, the gage is subjected only to the constant acceleration of gravity. The sensitivity of the gage is poor under constant acceleration conditions, and its response is a slow exponential decay according to the time constant of the gage. Such decay is shown in Figure 62. Here, the velocities histories are obtained by integrating the accelerometer

records. This decay is not present in the computed velocity histories. These computed histories were obtained from preliminary calculations conducted during the model's development, before the default material properties were selected. This discussion indicates having redundant measurements (the videos) serves as a good check on accelerometer measurements.

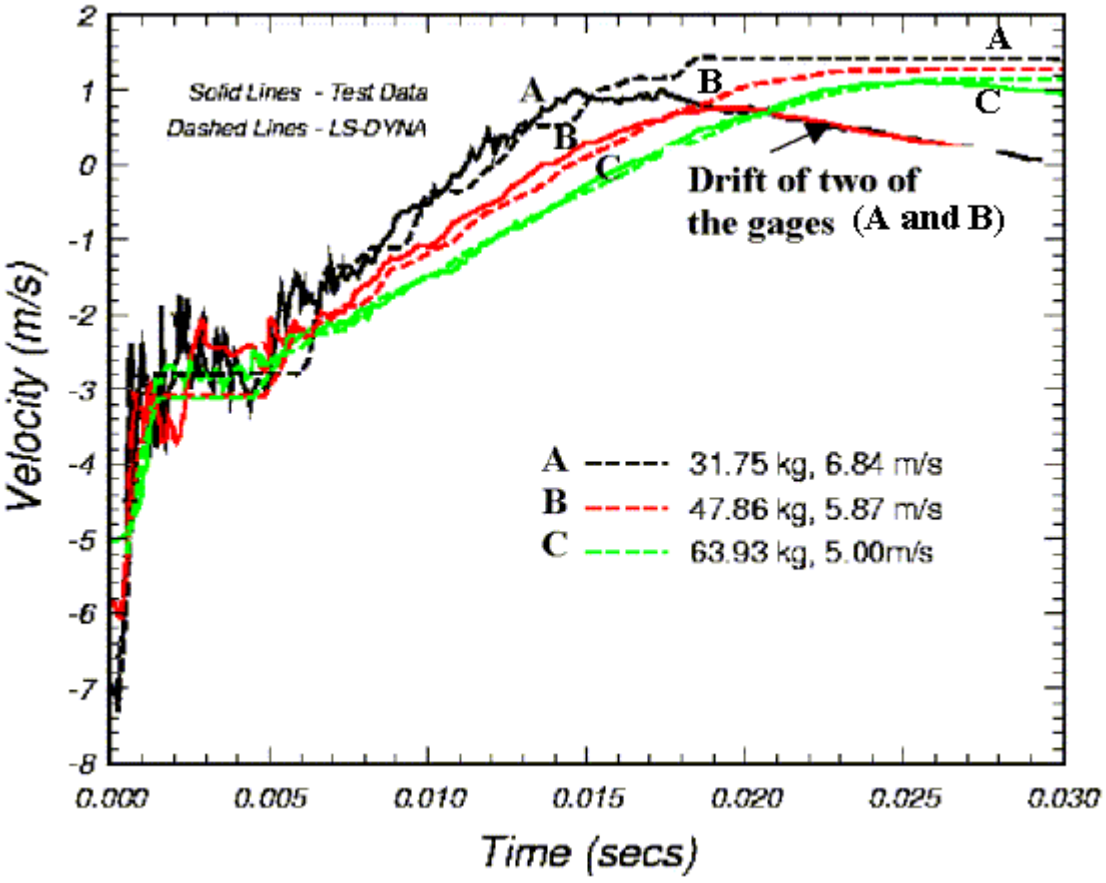

m/sec = 3.28 ft/sec

Figure 62. The processed velocity histories drift once the impactor separates from the beam during rebound at about 17 msec.

Under-reinforced beam behavior is shown in Figure 63 for one post-test beam specimen and in Figure 64 for the corresponding LS-DYNA simulation. In both the test and simulation, two major cracks initiate on the tensile face of the beam and propagate toward the compressive face, essentially splitting the concrete into three sections. Impact damage (crushing) is also visible beneath each impactor. Little rebound occurs, although the reinforcement does not break. The behavior shown is for the test and simulation conducted at 5.2 m/sec, (17.1 ft/sec) but it is typical of most test specimens and calculations.

Half of the test specimens also exhibited smaller but visible cracks originating on the top of the beam. These cracks are located approximately halfway between each impactor and each end of the beam, as shown in Figure 65 and listed in Table 6. The computed behavior previously shown in Figure 64 exhibits damage fringes, also originating on the top the beam, which are consistent with this behavior.

Figure 63. The damage mode measured for half of the under-reinforced beam specimens is two major cracks beneath the impactor points, without rebar breakage.

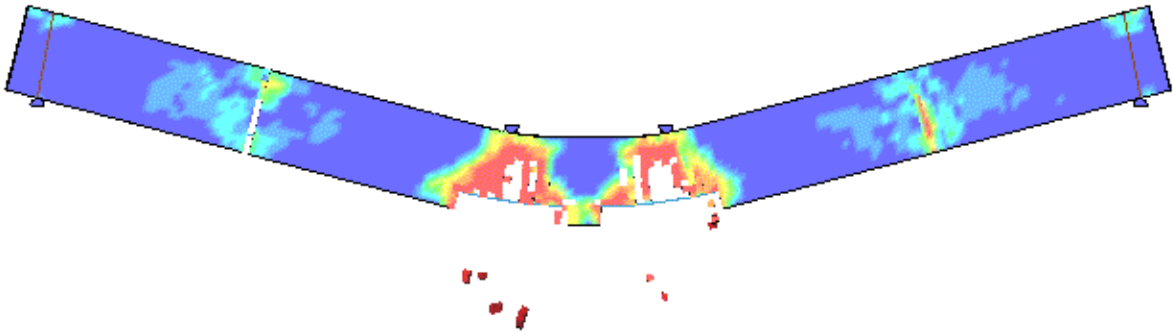

Figure 64. The damage mode simulated for all under-reinforced beam specimens is two major cracks beneath the impactor points, with additional damage toward the ends of the beam.

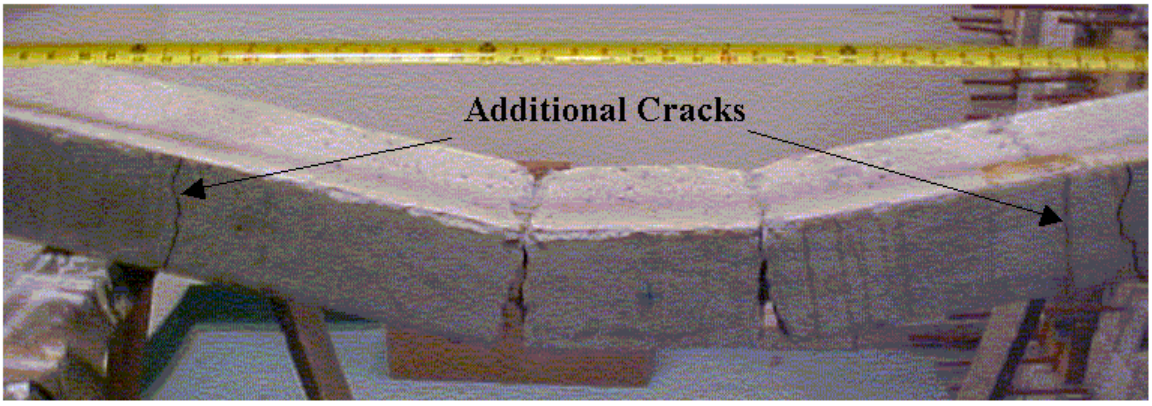

Figure 65. About half of the under-reinforced beam specimens exhibited cracks originating on the top of the specimen, and located halfway between the impactor points and ends of the beam.

Table 6. Crack analysis for one under-reinforced beam tested with an impactor mass of 31.75 kg (70 lb).

Crack #	Position x		Depth Front		Depth Front (%)	Depth Back		Depth Back (%)	Opening Top/ Bottom
	mm	(inches)	mm	(inches)		mm	(inches)		
1	349.250	(13.75)	114.300	(4.5)	100.000	114.300	(4.5)	100.000	T
2	660.400	(26)	114.300	(4.5)	100.000	114.300	(4.5)	100.000	B
3	863.600	(34)	114.300	(4.5)	100.000	114.300	(4.5)	100.000	B
4	1,168.400	(46)	114.300	(4.5)	100.000	114.300	(4.5)	100.000	T

No accelerometer measurements were made for the under-reinforced beams, so deflection histories are not available for plotting. However, peak deflections were extracted from the videos, as listed in Table 7. Two sets of deflections are listed. One, labeled "mid," gives the peak deflection measured at the horizontal midpoint of the beam. The other, labeled "max," gives the maximum deflection measured, which is not necessarily located at the midpoint of the beam. Although the beam is symmetric in design, the deformation doesn't remain symmetric once damage initiates. Also, the velocities listed are those used in the calculations, which differ by up to 7 percent from the actual velocities attained in the tests.

Table 7. Comparison of measured and computed deflections for the under-reinforced beams.

Specimen				Tests				Calculations			
Mass		Velocity		Mid		Max		Mid		Max	
kg	(lb)	(m/sec)	(ft/sec)	mm	(inches)	mm	(inches)	mm	(inches)	mm	(inches)
14.5	(32)	10.8	(35.4)	81	(3.2)	88	(3.5)	98	(3.9)	98	(3.9)
				106	(4.2)	113	(4.4)				
31.75	(70)	7.3	(24)	136	(5.4)	146	(5.7)	132	(5.2)	132	(5.2)
				144	(5.7)	150	(5.9)				
47.86	(106)	6.0	(19.7)	184	(7.2)	200	(7.9)	154	(6.1)	154	(6.1)
				200	(7.9)	>230	(>9.1)				
63.93	(141)	5.2	–	229	–	>230	–	167	–	167	–
				222	–	>230	–				

The computed deflections underestimate the measured deflections for the calculations conducted at the two lowest impact velocities of 5.2 and 6.0 m/sec (17.1 and 19.7 ft/sec). Parametric studies were conducted to determine what changes in boundary conditions, concrete properties, or rod reinforcement properties would improve the correlations. Changes in boundary conditions (strapped ends, free ends, nodal constraints on ends) and concrete properties (27 MPa to 31 MPa (3,916 to 4,496 lbf/inch^2) concrete) changed the peak deflection by less than 4 percent. However, changes in the steel rod properties proved significant. For example, removing rate effects from the rod model increased the peak deflections by nearly 50 percent. Changing the material model from MAT_PIECEWISE_LINEAR_PLASTICITY to MAT_PLASTIC_KINEMATIC reduced deflections by about 5 percent. Changing the rod yield strength from 476 MPa to 620 MPa (69,038 to 89,923 lbf/inch^2) reduced the deflections by about 20 percent. Hence, the controlling issue is the rod material model and its parameters.

In addition, the smooth rods used in the tests are not ribbed like rebar and slide relative to the concrete. During the calibration tests, the rods slipped and did not yield. Therefore, vise grips were clamped at both ends of the exposed rods to prevent them from pulling into the concrete specimen, although some slippage still occurred during the tests. This slippage is not modeled in the finite element model. The rods in the under-reinforced specimens are modeled identical to those in the over-reinforced specimens, with common nodes between the concrete hex elements and steel beam elements. This method models a stronger bond between the concrete and reinforcement than occurs during the tests. Additional efforts to model slippage might include separating the steel beam nodes from the concrete hex nodes, then coupling the steel to the concrete via the *CONSTRAINED_LAGRANGE_IN_SOLID command with frictionless sliding.

No additional efforts were made to improve correlations for the under-reinforced beams because this type of effort would focus on the smooth rod model and not the concrete model, which is the focus of this effort. The use of smooth rods in place of rebar was necessary due to scaling of the test structure. Rebar, rather than smooth rods, is used in full-scale roadside safety structures; therefore, continued efforts to improve the rod model are beyond the scope of this effort.

The peak deflections measured in the under-reinforced beam tests are about five times greater than those measured in the over-reinforced beam tests. Such differences in deflection are accurately simulated by the concrete and reinforcement models, as shown Figure 66 for the tests and simulations conducted at 7.3 m/sec (24 ft/sec). In this figure, one average displacement history (solid line) for the over-reinforced beams is compared with the corresponding LS-DYNA simulation (dashed line). The range in peak deflections extracted from the under-reinforced beam videos is also compared with the corresponding LS-DYNA simulation.

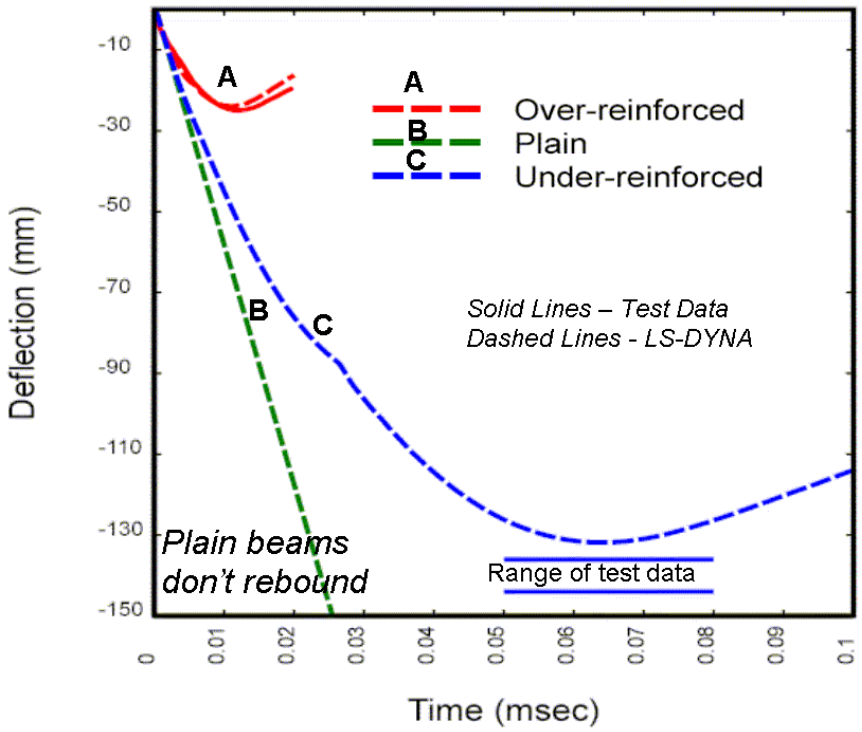

mm = 0.039 inch

Figure 66. Good displacement history and peak deflection comparisons of LS-DYNA drop tower impact simulations with test data for plain and reinforced concrete beams.

SUMMARY FOR DROP TOWER SIMULATIONS

Dynamic impact testing of over-reinforced, under-reinforced, and plain concrete beams indicates that each type of beam experiences a distinct deflection history and damage mode. The concrete model simulates, with reasonable accuracy, these deflection histories and damage modes. Like the test data, the model predicts that the under-reinforced beams deflect roughly five to nine times more than the over-reinforced beams, with no rebound of the plain beams. In addition, an increase in the impactor mass results in an increased beam deflection for both sets of reinforced beams. The over-reinforced beams experience multiple but fine tensile cracks that propagate through the beam thickness, while preserving the continuity of the beam. On the other hand, the under-reinforced and plain specimens primarily failed with two large, wide cracks beneath the impactor points, which disrupt the continuity of the beam.

CHAPTER 7. BEAM BOGIE VEHICLE IMPACT SIMULATIONS

TEST DATA

Three dynamic bogie vehicle impact tests were conducted on full-scale beams as part of this project. The reinforced concrete beams were simply supported and designed with longitudinal tensile reinforcement only. The bogie was setup with an impact head to produce four-point bending, as schematically shown in Figure 67. The test setup is similar to a concrete bridge rail impact, yet significantly simplified in order to isolate the concrete behavior. All tests were conducted with a 2,186.9 kilograms (kg) (0.05 lb) vehicle at speeds of 8.6, 15.9, and 33.km/h (5.3, 9.9, and 21 mi/h)). Observed damage consisted of flexural type cracks with beam rebound at low impact speed to inclined shear cracks and beam breakage (no rebound) at high impact speed. All testing procedures, tests results, and data reduction are documented in Bielenberg.[11] Figures of the test results and testing apparatus, shown in this section, are also reproduced from that reference.

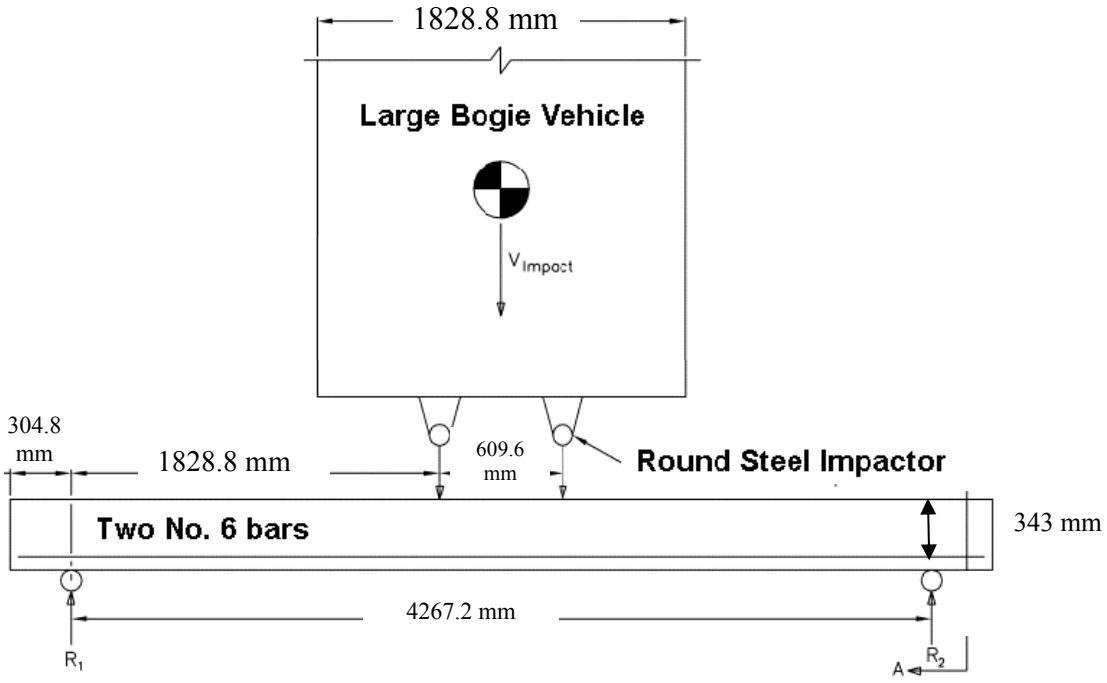

Figure 67. Schematic of bogie vehicle impacting reinforced concrete beam.

The beam is 4,887 mm (192.4 inches) long with a rectangular cross section that is 203 mm (8 inches) wide and 343 mm (13.5 inches) deep. The distance from the beam compression face to the single row of rebar is 279 mm (11 inches). The steel reinforcement is two No. 6 rebars (19-mm (0.75-inch) diameter).

The bogie head is fitted with two impact cylinders made of 76-mm (3-inch) diameter round bar stock. The beam reacts against two load frames, located near the ends of the beam, which are also fitted with 76-mm (3-inch) diameter round bar stock. The beam rests on two intermediate supports, placed between each impact cylinder and load frame. The beams are greased to reduce friction between the beam and support shelf, as shown in Figure 68.

Test instrumentation included videos, high-speed film, gages, and post-test photographs. Videos of each test were taken from overhead and from the side. These videos were used to determine deflection histories in two of the three tests. High-speed film was also used to record the event and to generate high-resolution photographs for documentation. The concrete beams were instrumented with strain gages on the compressive face of the beam. Strain gages were also placed on the rebar, but were under-ranged and yielded little information. The load frames were instrumented with strain gages on the angled tube of each frame, as shown in Figure 68. The bogie was instrumented with an accelerometer near its center of mass. The accelerometer failed to trigger in one test and yielded different force history results than the load frame gages in the other two tests. Therefore, the accelerometer data were considered unusable by those who conducted the tests.

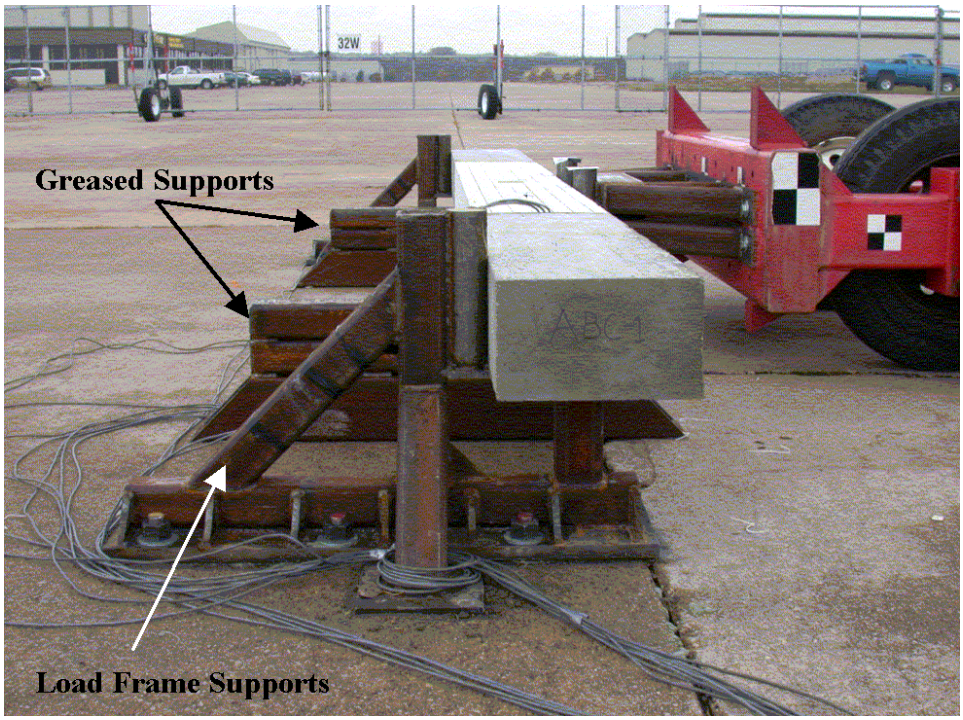

Figure 68. The beam rests on greased supports and reacts against two load frames.

To provide basic material property data for the analyses, the static compressive strength of the concrete was measured via cylinder compression tests. The nominal 40-day concrete compressive strength was 46 MPa (6,672 lbf/inch^2) at the time tests were conducted. The tensile strength was not measured. The static yield and ultimate strength of the No. 6 Grade 60 rebar

was also measured in tension. The average initial yield strength was 462 MPa (67,007 lbf/inch^2), and the ultimate strength was 721 MPa (104,572 lbf/inch^2).

LS-DYNA CORRELATIONS

All baseline calculations were conducted with default material properties for 46 MPa (6,672 lbf/inch^2) concrete with 19-mm (0.75-inch) aggregate. Unless otherwise stated, erosion was set to occur at 10 percent maximum principal strain. The concrete is modeled with 192 hex elements along the length of the beam, and 15 by 9 elements through the cross section. The reinforcement is modeled with beam elements with common nodes with the concrete hex elements. The steel impact and load frame cylinders are modeled with hex elements. In the calculations conducted at 8.6 km/h (5.3 mi/h), the supports that the beam rests on are modeled as rigid planes, with low friction between the beam and planes. Unless otherwise stated, the final calculations reported here were conducted with concrete material model MAT 159 implemented into LS-DYNA beta version 971 revision 2582.

High Velocity Impact

Two deformed configurations for the high velocity impact test conducted at 33.1 km/h (20.5 mi/h) are shown in Figure 69. Localized crushing from the cylinder heads occurs following impact on the compression face of the beam. Four diagonal shear cracks are visible in the photograph at 8 msec. The beam has broken into four or five major fragments by 48 msec, including a large trapezoidal-shaped block that forms along two of the inclined shear cracks. Bond failure along the steel reinforcement also is evident.

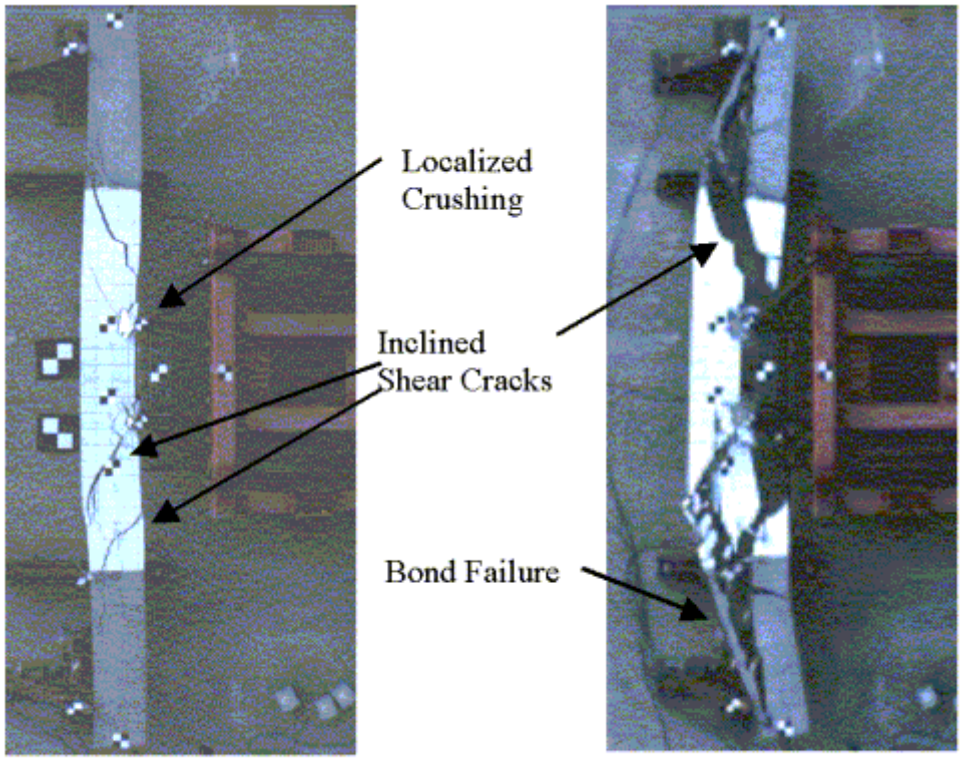

Figure 69. The beam tested at an impact velocity of 33.1 km/h (20.5 mi/h) exhibits inclined shear cracks, localized crushing, and bond failure.

Three deformed configurations for the high velocity impact simulation conducted at 33.1 km/h (20.5 mi/h) with baseline properties are shown in Figure 70. The deformed configuration of the high velocity simulation is localized crushing from the impact cylinders, inclined shear cracks originating on the compression face of the beam, plus peeling away of the concrete cover from the reinforcement on the tensile face of the beam (bond failure). The beam breaks into three major pieces. This damage is similar to that previously shown in Figure 69 for the corresponding test. Additional bond failure occurs in the simulation along the tensile face of the trapezoidal block that is not evident in the test. However, such centrally located bond failure is evident in the test conducted at 15.9 km/h (9.9 mi/h).

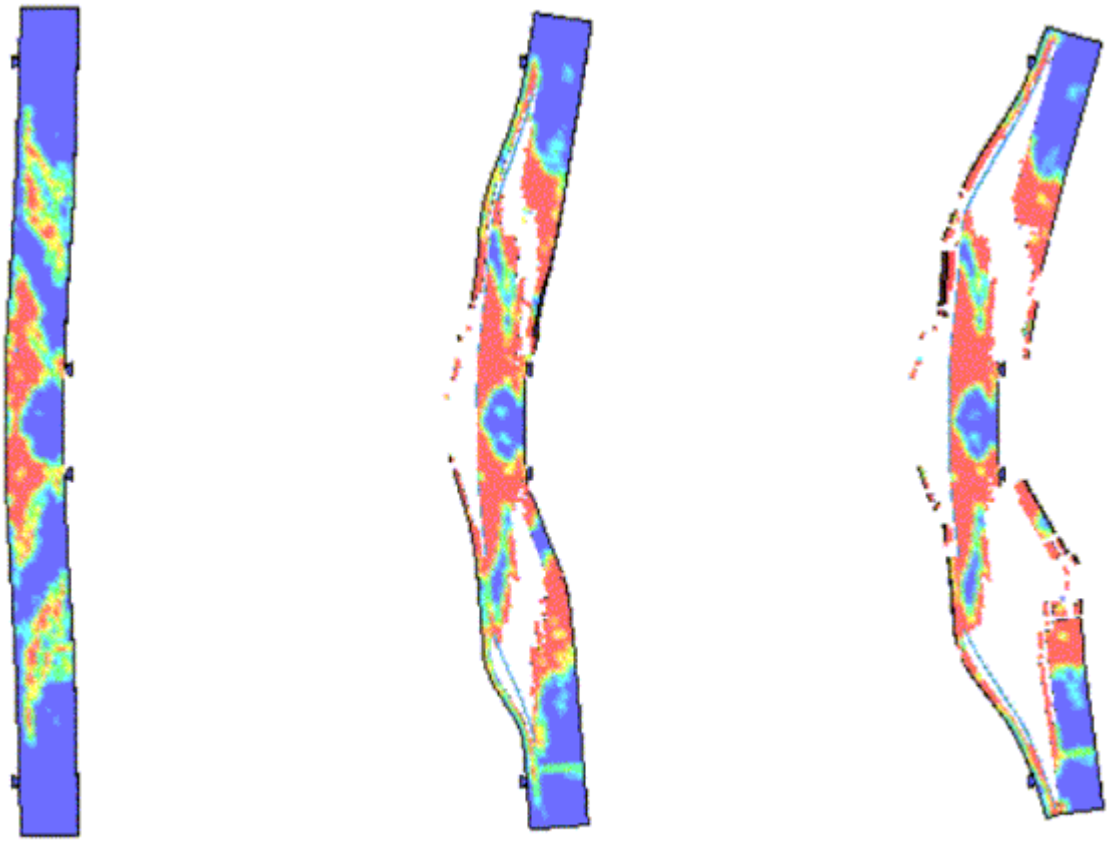

a. 8 msec. b. 48 msec. c. 80 msec.

Figure 70. Inclined shear cracks, localized crushing, and bond failure are simulated in the calculation conducted at 33 km/h (20.5 mi/h).

Intermediate Velocity Impact

Two deformed configurations for the intermediate velocity impact test conducted at 15.9 km/h (9.9 mi/h) are shown in Figures 71 and 72. The failure mode is predominantly inclined shear cracking and bond failure along the tensile reinforcement, with localized crushing beneath the impact cylinders. The failure dominates the right side of the beam. Here, one large shear crack forms at about 42 msec on the compression face and propagates at-angle toward the reinforcement on the tensile side. The crack then propagates along the tensile reinforcement, resulting in bond failure. Smaller shear cracks also form on the left side of the beam. The beam and bogie do not rebound.

Figure 71. The beam tested at an impact velocity of 15.9 km/h (9.9 mi/h) exhibits inclined shear cracks, localized crushing, and bond failure.

Figure 72. Damage dominates one side of the beam impacted at 15.9 km/h (9.9 mi/h).

Three deformed configurations for the intermediate velocity impact simulation, conducted at 15.9 km/h (9.9 mi/h) with baseline properties, are shown in Figure 73. The deformed

configurations exhibit slight localized damage from the impact cylinders, early time tensile damage, inclined shear damage, plus bond failure between the concrete and tensile reinforcement. Initially, tensile damage fringes and inclined shear fringes form in the vicinity of the impact cylinders (in the constant moment region), as shown at 8 msec. Additional inclined shear damage fringes form outside the constant moment region, as shown at 104 msec. Substantial bond failure is also evident at this time. The damage is similar to but less severe than that previously shown in Figure 71 for the corresponding test. One main difference between the simulation and test is that the beam rebounds at 104 msec in the simulation, but it did not rebound in the test. The second difference is that the damage is fairly symmetric from side to side in the simulation, but dominates one side of the beam in the test. The cause of the asymmetry in the test is not known.

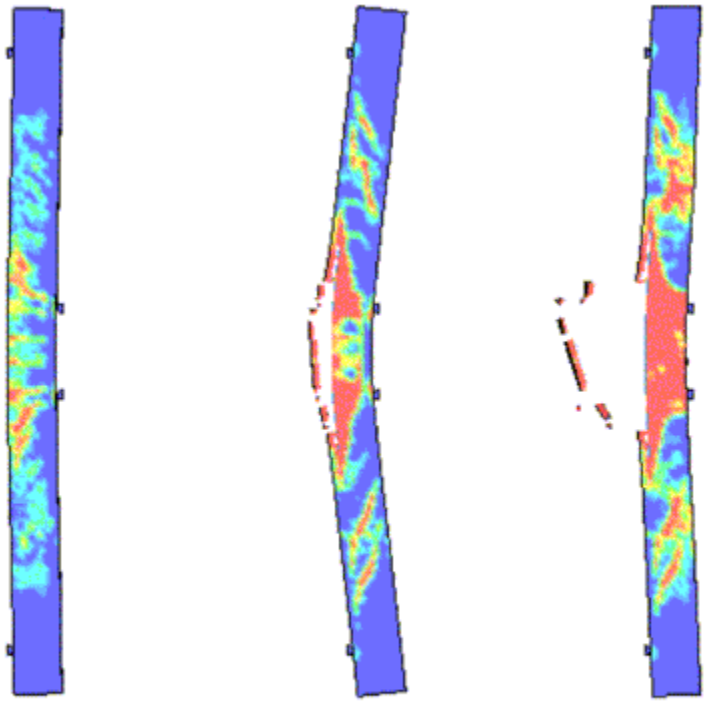

a. 8 msec. b. 104 msec. c. 240 msec.

Figure 73. Tensile damage, inclined shear damage, and bond failure are simulated in the calculation conducted at 15.9 km/h (9.9 mi/h) with erosion set to 10 percent strain.

One parametric study was conducted to determine the effect of impact velocity on the computed response. The impact velocity in the calculation just discussed was increased from 15.9 km/h (9.9 mi/h) to 18 km/h (11.2 mi/h). At 18 km/h (11.2 mi/h), fracture occurs through the thickness of the beam, along with substantial bond failure, as shown in Figure 74. The beam breaks into two major pieces. The beam and bogie do not rebound. The damage is qualitatively similar to that measured in the test, although less bond failure is evident. This study suggests that 15.9 km/h (9.9 mi/h) is close to the impact velocity at which the bogie just breaks through the beam without rebound.

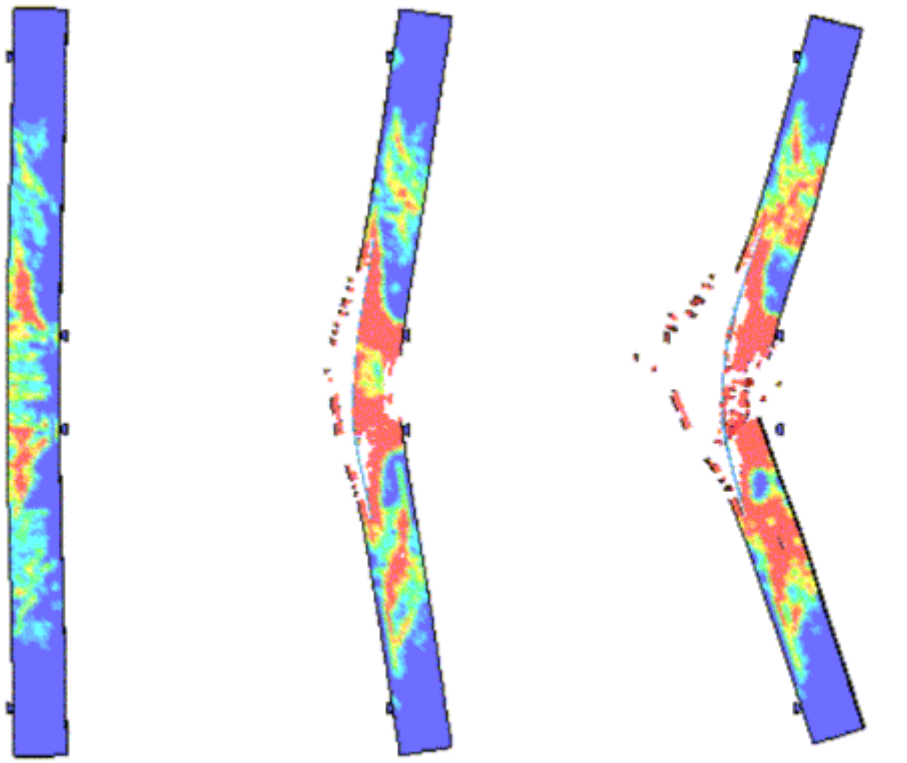

Figure 74. The beam breaks into two major pieces and does not rebound when impacted at 18 km/h (11.2 mi/h).

Another parametric study was conducted to determine the effect of erosion on the computed response. In the baseline calculation previously discussed, erosion is set to occur at 10 percent maximum principal strain. Two additional calculations were conducted with erosion set to 5 percent and 1 percent maximum principal strain. The strain value at which erosion occurs is an option set by the user. Erosion can only occur after damage exceeds 99 percent.

Damage fringes for the calculation conducted with erosion set to 5 percent strain are similar to those calculated at 10 percent strain (not shown). The peak deflection attained before rebound is 211 mm (8.3 inches), in agreement with that calculated at 10 percent strain. Damage fringes for the calculation conducted with erosion at 1 percent strain are shown in Figure 75. In this case, the erosion is more extensive than that calculated at 5 percent and 10 percent strain and breaks the beam into five major pieces. No rebound of the beam occurs. This computational comparison indicates that the erosion strain value affects the computed response, and lower erosion values tend to make the simulation more flexible. The developer has typically used 10 percent strain based on past experience. Numerous calculations throughout this report also use 5 percent strain.

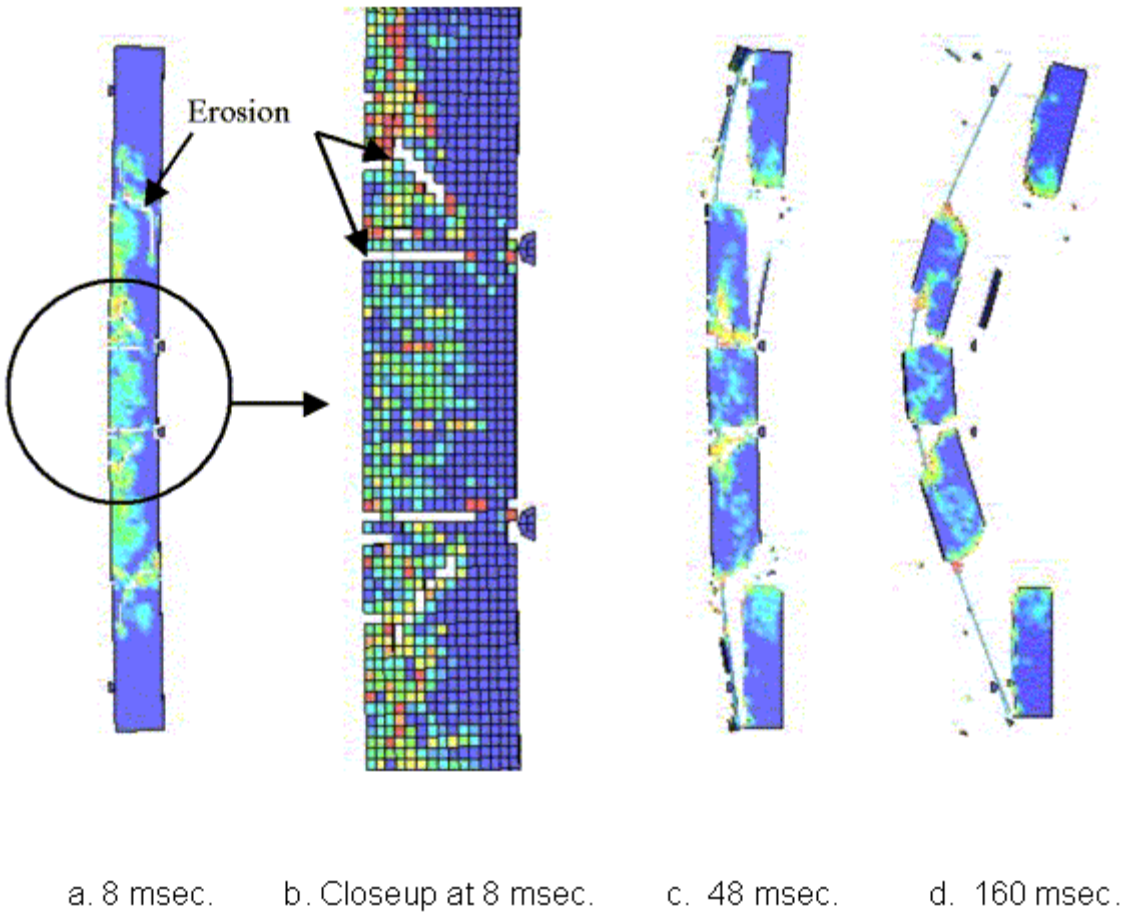

Figure 75. This damage modeled at 15.9 km/h (9.9 mi/h) with erosion set to 1 percent strain is more extensive than when erosion is set to 10 percent strain.

Low Velocity Impact

Three deformed configurations for the low velocity impact test conducted at 8.6 km/h (5.3 mi/h) are shown in Figures 76 and 77. Slight damage occurs beneath each impact cylinder upon contact. Cracks form on the tensile face and propagate toward the compression face. The cracks are most dominant in the impact (constant moment) region and extend about two-thirds of the way through the beam before the beam rebounds. Smaller cracks are observed outside the constant moment region. The beam reaches a maximum deflection of about 70 mm (2.8 inches) at 60 msec, then it rebounds, pushing the bogie vehicle backwards. Additional cracking occurs following rebound during reverse bending.

The deformed configuration of the low velocity test is similar to that of the ⅓-scale tests of over-reinforced concrete beams shown in the previous section. This similarity is because the drop tower test beams are approximate scaled versions of the bogie vehicle test beams. These beams exhibit substantial cracking, but retain their integrity and rebound.

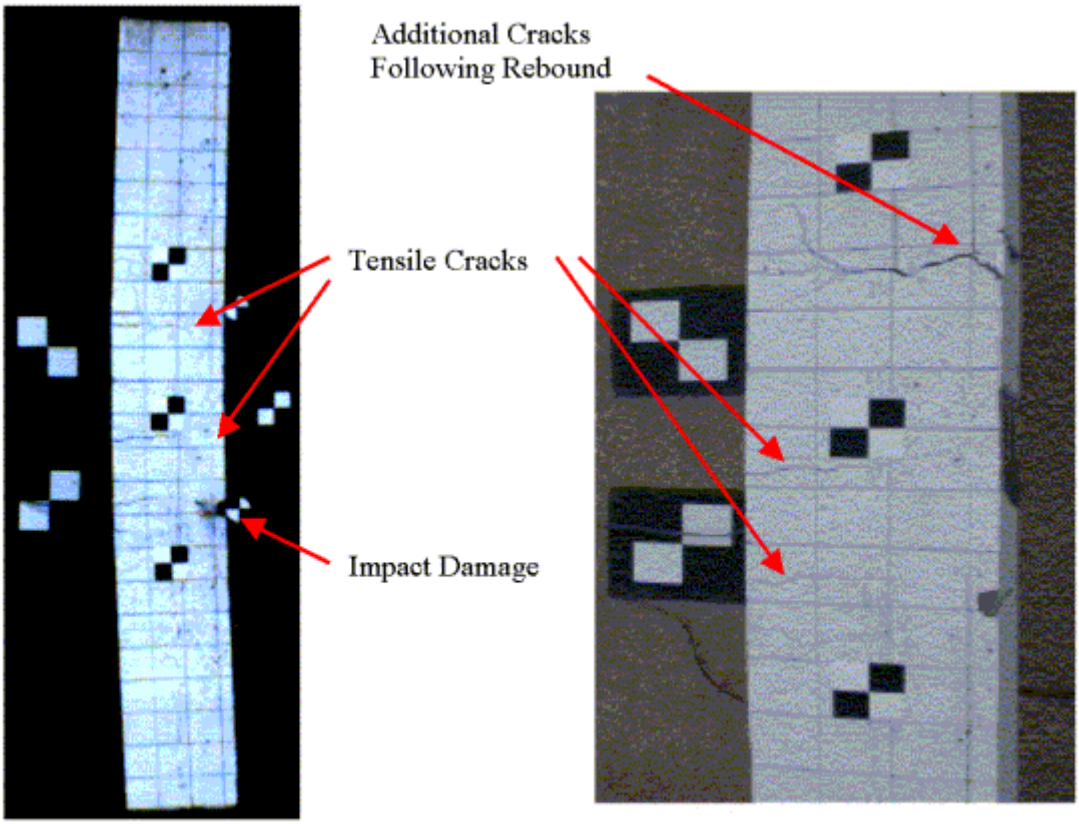

Figure 76. Cracks form on the tensile face of the beam impacted at 8.6 km/h (5.3 mi/h) and propagate toward the compression face.

Two deformed configurations for low velocity impact simulation conducted at 8.6 km/h (5.3 mi/h) with baseline properties are shown in Figure 78. Damage fringes form on the tensile face and are most dominate in the impact region. They extend about three-quarters of the way through the beam before the beam rebounds at about 64 msec. The peak deflection is 69 mm (2.7 inches), which agrees with measurements in the tests. Substantial additional damage occurs during reverse bending following rebound.

Figure 77. The beam rebounds when impacted at 8.6 km/h (5.3 mi/h), pushing the bogie vehicle backward.

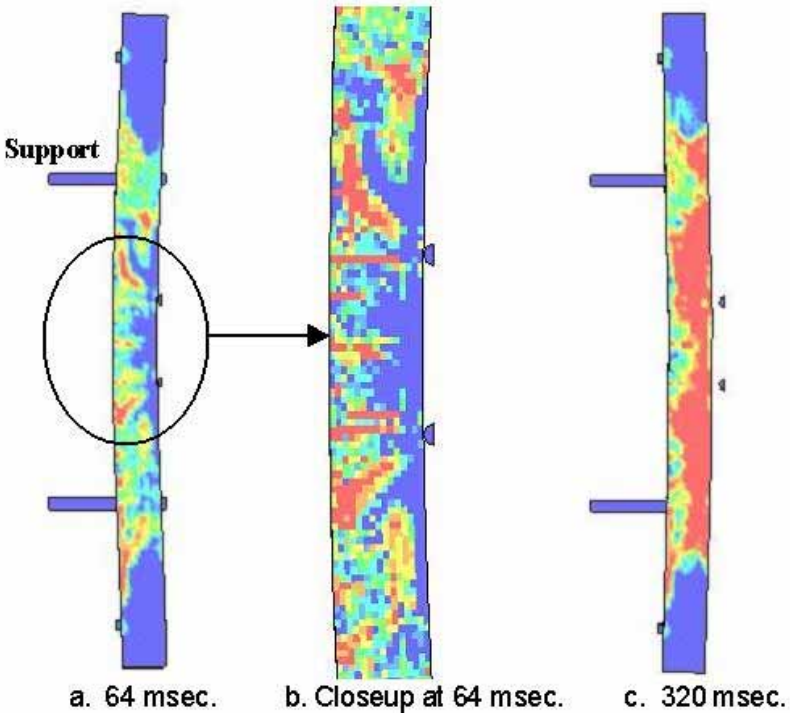

Figure 78. The simulation of the beam impacted at 8.6 km/h (5.3 mi/h) exhibits substantial damage, but retains its integrity and rebounds.

Displacement Histories

Displacement history comparisons are shown in Figure 79 for the low and high velocity tests and simulations. Solid lines represent the data; dashed lines represent the simulations. Histories for both the beam and bogie vehicle are given at low velocity, because the vehicle separates from the beam upon rebound. The simulations accurately calculate the displacement histories through rebound. Some discrepancy exists following rebound at low velocity, in which the simulated beam and vehicle rebound more significantly than during the test. A displacement history is not shown for the intermediate velocity test because the overhead camera did not function.

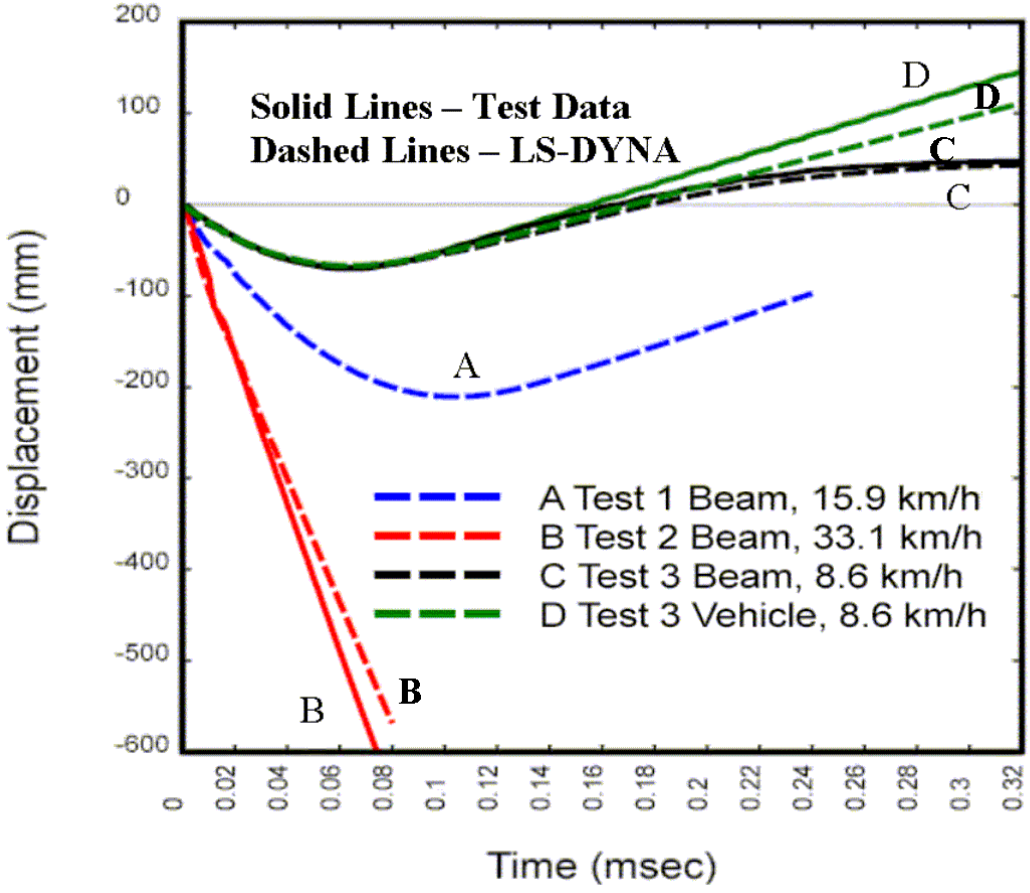

mm = 0.039 inch

Figure 79. The displacement histories from the LS-DYNA bogie vehicle impact simulations compare well with the test data.

One parametric study was conducted to determine the effect of modeling the four supports (load frame and intermediate) on the computed displacement history. Little effect is noted at high impact velocity. However, at low impact velocity, inclusion of the supports affects the rebound displacement history, as shown in Figure 80. Without modeling the supports, the beam impacted at 8.6 km/h (5.3 mi/h) rebounds, but to a greater extent than that measured in the tests. Better agreement with the tests is obtained if the supports are modeled. This agreement was accomplished by modeling the four supports as rigid planes. Dynamic relaxation was used to achieve contact between the beam and supports before impact. The computational a coefficient

of friction of 0.3. Gravity was applied to the beam. Results previously shown in Figures 78 and 79 were conducted with the supports modeled.

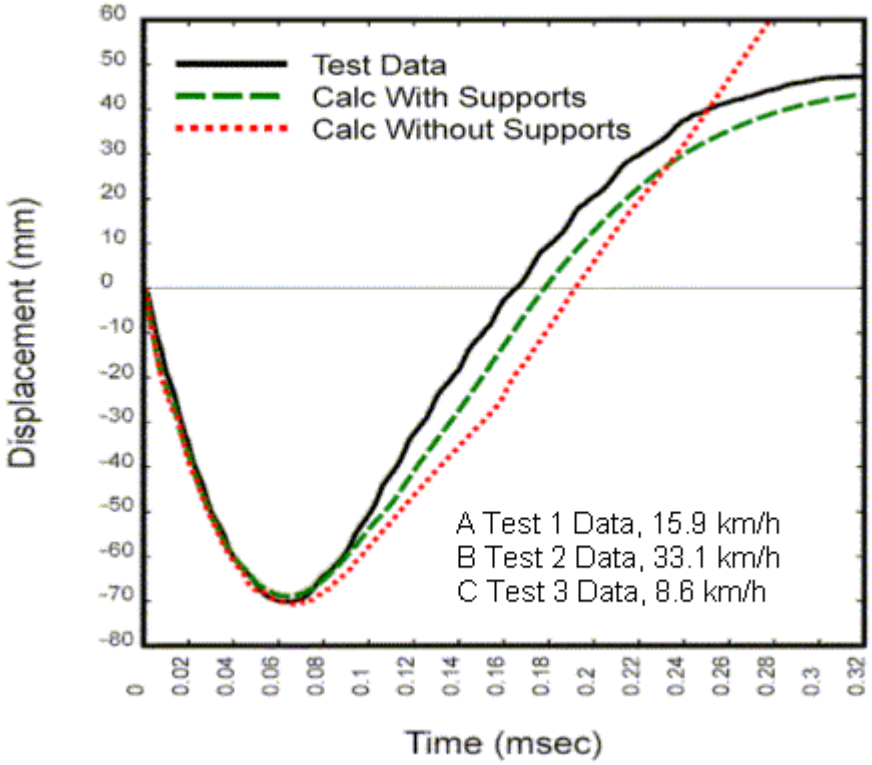

mm = 0.039 inch

Figure 80. The calculations conducted at 8.6 km/h (5.3 mi/h) correlate best with the test data if the supports are modeled.

Strain Histories

Strain histories were measured on the concrete compressive face midway along the length of the beam. One gage was placed 32 mm (1.26 inches) above the centerline, the other 32 mm (1.26 inches) below the centerline. Approximate peak values are 0.0025 and 0.0027 for test 2 at 33.1 km/h (20.6 mi/h), 0.0021 and 0.0023 for test 1 at 15.9 km/h (9.9 mi/h), and 0.0023 for test 3 at 8.6 km/h (5.3 mi/h). The three strain histories measured below the centerline are shown in Figure 81. The strain histories measured above and below the centerline are similar (not shown). The peak strain attained is similar in each test and is approximately 0.23 percent.

Strain histories calculated on the compressive face of the beam, just below the centerline, are shown in Figure 82. Histories calculated above and below the centerline are similar; therefore, only one history is shown. Unlike the measured histories, the calculated histories attain different peaks in each simulation. The peak strain is lowest for the high velocity impact simulation conducted at 33.1 km/h (20.6 mi/h). It is low because the beam breaks centrally into a large trapezoidal piece, and the compressive face of this piece bends less than during pure bending.

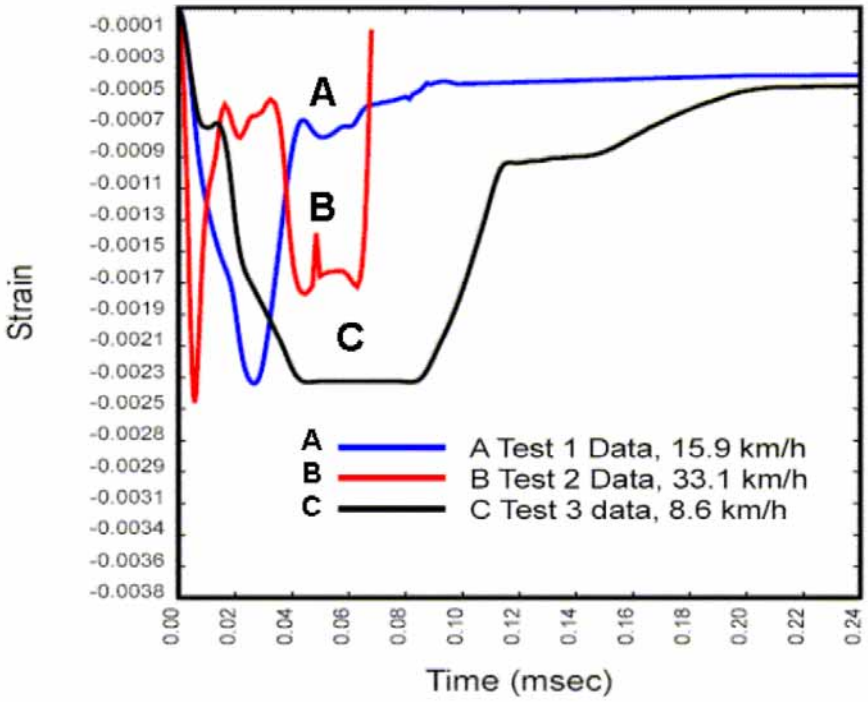

km/h = 0.621 mi/h

Figure 81. Strain histories measured on the compressive face of each beam peak around 0.23 percent strain.

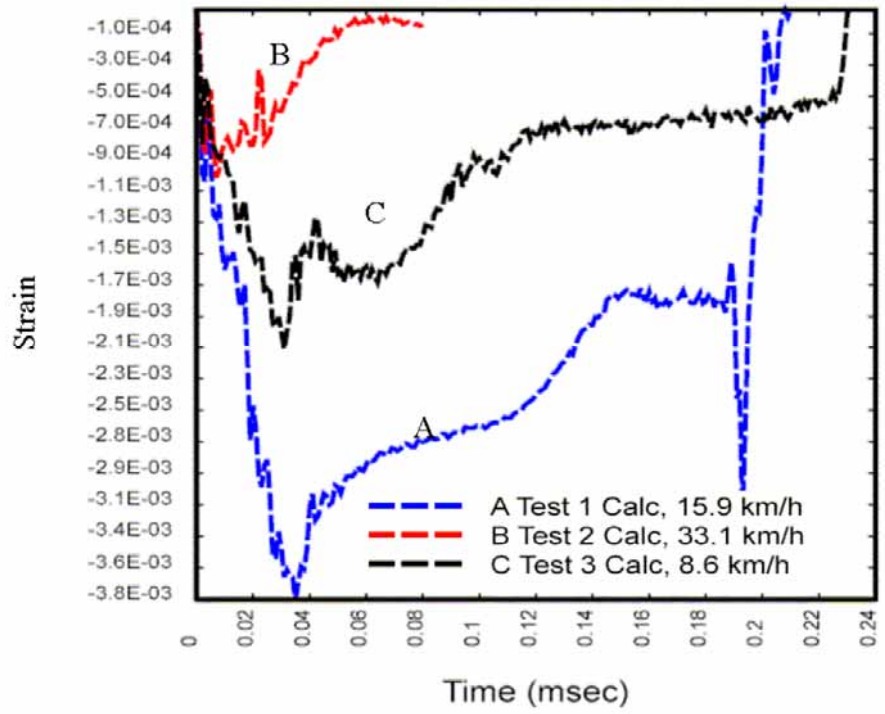

km/h = 0.621 mi/h

Figure 82. The strain histories from the LS-DYNA bogie vehicle impact simulations vary with impact velocity.

The peak strain attained for the low velocity simulation conducted at 8.6 km/h (5.3 mi/h) is approximately 0.21 percent, which is about twice that attained at high impact velocity. This beam retains its integrity during bending and then rebounds; thus, larger bending strains are calculated than at high impact velocity. The peak strain attained is similar to that measured at low impact velocity. However, the calculated strains go into tension at about 230 msec, while the measured strains remain compressive at about 0.058 percent for the duration of the recording to 468 msec. It is unclear why the measurements remain compressive once the test beam rebounds and goes into reverse flexure at about 200 msec.

The peak strain attained for the intermediate velocity simulations conducted at 15.9 km/h (9.9 mi/h) is approximately 0.38 percent. In this simulation, the bending calculated between the two impact cylinder locations is significant, while little bending occurs between each impact cylinder and edge of the beam. The strains become tensile once the beam rebounds.

These comparisons demonstrate how difficult it is to correlate strain measurements, even when good correlations are obtained for deformed configurations and deflections. The difficulty lies in the fact that strain histories are local behaviors that can vary significantly from position to position along the beam.

SUMMARY FOR IMPACT SIMULATIONS

The response of the three beams tested depends on the impact velocity. The computational model accurately simulates the substantially different displacement histories and damage modes measured between high (33.1 km/h (20.6 mi/h) and low (8.6 km/h (5.3 mi/h)) velocity impact. At high velocity impact, damage is dominated by inclined shear cracks, and the beam breaks into several large pieces without rebounding. At low velocity impact, tensile cracks form, but the beam retains its integrity and rebounds.

At intermediate velocity (15 km/h (9.3 mi/h)), a combination of bending and shear was observed in the test. The beam ultimately failed on one side without rebounding due to large tensile and shear cracks. The simulation exhibited a more symmetric behavior with a combination of bending and shear cracks, but ultimately rebounded. However, the computed damage becomes similar to the measured damage, without rebound, if the impact velocity is increased from 15.9 km/h (9.9 mi/h) to 18 km/h (11.2 mi/h). This suggests that the 15.9 km/h (9.9 mi/h) impact velocity tested is close to the velocity needed to transition from rebound to breakthrough. An additional parametric study indicates that reducing erosion strain from 5 percent to 1 percent also improves correlations by transitioning the simulation results from rebound to breakthrough.

CHAPTER 8. TEXAS T4 BRIDGE RAIL

USER INTRODUCTION

This chapter, parts of chapter 9, and appendix A present findings related to the evaluation of the concrete material model by a potential end user of the model. The evaluation consisted of a series of verification calculations and validation analyses using the LS-DYNA implementation of the concrete material model (MAT type 159 or MAT_CSCM). The user obtained a beta binaries release of LS-DYNA version 971 for the following platforms: Silicon Graphics, Inc. (SGI) IRIX® (version 971 release 1490 double precision), MS-Windows (version 971 release 1612 single precision), and Linux Intel 32 bit architecture (version 971 release 1708 single precision). Because LS-DYNA version 971 is a beta release, several releases of these binaries were added during the project period. The research team used the Linux Intel 32 bit architecture (version 971 release 1708 single precision) release to maintain consistency and avoid potential software glitches associated with beta releases that occurred subsequent to the project's initiation.

The work plan followed in the model evaluation process consisted of two tasks. First, calculations were performed to establish that the executable of LS-DYNA obtained by the user gave the same results as the executable used by the developer. This was accomplished by reproducing five developer evaluation calculations using developer-supplied input files. The calculations included three concrete impact simulations that correlate with bogie impact tests of reinforced concrete beams, and two drop-tower simulations that correlate with drop-tower tests. Results of these calculations are given in appendix A.

Second, the concrete material model was used in the impact analysis of a roadside safety structure in which some concrete failure was observed. The structure selected for analysis was the Texas T4 bridge rail. After the initial evaluation of the concrete material model, the roadside safety structure model was used in a parametric study to evaluate model sensitivity to variations in key material parameters. Results of calculations conducted by the user are given in this chapter . Additional support calculations conducted by the developer are given in appendix B.

The user wanted to more fully evaluate the concrete material model in other roadside safety structures. Considerable test data exist for various bridge rail parapets, bridge decks supporting metal rails, and portable concrete barriers in which varying degrees of concrete damage and/or failure occurred. However, the resources allocated for the evaluation and validation effort were not sufficient to support additional model development and analyses. A model of a safety-shape bridge rail with New Jersey profile was developed under this research effort. Data available for this bridge rail included quasi-static load tests to failure and two full-scale vehicular crash tests. Although some preliminary calculations were performed on this model, project resources were depleted before the structure could be fully analyzed by the user. Preliminary calculations performed by both the user and developer are discussed in chapter 9.

OVERVIEW

This task involved modeling and analyzing a roadside safety structure made of concrete and using the results to help define the applicability of the concrete material model to the analysis and design of concrete roadside safety structures. The structure selected for analysis was the Texas Type T4 bridge rail.

Two different design variations of the T4 rail were evaluated through dynamic pendulum testing under a previous research study.[12] Using these tests for evaluation of the concrete model has several benefits. First, the tests provide an opportunity to assess the concrete model in a roadside safety application. Second, use of the pendulum bogie makes the tests more controlled and eliminates the variability associated with full-scale vehicles. Third, two specimens were tested for each design variation, which provides some information about system variability. Finally, the two design variations demonstrated different levels of damage and, therefore, provide the ability to assess sensitivity of the concrete model to small design changes under similar loading conditions.

PENDULUM TESTING

The T4 railing consists of a 381-mm- (15-inch-) tall metal rail anchored to the top of a 457.2-mm- (18-inch-) tall concrete parapet wall, providing an overall rail height of 838.2 mm (33 inches). The metal rail consists of a short section of an elliptically shaped steel tube welded atop a post fabricated from steel plate. The steel post is welded to a steel base plate that is anchored to the concrete parapet.

In one design variation, the width of the steel-reinforced concrete parapet is 254 mm (10-inch), and the steel rail is attached to the parapet using four 22.2-mm- (0.087-inch-) diameter anchors. In the second variation, the width of the concrete parapet is 317.5 mm (12.5 inches), and the steel rail is attached to the parapet using three 22.2-mm- (0.087-inch-) diameter anchors. Vertical reinforcement in the parapets consisted of #5 V bars spaced 266.7 mm (10.5 inches) apart. Longitudinal reinforcement in the parapets consisted of two #5 bars equally spaced at the top of each parapet and within the V bars.

Detailed drawings of the bridge rail specimens are shown in Figures 83 and 84 for the 254-mm- (10-inch-) and 317.5-mm- (12.5-inch-) wide parapet designs, respectively. A photograph of a test specimen with a 254-mm- (10-inch-) wide parapet is shown in Figure 85; a photograph of the test installation with a 317.5-mm- (12.5-inch-) wide parapet is shown in Figure 86.

To simulate the actual connection of the rail system to a bridge, each parapet was constructed on top of a 203.2-mm- (8-inch-) thick steel-reinforced concrete bridge deck that was cantilevered off a concrete beam a distance of 736.5 mm (29 inches). Transverse reinforcement in the deck cantilevers consisted of two layers of #5 bars located 152.4 mm (6 inches) apart. Longitudinal reinforcement in the top layer of each deck consisted of #4 bars located 228.6 mm (9 inches) apart. Longitudinal reinforcement in the bottom layer of the deck cantilevers consisted of two #5 bars located near the field side edge spaced approximately 76.2 mm (3 inches) apart with the

next adjacent bar located 304.8 mm (12 inches) away. Average concrete compressive strengths for the decks and parapets were determined on the day of testing to be:

- 35.50 MPa (5,149 lbf/inch^2) for the decks for all tests.
- 30.44 MPa (4,415 lbf/inch^2) for the parapets for all tests.

TEST RESULTS

Testing was conducted with a gravitational pendulum equipped with a crushable nose assembly. The pendulum bogie was built in accordance with the specifications of the Federal Outdoor Impact Laboratory's (FOIL) pendulum. The crushable nose assembly is the FOIL 10-stage honeycomb nose that uses expendable aluminum honeycomb material of differing densities in a sliding frame structure. Frontal crush stiffness of the staged nose assembly is calibrated to represent the frontal crush stiffness of a small passenger car. The pendulum body was instrumented with an accelerometer. The mass of the instrumented pendulum bogie was 838 kg (1,848 lb), and it was raised to a height sufficient to achieve an impact speed of 9,835 mm/sec, (387.2 inches/sec), which is 35.4 km/h (22 mi/h)). The nose of the pendulum bogie contacted the elliptical tube on the steel rail portion of the system. The impact loads were transferred to the concrete parapet and deck through the steel rail.

For each design variation of the T4 bridge rail, two identical specimens were constructed and tested. For the design variation with the 254-mm- (10 inch-) wide parapet, the test designations were P3 and P4. For the design variation with the 317.5-mm- (12.5-inch-) wide parapet, the test designations were P5 and P7.

The observed failure mode in tests P3 and P4 was punching shear failure of the field side of the concrete parapet due to load applied through the anchor bolts and base plate. In each test, the impact forces caused the concrete to fracture and spall off the field side of the parapet. In addition, cracks in the top of the concrete parapet radiated outward from the outside anchor bolts of the base plate and pieces of concrete were pushed out on the field side of the parapet. Damage to the test specimen with a 254-mm- (10 inch-) wide parapet after test P3 is shown in Figure 87. Post-test damage from test P4 is shown in Figure 88.

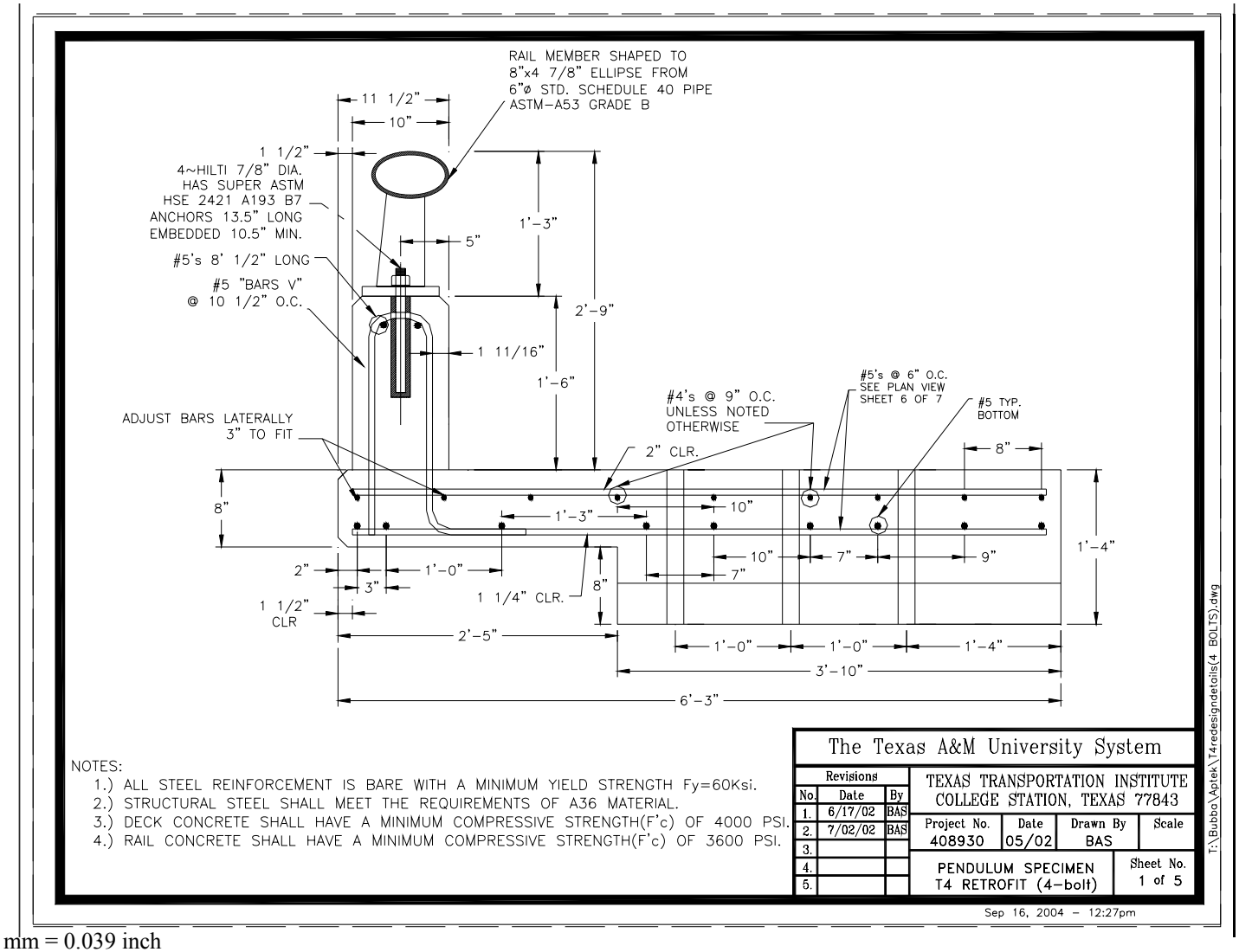

mm = 0.039 inch

Figure 83. Details of T4 rail with four-bolt anchorage and 254-mm- (10-inch-) wide parapet.

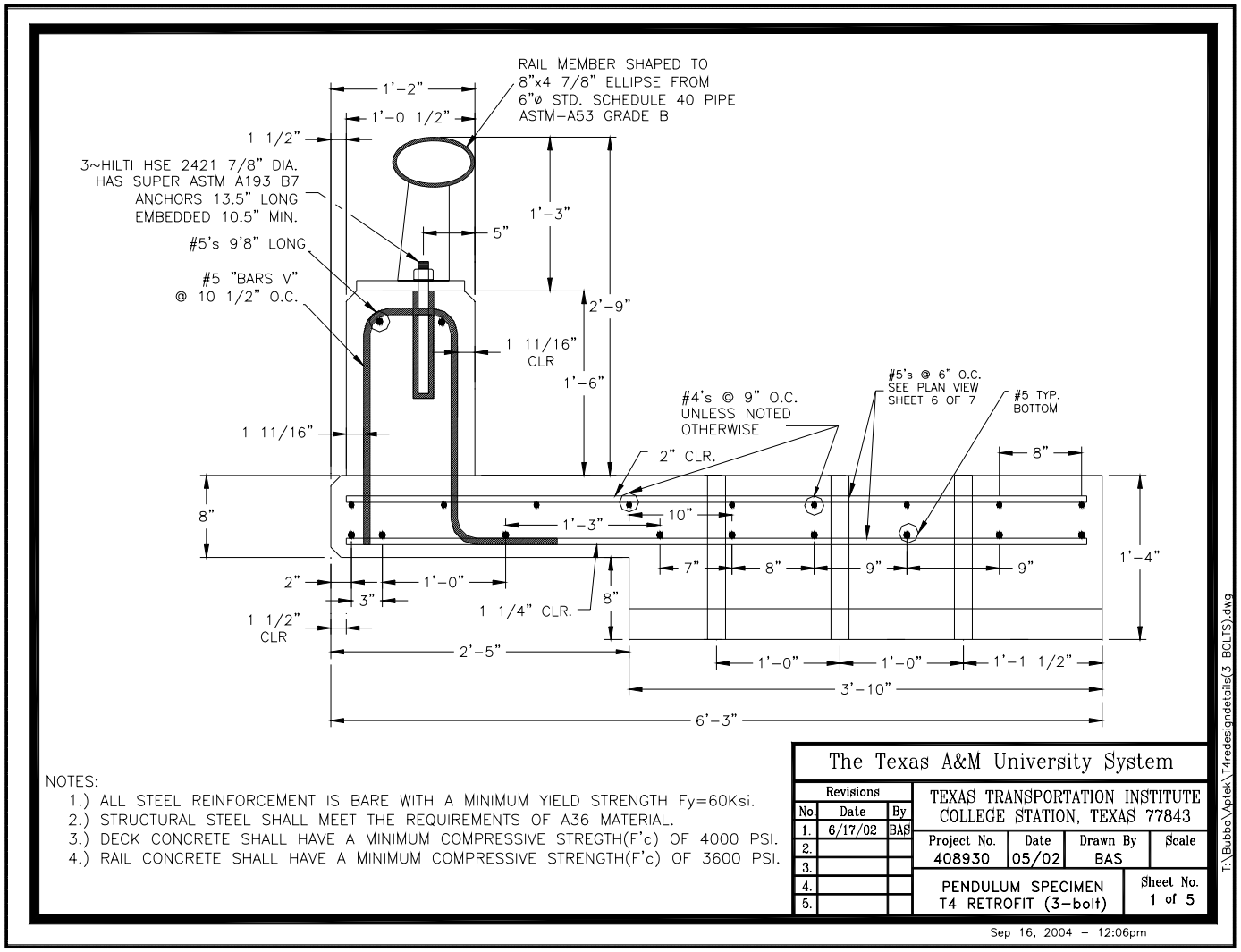

mm = 0.039 inch

Figure 84. Details of T4 rail with three-bolt anchorage and 317.5-mm- (12.5-inch-) wide parapet.

Figure 85. Parapet before test P3.

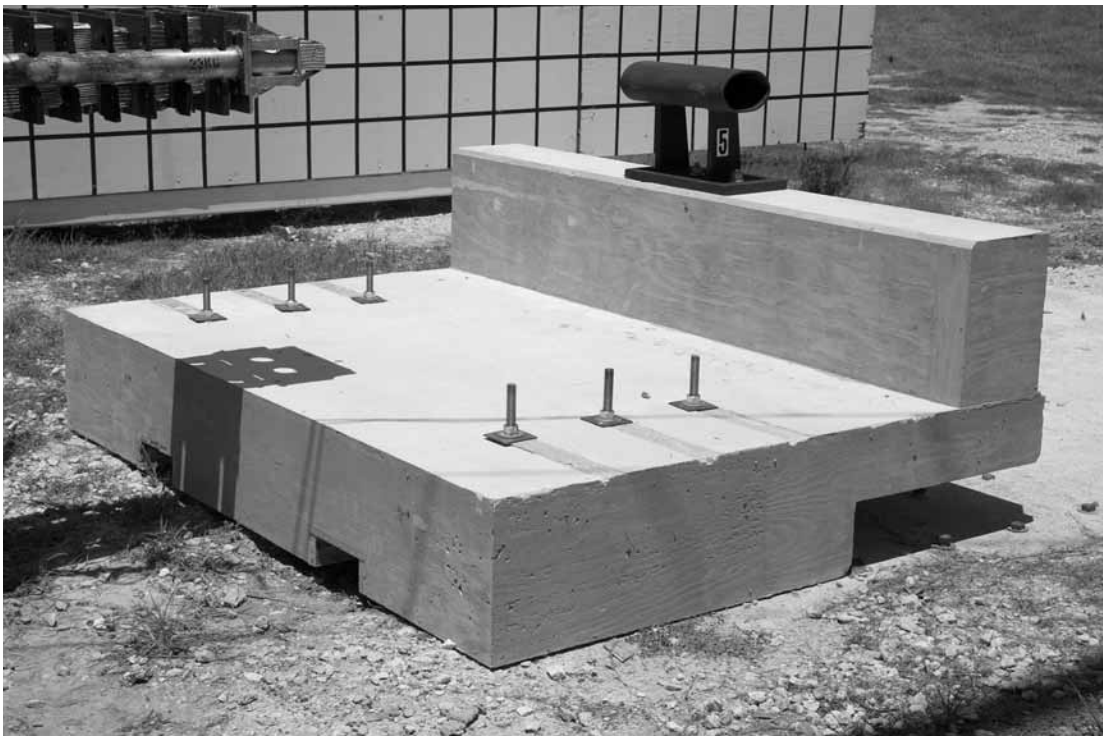

Figure 86. Parapet before test P5.

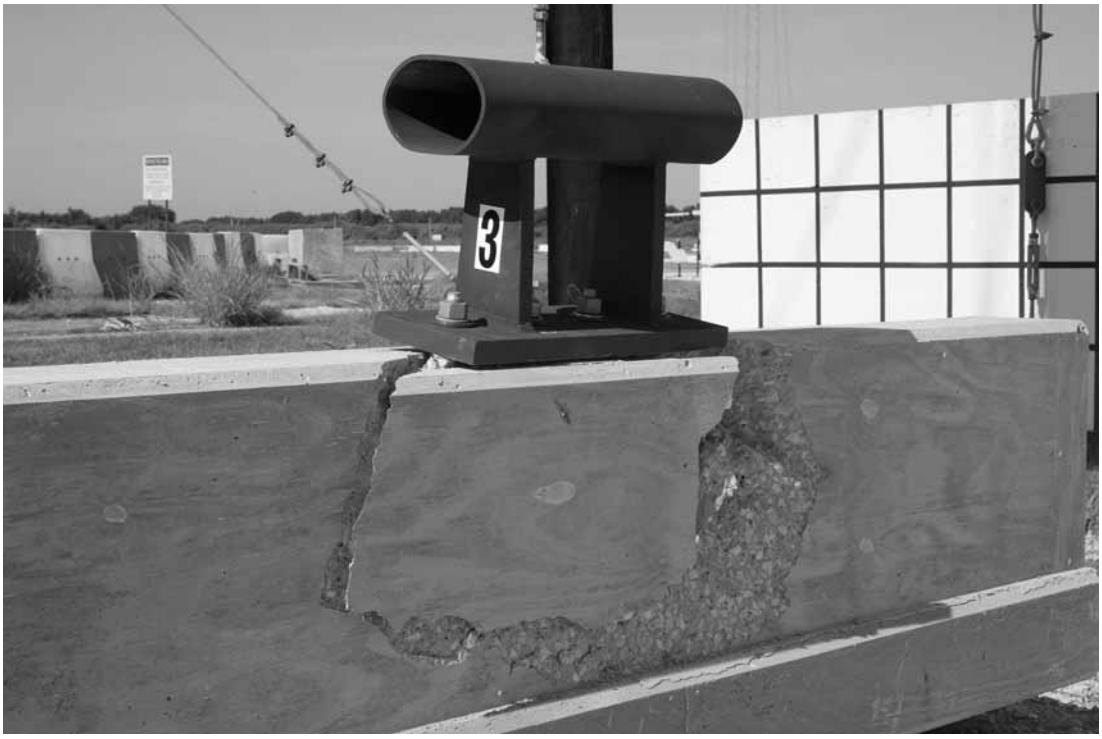

Figure 87. Parapet damage after test P3.

Figure 88. Parapet damage after test P4.

In test P5, a T4 rail with three-bolt anchorage design and a 317.5-mm- (12.5-inch-) wide parapet was evaluated. The pendulum impact caused no visible damage to the concrete parapet or deck. Damage to the test specimen with a 317.5-mm- (12.5-inch-) wide parapet after test P5 is shown in Figures 89 and 90. The same parapet was tested again (test P6) with different staging of the pendulum nose assembly. The impact caused small cracks to be formed in the concrete parapet. The cracks radiated out at an angle from the anchor bolts on the top of the parapet and continued at an angle down the field side of the parapet into the bridge deck.

The second test specimen with 317.5-mm- (12.5-inch-) wide parapet was evaluated in test P7. The impact conditions and pendulum configuration were the same as those used in tests P3, P4, and P5. The impact forces imparted by the pendulum caused the formation of thin hairline cracks in the top of the concrete parapet that radiated out from the anchor bolts of the base plate and down the field side of the parapet into the bridge deck. Post-test damage from test P7 is shown in Figure 91.

SIMULATION METHODOLOGY

The methodology followed to model the bridge parapets, simulate pendulum impacts, and evaluate the concrete material model consisted of the following steps:

1. Modify, optimize, and calibrate the crushable nose pendulum model.
2. Construct finite element model of the two variants of the T4 rail system.
3. Incorporate the new concrete material model for concrete parts (e.g., parapet and bridge deck).
4. Identify critical parameters of the model and investigate the performance of the model through finite element analysis.
5. Compare results with test data and identify any further investigation needed.

PENDULUM MODEL CALIBRATION

To simulate the test conditions described here, it is critical to have an accurate representation of the impacting device. A model of the FOIL pendulum with crushable honeycomb nose assembly was obtained from NCAC. The internal honeycomb cartridges and spacers comprising the nose of the pendulum (see Figure 92) were replaced with a single nonlinear spring as shown in Figure 93. The external honeycomb cartridge on the leading edge of the nose assembly was maintained in the model. However, its density was increased to account for mass of the removed cartridges. Previous experience with the original model with honeycomb nose required runtimes of around 8 central processing unit hours on a mainframe computer to complete a calibration run with the pendulum impacting a rigid pole. The modified pendulum model requires only 15 minutes on a personal computer for a similar problem. The spring-based pendulum (SBP) model was calibrated using a test of the pendulum impacting a rigid pole. The stiffness values of the nonlinear spring were iteratively adjusted until the force-time history obtained from the SBP model closely matched data measured in the rigid pole test.[13]

Figure 89. Parapet damage after test P5, side.

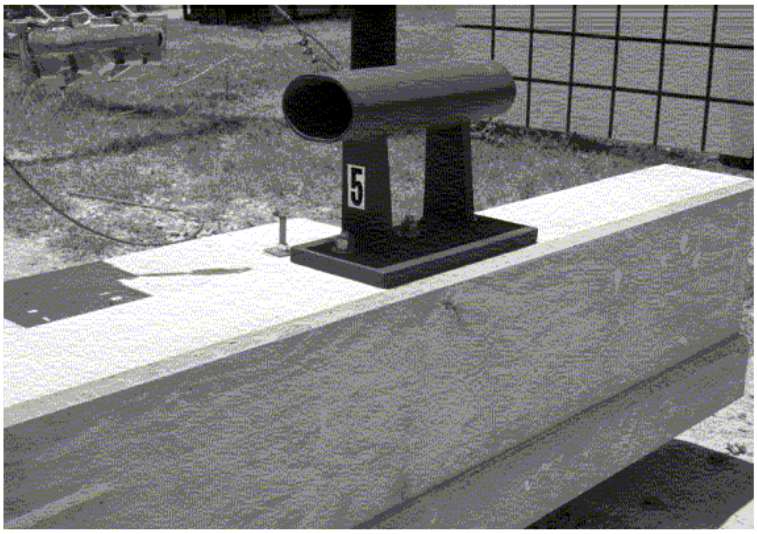

Figure 90. Parapet damage after test P5, rear.

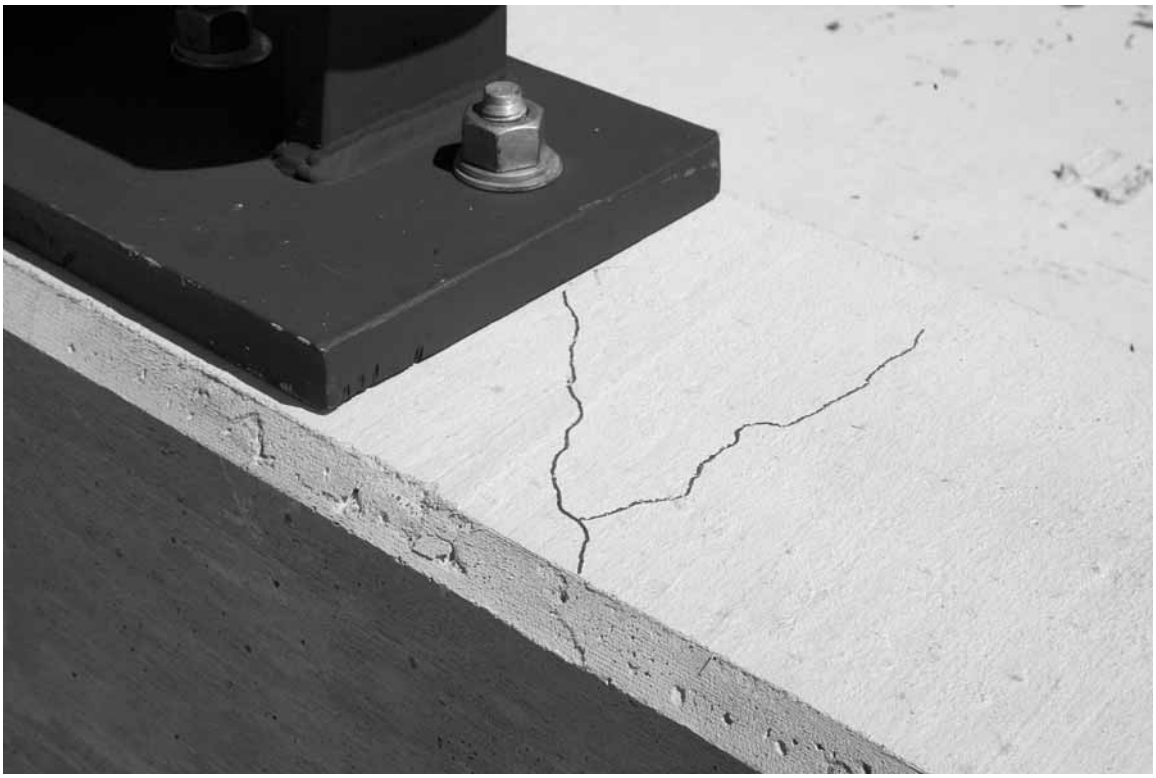

Figure 91. Parapet damage after test P7.

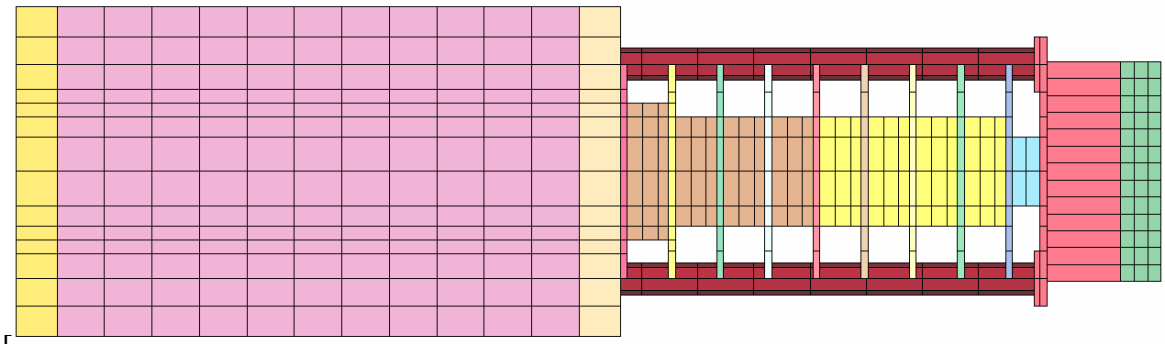

Figure 92. Original pendulum model.

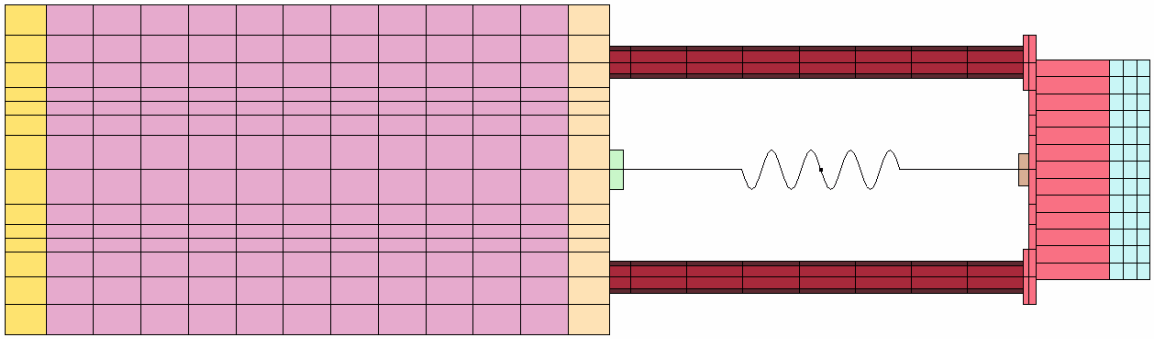

Figure 93. Modified pendulum model.

As shown in Figure 94, the SBP model's force-time history closely matches the rigid pole pendulum calibration test. This calibrated model was used in initial simulations of both variations of the T4 bridge rail system. As the research progressed, it was observed that the impact forces imparted by the pendulum model did not correspond to those measured in the pendulum tests. Comparison of the T4 bridge rail test data with the original pendulum calibration test data indicated that the initial segments of the pendulum nose used in the T4 bridge rail tests were stiffer than those used in the original rigid pole calibration tests. Whereas the pendulum response in tests P3, P4, P5, and P7 appeared reasonably consistent, the response measured in the calibration tests differed.

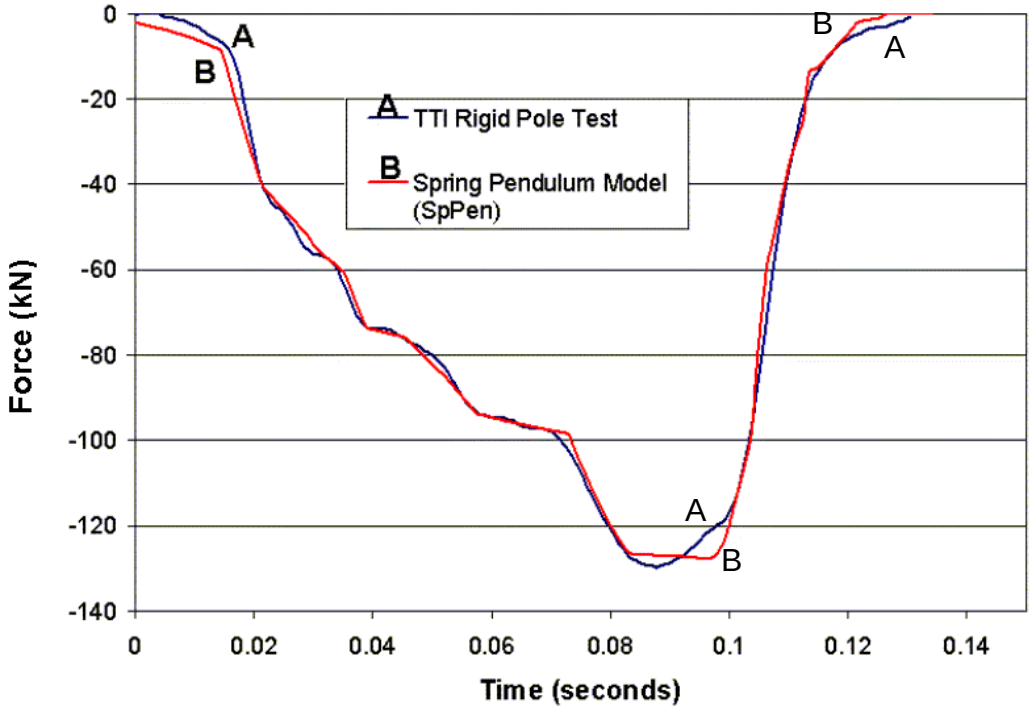

kN = 225 lbf

Figure 94. Comparison of the SBP model to rigid pole calibration test.

Aluminum honeycomb is known to be a variable material. While crush characteristics of the honeycomb used in the rigid pole calibration were quantified through separate axial compression tests, no such tests were performed prior to the T4 bridge rail tests. It is speculated that the crush properties of the honeycomb material used to construct the crushable nose assembly in the 1997 rigid pole calibration tests differed from those of the honeycomb materials used in the 2002 pendulum tests of the T4 bridge rail specimens. Any change in pendulum stiffness would affect the force-time history response and, hence, the energy applied to the barrier.

Because proper load application is critical to evaluating barrier damage and the concrete material model, a recalibration exercise was undertaken. Test P5 on the T4 bridge rail alternative with three-bolt anchorage and 317.5-mm- (12.5-inch-) wide parapet was used for recalibrating the nonlinear spring representing the honeycomb cartridges. This test was selected because no damage to the parapet was observed after the test. However, the rail system did undergo some

elastic deformation and rebound during the test. Thus, the calibration process involved applying a prescribed displacement to the elliptical steel rail. The displacements that were prescribed on the rail were obtained from the test using high-speed film analysis measurements. By explicitly accounting for the displacement of the rail, the pendulum response can be uniquely obtained.

As with the original calibration, the recalibration process involved iteratively adjusting the stiffness values of the nonlinear spring model until the resulting force-time history closely matched data measured in the test P5. The recalibrated pendulum model was labeled SBP2. As shown in Figure 95, the pendulum configuration used in the rigid pole test has a different force-time history than the pendulum used in the test of the almost rigid T4 rail with 317.5-mm- (12.5-inch-) wide parapet (test P5). The good correlation achieved between the recalibrated pendulum model (SBP2) and the pendulum configuration used in test P5 can also be observed in Figure 95.

Figure 96 presents the force-deflection relationships obtained from both simulation and testing of both the rigid pole and T4 bridge rail with 317.5-mm- (12.5-inch-) wide parapet (test P5). As shown in this figure, the crushable nose used in test P5 is indeed stiffer than that used in the original rigid pole pendulum calibration test. It can also be observed from Figure 96 that the recalibrated pendulum model provides reasonable correlation with the pendulum used in test P5. The pendulum model follows the same stiffness trend, and the difference in energy between simulation and test is less than 1.0 percent.

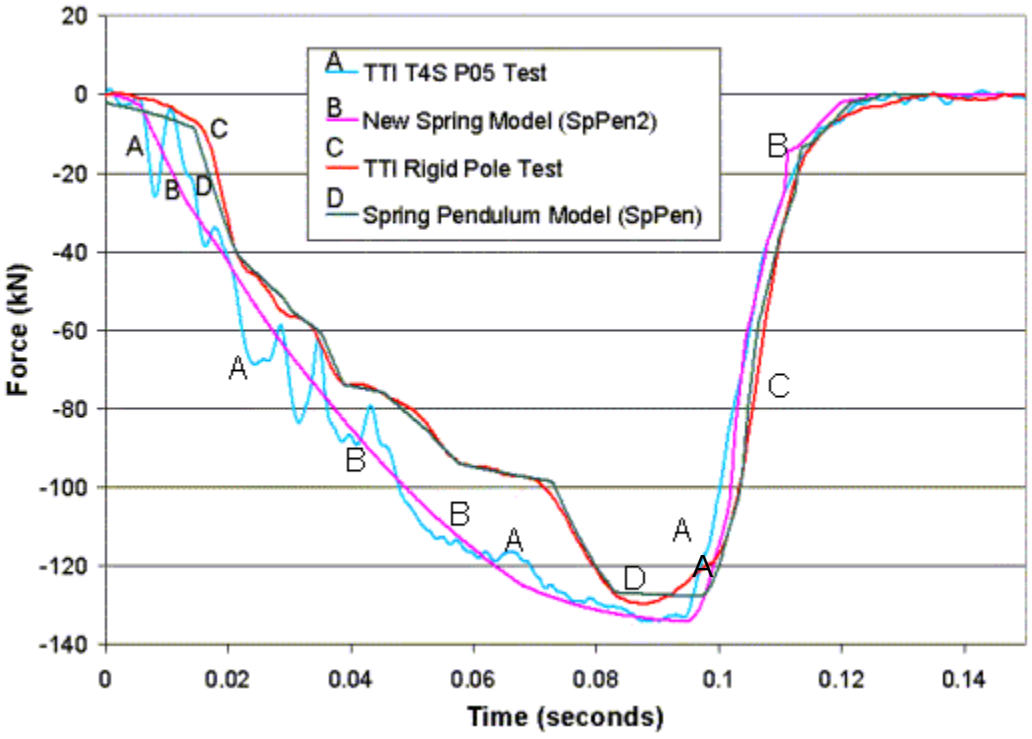

kN = 225 lbf

Figure 95. Force-time histories for benchmark tests and spring models.

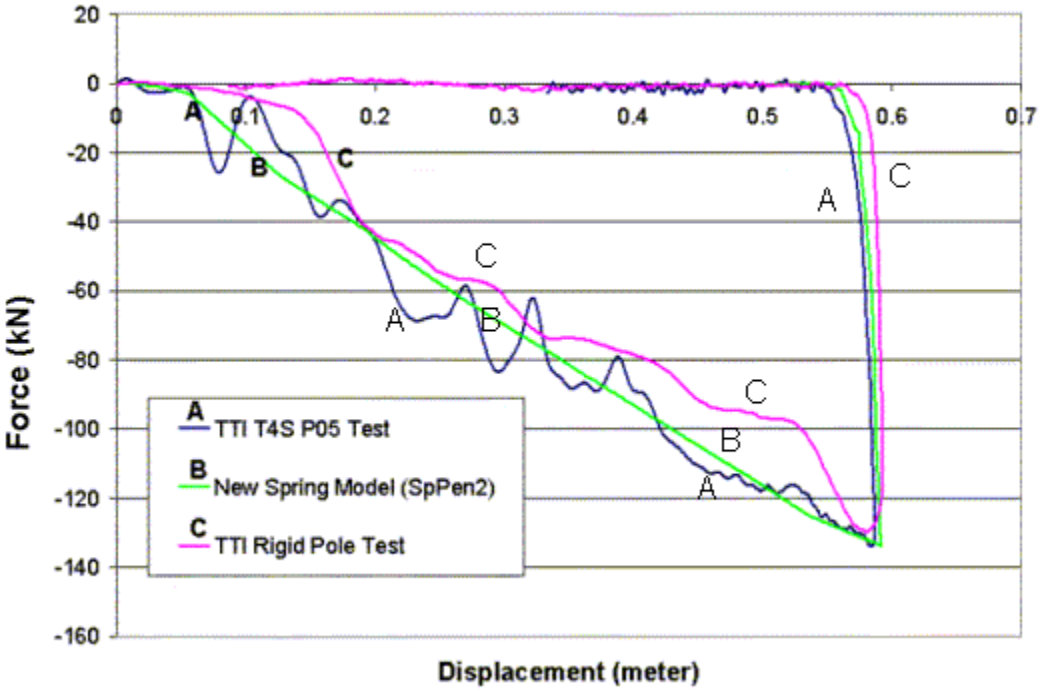

kN = 225 lbf

Figure 96. Force-displacement relationships for benchmark tests and SBP2 model.

FINITE ELEMENT MODEL OF T4 BRIDGE RAIL

Finite element analysts typically follow certain procedures before and after running the numerical solver to help maintain quality control and achieve efficient analysis. The solver used for this study was LS-DYNA. LS-DYNA is an explicit-implicit, multiphysics, nonlinear finite element solver. The pre-processor used for this study was HyperMesh®. The post-processor used was LS-POST. The following steps were followed in analyzing the application of the new concrete material model in the T4 bridge rail system:

1. Geometrical modeling of the structure's components. This step includes defining the spatial topology of the model.
2. Meshing the model. In this step, the spatial topology of each model component is discretized into thousands of small elements (i.e. finite elements).
3. Defining sectional properties. This step includes establishing the thickness of shell elements, the cross-sectional properties of beam elements, and prescribing an element formulation for all element types.
4. Prescribing boundary conditions, contacts, initial velocity, and other constraints needed for accurately representing the physics of the impact.
5. Incorporating material models for all parts including concrete components.
6. Conducting the analysis.
7. Post-process results and comparing these results to test data.

Various steps of this process were systematically repeated to evaluate sensitivity of the model's response to changes in certain modeling and material parameters.

Overview of T4 Parapet/Deck Model

The finite element representation of the T4 bridge rail specimens consists of the following components:

- Concrete parapet and deck.
- Steel reinforcement and anchor bolts.
- Steel elliptical rail, post, and base plate.

Figures 97 and 98 show the model components for the four-bolt and three-bolt parapet designs, respectively. The concrete parapet and bridge deck were modeled using solid elements, as were the steel base plate and the plates comprising the steel post. Shell elements were used to model the elliptical steel rail. Beam elements were used to model the anchor bolts and steel reinforcement inside the parapet and bridge deck.
Figure 99 shows a closeup view of the steel portion of the bridge rail model, including the elliptical rail, post, base plate, and anchor bolts. Figures 100 and 101 show the steel reinforcement and anchor bolts incorporated into the four-bolt and three-bolt parapet models, respectively. All vertical and longitudinal steel were explicitly modeled.

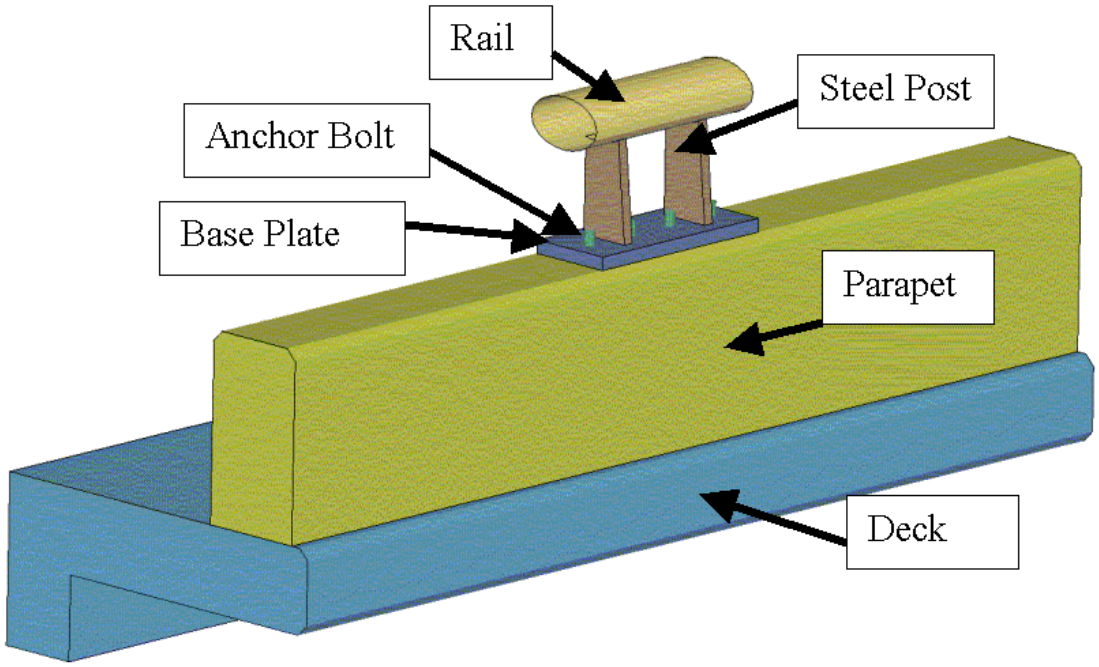

Figure 97. Model of T4 bridge rail specimen with four-bolt anchorage and 254-mm- (10-inch-) wide parapet.

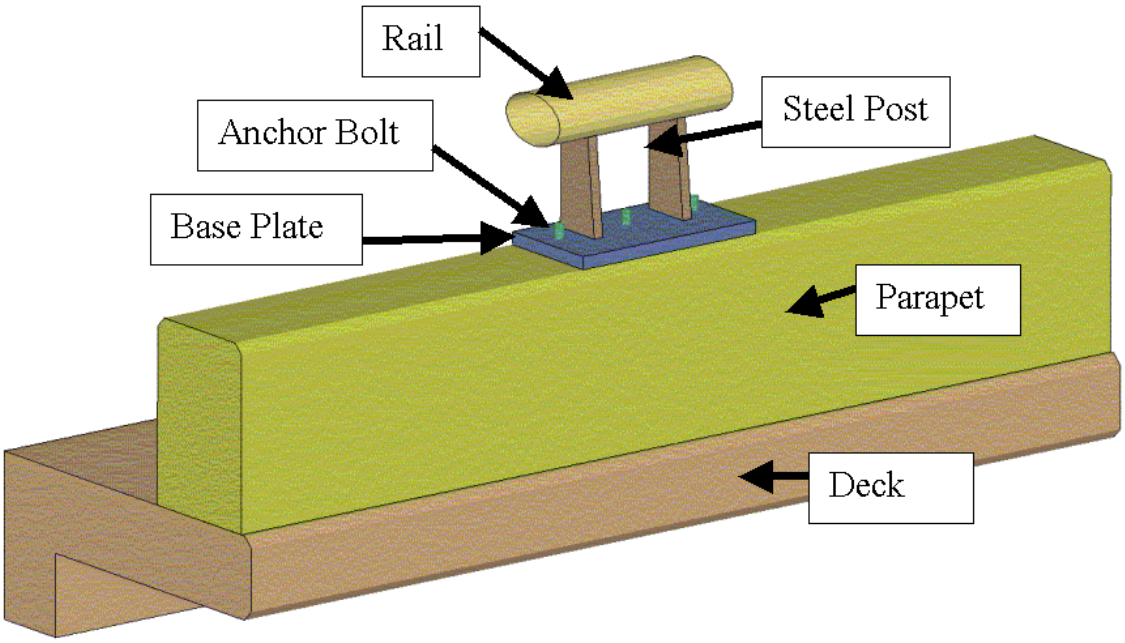

Figure 98. Model of T4 bridge rail specimen with three-bolt anchorage and 317.5-mm- (12.5-inch-) wide parapet.

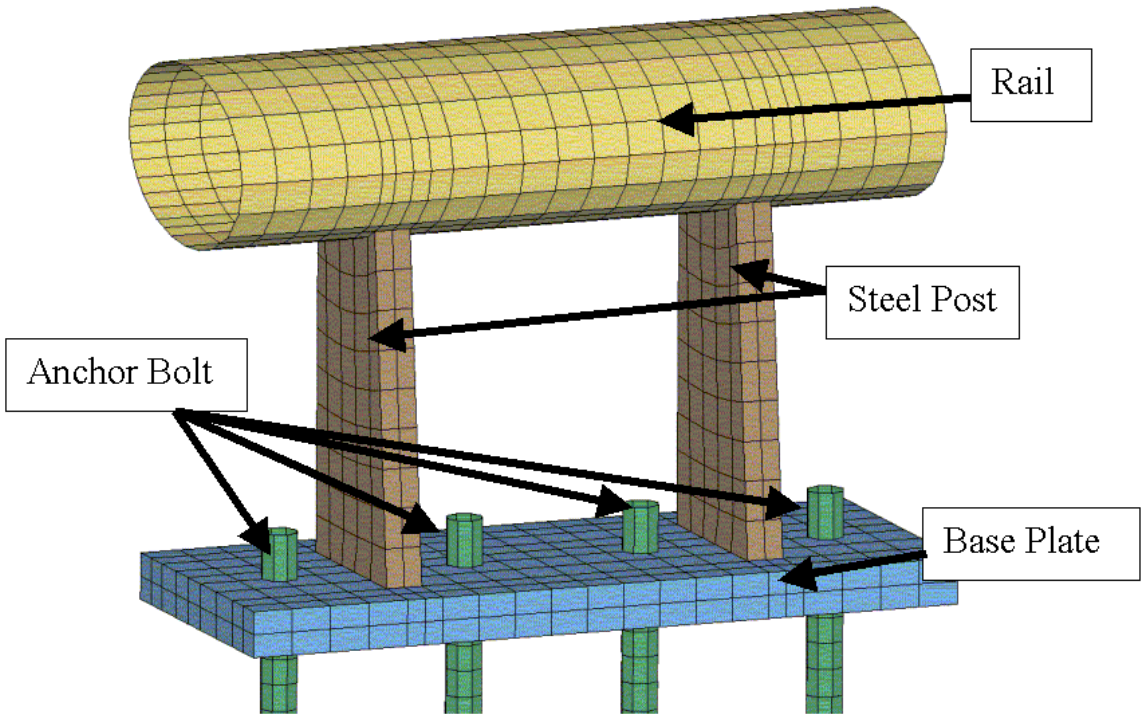

Figure 99. Closeup view of steel rail system with four-bolt anchorage.

.

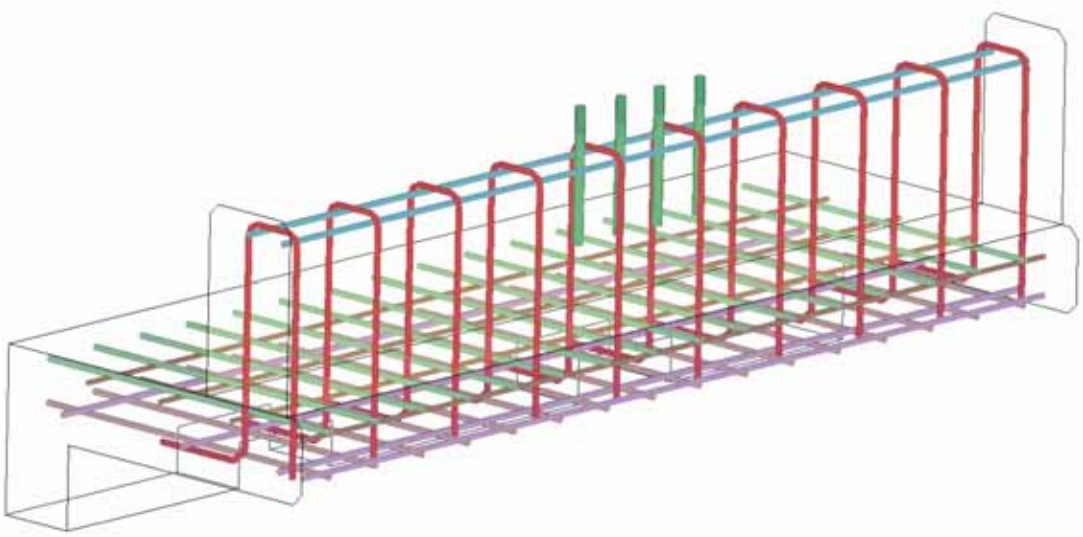

Figure 100. Steel reinforcement and anchor bolts for T4 bridge rail specimen with four-bolt anchorage and 254-mm- (10-inch-) wide parapet.

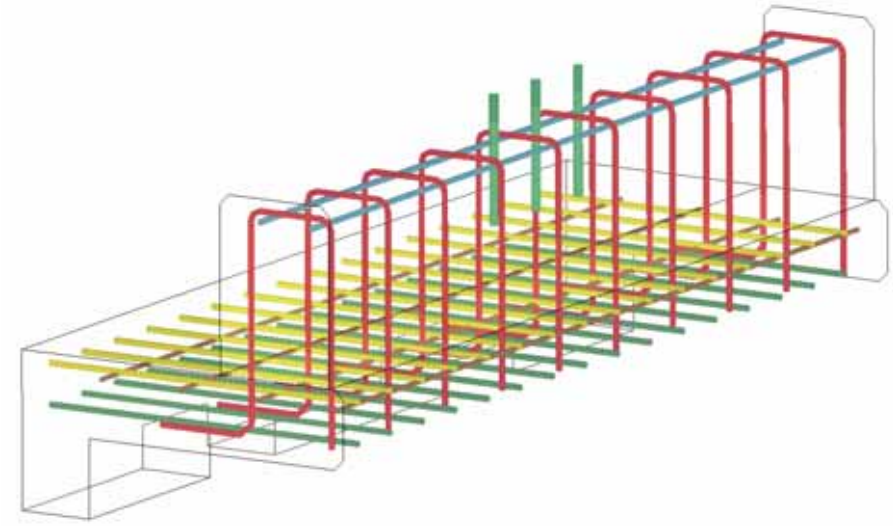

Figure 101. Steel reinforcement and anchor bolts for T4 bridge rail specimen with three-bolt anchorage and 317.5-mm- (12.5-inch-) wide parapet.

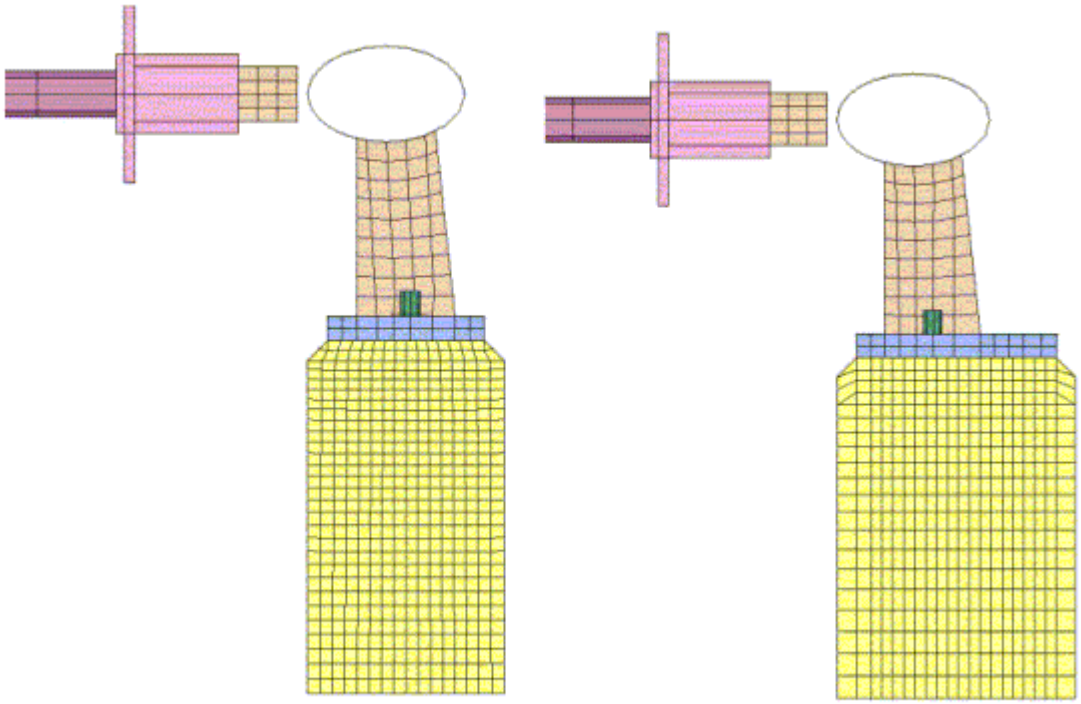

a. Four-bolt design. b. Three-bolt design.

Figure 102. Right end view of parapet-only model for four-bolt design and three-bolt design.

The investigations included evaluating model sensitivity to variations in material parameters and making any needed changes to the default values coded into the material model subroutine. To facilitate this effort and reduce the computational time required to perform numerous parametric runs, the parapet models were extracted from the bridge rail system models as shown in Figure 102. The bottom edge of the parapet in these subsystem models was constrained against movement. Although this artificially increased the stiffness of the parapet to some degree, it provided a more computationally efficient means of evaluating the effect of model changes on parapet response. After converging on a reasonable set of parameters, the full system models (including bridge deck) were simulated and the results compared to measured and observed test data.

Meshing

As indicated previously, the concrete parts were meshed with solid elements, the steel base plate and post were meshed with solid elements, the tubular rail element was meshed using shell elements, and the steel reinforcement and anchor bolts were meshed using beam elements. The meshes for these components were kept fixed during this study except for the mesh of the concrete parapet.

The original mesh of the parapet was constructed to enforce matching between nodes of concrete and those of the steel reinforcement. This construction enables coincident nodes to be merged, thus ensuring connectivity between the concrete and steel components. This parapet mesh is depicted in Figure 103. Together, the concrete parapet and deck models had a total of 115,000 elements. The requirement of matching nodes led to elements with poor aspect ratios and the creation of unnecessarily small element sizes (e.g., 7 mm (0.276 inch) and 5.6 mm (0.22 inch)), which has a significant effect on time step control.

To mitigate this problem, a different connection scheme was utilized between the parapet and the steel reinforcement, which permits a more regular, uniform mesh to be used throughout the parapet. Use of coupling (*CONSTRAINED_LAGRANGE_IN_SOLID) permits the concrete mesh to be assigned without consideration of the location of steel reinforcement. Details of this connection scheme are explained in the Constraints and Boundary Conditions section of this report.

A uniform mesh of 25.4-mm (1-inch) solid elements was used in some preliminary calculations. However, an alternate meshing strategy with a biasing scheme was ultimately used in the evaluation to provide desired refinement in critical areas of the model without significantly affecting the overall size and run time of the model. A two-dimensional biasing scheme was incorporated into the model of the concrete parapet. Along the parapet height, the elements were linearly biased from approximately 20 mm (0.79 inch) at the bottom of the parapet to 13 mm (0.51 inch) at the top of the parapet using a linear biasing function in HyperMesh. A bell curve biasing was used along the length of the parapet with element sizes ranging from approximately 36 mm (1.42 inches) at the ends of the parapet to 16 mm (0.63 inch) in the middle of the parapet. The meshing across the width of the parapet was kept semi-uniform with an element size of 16 mm (0.63 inch). Thus, the largest solid element in the parapet was 16 mm (0.63 inch) by 20 mm (0.79 inch) by 36 mm (1.42 inches); the smallest was approximately 14-mm by (0.55 inches) by 13 mm (0.51 inch) by 16 mm (0.63 inch). A cross section of the revised parapet mesh is shown in Figure 104.

The bridge deck was meshed uniformly along its length using an element size of 25.4 mm (1 inch). A linear biasing technique was used across the width of the deck (i.e., along the impact direction), with larger elements used at the front deck and smaller elements used at the back of the deck where it ties into the parapet. The biased meshing scheme used for the parapet and deck system, which consists of approximately 76,000 elements, is shown in Figures 105 and 106.

Sectional Properties

The thickness for the shell elements comprising the elliptical steel rail and the cross-sectional properties of the beam elements used to model the steel reinforcement and anchor bolts were assigned according to the details and specifications of the Texas Type T4 bridge rail system. Fully integrated elements (type 16) were used for the steel rail, and the Hughes-Liu beam element with cross section integration (type 1) was used for the steel reinforcement and anchor bolts. The concrete brick elements were type 1 (underintegrated) with stiffness form of hourglass control (type 5) specified.

Constraints and Boundary Conditions

For cases in which the bridge deck was included in the analysis, the constraints were imposed on the front side of the deck and beam, the bottom of the beam, and the ends of the transverse steel reinforcement in the deck as shown in Figure 107. In the simulations conducted with the parapet-only subsystem, the bottom of the parapet and the lowermost points of the vertical reinforcement were constrained (i.e., fixed) in all degrees of freedom. Figure 107 also shows an illustration of the boundary condition setup for this case.

Boundary conditions were also imposed on some of the nodes of the rigid pendulum body to constrain the motion of the pendulum body in both the vertical and the lateral directions (both of which are perpendicular to the impact direction). Motion of the pendulum in these two directions is limited by the cables attaching the pendulum to its support towers. Note that the pendulum follows a circular arc. Thus, the linear motion prescribed is an approximation, which is accurate within a small displacement setting as is the case with the T4 bridge rail.

A constraint was used to represent the interaction between the anchor bolts, steel reinforcement, and the surrounding concrete continuum. The steel reinforcement and anchor bolts are coupled (rather than merged) to the surrounding concrete continuum. This coupling was achieved using the *CONSTRAINED_LAGRANGE_IN_SOLID feature in LS-DYNA. In this constraint, the steel reinforcement and anchor bolts are treated as slave material that is coupled with a master material comprised of the deck and parapet concrete. Using this methodology, the slave part(s) can be placed anywhere inside the master continuum part without any special mesh accommodation.

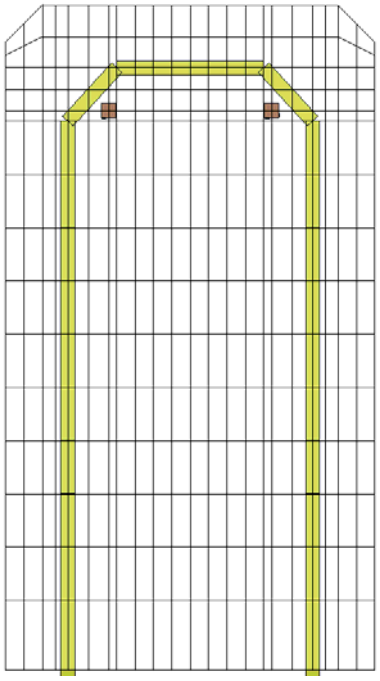

Figure 103. Original parapet mesh used for merging nodes with steel reinforcement.

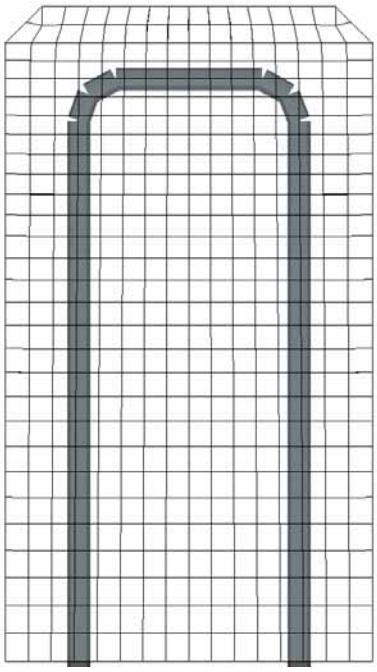

Figure 104. Revised parapet mesh with steel reinforcement.

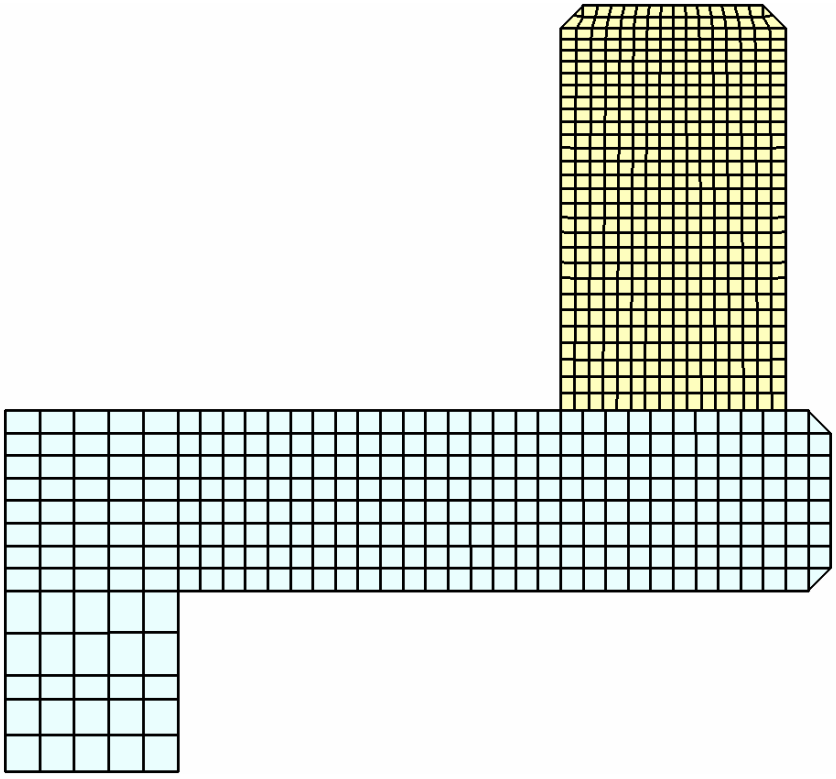

Figure 105. Linear mesh biasing along the height of parapet and width of deck.

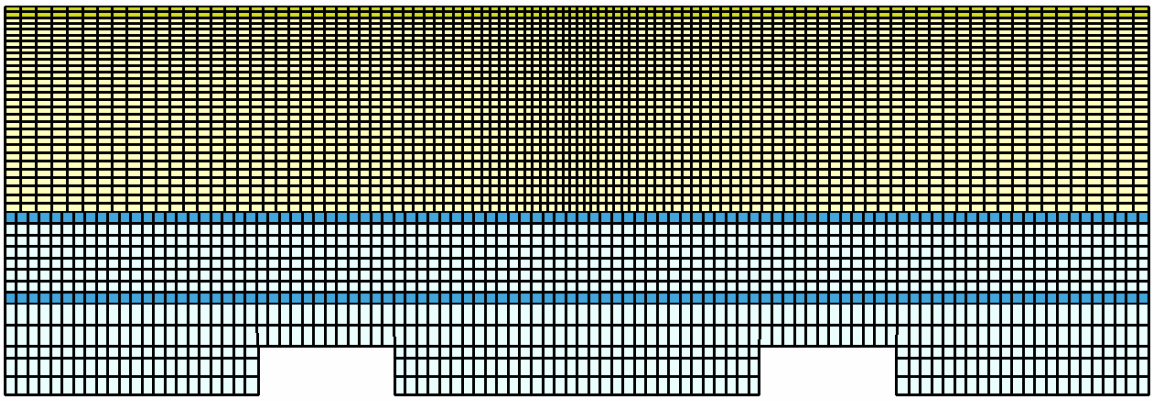

Figure 106. Bell curve mesh biasing along length of parapet and uniform meshing along length of deck.

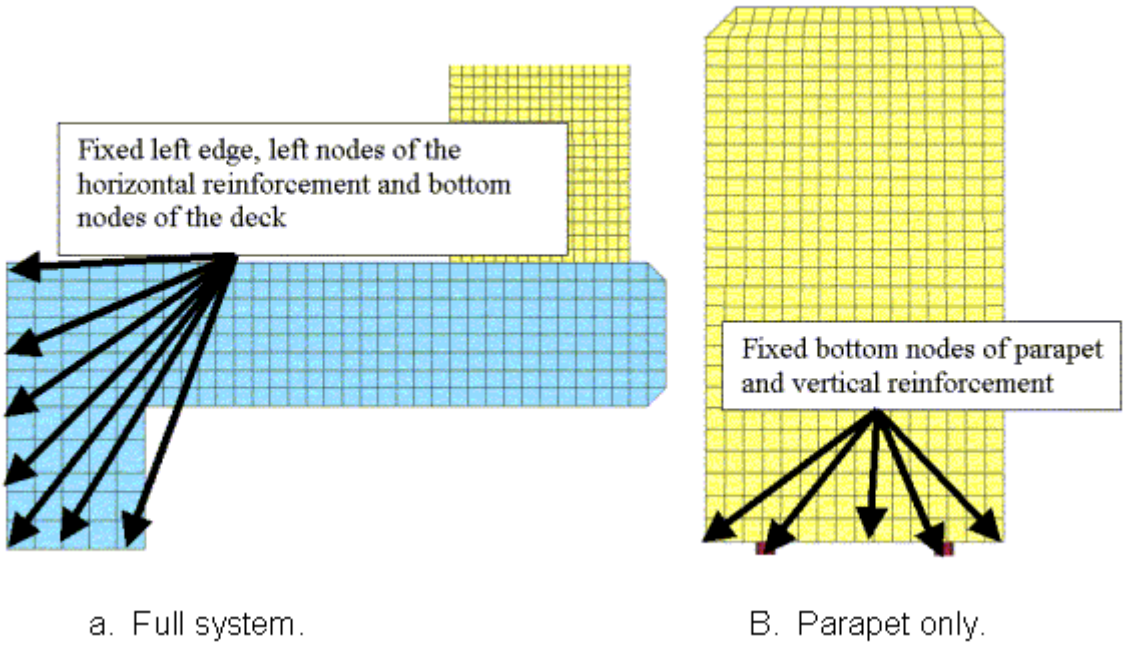

Figure 107. Boundary conditions used for the full system model with deck and for the parapet-only model.

To verify the proper functionality of this method, an example of a reinforced concrete beam modeled with merged nodes as supplied by the developer was modified and rerun using the coupling methodology. The response and damage obtained for the two runs was very close.

The anchor bolts are also constrained to the steel base plate via node merging. Each bolt is merged to one node on the upper surface and one node on the lower surface of the base plate. This constraint is illustrated in Figure 108.

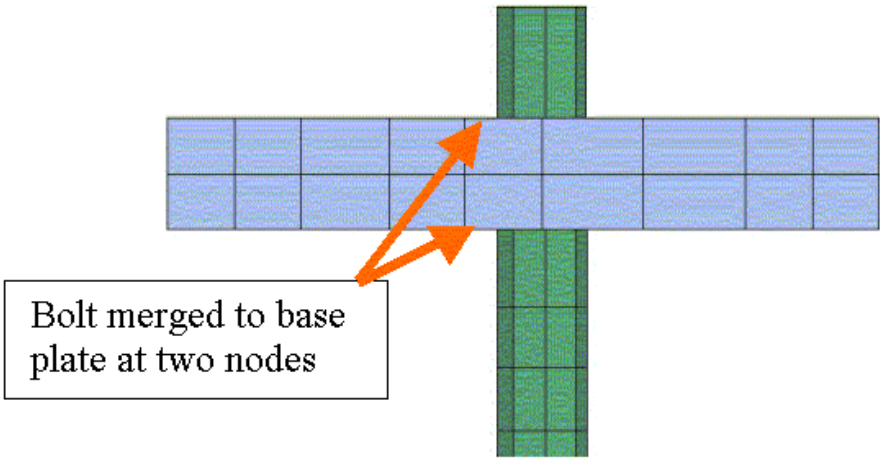

Figure 108. Anchor bolt constraint to base plate.

Three contacts were defined within the bridge parapet model to account for interactions between various components: one between the lower surface of the base plate and the top of the parapet, one between the lower surface of the parapet and the deck, and one for interaction among the steel reinforcement bars. Note that the bridge rail test specimens were constructed using two different concrete pours: one of the deck and one for the parapet. The contact definition between the parapet and deck represents the construction joint that exists between these two components. This contact definition was not used when the parapet-only model was being analyzed.

It is also noteworthy that the pendulum model has its own internal contact definition as well as an additional contact definition between the front cartridge of the crushable nose and the tubular steel rail section. All of these contact definitions are depicted in Figure 109.

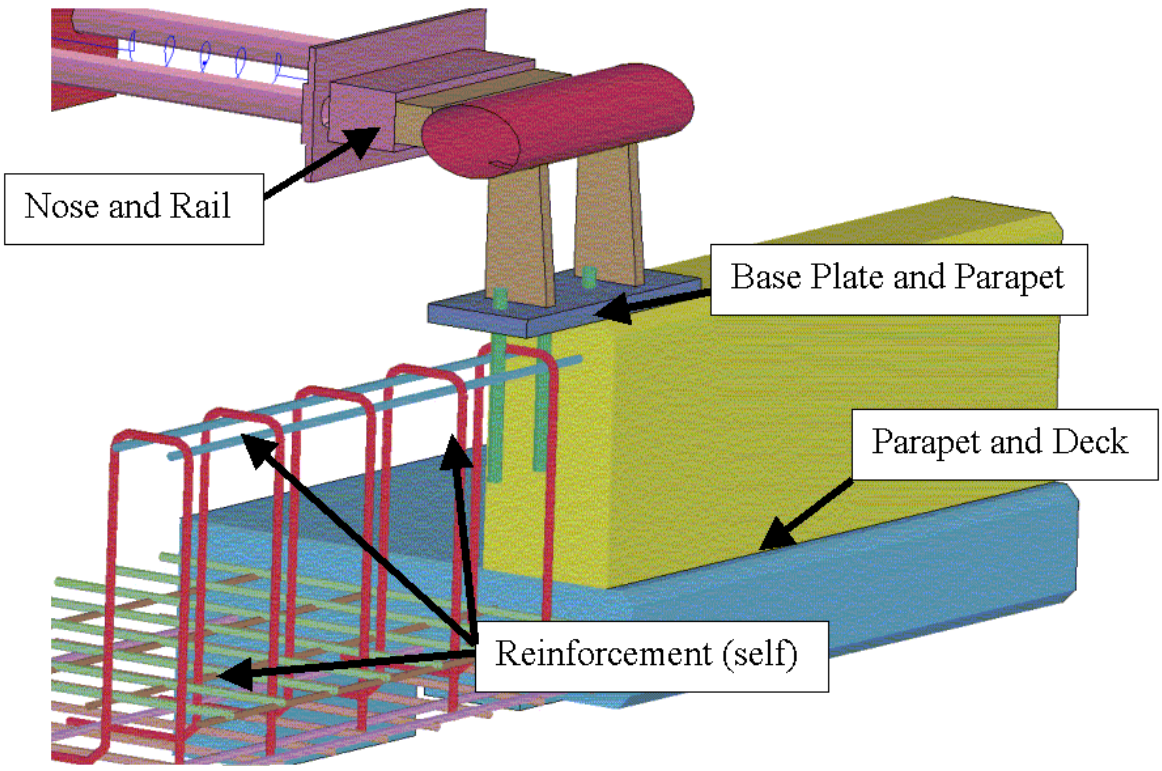

Figure 109. Contacts definitions for the T4 bridge rail model.

Material Definitions

Material models are essential to accurately studying the performance of any system. This research focuses specifically on the newly developed concrete material model; however, other material models (e.g., steel) also had to be implemented to achieve appropriate system response. All steel reinforcement was modeled using an elastoplastic material model that incorporates a strain rate effect on yield strength. The anchor bolts were modeled using elastic steel definition due to their size (19.05-mm- (0.75-inch-) diameter), material composition (high strength steel), and the behavior observed in the full-scale pendulum tests. It was analytically verified through careful monitoring of bolt stresses that none of the anchor bolts reached yield stress at any time during simulation. The tubular rail, the base plate, and the steel posts were modeled using an elastoplastic material model definition.

The parapet and deck were both modeled using the new concrete material model developed by APTEK. In the beta version of LS-DYNA 971, it is designated as material type 159. The model name is *MAT_CSCM_CONCRETE or *MAT_CSCM. The "_CONCRETE" suffix indicates a short input format that utilizes hard-coded default values for numerous variables; the other name indicates a long input format for which the user must supply values for all the required input parameters. Input parameters are not listed here because they are explained in the companion Users Manual for the material model. However, some salient parameters studied in this research are discussed. These parameters are (as excerpted from the Users Manual):

ERODE	Elements erode when damage exceeds 0.99 and the maximum principal strain exceeds 1 − ERODE. For erosion that is independent of strain, set ERODE equal to 1.0. Erosion does not occur if ERODE is less than 1.0.
f'_C	Unconfined compression strength. If left blank, default is 30 MPa (4,351 lbf/inch^2).
Dagg	Maximum aggregate size. If left blank, default is 19 mm (0.75 inches).
G_{fc}	Fracture energy in uniaxial compression.
G_{ft}	Fracture energy in uniaxial tension.
G_{fs}	Fracture energy in pure shear.
repow	Power that increases fracture energy with rate effects.

The element erosion parameter (ERODE) is part of both input formats. The compression strength of concrete (f'_C) and the maximum aggregate size (Dagg) are required as part of the short input format. The fracture energy related parameters (G_{fc} ,G_{ft} , G_{fs}, *repow*) are part of the long input format. The short input format will work with default model parameters based on the user-supplied compression strength of concrete (f'_C) and the maximum aggregate size (Dagg); the long format requires the user to explicitly define all the model parameters.

For the T4 bridge rail analysis, the concrete had a maximum aggregate size of 25.4 mm (1 inch). The concrete used for the bridge deck had an average compressive strength of 35.5 MPa (5,149 lbf/inch^2) on the day of testing. The parapet concrete had an average compressive strength of 30.44 MPa (4,415 lbf/inch^2).

In this study, the short input format was used to generate and list the full set of parameters in the LS-DYNA output file. These parameters were then used in the long input format, and selected parameters were varied as part of the performance/sensitivity study.

ANALYSES OF T4 BRIDGE RAIL

Numerous analyses were conducted using the models of the T4 bridge rail variants as part of the evaluation of the concrete material model. Only the significant analyses are reported here.

Baseline Parameters

All dimensional parameters are based on the following units:

- Megagram for mass.
- Second for time.
- Millimeter for length.
- Newton for force.
- Megapascal for stress or pressure.
- Millijoules for energy.

This corresponds to the UNITS field being set to "2" in the third line of the short input format. For the T4 parapet model, which had an average compressive strength of 30.44 MPa (4,415 lbf/inch^2) and a maximum aggregate size of 25.4 mm (1 inch), the short input is shown in t Table 8. For the bridge deck, which had an average compressive strength of 35.5 MPa (5,149 lbf/inch^2) and a maximum aggregate size of 25.4 mm (1 inch), the short input is shown in Table 9.

Table 8. Short input format for parapet concrete material model.

*MAT CSCM CONCRETE							
$ mid	Ro	nplot	incre	irate	erode	recover	iretract
159	**2.32-09**	**0**	**0.00E+00**	**1**	**1.1**	**1.00E+01**	**0**
$							
$ PreD							
0							
$							
$ f'c	Dagg	Units					
30.44	**25.4**	**2**					

Table 9. Short input format for bridge deck concrete material model.

*MAT CSCM CONCRETE							
$ mid	ro	nplot	incre	irate	erode	recover	iretract
159	**2.32-09**	**0**	**0.00E+00**	**1**	**1.1**	**1.00E+01**	**0**
$							
$ PreD							
0							
$							
$ f'c	Dagg	Units					
35.52	**25.4**	**2**					

Values for the parameters comprising the long input format of the concrete model were obtained from the d3hsp (ASCII output) file of LS-DYNA. However, when these values were obtained, it was noticed that the printed output did not correspond to the format provided in the draft manual. This identification mismatch affected the parameters *K*, *G* (modulus), alpha, theta, lambda, and beta of all three surfaces (triaxial compression, torsion, and triaxial extension as well as *R* and *X0*. These format errors were communicated to the developer, and corrections were made for later releases of LS-DYNA 971 to make the manual consistent with the output routine.

To avoid any confusion or possible modeling errors, the long format input parameters for the concrete material models used in the analyses of the T4 bridge rail alternatives were submitted to the developer for a correctness check. The long input format parameters for the parapet and deck concrete are shown in Table 10 and Table 11, respectively. The values shown in these tables are herein referred to as the "baseline values." Changes to the material model were made with reference to these baseline values. The parameters that were varied as part of the material model evaluation are shown as shaded. Note that these baseline values *are not* the default values

currently implemented in LS-DYNA version 971. They are preliminary values that were later adjusted based on results of all calculations presented within this evaluation report.

Table 10. Long input format for parapet concrete material model.

*MAT_CSCM_TITLE							
Parapet concrete f'c =4415 psi							
MID	RO	NPLOT	INCRE	IRATE	**ERODE**	RECOV	IRETRC
14	2.32E-09	1	0	1	**1.1**	10	0
PreD							
0							
G	K	α	θ	λ	β	N_H	C_H
11520	12610	14.56	0.2979	10.51	0.01929		
α_1	$\theta\theta_1$	λ_1	β_1	α_2	θ_2	λ_2	β_2
0.7473	0.001139	0.17	0.07014	0.66	0.001374	0.16	0.07014
R	X_0	W	D_1	D_2			
5	90.74	0.05	2.50E-04	3.49E-07			
B	**G_{fc}**	D	**G_{fs}**	**G_{ft}**	*pwrc*	*pwrt*	*pmod*
100	**9.487**	0.1	**9.49E-02**	**9.49E-02**	5	1	0
$\eta_{0\chi}$	N_c	$\eta_{0\tau}$	N_t	*overc*	overt	Srate	**repow**
1.01E-04	0.78	6.22E-05	0.48	21.63	21.63	1	**1**

Table 11. Long input format for bridge deck concrete material model.

*MAT_CSCM_TITLE							
concrete for the deck f'c=5152 psi							
MID	RO	NPLOT	INCRE	IRATE	**ERODE**	RECOV	IRETRC
15	2.32E-09	1	0	1	**1.1**	1	0
PreD							
0							
G	K	α	θ	λ	β	N_H	C_H
12120	13280	15.16	0.3143	10.51	0.01929		
α_1	θ_1	λ_1	β_1	α_2	θ_2	λ_2	β_2
0.7473	9.95E-04	0.17	0.0646	0.66	0.001201	0.16	0.0646
R	X_0	W	D_1	D_2			
5	93.31	0.05	2.50E-04	3.49E-07			
B	**G_{fc}**	D	**G_{fs}**	**G_{ft}**	*pwrc*	*pwrt*	*pmod*
100	**10.57**	0.1	**1.06E-01**	**1.06E-01**	5	1	0
$\eta_{0\chi}$	N_c	$\eta_{0\tau}$	N_t	*overc*	overt	Srate	**repow**
1.13E-04	0.78	6.71E-05	0.48	24.02	24.02	1	**1**

Baseline Analysis

A dynamic pendulum impact into the T4 bridge rail with four-bolt anchorage and 254-mm- (10-inch-) wide parapet was simulated using the aforementioned baseline values for the concrete material model and the initial SBP pendulum model. As shown in Figure 110, the damage fringe obtained from the simulation approximates that observed during the testing (see Figure 88). The damage fringes depict the damage of each element on a scale from 0 to 1 where the value 0 indicates no damage and the value 1 indicates total damage (i.e., the element is not capable of carrying load). However, unlike the tests, no material failure (i.e., element erosion) was observed in this simulation.

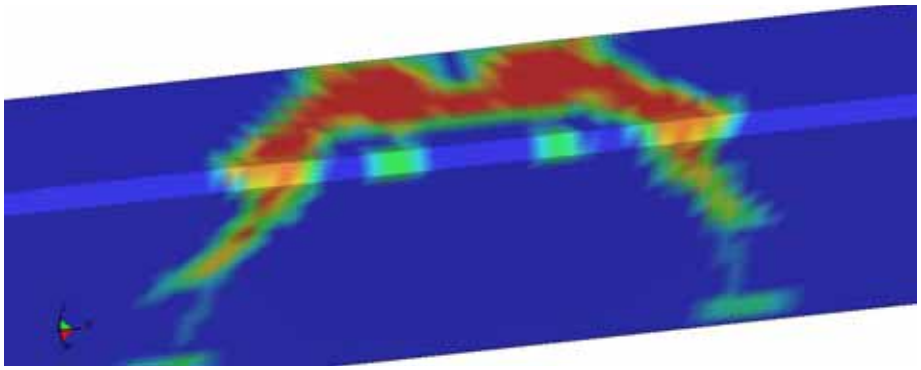

Figure 110. Damage fringe for baseline simulation of T4
with four-bolt anchorage and 254-mm- (10-inch-) wide parapet.

Parametric Analyses

Given that the baseline values did not provide the desired failure response, a sensitivity study was conducted to investigate system sensitivity to selected parameters. Another analysis (case02) was conducted for which erosion was enabled independent of strain (i.e., ERODE equal to 1.0). The other variables were unchanged from their baseline values.

As shown in Figures 111 and 112, elements were eroded from both the parapet and the deck. With ERODE set to 1.0, the elements eroded based on a set damage threshold (i.e., above 0.99) without consideration of strain. Damage fringes for this simulation case are shown in Figure 113.

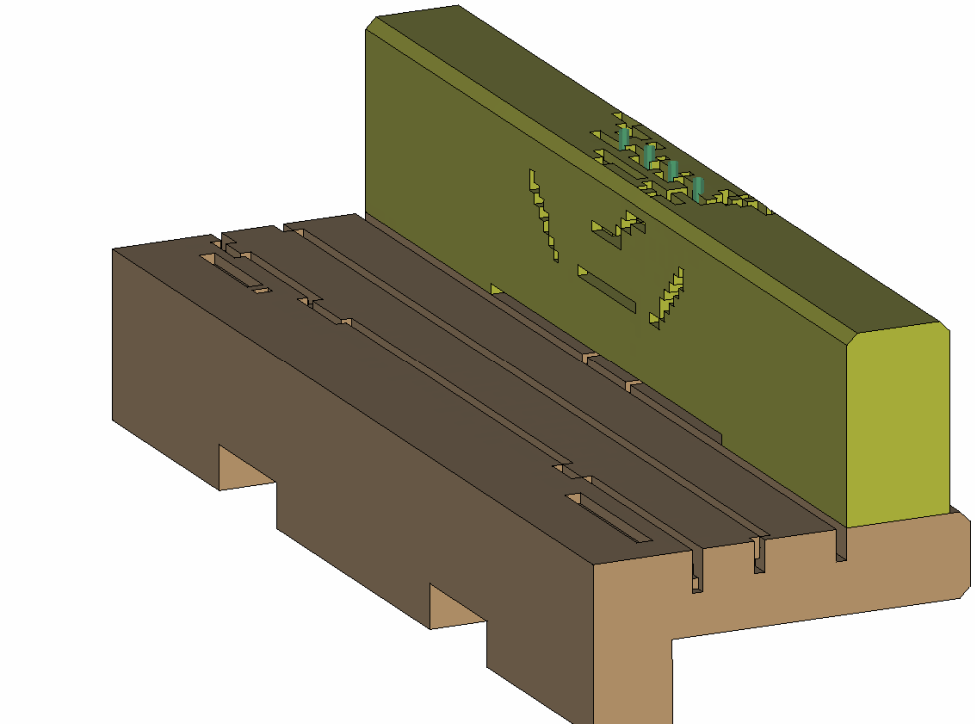

Figure 111. Element erosion profile (simulation case02, ERODE =1) on traffic side.

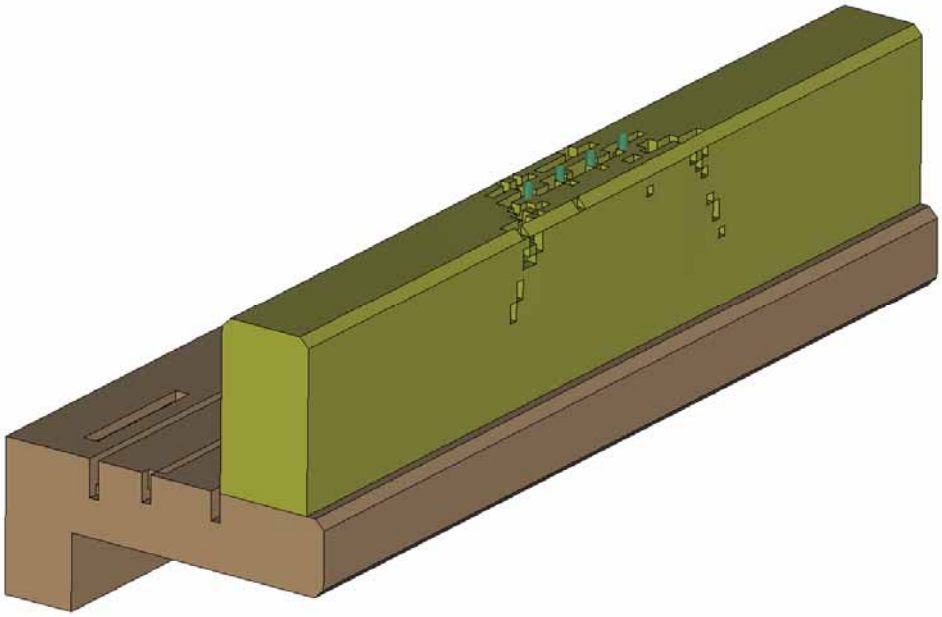

Figure 112. Element erosion profile (simulation case02, ERODE =1)
on field side.

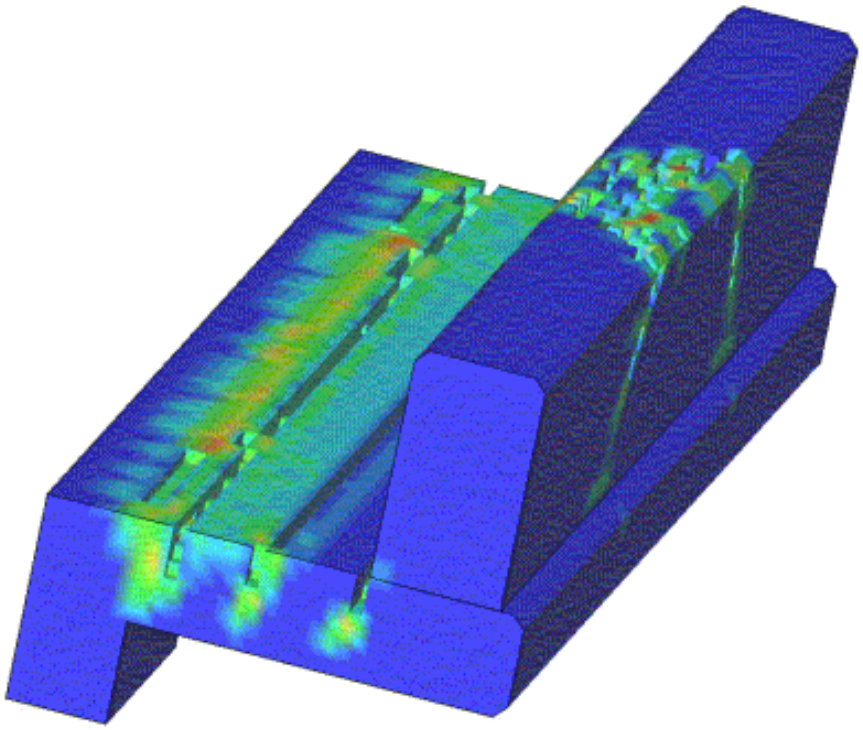

Figure 113. Damage fringes for simulation case02 (ERODE =1).

Elements eroded on the field side of the parapet (see Figure 112) propagated in a pattern similar to that observed in the test. However, element erosion on the traffic face of the parapet and the tension (top) face of the bridge deck (see Figure 111) does not replicate test results. Recall that no visible damage or cracks were observed on either of these faces after tests P3 or P4. This result indicates that element erosion should not be used independent of a maximum principal strain criterion.

Another simulation was conducted with the value of the ERODE parameter set to 1.05. Although the pattern of the damage fringes was generally consistent with that observed in the pendulum tests, no element erosion/failure occurred, which makes the results similar to those from the baseline simulation with ERODE = 1.1.

The focus then shifted toward studying the effect of the fracture energies (G_{fc}, G_{fs}, and G_{ft}) on the damage profile and erosion of elements. Initially, very low values of the fracture energies (20 percent of the original baseline values) were used. As might be expected, this change resulted in extensive element erosion and very weak parapet response as shown in Figure 114.

It was noticed during this simulation that the energy balance of the model changed during the analysis. More specifically, the total energy of the system increased. The change was attributed to an inappropriate increase in total internal energy of the system. Further investigation revealed

that this unrealistic increase in energy, shown in Figure 115, was traceable to the concrete material. Beginning at about 0.05 s, the total energy increases 2.5 times its original value. The changes in the internal energy of the concrete material correspond to this change in the total system energy and appear to be related to the damage calculations. As damage of the concrete components increases (as indicated by the damage fringes and contours), the total system energy increases.

Similar behavior was present in the baseline simulation as well. However, this behavior was not as readily detectable because the percentage of increase in energy is related to the damage induced in the concrete. This behavior was disclosed to the developer during the early stages of model validation, and a fix was incorporated into later releases of LS-DYNA version 971.

Continuing with the parametric evaluation, the values of fracture energies were next increased to 50 percent of the baseline values. As shown in Figure 116, the associated fracture profile radiated out from the outer anchor bolts on the top of the parapet but did not extend to the field side of the parapet.

A process of bisection of fracture energy values was followed until a set of values that produced a similar fracture profile to that observed in the test was identified. With the fracture energy values set at 27.5 percent of their baseline values, the simulation resulted in a damage pattern and fracture profile similar to those observed in the test. The fracture profile shown in Figure 117 indicates that a piece of concrete similar in shape and size to those that fractured in tests P3 and P4 would fracture and possibly spall off. Additionally, the model captures the deflection and rotation of the anchor bolts inside the parapet wall similar to that observed in the tests.

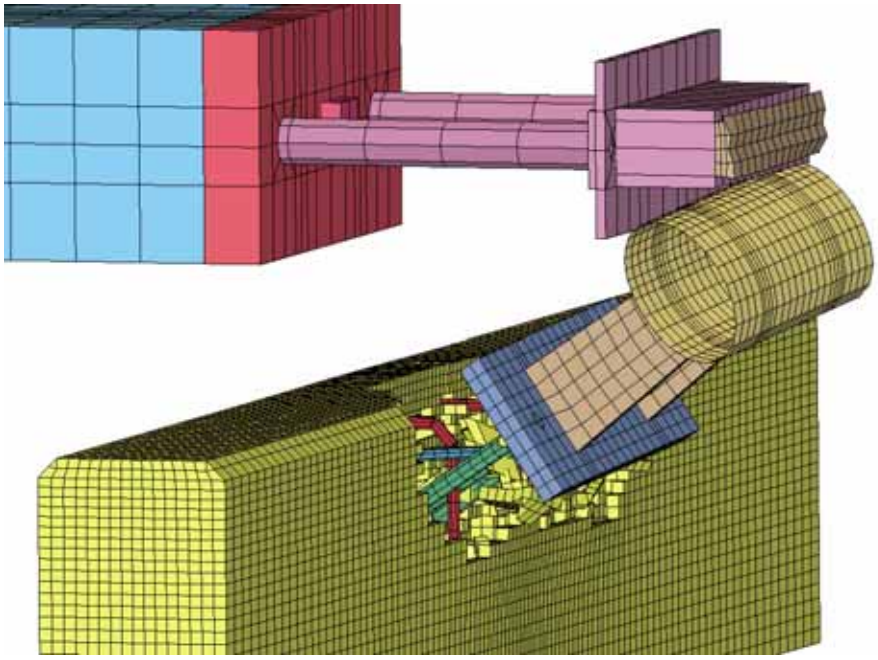

Figure 114. Parapet failure with fracture energies at 20 percent of baseline values.

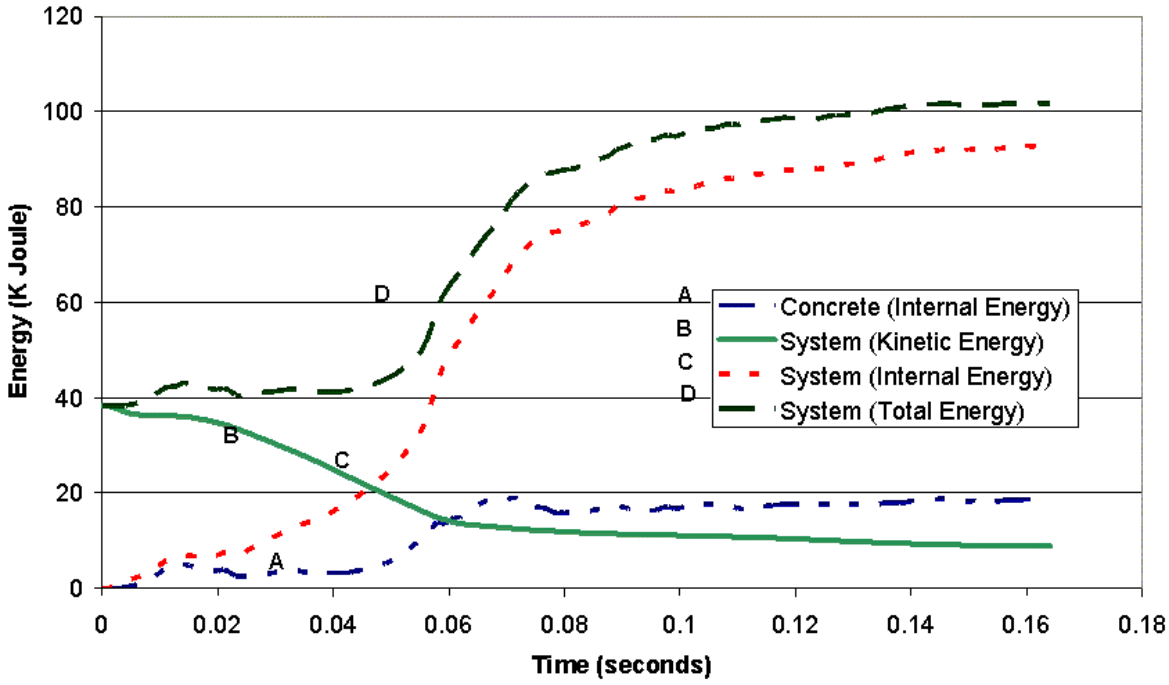

Joule = 0.73756 ft-lb

Figure 115. Energy-time histories for pendulum impact of T4 bridge rail with fracture energies at 20 percent of baseline values.

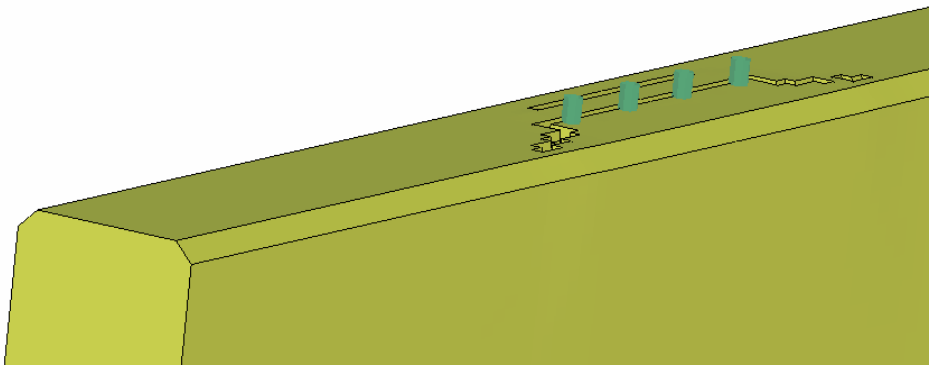

Figure 116. Parapet failure with fracture energies at 50 percent of baseline values.

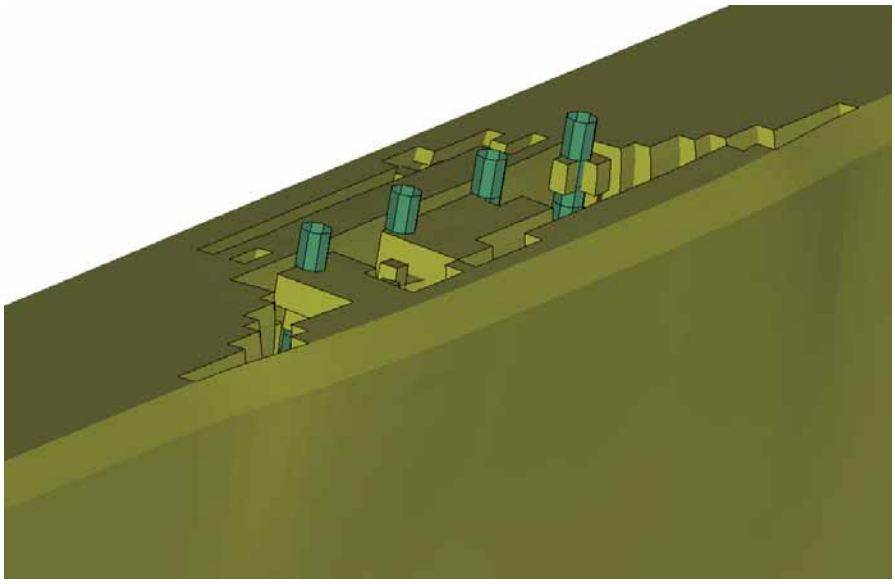

Figure 117. Parapet failure with fracture energies at 27.5 percent of baseline values.

The energy-time histories associated with this run are shown in Figure 118. As previously discussed, an increase in the total system energy can be observed to coincide with a significant increase in the internal energy of the system at about 0.05 sec. The extent to which the calculations are affected by this behavior is not known. The developer indicated that the problem was confined to a reporting issue and does not affect the simulation outcome. A fix was incorporated into later releases of LS-DYNA version 971.

Realizing that fracture energies set at 27.5 percent of the baseline values could not be physically justified, two other aspects of the model were further investigated. First, in consultation with the developer, the stiffness of the crushable nose of the pendulum impactor was studied to see whether the impact energy absorbed by the pendulum and transferred to the barrier agreed with test data. The second aspect investigated was an enhancement of the anchor bolt connection between the base plate and concrete parapet.

Comparison of data from the rigid pole calibration tests and the T4 bridge rail impacts showed a discrepancy in the stiffness of the nose assembly. Additional checks on the properties of the aluminum honeycomb material commonly used in the crushable nose assembly of the pendulum bogie indicated that the material stiffness can vary considerably (e.g., 10 percent to 20 percent) among different batches. Because the properties of the honeycomb used in the pendulum testing of the T4 bridge rail were not directly measured, a new stiffness curve for the pendulum spring (SBP2) was developed based on test P05 as previously described. The net result is a stiffer pendulum nose that correlates with the honeycomb material used in the actual pendulum tests of the T4 bridge rail systems.

Upon consultation with the developer, it was suggested that a set of fracture energy values at 80 percent of the baseline values is a reasonable lower bound for concrete having a maximum aggregate size consistent with that used in the T4 bridge rail installations. Consequently, the modified SBP2 pendulum model was used in an impact analysis of the T4 parapet system with four-bolt anchorage and 254-mm- (10-inch-) wide parapet using 80 percent of the baseline

fracture energy values. However, this configuration did not result in a significant change to the damage profile compared with the parapet impacted by the lower stiffness pendulum (SBP).

Next, further study was devoted to the connection between the base plate and anchor bolts. Initially, nodes on the anchor bolts were merged to corresponding nodes on the base plate. This merging constrained the base plate from rotation, a behavior that was observed in the high-speed video of the pendulum tests. The interaction between the base plate and anchor bolts was subsequently enhanced by removing the merged nodes connection and adding washers on the top surface of the base plate to constrain upward vertical motion of the base plate. The washers were tied to the anchor bolts. A *CONSTRAINED_NODE_SET was added between nodes of the anchor bolts and the closest base plate nodes to constrain motion in the horizontal plane of the base plate.

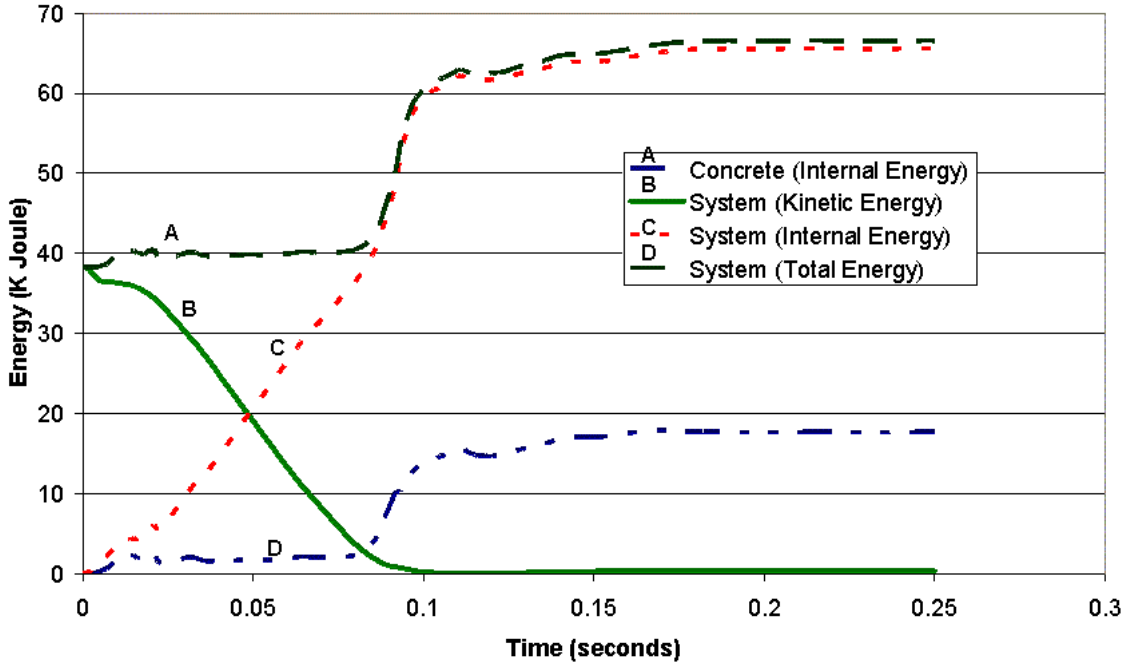

Joule = 0.73756 ft-lb

Figure 118. Energy-time histories for pendulum impact of T4 bridge rail with fracture energies at 27.5 percent of baseline values.

This configuration gives the base plate more freedom to rotate when subjected to an applied moment due to rail impact based on the material properties of the bolts and washers. The vertical downward constraint on the base plate was handled by contact with the top surface of the concrete parapet. This modeling change was considered to more accurately represent the behavior of the actual connection without significantly affecting computer processing time. The enhanced connection model between the base plate and anchor bolts is depicted in Figure 119.

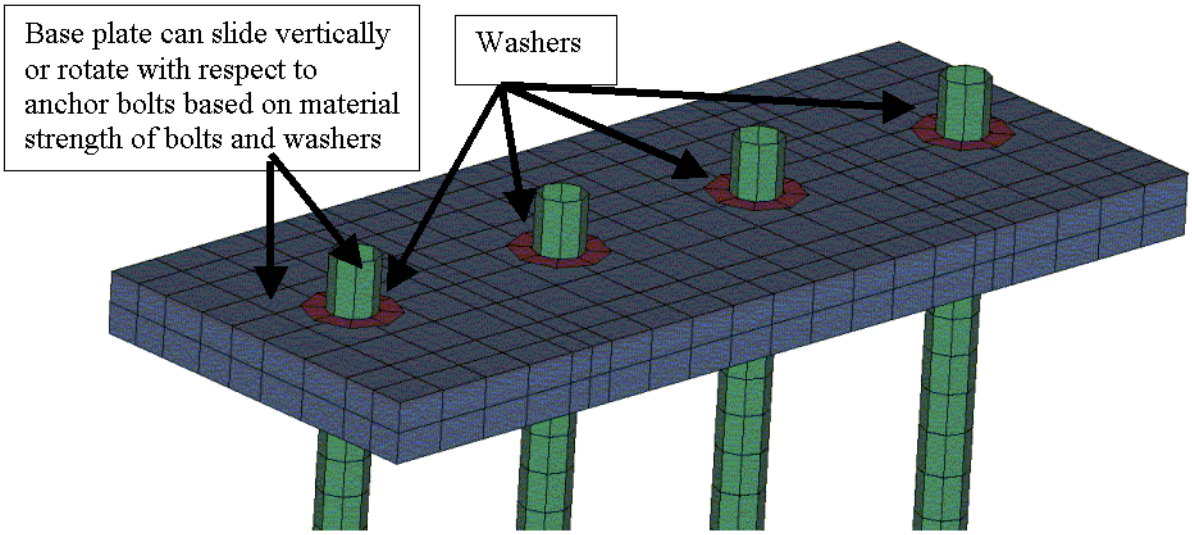

Figure 119. Enhanced anchor bolt-to-base plate connection model.

Modified System Analyses

An LS-DYNA model was constructed using the SBP2 pendulum model, the lower end of the recommended fracture energy values (80 percent of baseline values), and the enhanced base plate-to-anchor bolt connection. The parapet-only model of the T4 parapet system with four-bolt anchorage and 254-mm- (10-inch-) wide parapet (discussed previously) was used in the simulation to reduce computational time.

Figures 120–122 show sequential views of the simulation at different times. Although the general pattern was similar, the fracture damage profile was more extensive than that observed in the pendulum tests (tests P3 and P4). This result was expected in part due to the use of the parapet-only model, which is less flexible than the more detailed model configuration that incorporates the bridge deck. It is noteworthy that the rail-post-base plate assembly rigidly rotated and subsequently rebounded as observed in the actual pendulum tests.

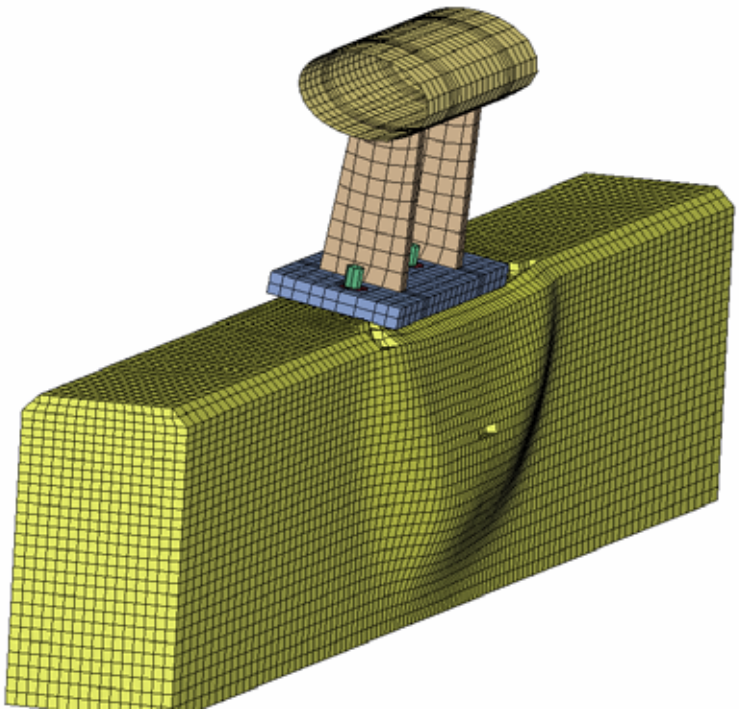

Figure 120. Fracture profile of modified T4 system at 0.080 seconds.

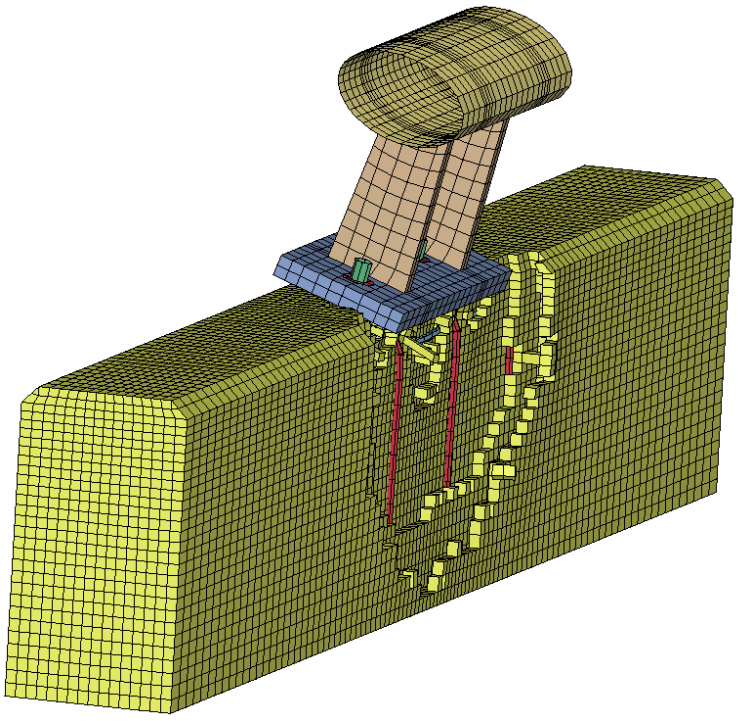

Figure 121. Fracture profile of modified T4 system at 0.115 seconds.

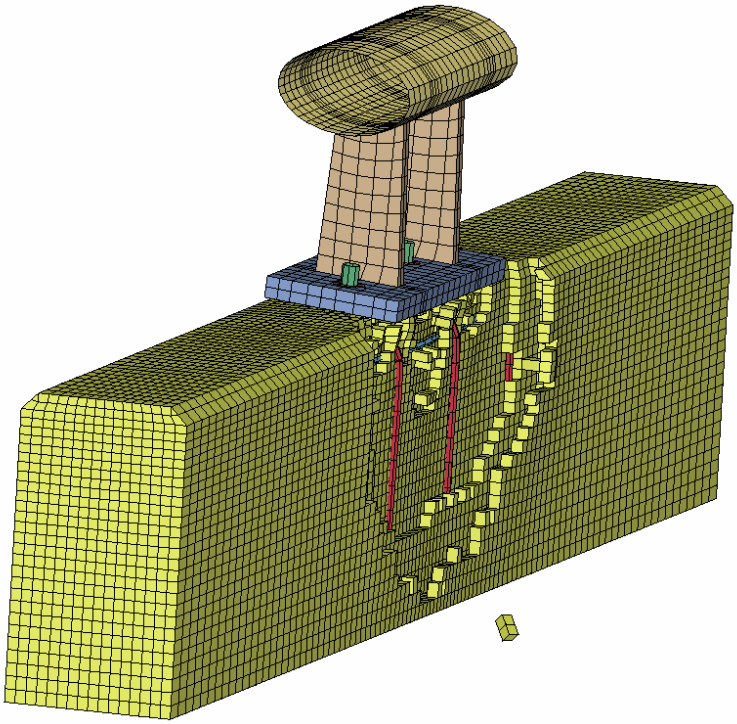

Figure 122. Fracture profile of modified T4 system at 0.250 seconds.

Full System Analysis: Four-Bolt Design

The parameters used in the analysis of the parapet-only simulation of the modified T4 parapet system with four-bolt anchorage and 254-mm- (10-inch-) wide parapet were incorporated into the full system model that included the bridge deck. As before, the SBP2 pendulum model was used as the impactor.

A profile of the damaged bridge rail system after impact is shown in Figure 123. The fracture profile of the parapet is shown in Figure 124 with the steel components of the parapet removed for better visualization. Due to the inherent flexibility of the bridge deck, the fracture profile of the concrete parapet was less severe than that for the parapet-only model and was similar to that observed in the pendulum tests. Element erosion radiated from the outer anchor bolts and extended to the back edge of the parapet and down the field side of the parapet wall.

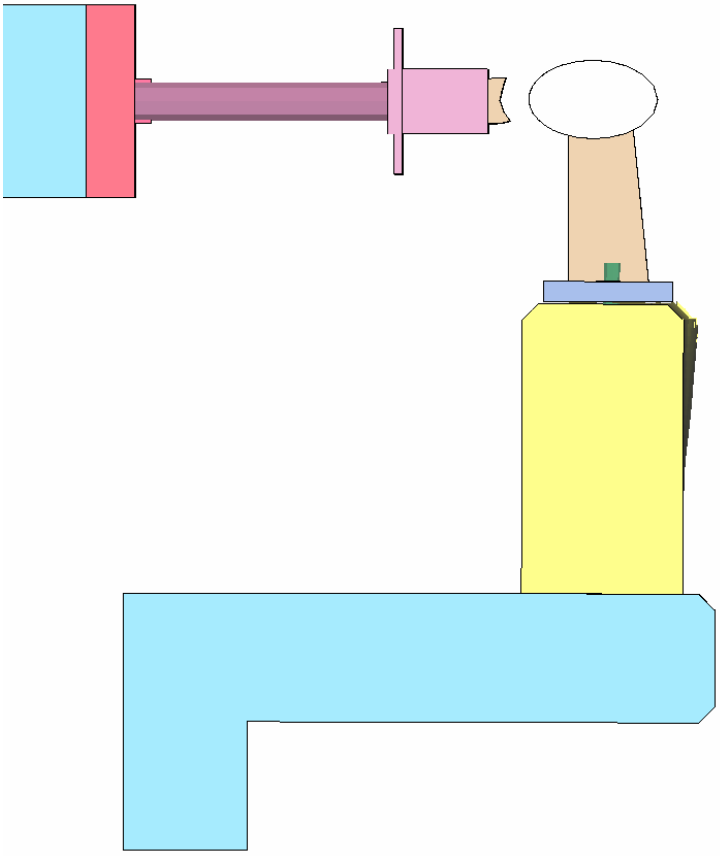

Figure 123. Profile of damaged T4 bridge rail system with four-bolt anchorage after pendulum impact.

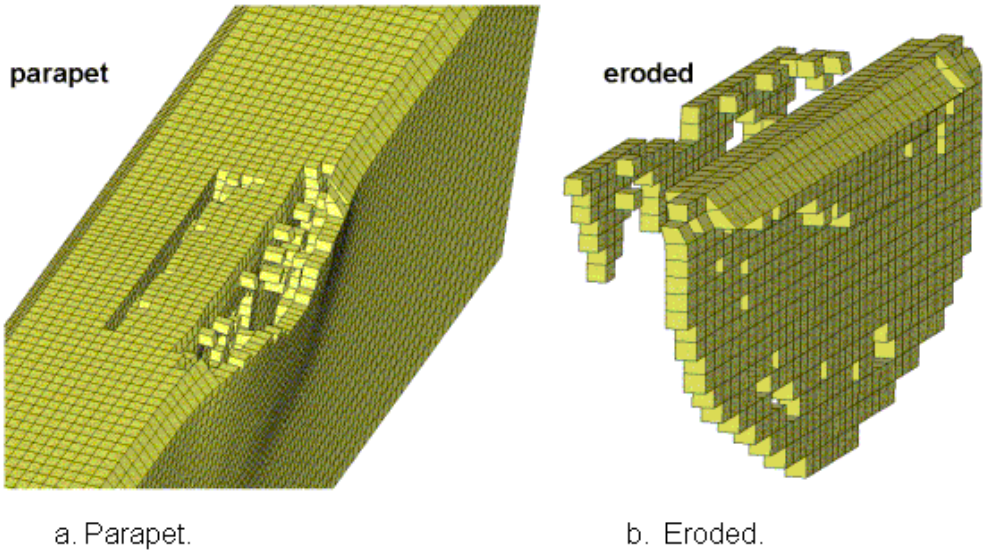

Figure 124. Fracture profile for T4 bridge rail with four-bolt anchorage for parapet and eroded elements.

As shown in Table 12, the peak impact force in the simulation of the T4 bridge rail system with four-bolt anchorage compares favorably with those measured in the corresponding pendulum tests. Acceleration-time histories for the tests and simulation, filtered at 180 Hertz (Hz), are compared in Figure 125. The simulation data tracks the test data reasonably well up to the time of peak acceleration. After this time, the rebound portion of the pendulum simulation data deviates from the tests. However, this rebound phase does not have direct bearing on the evaluation of the concrete material model or roadside safety structure.

Table 12. Force comparison between tests and simulation for T4 rail system with four-bolt anchorage.

Description	Maximum Peak Impact Force kilonewtons (kN) (kips)
Test P3	145.0 (32.6)
Test P4	129.0 (29.0)
Four-Bolt Simulation	130.3 (29.3)

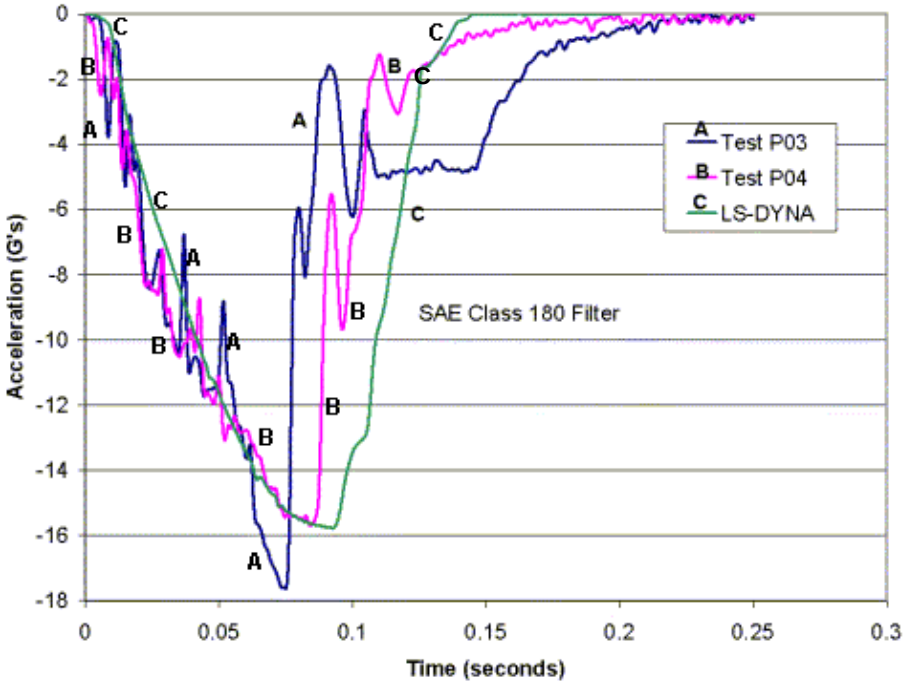

Figure 125. Pendulum bogie accelerations for impact of T4 bridge rail with four-bolt anchorage and 254-mm- (10-inch-) wide parapet.

The peak impact force for test P3 is approximately 10 percent greater than the peak impact force for test P4 and the simulation. Because the test specimens and impact conditions are nominally similar, this difference is attributed to normal material and test variation. The acceleration pulse indicated during the rebound phase of test P3 is attributed to pitching and "bucking" of the suspended pendulum mass.

Figure 126 presents the velocity-time histories for the pendulum tests and simulation. Because these data are based on integration of the acceleration data, they are expected to be smoother and correlate better. Note that the negative portions of the velocity curves represent rebound of the pendulum. The simulation data tracks the data from test P4 up to the rebound phase of the impact (velocity < 0). The data for test P3 deviates from test P4 and the simulation before rebound.

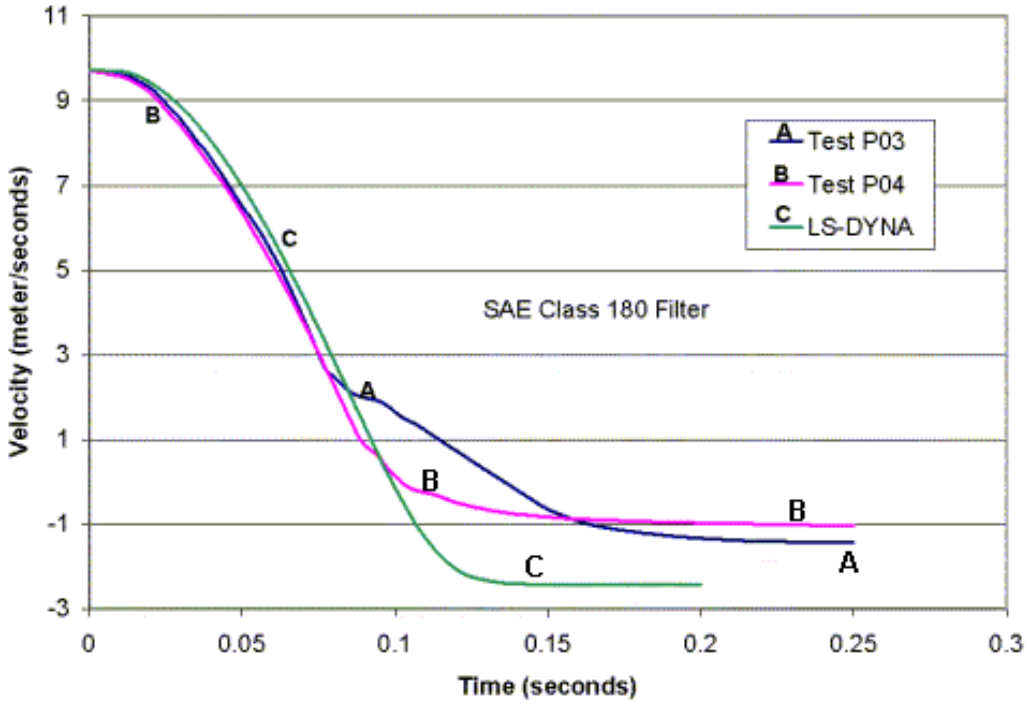

m/sec = 3.28 ft/sec

Figure 126. Pendulum bogie velocities for impact of T4 bridge rail with four-bolt anchorage and 254-mm- (10-inch-) wide parapet.

Overall correlation between the simulation and test data is considered to be good. The simulation matches particularly well with test P4. Thus, researchers decided to proceed to simulation of the T4 bridge rail system with three-bolt anchorage and 317.5-mm- (12.5-inch-) wide parapet to further evaluate the concrete material model. When tested, this design variation had a different level of damage than the system with four-bolt anchorage and 254-mm- (10-inch-) wide parapet, thus providing an opportunity to assess the sensitivity of the concrete model to small design changes under similar impact loading conditions.

Full System Analysis: Three-Bolt Design

The same parameters used in the simulation of the T4 bridge rail with four-bolt anchorage and 254-mm- (10-inch-) wide parapet were incorporated into the full system model of the T4 bridge rail with three-bolt anchorage and 317.5-mm- (12.5-inch-) wide parapet. As discussed previously, the full system model incorporates the bridge deck. The modified SBP2 pendulum model was used as the impactor.

Figure 127 shows the calculated response of the parapet-deck system after being impacted by the pendulum. No element erosion occurred in the analysis. The rail/parapet assembly rebounded after a small deflection. Recall that no visible damage was observed after test P5, and only small hairline cracks were found after test P7. Figures 128 and 129 show the damage fringes from the simulation. The fringe pattern is similar to the cracking pattern observed in test P7, which indicates that under a more severe impact, the concrete would fail in a pattern similar to that initiated in test P7.

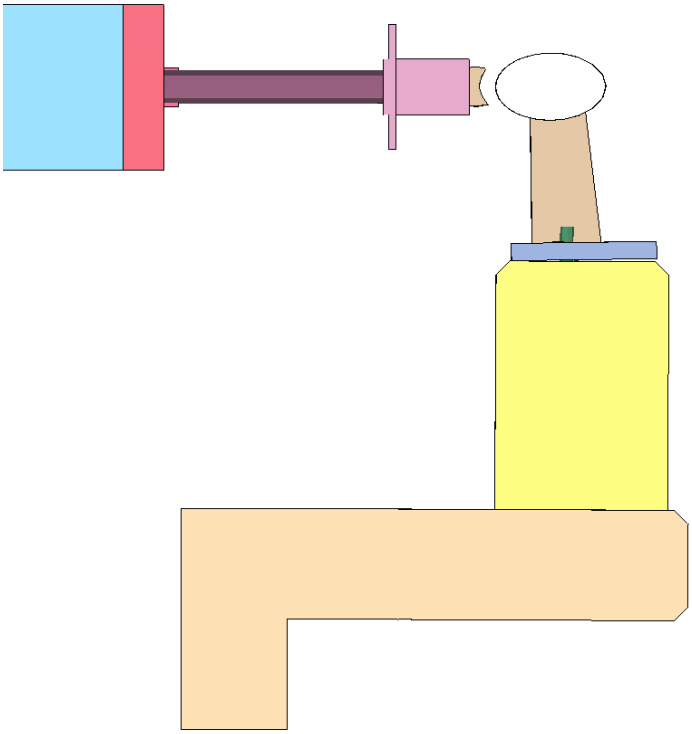

Figure 127. Profile of T4 bridge rail system with three-bolt anchorage after pendulum impact.

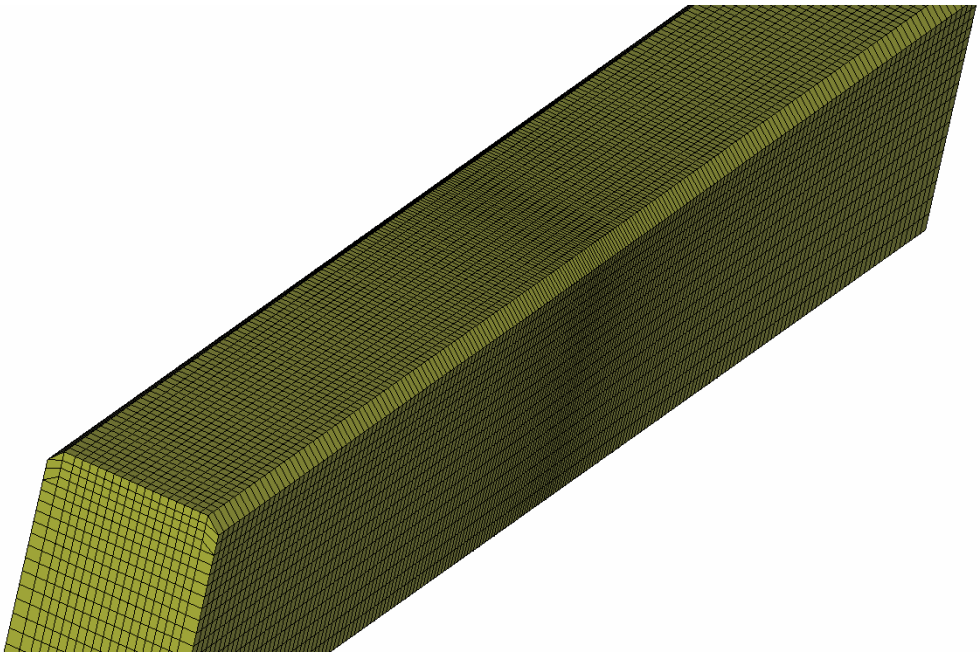

Figure 128. Damage to 317.5-mm- (12.5-inch-) wide parapet after pendulum impact showing element erosion.

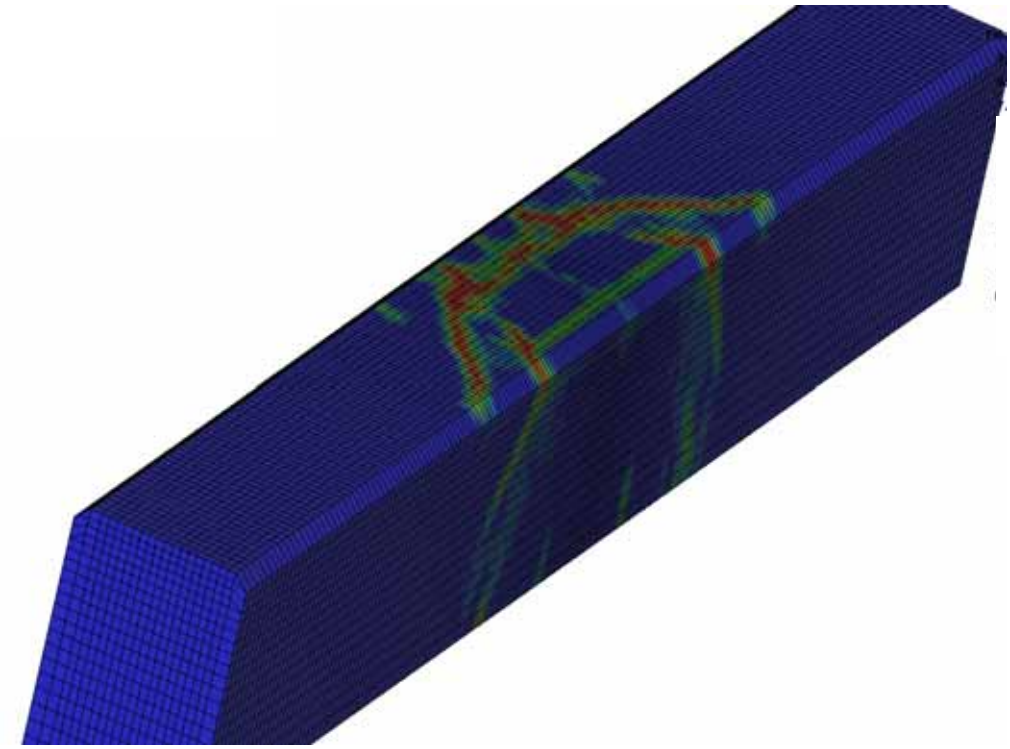

Figure 129. Damage to 317.5-mm- (12.5-inch-) wide parapet after pendulum impact showing damage fringes.

The maximum impact force calculated in the simulation compares very favorably with those measured in the test P5 as shown in Table 13. A considerable difference exists between the peak force measured in test P5 and test P7. These tests were conducted on the same day on two different test specimens under nominally similar impact conditions. Beyond test variability, the cause of the difference in peak force is not known.

Table 13. Force comparison between tests and simulation for T4 rail system with three-bolt anchorage.

Description	**Maximum Peak Measured Force kN (kips)**
Test P5	133.9 (30.1)
Test P7	176.7 (39.7)
Three-Bolt Simulation	134.8 (30.3)

Acceleration-time histories for the pendulum tests and simulation of the T4 rail system with three-bolt anchorage and 317.5-mm- (12.5-inch-) wide parapet are compared in Figure 130. The simulation data tracks the test data reasonably well during both the loading and unloading (i.e., rebound) phases of the impact. Recall that data from test P5 was used for the recalibration of the pendulum model. Test P7 is an independent test of a similar installation under similar impact conditions. Figure 43 shows that the peak acceleration for test P7 exceeds that for test P5 and the simulation.

Velocity-time histories for the pendulum tests and simulation are presented in Figure 131. The simulation data tracks the test data reasonably well during both the loading and unloading (i.e., rebound) phases of the impact.

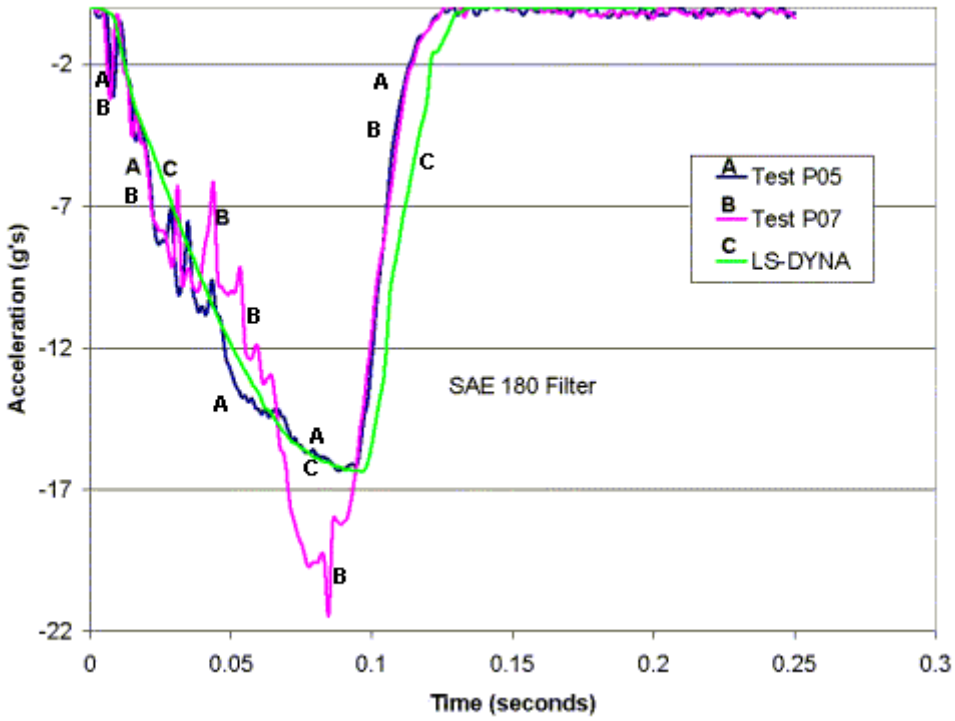

Figure 130. Pendulum bogie accelerations for impact of T4 bridge rail with three-bolt anchorage and 317.5-mm- (12.5-inch-) wide parapet.

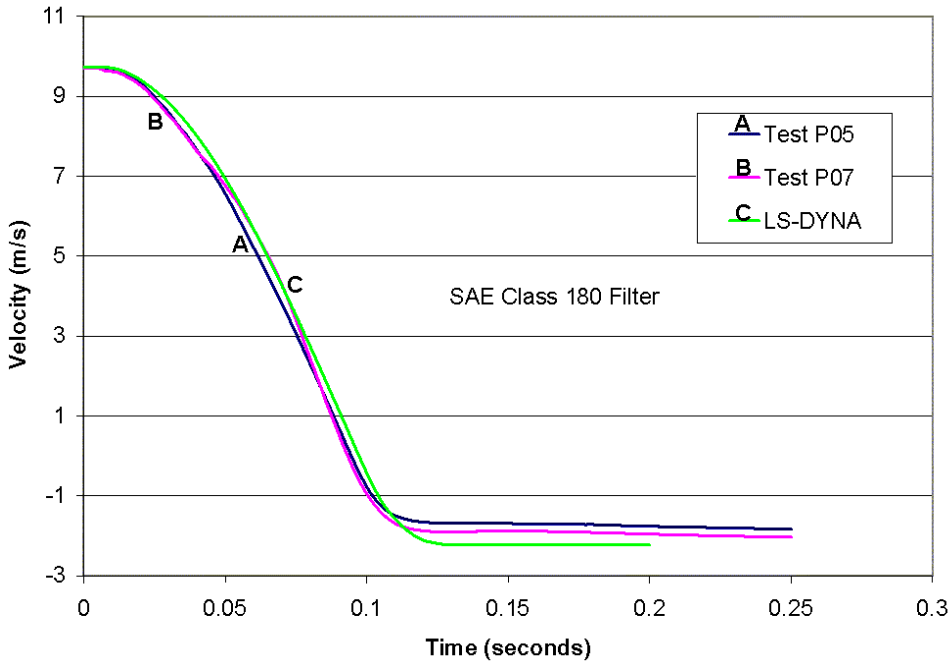

m/sec = 3.28 ft/sec

Figure 131. Pendulum bogie velocities for impact of T4 bridge rail with three-bolt anchorage and 317.5-mm- (12.5-inch-) wide parapet.

Overall correlation between the simulation and test data is considered to be good. The simulation matches particularly well with test P5 in terms of damage, peak force, and acceleration-time history.

SUMMARY FOR BRIDGE RAIL ANALYSES

The analyses of the T4 bridge rail alternatives provided a good benchmark for evaluating the application of the new concrete material model in roadside safety applications. Use of the pendulum bogie provided more controlled tests and eliminated many variables associated with the comparison of simulation to full-scale vehicle crash tests. Two specimens were tested for each design variation, providing some information regarding system variability. Furthermore, the two design variations demonstrated different levels of damage to the concrete parapet, which provided an opportunity to assess the sensitivity of the concrete model to small design changes under similar loading conditions.

After calibration of the material model parameters and enhancement of the base plate connection model, simulations of the two bridge rail alternatives were able to capture the general pattern and severity of concrete damage observed in pendulum tests of both the 254-mm- (10-inch-) and 317.5-mm- (12.5-inch-) wide parapets. As mentioned previously, the user desired to more fully evaluate the concrete material model in other roadside safety structures. A model of a safety-shape bridge rail with New Jersey profile was developed for this purpose. Although some preliminary calculations were performed on this model, project resources were depleted before the structure could be fully analyzed. More details of this bridge rail model, available test data, and discussions of preliminary calculations are presented in the next chapter.

CHAPTER 9. ANALYSES OF SAFETY-SHAPED BARRIER

The user conducted static and dynamic tests on a Florida safety-shape barrier with New Jersey profile.[8] The tests were conducted prior to, and separate from, this effort. Test data available for this barrier include quasi-static load tests to failure at both the end and middle of the parapet. The initial test case selected for evaluating the barrier model was a quasi-static load test to failure on the end of the parapet section (TTI test 421323-S1). Test S1 was performed on the upstream end of the test installation and was intended to represent loading at the barrier ends or at an interior bridge expansion joint.

The test setup is shown in Figure 132. The load was applied using a hydraulic cylinder with an inline load cell. The hydraulic cylinder was attached to a fabricated steel frame that was bolted to the concrete deck structure. A steel wide flange beam stiffened with welded gussets was clamped to the face of the parapet to distribute the applied load over a distance of 1,219 mm (48 inches) A tapered wood block was placed between the back flange of the beam and the sloped face of the concrete parapet to permit horizontal application of the load. The steel beam was mounted to the parapet with the top edges of the flanges flush with the top surface of the parapet. The hydraulic cylinder applied the load to the middle of the steel beam. Displacement of the barrier was measured using a string pot.

Figure 132. Test setup for static load tests on safety-shaped barriers.

The maximum load attained in test S1 was 156 kN (35.1 kips). The resulting failure mode and force-deflection curve are shown in Figures 133 and 134. The load capacity calculated from a yield line analysis was 185 kN (41.6 kips). Subsequent destructive inspection of the test installation showed the last stirrup was spaced approximately 152 mm (6 inches) from the end of the parapet wall rather than 50.8 mm (2 inches) and likely contributed to the lower than expected fracture load.

Figure 133. Failure mode at end of the safety-shaped barrier.

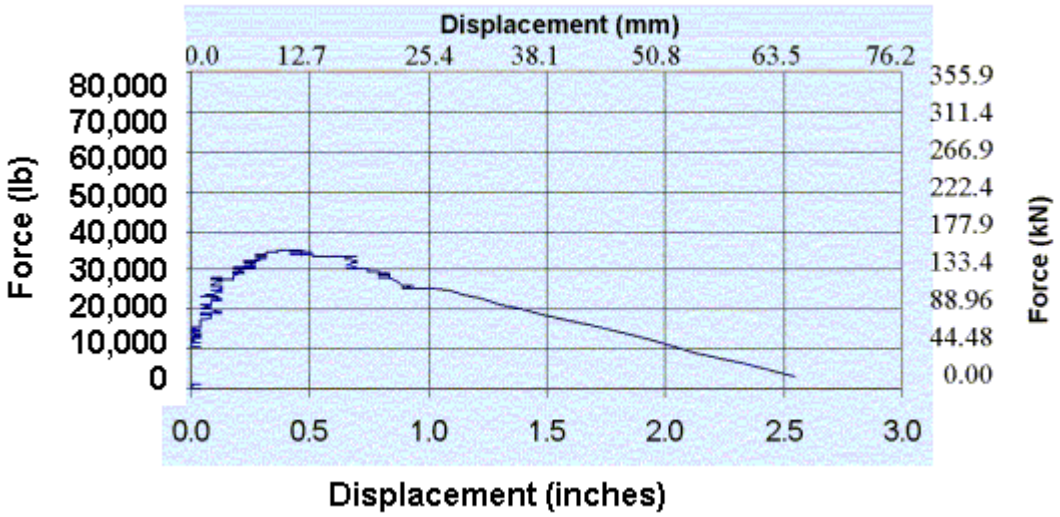

Figure 134. Measured load versus displacement for the safety-shaped barrier.

FINITE ELEMENT MODEL

A finite element model of a steel-reinforced concrete safety-shape bridge rail with New Jersey profile was developed by the user. The model conformed to details and specifications of a rail that was once a standard of the Florida Department of Transportation (FDOT) (FDOT Sheet Index No. I-799). The 813-mm- (32-inch-) tall barrier is 152 mm (6 inches) at the top and 382 mm (15 inches) at its base. The barrier was cast atop a 178-mm- (7-inch-) thick reinforced concrete bridge deck cantilevered off of a concrete beam. The concrete used in the bridge rail parapet had a maximum aggregate size of 25.4 mm (1 inch) and an average compressive strength of 24.9 MPa (3,611 lbf/inch^2). The bridge deck concrete had a maximum aggregate size of 25.4 mm (1 inch) and an average compressive strength of 27.1 MPa (3,931 lbf/inch^2). Dimensions of the barrier system and steel reinforcement details are shown in Figure 135.

A modeling approach similar to that used for the Texas T4 bridge rail was followed for the New Jersey safety-shape rail system. The concrete parapet and bridge deck were modeled using solid elements. Beam elements were used to model the steel reinforcement inside the parapet and bridge deck. The element formulation used for the steel reinforcement was the Hughes-Liu beam element with cross section integration (type 1). The concrete brick elements were type 1 (underintegrated) with stiffness form of hourglass control (type 5) specified. The short input format for the new concrete material model was used to generate the values for the parameters required in the long input format, and these established the baseline input values for the Florida safety-shaped barrier model.[8] The steel reinforcement was coupled to the surrounding concrete using the *CONSTRAINED_LAGRANGE_IN_SOLID feature in LS-DYNA. Figure 136 shows the meshing for the parapet and the deck and the layout of steel reinforcement in both. Figure 137 shows the overall steel reinforcement layout in the model.

The steel reinforcement in the parapet model was revised to reflect the actual construction details of the stirrups, which were 152.4 mm (6 inches) from the end. A simple surrogate impactor was modeled to represent the hydraulic cylinder. The wood block was modeled to account for any compliance associated with the load transfer to the parapet. Figure 138 illustrates the load application setup with respect to the bridge rail model.

The impactor was forced to follow a displacement-time curve that simulated the quasi-static loading condition. The long duration of the test is problematic to reproduce in an explicit analysis procedure. Therefore, the solution must take into account effects. In the analysis, the duration of the simulation was 0.150 sec, which is a fraction of the actual test duration.

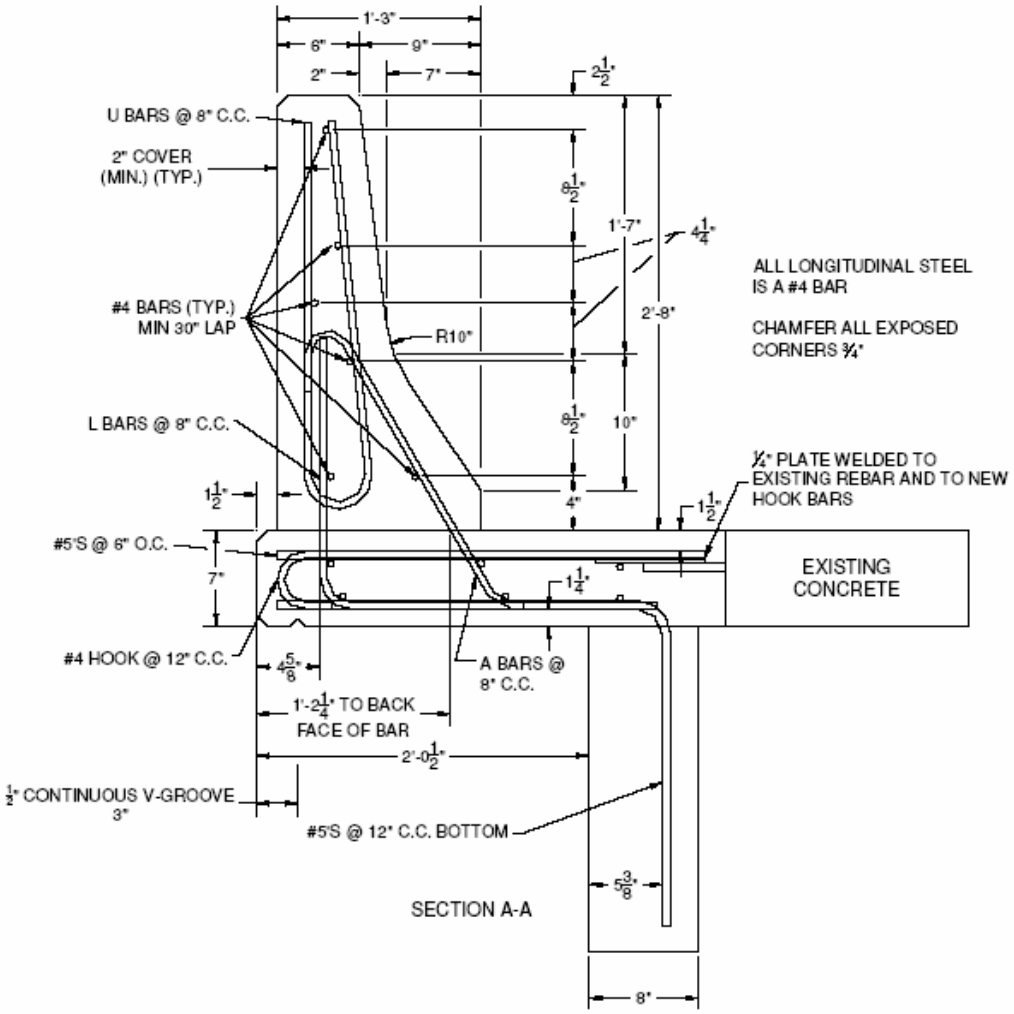

mm = 0.039 inch

Figure 135. Cross section of the Florida safety-shaped barrier with New Jersey profile.[8]

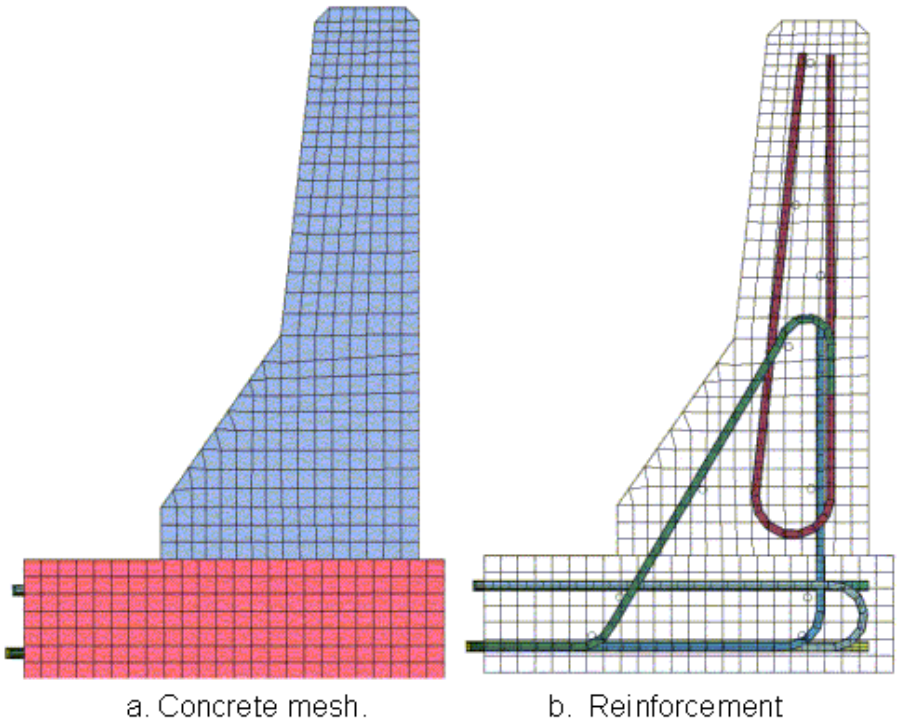

Figure 136. Cross section of Florida barrier model concrete mesh and reinforcement layout.

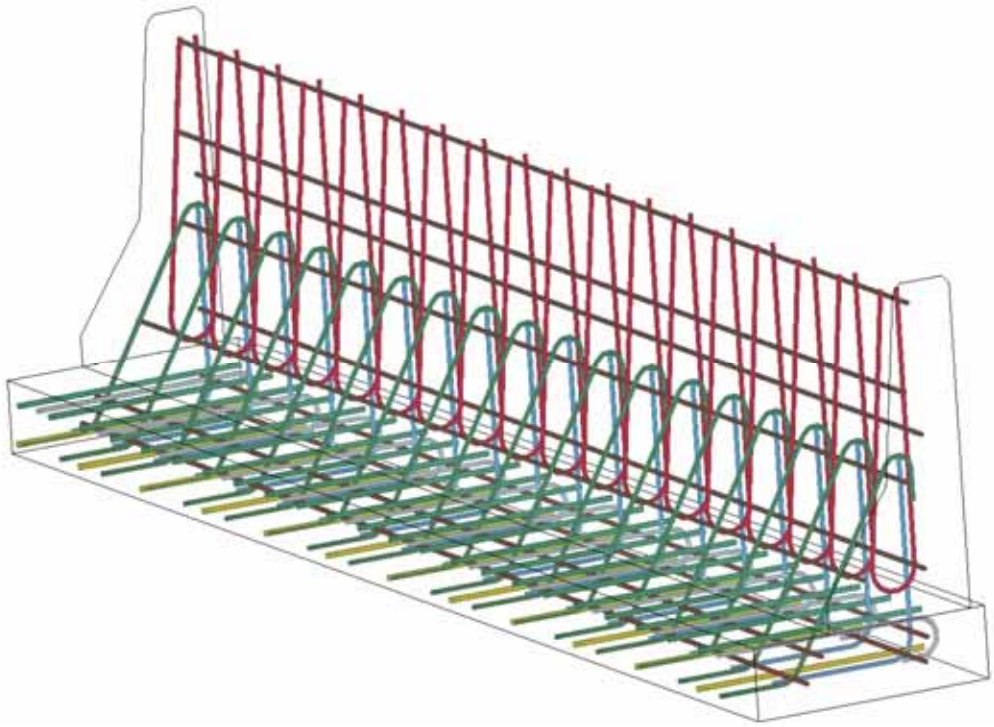

Figure 137. Isometric view of steel reinforcement in Florida barrier model.

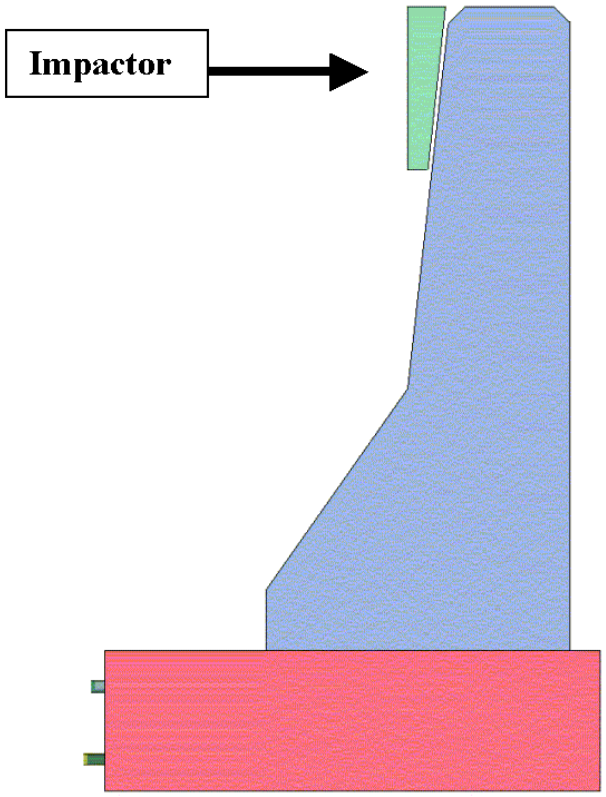

Figure 138. Model of quasi-static load test setup.

USER EVALUATION RESULTS

As shown in Figure 139, simulation results using the preliminary baseline concrete material properties indicate fracture damage (i.e., element erosion) along the cold construction joint between the parapet and the deck, at the transition between the toe of the barrier and parapet wall, and on the edge of the parapet wall just below the impactor. Additional analyses were conducted using 80 percent and 27.5 percent of the baseline fracture energies without significant change in the fracture profile.

Due to time and resource constraints, the user could not perform additional investigation of this barrier system. The user suggested that the following actions should be undertaken: changing the contact definition at the cold construction joint between the parapet and the deck, adjusting the impactor interaction with the parapet, and studying the sensitivity of the system to the rate effect parameters in the concrete model. The developer followed up on some of these suggestions, and evaluations of these activities are provided in the following section.

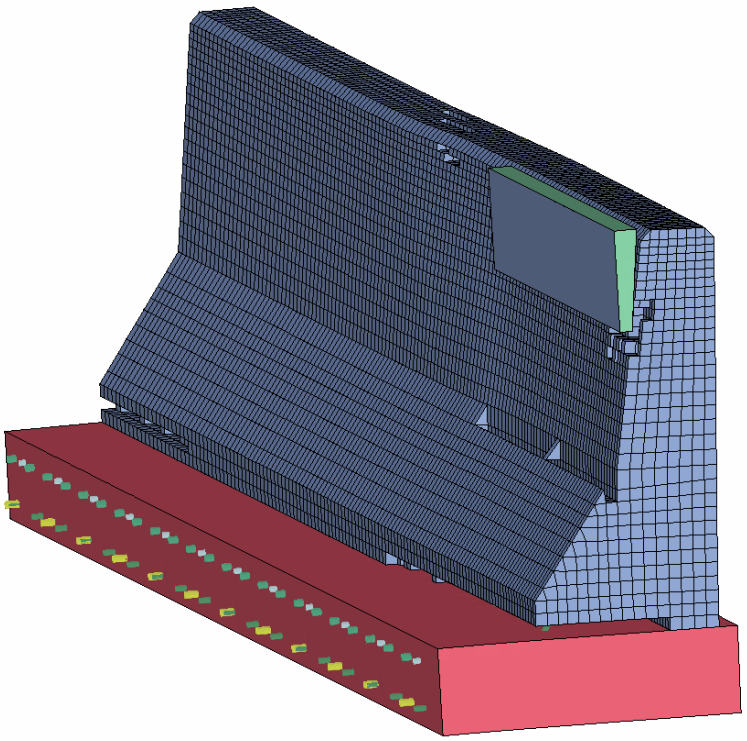

Figure 139. Fracture profile of Florida safety-shaped barrier.

DEVELOPER BASELINE CALCULATIONS

The developer began the calculations using the mesh setup by the user, as previously shown in Figure 138, but made a few adjustments. All concrete material properties were adjusted to default properties, except the shear fracture energy was set to $G_{fs} = ½\ G_{ft}$ instead of $G_{fs} = G_{ft}$. This reduced fracture energy was used in shear because it proved appropriate in some of the bridge rail analyses discussed in appendix B. Unless otherwise specified, each calculation was conducted with erosion occurring at 99 percent damage with a maximum principal strain of 5 percent (ERODE = 1.05). A joint exists between the deck and parapet that is much weaker than solid concrete. This joint interface was adjusted from *CONTACT_TIED_NODES_TO_SURFACE to *CONTACT_NODES_TO_SURFACE, to allow separation in tension.

Rate effects were turned from on to off in the concrete model. Turning rate effects off allowed the quasi-static simulations to run at a higher rate than the quasi-static test. Performing this step is typical and necessary. The turnaround time of the calculations would be extremely long (days) if the calculations were run at the same slow rate as the tests.

As previously mentioned, the quasi-static load was generated using lateral displacements applied directly to all nodes of the steel spreader plate (modeled as rigid shell elements connected to the timber hex elements). The applied displacements increase linearly from 0 to 38.1 mm (0 to 1.5 inches) over 150 msec, as setup by the user. This increase is slow enough to eliminate wave propagation effects.

Damage fringes at about 70 msec are shown in Figure 140. At this time, the parapet has displaced laterally about 16 mm (0.63 inches). Three regions of high damage are noted. First, parapet damage extends from the front at midlevel to the back at deck level, similar to that observed in the post-test photograph. A large inclined shear crack also extends from midlevel upward to the top of the parapet. Finally, concentrated damage is also noted where the lower edge of the timber contacts the parapet. This concentrated damage is not observed in the post-test photograph.

Close examination of the computed results indicates that the timber is not remaining in complete contact with the parapet, also shown in Figure 140. The contact is concentrated at the bottom of the timber spreader, resulting in a stress concentration in the concrete at the point of this contact. This concentration may not be realistic. The developer thinks that complete contact likely occurred during the tests due to the presence of the clamps, or slight deformation of the timber, as previously shown in Figure 133. The timber is modeled as elastic using material model 1 with a modulus of 247 MPa (35,824 lbf/inch^2).

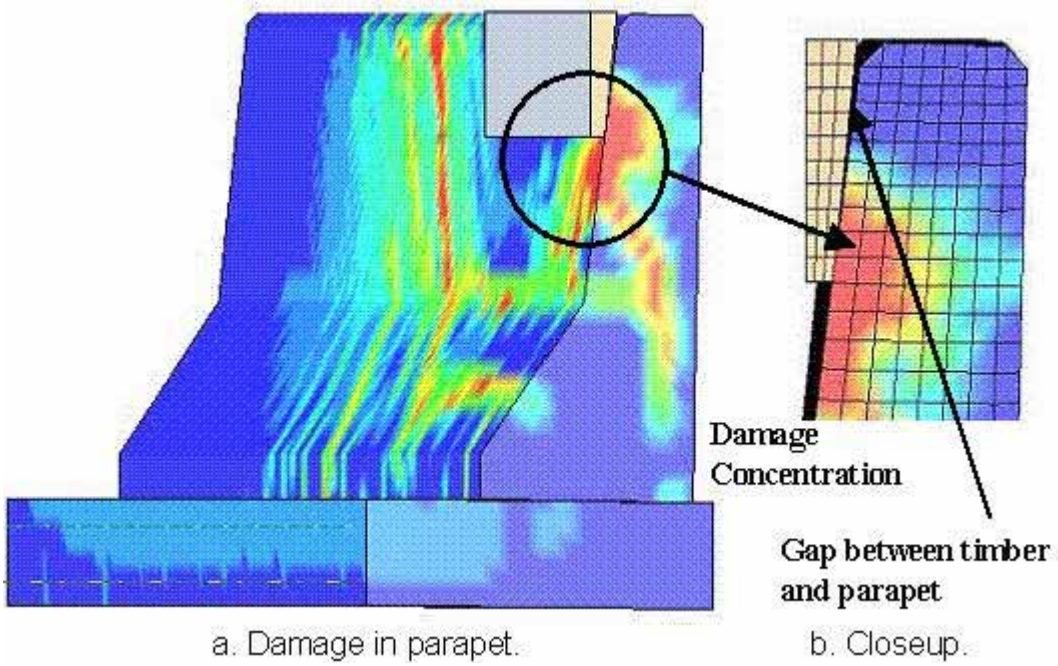

Figure 140. A damage concentration is simulated in the parapet due to application of the steel/timber spreader plate that is not observed in the post-test parapet.

Therefore, a second calculation was performed with the timber modeled as a plastically deformable, damageable material using wood model 143. Properties selected are defaults for saturated Grade 1 pine at room temperature. The modulus in the loading direction is 247 MPa (35,824 lbf/inch^2), which is the same as that used in the elastic timber model of the previous calculation. Damage fringes are shown in Figure 141 at 16.5 mm (0.65 inches) and 38.1 mm (1.5 inches) of lateral deflection. Switching the timber model from elastic to elastoplastic with damage relieves the stress concentration previously calculated at the lower edge of the spreader beam. However, a gap between the beam and parapet is still noted, and late-time unexpected damage occurs near the base of the parapet that is not evident in the test. In addition, the peak

force attained in the calculation is 282 kN (63.4 kips), which is 81 percent higher than the 156 kN (35.1) measured during the test.

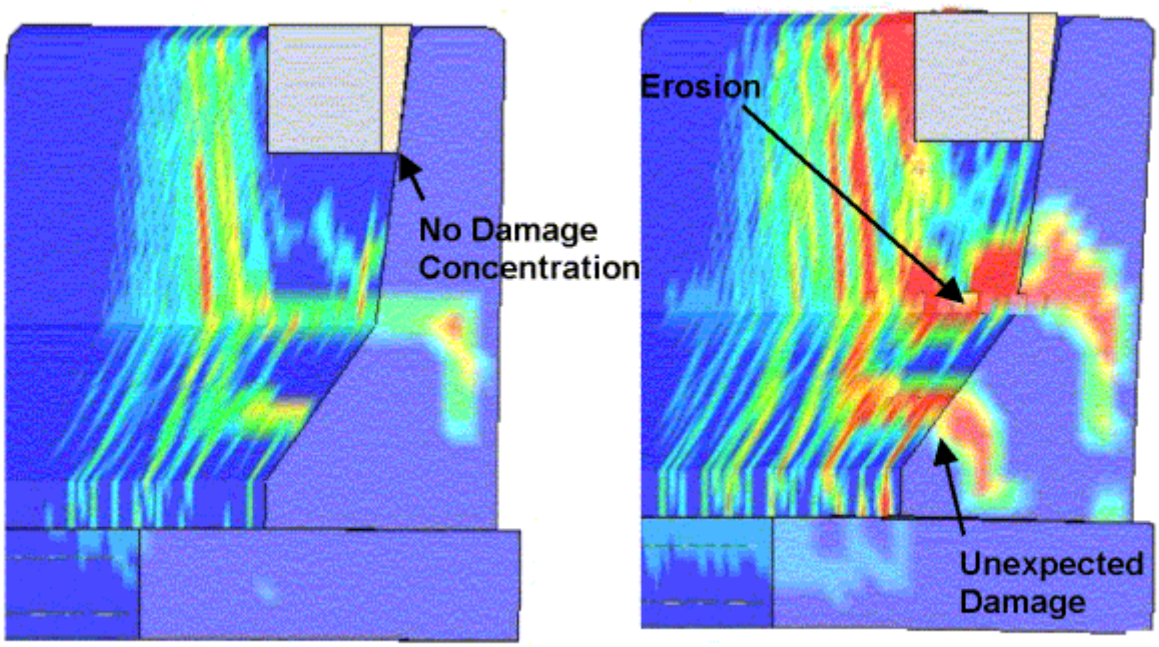

Figure 141. The damage concentration is relieved if the timber is realistically modeled as an elastoplastic damaging material.

Finally, two additional calculations were conducted in an attempt to retain contact between spreader beam and parapet and to reduce the computed peak force. Figure 142 is an example of how the finite element model was enhanced to include a single rigid element representing the load application face of the hydraulic ram. The quasi-static load is generated using a lateral displacement history applied directly to the nodes of the ram element, rather than the steel spreader beam. A contact surface (CONTACT_NODES_TO_SURFACE) separates the ram element from the spreader beam elements that allows for separation but not penetration. In this way, the spreader beam can rotate slightly relative to the ram element and retain contact with the parapet during displacement.

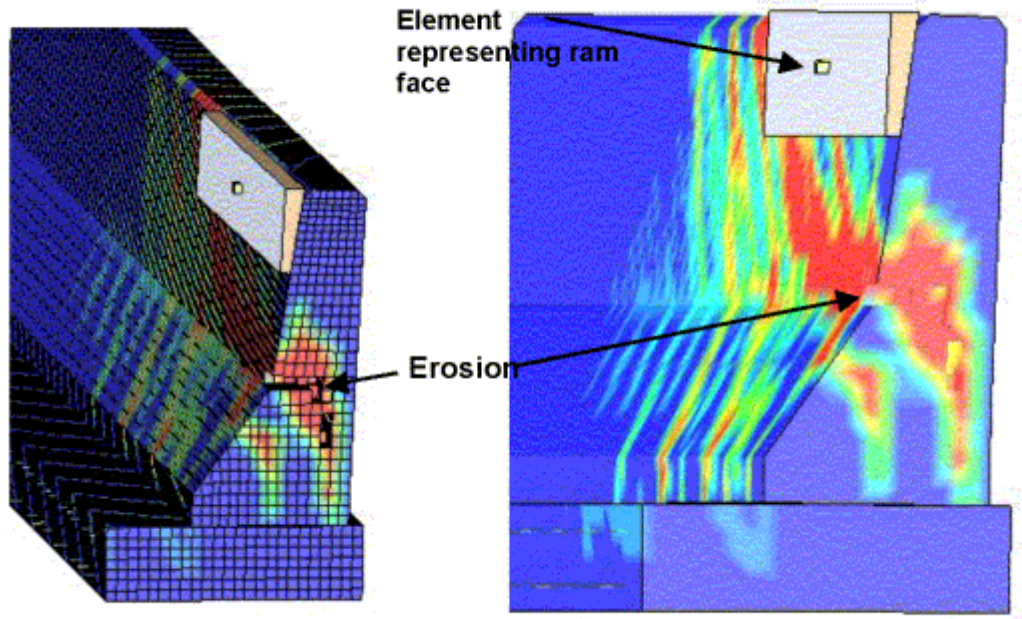

mm = 0.039 inch

Figure 142. A realistic damage and erosion pattern is simulated if the timber remains in contact with the parapet (ERODE = 1.05).

Damage fringes for one calculation are shown in Figure 142 at 20 mm (0.8 inches) of lateral deflection. Rate effects were also removed from the steel reinforcement. This calculation was conducted with erosion occurring at 99 percent damage with a maximum principal strain of 5 percent, like all previously discussed calculations (ERODE = 1.05). The pattern of erosion and damage is consistent with that observed in the test, as previously shown in Figure 133. The peak force attained in this calculation is 183 kN (41.1 kips) at 31 mm (1.2 inches) deflection, which is consistent with the 185 kN (41.6 kips) force the user expected to measure, but is 17 percent higher than the force actually measured.

Damage fringes for the second calculation are shown in Figure 143 at 10 mm and in Figure 144 at 20 mm (0.8 inches) of lateral deflection. This calculation was conducted with erosion occurring at 99 percent damage, regardless of maximum principal strain value (ERODE = 1.0). The peak force is measured at approximately 10 mm (0.4 inches) of deflection. The final measurement before loss of strength is made at approximately 20 mm (0.8 inches) of deflection. Two views are shown—with and without the visible mesh—to better view the erosion. In this case, the damage pattern is less diffuse, and the erosion pattern is much more prominent, than calculated with ERODE = 1.05.

Again, the calculated erosion and damage pattern in the parapet is consistent with the post-test cracking pattern previously shown in Figure 133. However, additional erosion occurs in the deck that is not visible in post-test photo. The developer thinks erosion occurs because the deck

section modeled is not nearly as long as the actual test section, due to the need to retain a reasonable run time with a reasonable number of elements. Hence, the cantilever-type bending of the short deck produces tensile stresses in the concrete that are higher than those that would be produced in a longer deck.

The peak force attained in this calculation is 181 kN (40.1 kips) at 31 mm (1.2 inches), which is within 16 percent of the measured value. The calculated force versus deflection history is shown in Figure 145. It is in good agreement with that previously shown in Figure 134 for the first 12 mm (0.5 inches) of deflection. However, the peak force continues to increase beyond 12 mm (0.5 inches) to a higher force, and with more ductile behavior, than measured. The computed force remains fairly constant (or increases slightly) with increasing deflection beyond 31 mm (1.2 inches), while the measured force decreases in magnitude. It is not clear, at least to the developer, why the measured force drops down to near 0 even though the steel reinforcement remains intact.

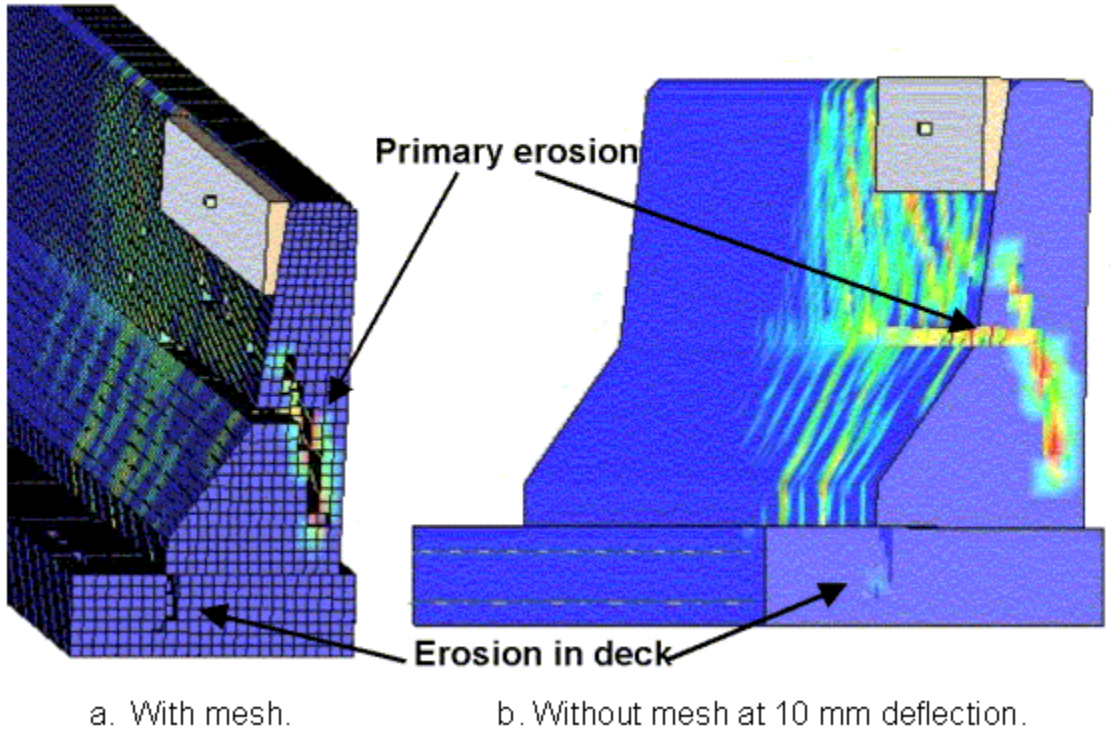

mm = 0.039 inch

Figure 143. The primary erosion agrees with the measured crack pattern if the timber remains in contact with the parapet (ERODE = 1.0).

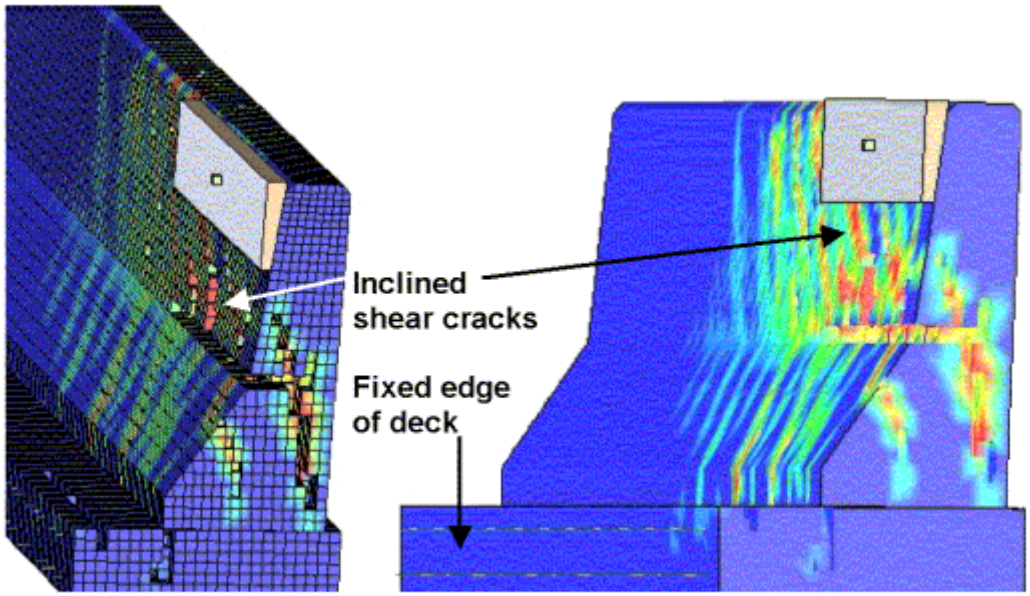

mm = 0.039 inch

Figure 144. The primary erosion agrees with the measured crack pattern if the timber remains in contact with the parapet (ERODE = 1.0).

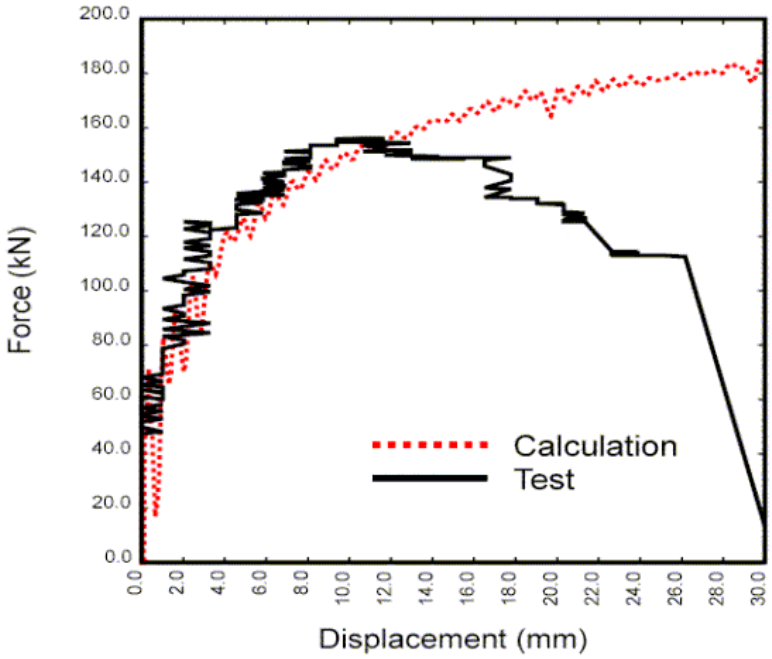

mm = 0.039 inch, kN = 225 lbf

Figure 145. The calculated force versus deflection history is in reasonable agreement with the measured curve for the first 12 mm (0.5 inches) of deflection.

DEVELOPER APPLIED FORCE CALCULATIONS

One alternative method of simulating the barrier test is to simplify the geometric model and loading conditions. Simplified loading conditions are often used as a first step in performing a finite element analysis and are quite often sufficient. The timber remains in contact with the parapet during the test; thus, the timber applies lateral force to the parapet over the entire contact region. Therefore, concentrated lateral forces are directly applied to the nodes of the parapet over the timber-to-parapet contact region. The total load applied increases nonlinearly from 0 to 156 kN (0 to 35.1 kips) in 40 msec, remains at 156 kN (35.1 kips) until 50 msec, then drops to 18 kN (4.0 kips) by 260 msec. The steel/timber spreader plate is completely removed from the finite element model.

Damage fringes are shown in Figure 146 for two calculations conducted with different erosion values. One force-displacement history is shown in Figure 147. The damage simulated extends from the front at midlevel to the back at deck level. Inclined shear damage lines are also present. The computed damage is similar to the damage observed in the post-test photograph. It is also similar to that calculated and previously shown in Figure 144 where the timber remains in contact with the parapet. As desired, concentrated damage in the loading regime is not simulated. Nor is unexpected damage near the base of the parapet.

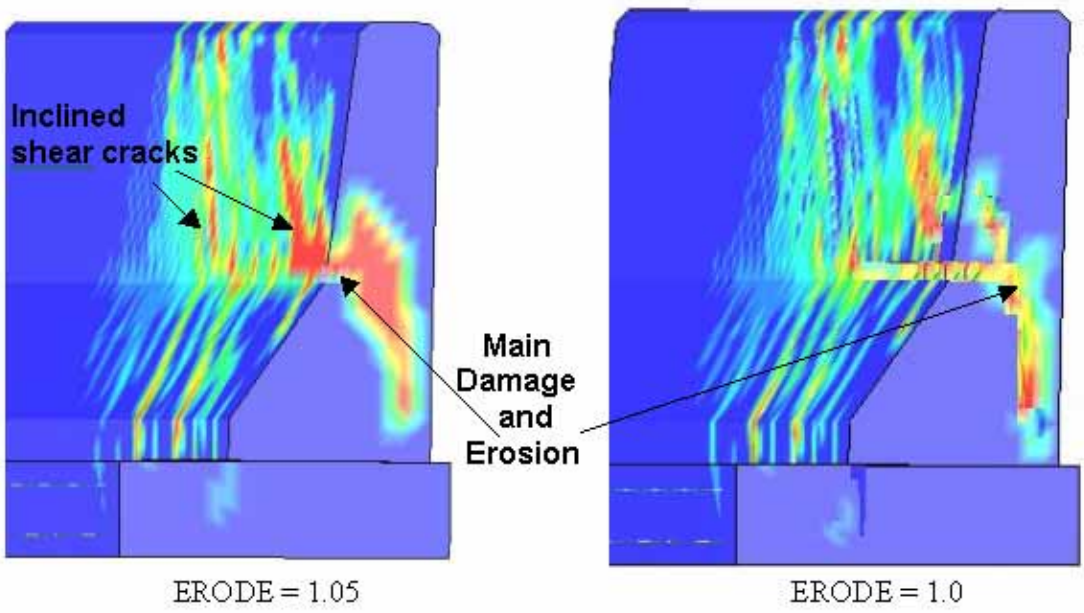

Figure 146. The computed damage mode is similar to that measured if the load is applied via concentrated nodal point forces (at 11- to 12-mm (0.43- to 0.5-inch) deflection).

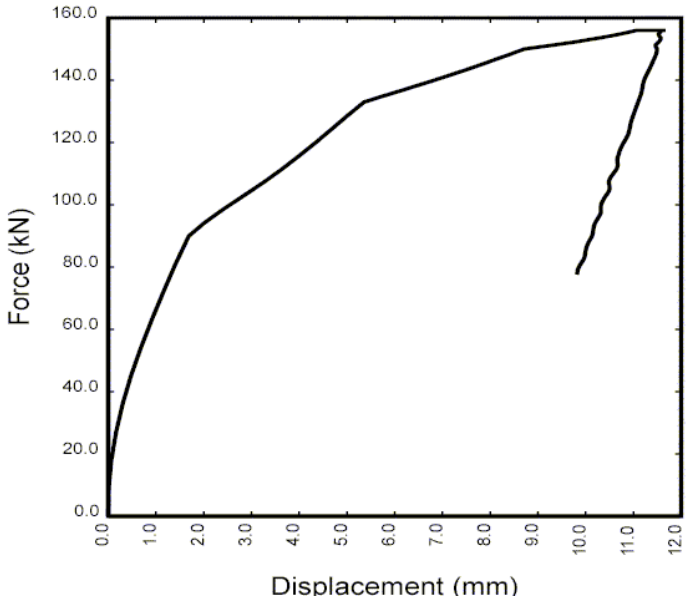

mm = 0.039 inch, kN = 225 lbf

Figure 147. The computed force versus displacement unloads, when the load is applied via concentrated nodal point forces (ERODE = 1.05).

Approximately 11 mm (0.43 inches) to 12 mm (0.5 inches) of parapet displacement are computed at the center of the loading region when the applied load is 156 kN (35.1 kips), in good agreement with the measured displacement previously shown in Figure 134. However, once the applied force begins to drop at 50 msec, the barrier displacement begins to decrease, which is not realistic. The drawback of this calculation is that the force history is applied and its magnitude is assumed equal to that measured (the timing of the application is not available).

SUMMARY FOR SAFETY-SHAPED BARRIER CALCULATIONS

The application of the load in the static test of the safety-shaped barrier proved critical to accurate modeling of the damage mode. The simplest calculation conducted using concentrated nodal forces applied directly to the parapet provides good correlations with the measured damage mode and with the force versus displacement history to peak strength. However, the drawback of this calculation is that the applied force history is assumed, not predicted.

The best correlations are obtained when the timber plate is free to adjust orientation in order to maintain good contact between the timber and concrete. This situation was accomplished by representing the load application face of the hydraulic ram as a single rigid element, with flexibility between this element and the timber/spreader plate. If the timber is restrained from adjusting orientation, then a gap forms between the timber and concrete, which produces undesirable damage concentrations in the concrete. The main difference between this calculation and the measured results is that the computed force attained agrees with the pretest estimated value of 185 kN (41.6 kips), but is higher than the measured value of 156 kN (35.1 kips).

All safety-shaped barrier calculations conducted focused on applying the load correctly, setting the proper contact surface conditions at the joint between the parapet and deck, and in turning off rate effects to better simulate quasi-static behavior. No parametric studies were conducted related to the concrete model or its properties. All calculations used default properties for the concrete except for setting $G_{fs} = \frac{1}{2}G_{ft}$. This reduced shear modulus was used because the Texas T4 bridge rail simulations indicate that a reduced shear modulus may be appropriate. Ultimately, a reasonable damage mode was predicted using these reduced properties and appropriate load and boundary conditions.

This series of calculations demonstrates that well-defined load and boundary conditions are essential when analyzing tests for material model evaluation. Otherwise, a good portion of the effort may be spent refining the load and boundary conditions, rather than evaluating the material model. However, tests such as the safety-shaped barrier just analyzed often are conducted for purposes other than material model evaluation. Financial and time constraints require that published and available test data are used. The analyst must be prepared to critically review all aspects of the geometric and material models being used in the simulation and not just inspect the particular material model under evaluation.

CHAPTER 10. SUMMARY AND RECOMMENDATIONS

DEVELOPER COMMENTS

A material model for concrete was developed and implemented into the LS-DYNA finite element code. Also implemented was a suite of default material properties as a function of concrete compressive strength and maximum aggregate size. The model and default properties were evaluated for use in roadside safety applications through correlations with test data. Some of the test data—including those related to drop tower and bogie vehicle impact into reinforced concrete beams—as generated specifically for this effort. Some of the test data was generated prior to this effort but made available for this study, including pendulum impact into bridge rails and quasi-static loading of a safety-shaped barrier.

Analyses of these tests indicate that in most cases, damage modes and deflection histories were accurately simulated using default material properties. In a few cases, alternative properties were suggested to simulate additional damage. The properties that seemed to be most critical are the fracture energies (G_{ft} in tension, G_{fs} in shear, G_{fc} in compression), the rate effect on fracture energy (*repow*), and the maximum principal strain at which erosion occurs (ERODE). In general, the developer recommends using default properties of $G_{fs} = G_{ft}$ with $G_{fc} = 100\ G_{ft}$ with *repow* = 1. The fracture energy in tension was obtained from values listed in the CEB. If more shear or compression based damage is desired, then use of $G_{fs} = ½\ G_{ft}$ or $G_{fc} = 50\ G_f$ are reasonable reductions. If more overall damage is desired, then *repow* = 0.5 is a reasonable reduction. Reductions below these values are not recommended.

Erode is a control parameter. If a value is not specified (ERODE = 0.0), then erosion will not occur. The recommendation is to specify erosion between 5 and 10 percent maximum principal strain ($1.05 \leq \text{ERODE} \leq 1.10$). By taking this step, severe damage is able to accumulate and be maintained before erosion occurs. In numerous calculations, erosion set to 5 and 10 percent strain gave similar results. Erosion at 1 percent strain was evaluated but typically simulates a structural response that is more flexible than at 5 to 10 percent strain and may be more flexible than measured. Once an element erodes, then a 25- to 38-mm (1- to 1.5-inch) gap forms (the dimension of the element eroded). This type of gap is much larger than a hairline crack. Thus, it is reasonable to delay erosion for lightly cracked structures, particularly if the structures are cycling between tension and compression (opening and closing cracks).

During the computational review of the concrete material model, the user recommended the following changes:

- Adjust fracture energies to 80 percent of the preliminary values used by the user. This change was made, and any reference to default values within this report refers to the updated fracture energies. These updated fracture energies are those documented in the companion to this report's Users Manual and are in agreement with those tabulated in the CEB. The updated fracture energies are, however, 80 percent less than those predicted by the formula given in the CEB. An inconsistency appears to exist between the tabulated

values and formula documented in CEB for aggregate sizes greater than 19 mm (0.75 inches).

- Correction to an unrealistic increase in the concrete internal energy. This correction was made to the material model energy term.

- Correction to some reporting problems associated with the long input format of the concrete material model. These corrections were made. The companion to this report Users Manual and material model printout routines reflect these changes.

USER COMMENTS

Numerical analyses were conducted using the newly developed LS-DYNA concrete material model. The analyses showed very good potential for useful application of the model in analyses of steel-reinforced concrete roadside safety structures. The T4 bridge rail study is a good example of this potential. The analyses of the T4 bridge rail alternatives provided a good benchmark for evaluating the strengths, sensitivity, and usability of the new concrete material model. Use of the pendulum tests provided more controlled impact conditions and eliminated many variables associated with the comparison of simulation to full-scale vehicle crash tests. Two specimens were tested for each design variation, providing some information regarding system variability. Furthermore, the two design variations demonstrated different levels of damage to the concrete parapet, which provided an opportunity to assess the sensitivity of the concrete model to small design changes under similar loading conditions.

After adjusting the fracture energies to 80 percent of their preliminary baseline values, good overall correlation was achieved between the T4 bridge rail simulations and pendulum test data for both design alternatives investigated. The simulation matches reasonably well with respect to the damage profile, concrete fracture (i.e., element erosion in simulation), peak impact force, and acceleration-time history of the pendulum impactor.

After calibrating the fracture energies, the simulation of the T4 bridge rail system with three-bolt anchorage and 254-mm- (10-inch-) wide parapet captured the punching shear failure of the concrete underneath the steel base plate and post. As in the pendulum tests, the concrete failure radiated out from the anchor bolts across the top surface of the concrete parapet and extended down the back side of the parapet wall. When the same material properties were used in a subsequent simulation of the T4 bridge rail with four-bolt anchorage and 317.5-mm- (12.5-inch-) wide parapet, the results again correlated with the test data. No concrete fracture was observed, and the damage fringes matched the pattern of hairline cracks observed in one of the test specimens.

The user recommended that the default fracture energies be adjusted to levels found to provide damage correlation between simulations and tests. The developer followed this recommendation, which is available in subsequent releases of LS-DYNA 971. Results of the parametric analyses also indicate that element erosion should be used in conjunction with a maximum principal strain failure criterion (i.e., the ERODE parameter should be set greater than 1.0). The current default setting (ERODE = 1.1) accomplishes this recommendation.

The model is stable and has a reasonable time step. Some problems were identified with the energy balance associated with use of the concrete material model. As damage accumulates in the concrete structures, an artificial or nonphysical increase in internal energy appears to causes the total energy of the system to increase dramatically. This glitch was reported to the developer, and a fix was implemented in subsequent releases of LS-DYNA 971.

Some reporting problems related to the long input format of the concrete material model were also identified. The parameter listing generated by the output routines does not correspond to the written documentation of the model. Details of this problem were reported to the developer, and corrections were made in subsequent releases of LS-DYNA 971.

The short input format is recommended for a first cut analysis and to generate the long input format values. However, the user is encouraged to perform experiments to determine values that best fit his or her concrete data.

All analyses reported herein were conducted using a single processor on a Linux platform because releases for other hardware and multiple processors were not available or were unstable. However, a few analyses were conducted using different platforms and multiple processors as some of the beta binaries became available during the course of the project. The analyses conducted on different platforms showed some differences in the number of eroding elements in the simulations involving concrete fracture. However, the differences are not considered to be significant or indicative of a flaw in the material model. Moreover, the eroding pattern was the same across all calculations for a given case. Note that erosion takes place when the damage value associated with a particular element exceeds a prescribed threshold (if desired by the user). The numerical analysis has established that different hardware platforms, roundoff errors, and number of processors have an influence on results consistency. This influence was observed in other research efforts where a sudden collapse, element erosion, and any other discontinuity phenomenon were numerically analyzed. Therefore, the researchers believe that these differences for the cases studied are not attributed to the material model but rather to other factors.

Although the results of the evaluation of the concrete material model are encouraging, resource limitations precluded a more indepth evaluation of the model. Further study is recommended to more fully quantify the applications and limitations of the material model. The investigation of the New Jersey safety-shape bridge rail is incomplete due to lack of time and resources. Further investigation of the quasi-static load tests would be helpful. Additionally, an analysis of the pickup truck impact into this barrier and/or a portable concrete barrier is recommended.

CHAPTER 11. APPENDIX A. USER CODE VERIFICATION

INTRODUCTION

This task involved repeating the finite element calculations previously performed by the developer using input files supplied by the developer, and comparing the results of these calculations. Five models were supplied to the user by the developer. The models included a single element model (three load cases), concrete cylinder under tension, plain (unreinforced) concrete beam under impact loading, over-reinforced concrete beam under impact loading, and reinforced concrete beam under impact loading by surrogate vehicle.

All the input files incorporate the new material (MAT type 159 or MAT_CSCM) to be released in LS-DYNA version 971. The user obtained a beta binaries release of LS-DYNA version 971 for the following platforms/operating systems: SGI IRIX (version 971 release 1490 double precision), MS-Windows (version 971 release 1612 single precision), and Linux Intel 32 bit architecture (version 971 release 1708 single precision). The SGI IRIX binary crashed with a floating point exception error during the initialization phase of reading an input file. The researchers believe the crash occurred because the SGI binary beta release (1490) might not be as “bug free” as the other binaries.

CASE 1. SINGLE ELEMENT SIMULATIONS

In this case, a single solid element was used to verify the basic behavior of the material model. There are three loading conditions for this case. The first load case was compression of the element as shown in Figures 148 and 149. The second load case was application of a tensile load to the element as shown in Figures 150 and 151. The last load case was a shear load applied on the element as shown in Figures 152 and 153. For each of these load conditions, the user calculations precisely matched the developer’s calculations as Figures 148–153 indicate.

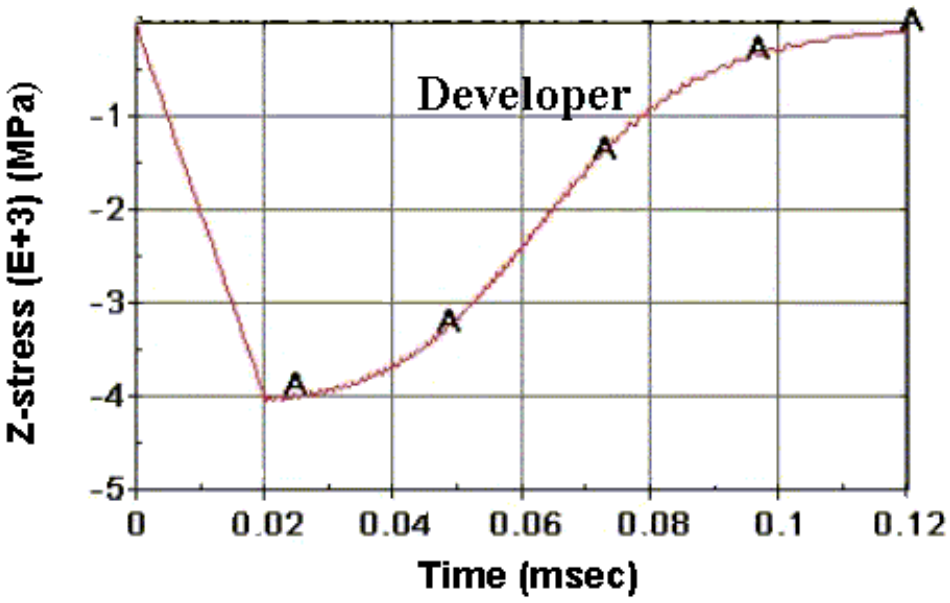

psi = 145.05 MPa

Figure 148. Single element under compressive loading, developer.

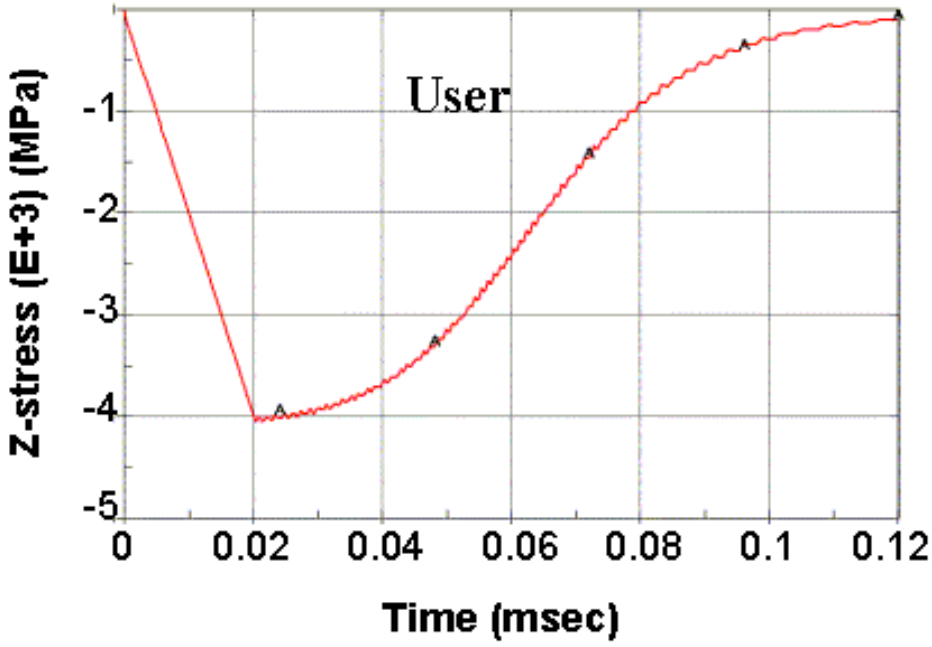

psi = 145.05 MPa

Figure 149. Single element under compressive loading, user.

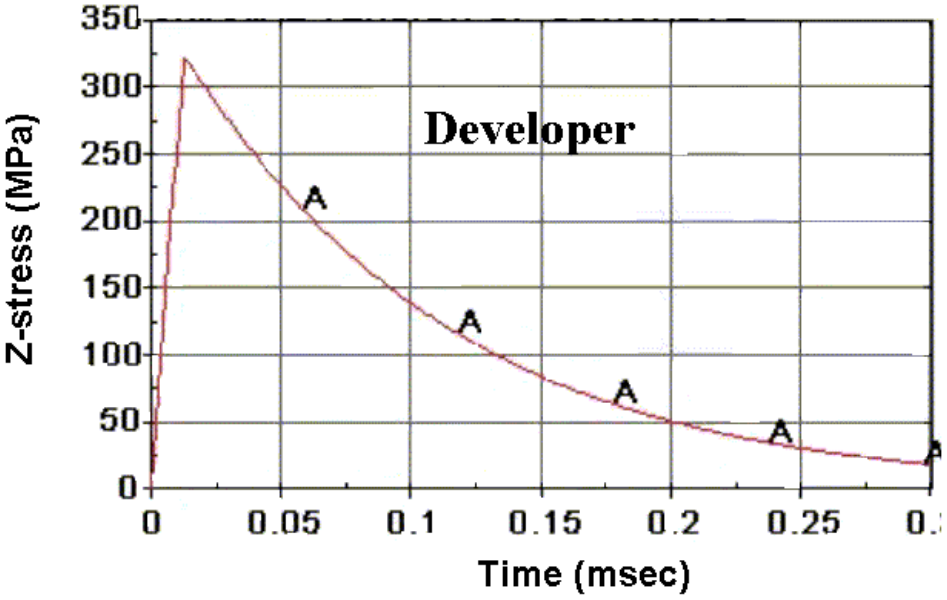

psi = 145.05 MPa

Figure 150. Single element under tensile loading, developer.

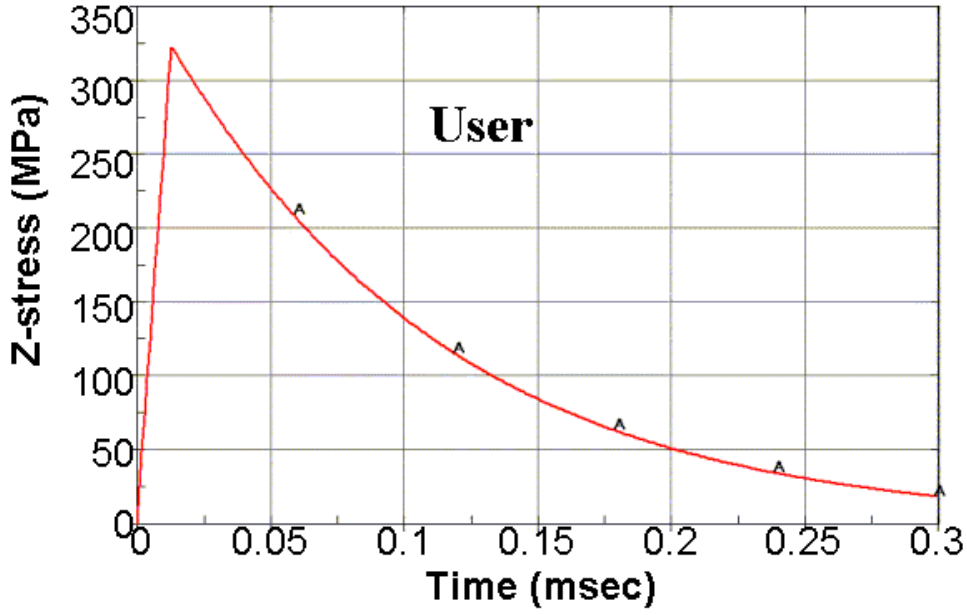

psi = 145.05 MPa

Figure 151. Single element under tensile loading, user.

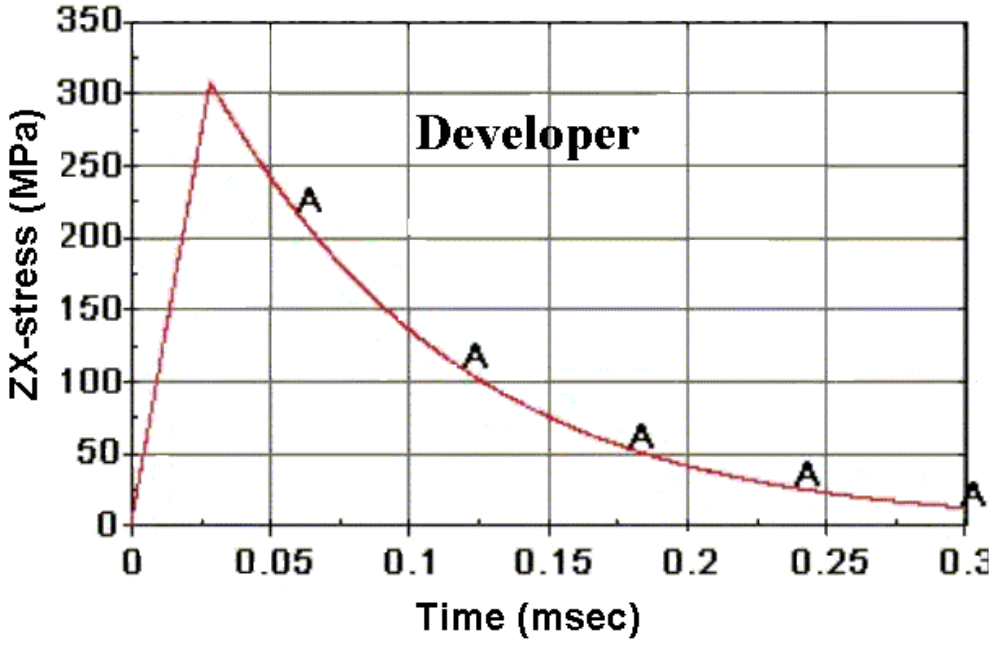

psi = 145.05 MPa

Figure 152. Single element under pure shear loading, developer.

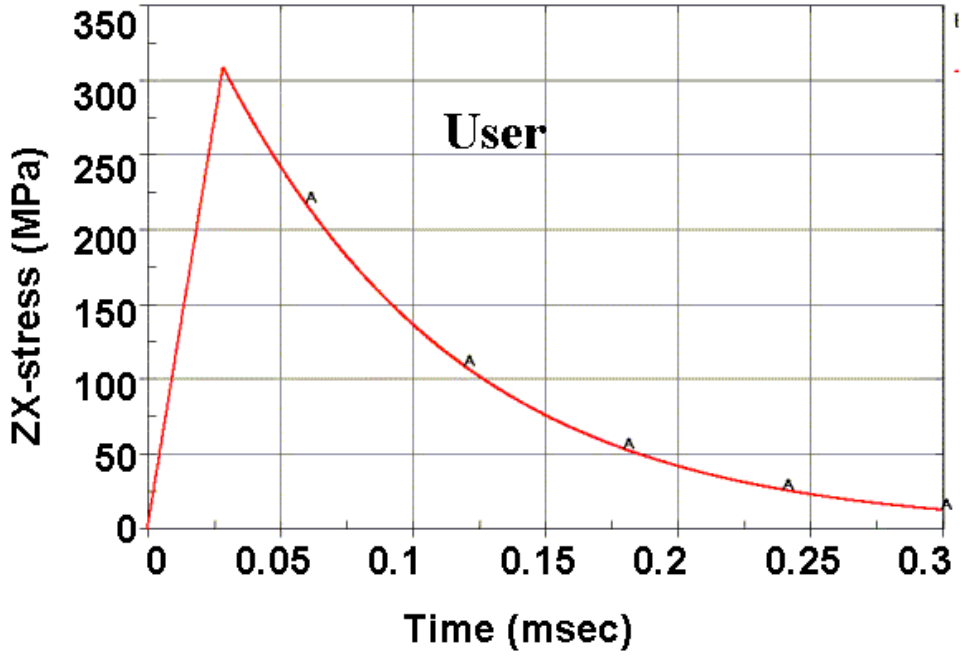

psi = 145.05 MPa

Figure 153. Single element under pure shear loading, user.

CASE 2. CYLINDER RUNS

This case consists of a plain unreinforced concrete cylinder subject to tensile loading. The tension loading was simulated by pulling both ends of the cylinder at a constant velocity. An inclined cross section was defined in the model to track force versus time, as shown in Figure 154 below.

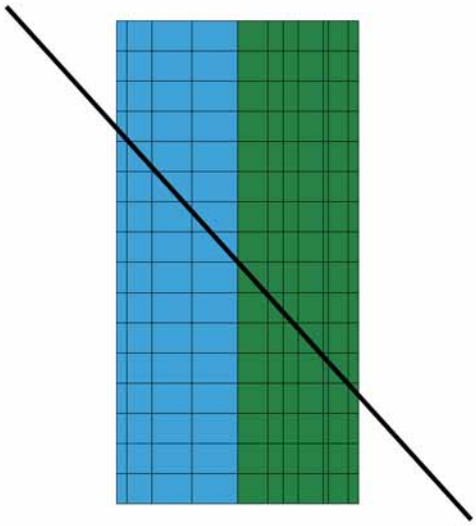

Figure 154. Concrete cylinder model with inclined cross section.

Fringes of the damage to the materials were plotted at various times during the analysis. The damage parameter plotted is the maximum of brittle and ductile damage calculated by the material model. It is noteworthy that damage is a normalized entity from 0 (no damage) to 1.0 (complete damage).

Figures 155–157 show these damage fringe plots at key times. Figures 158 and 159 show the cross-sectional force versus time measured on the inclined plane from the developer calculation and the user calculation, respectively. The user calculations matched the developer's calculations in terms of both damage fringes and cross-sectional force for this model. Two binaries were used for this calculation; however, only the Windows results are presented because there was no significant difference between the computed results.

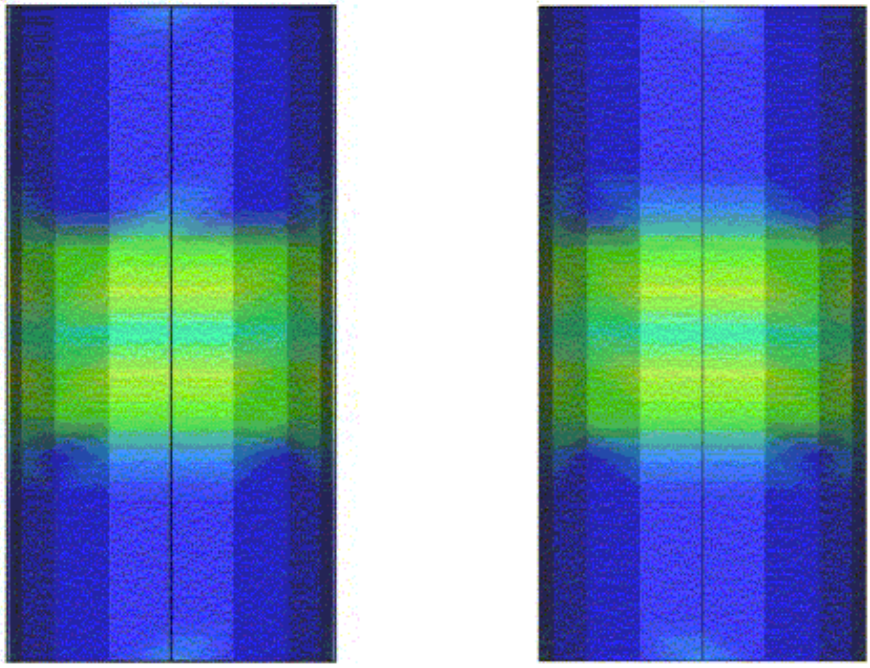

a. Developer. b. User.

Figure 155. Damage fringe t = 13.498 msec.

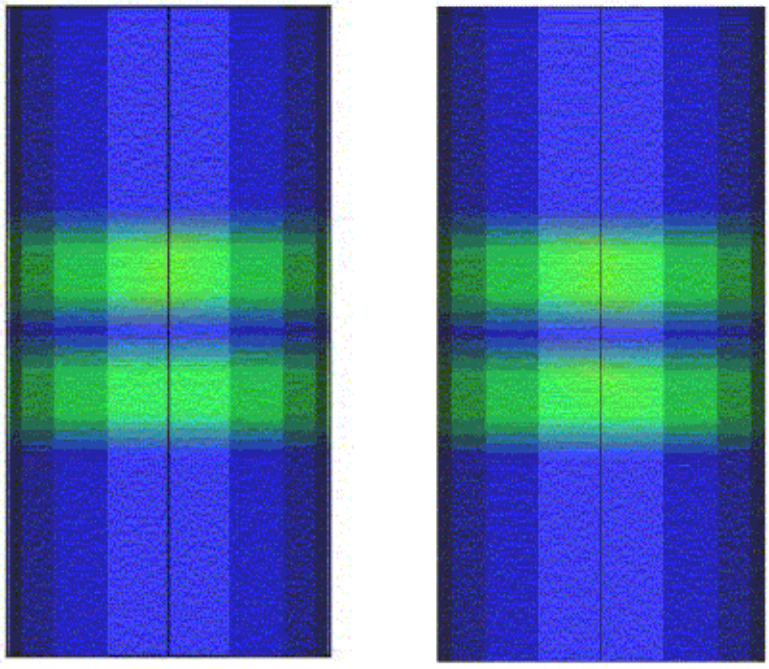

a. Developer. b. User.

Figure 156. Damage fringe t = 13.598 msec.

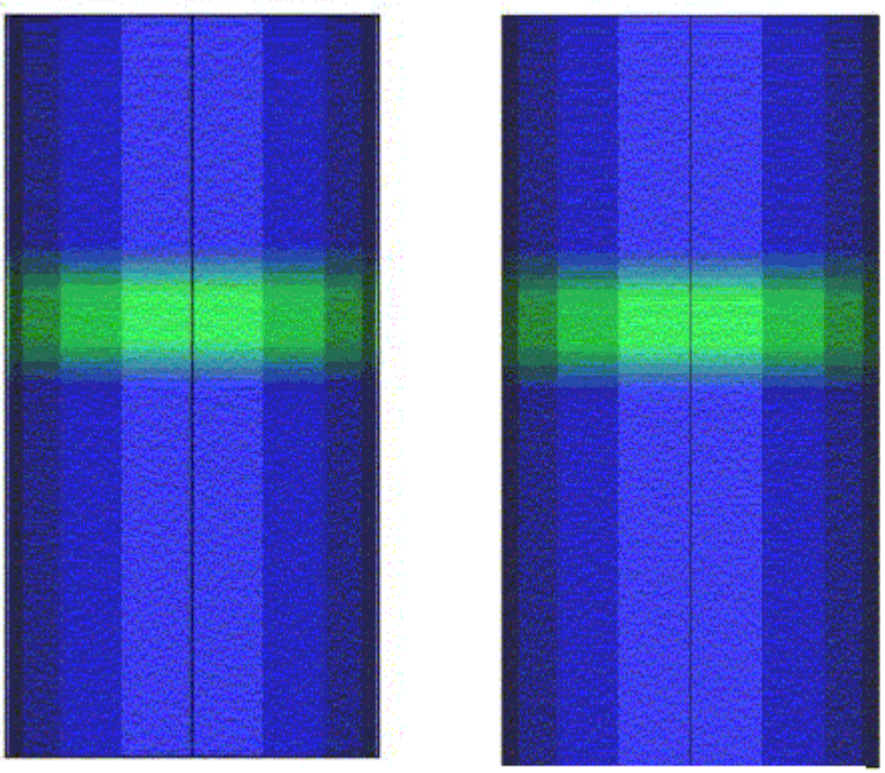

Figure 157. Damage fringe at t = 40 msec.

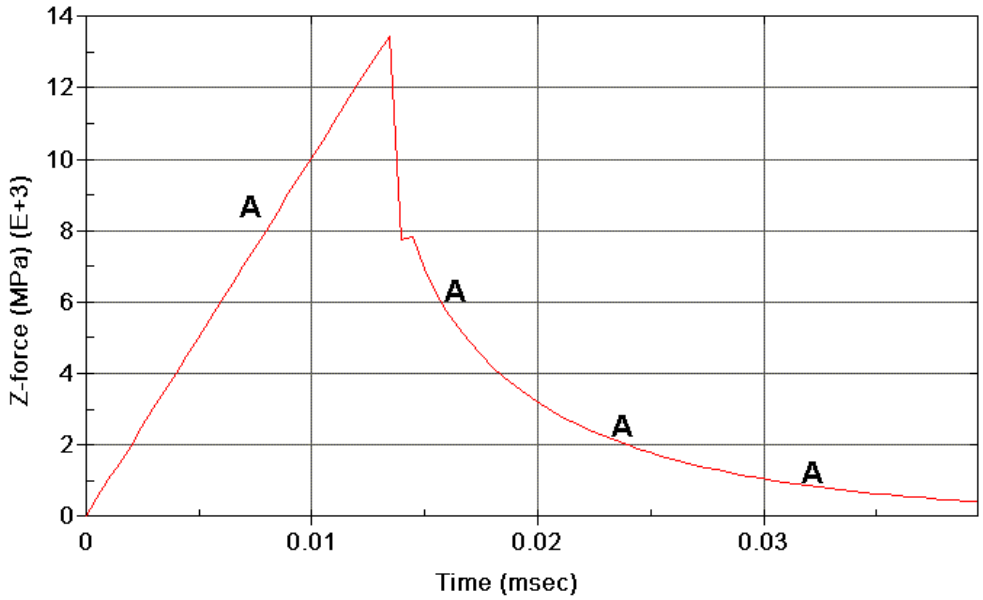

psi = 145.05 MPa

Figure 158. Cross-sectional force (developer).

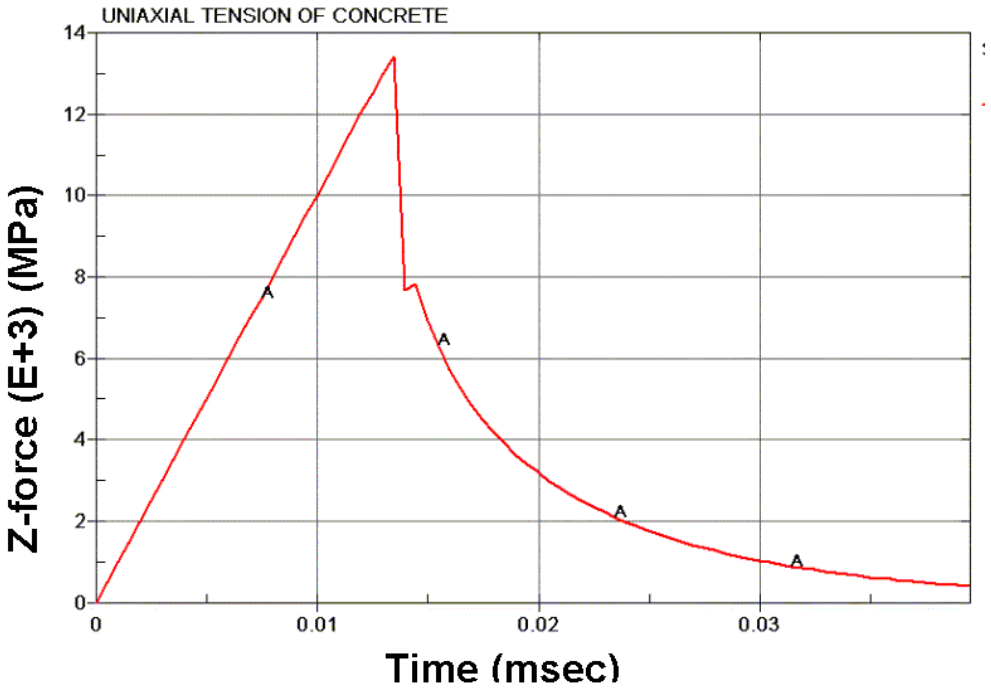

psi = 145.05 MPa

Figure 159. Cross-sectional force (user).

CASE 3. PLAIN CONCRETE BEAM

In this case, an unreinforced concrete beam was modeled using the CSCM concrete model. Unlike previous cases, this model incorporates element erosion and contact definitions. The element erodes based on a set damage threshold above 0.99. Contacts were defined to represent surface interaction between parts (beam, impact parts, support parts, etc.).

Damage fringes were plotted at simulation times (t) of 1, 4, 20, and 30 msec. Figures 160–163 show the respective damage fringe plots obtained from the developer calculations for these simulation times. Figures 164–167 show the corresponding damage fringes plots from the user's calculations using the Linux binary. Similarly, Figures 168–171 show the respective damage fringe plots from the user's calculations using the Windows binary for the aforementioned simulation times.

At 1 msec of simulation time, the beam was already experiencing damage as shown in Figure 160 (developer), Figure 164 (user Linux), and Figure 168 (user Windows). The damage fringe from all three calculations looks very similar. Some elements were already eroded at $t = 4$ msec as shown in Figure 161 (developer), Figure 165 (user Linux), and Figure 169 (user Windows). Although the number of eroded elements is different among the three calculations, the fracture pattern is considered to be bounded within expected behavior of concrete. This same degree of variation in cracking patterns is observed among identical laboratory tests.

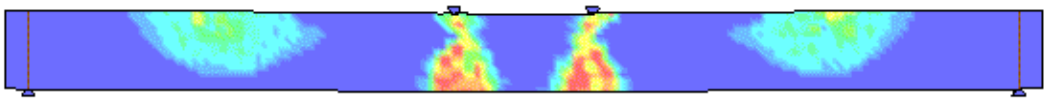

Figure 160. Plain concrete damage fringe at 1 msec (developer).

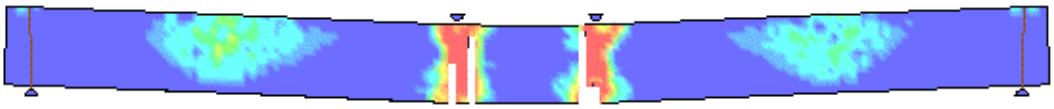

Figure 161. Plain concrete damage fringe at 4 msec (developer).

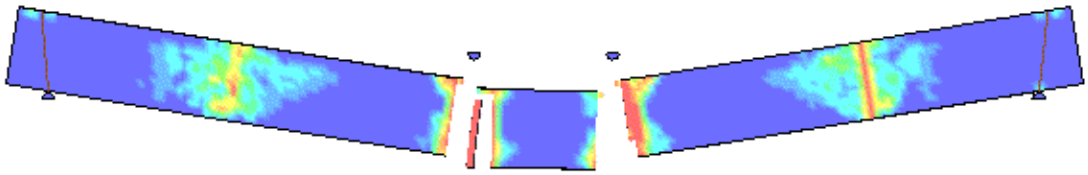

Figure 162. Plain concrete damage fringe at 20 msec (developer).

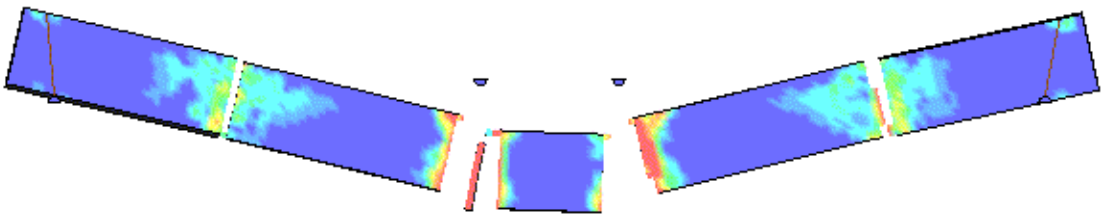

Figure 163. Plain concrete damage fringe at 30 msec (developer).

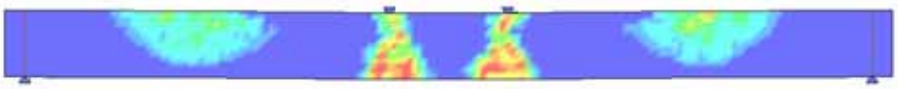

Figure 164. Plain concrete damage fringe t =1 msec (user Linux).

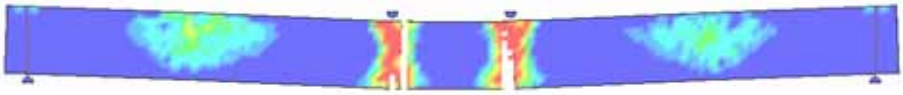

Figure 165. Plain concrete damage fringe t = 4 msec (user Linux).

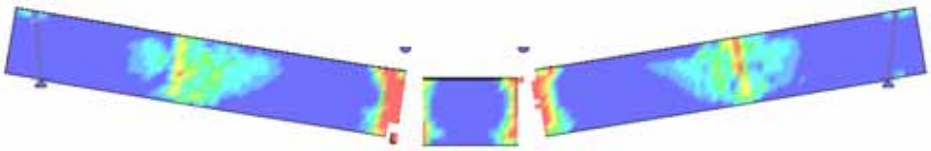

Figure 166. Plain concrete damage fringe t = 20 msec (user Linux).

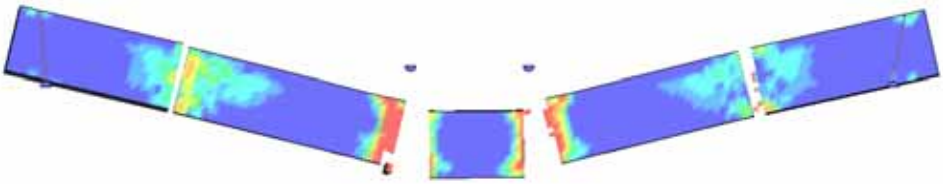

Figure 167. Plain concrete damage fringe t = 30 msec (user Linux).

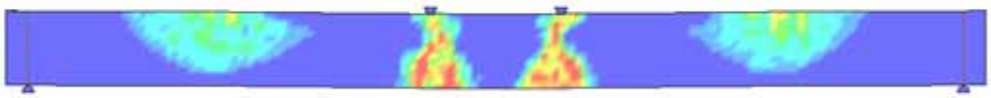

Figure 168. Plain concrete damage fringe t = 1 msec (user Windows).

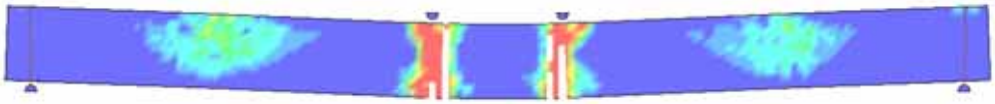

Figure 169. Plain concrete damage fringe t = 4 msec (user Windows).

Figure 170. Plain concrete damage fringe t = 20 msec (user Windows).

Figure 171. Plain concrete damage fringe t = 30 msec (user Windows).

CASE 4. REINFORCED CONCRETE BEAM

In this case, an over-reinforced concrete beam was modeled using the CSCM concrete model. The setup is similar to the model used in case 3 with the exception that beam elements are added to model the steel reinforcement inside the concrete beam. Both Windows and Linux binaries were used for conducting calculations with this model. Due to their similarity to one another, only one set of results (from the Linux binary) is presented in this report. Figures 172–175 show the damage fringes plots obtained from the developer calculations at simulation times corresponding to 1, 4, 16, and 20 msec, respectively. Figures 176–179 show damage fringe plots from the user Linux's calculations using the same simulation times. Figures 180 and 181 show the displacement history plot of a node on the impacting heads using the developer and user calculations, respectively.

Due to the over-reinforced nature of the beam, element erosion did not initiate in this analysis case. Close correlation was obtained between the user and the developer calculations for both the damage fringes and the displacement history of the impactor node. The minor variations that exist are well within the anticipated range of behavior.

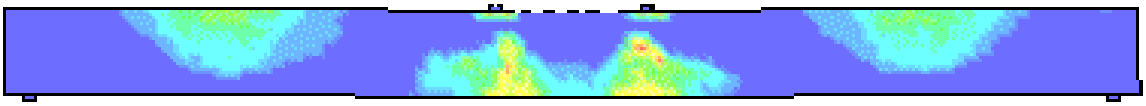

Figure 172. Reinforced concrete damage fringe t = 1 msec (developer).

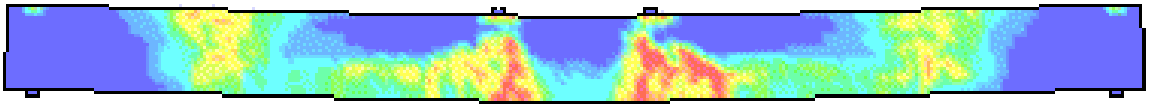

Figure 173 Reinforced concrete damage fringe t = 4 msec (developer).

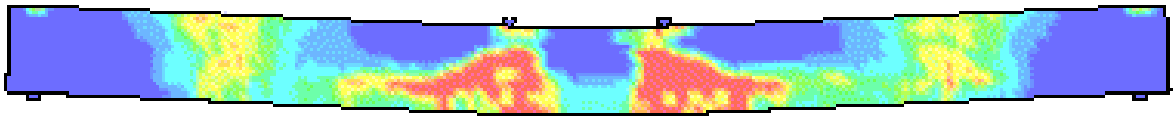

Figure 174. Reinforced concrete damage fringe t = 16 msec (developer).

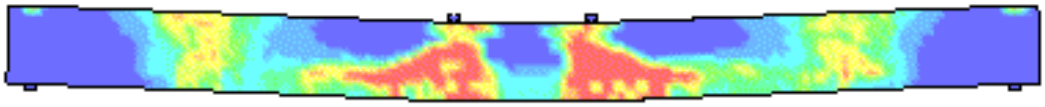

Figure 175. Reinforced concrete damage fringe t = 20 msec (developer).

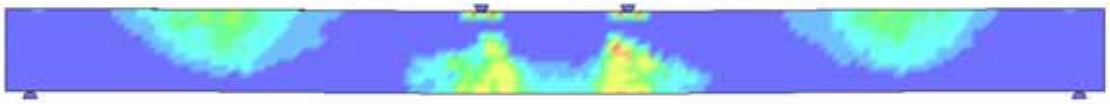

Figure 176. Reinforced concrete damage fringe t = 1 msec (user Linux).

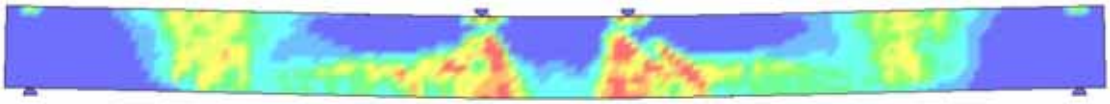

Figure 177. Reinforced concrete damage fringe t = 4 msec (user Linux).

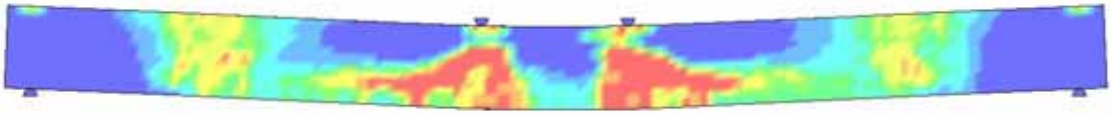

Figure 178. Reinforced concrete damage fringe t = 16 msec (user Linux).

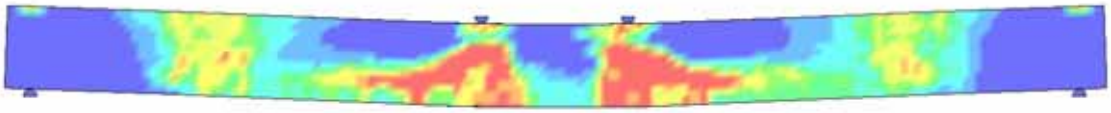

Figure 179. Reinforced concrete damage fringe t = 20 msec (user Linux).

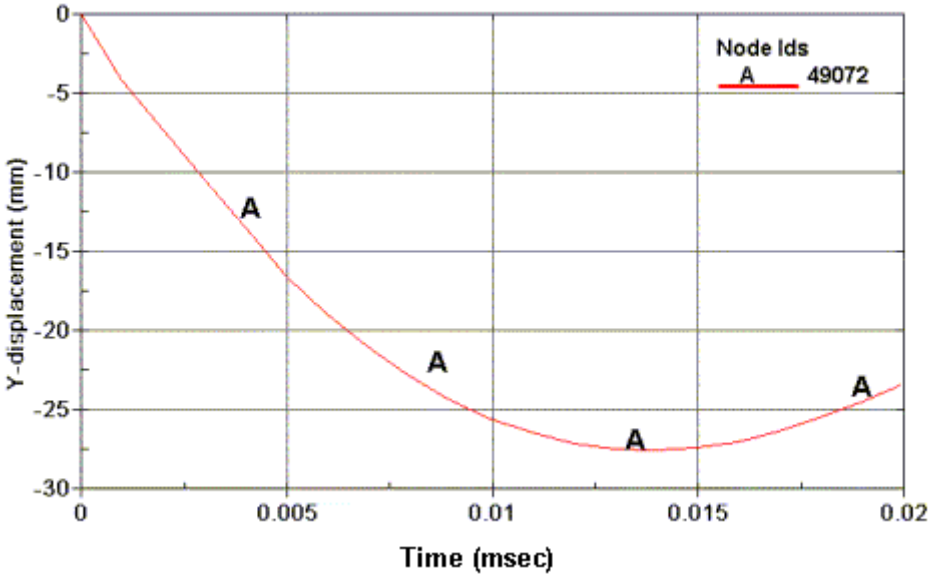

mm = 0.039 inch

Figure 180. Displacement of node 49,072 in millimeters (developer).

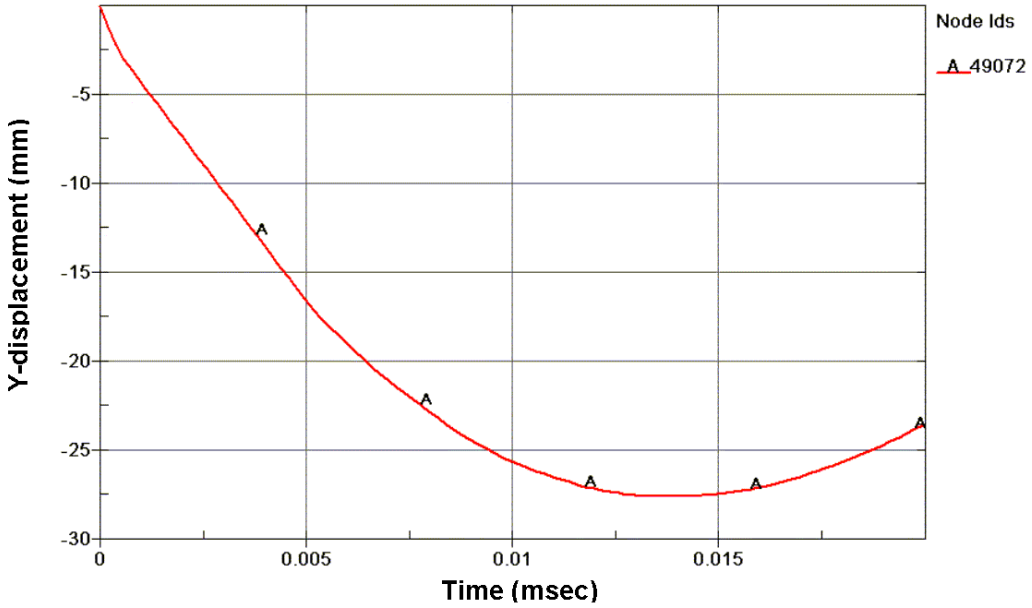

mm = 0.039 inch

Figure 181. Displacement of node 49,072 in millimeters (user Linux).

CASE 5. BOGIE IMPACT TESTS

In the final case, another steel-reinforced concrete beam was modeled using the CSCM concrete model. The loading condition represents a bogie vehicle impacting the reinforced beam at a speed of 33 km/h (20.5 mi/h). Figures 182–185 show the damage fringes plots from developer calculations at simulation times of 4, 8, 48, and 80 msec, respectively. Figures 186–189 show damage fringes plots from user Windows binary calculations at these same simulation times. Figures 190–193 show the corresponding damage fringes plots from user Linux binary calculations.

As for the beam analyzed in case 3, the damage fringes for the impacted beam in the user calculations developed similarly to those obtained from the developer calculations, and the subsequent element erosion pattern representing the cracking and failure of the beam shows differences for each calculation. However, the element erosion/fracture patterns are bounded within the same physical regions of the beam and the differences are considered to be within normal variability and range of behavior expected of a concrete member of this type.

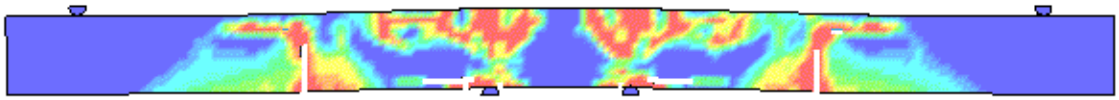

Figure 182. Bogie damage, t = 4 msec (developer).

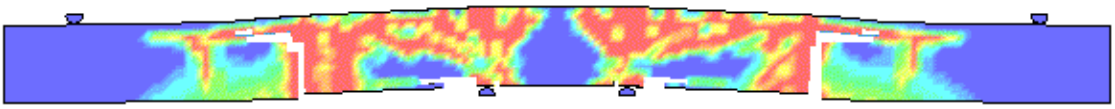

Figure 183. Bogie damage t = 8 msec (developer).

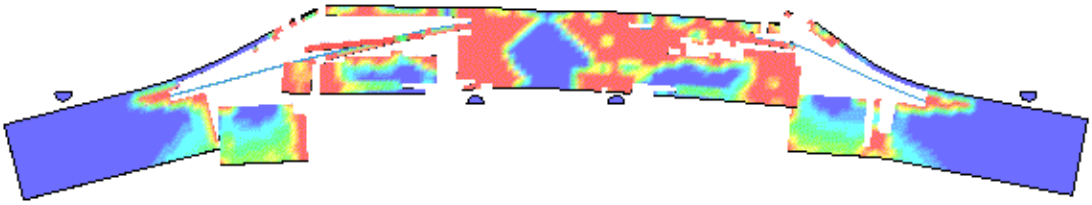

Figure 184. Bogie damage, t = 48 msec (developer).

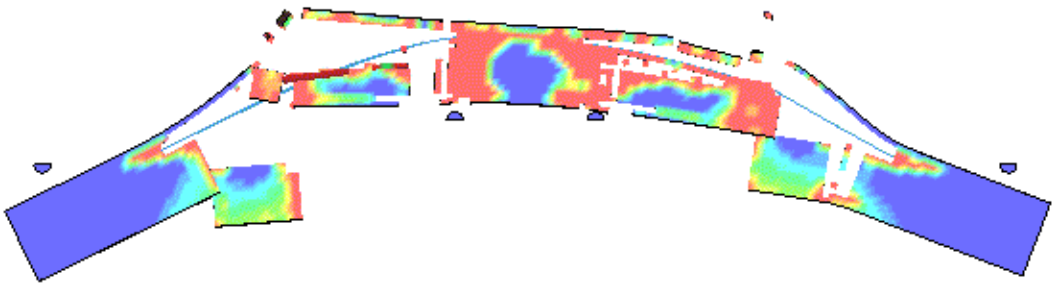

Figure 185. Bogie damage, t = 80 msec (developer).

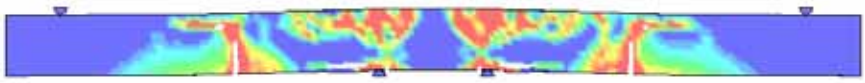

Figure 186. Damage fringes t = 4 msec (user Windows).

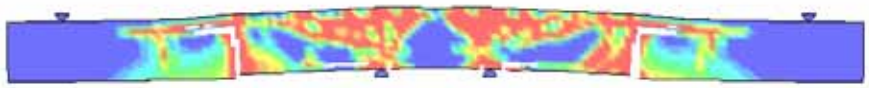

Figure 187. Damage fringe t = 8 msec (user Windows).

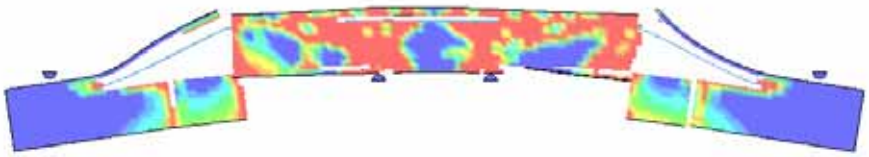

Figure 188. Damage fringe t = 48 msec (user Windows).

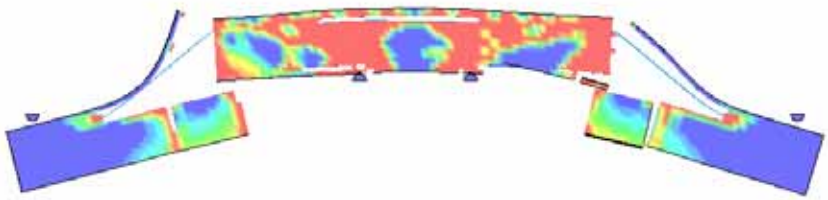

Figure 189. Damage fringe t = 80 msec (user Windows).

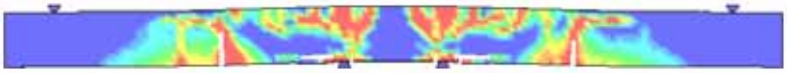

Figure 190. Damage, t = 4 msec (user Linux).

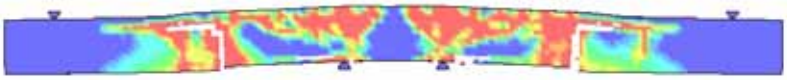

Figure 191. Damage, t = 8 msec (user Linux).

Figure 192. Damage, t = 48 msec (user Linux).

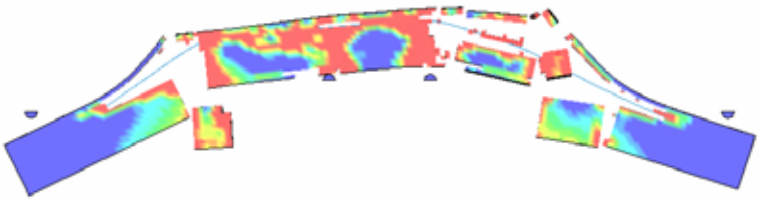

Figure 193. Damage t = 80 msec (user Linux).

APPENDIX B. DEVELOPER SUPPORT OF THE TEXAS T4 BRIDGE RAIL ANALYSES

INTRODUCTION

This appendix discusses the calculations performed by the developer in support of the evaluation of the Texas T4 bridge rail conducted by the user. These calculations examine bridge rail response and deflection as a tradeoff between the concrete material properties and the spring material properties. They were conducted after the user explored the use of reduced fracture energies for concrete, but before recalibration of the spring model and adjustment of the anchor bolt model. They should be considered preliminary calculations, not the final result. They are included here to show how the calculations evolved from being overly stiff to reasonable, and to show the thought process involved in the effort.

Pertinent conclusions drawn from these calculations are:

- Approximately 85 to 90 percent of the available kinetic energy is absorbed by the pendulum spring and honeycomb. Therefore, a 10 percent change in pendulum energy absorption results in a 100 percent change in concrete energy absorption. This suggests that accurate models of the pendulum spring and honeycomb are needed to get accurate delivery of energy to the bridge rail.

- Data-to-data comparisons indicate that the honeycomb in tests P3 through P7 is slightly stiffer than that in the calibration tests; therefore recalibration of the spring model was warranted. The developer's approximate technique was to scale up the stiffness of the existing spring model, as discussed in this appendix, to correlate measured and computed spring/honeycomb compressions. The user's more thorough technique was to develop a new spring model through correlations with test P5, as discussed in chapter 8. The developers data-to-data comparisons for the pendulum stiffness are not included in this report (but are available upon request), because the focus of this report is the concrete model, and not the spring/honeycomb model.

- With use of the developer's scaled spring model, calculated deflections correlate well with test P4 with 51 mm (2 inches) of rail deflection if default concrete material properties are used (*repow* = 1.0 and $G_{fs} / G_{ft} = 1.0$). Calculated deflections correlate best with test P5 with 117 mm (4.6 inches) of rail deflection if slightly reduced fracture energies are used (*repow* = 0.5 and $G_{fs} / G_{ft} = 0.5$).

Unless otherwise specified, these calculations were performed with:

- The original SBP spring model before recalibration with test P5. Scaling of the original SBP model is used to stiffen the spring in numerous calculations.

- The original anchor bolt model with nodes merged to the base plate.

- Concrete fracture energies that are approximately 80 percent of the preliminary properties originally tabulated by the user. These 80 percent values are the default fracture energies currently implemented in LS-DYNA (at the time this report was written). They are referred to as the developer's baseline properties.

BRIDGE RAIL DATA

The user conducted five pendulum impact tests on the Texas Department of Transportation T4 Bridge Rail.[12] The pendulum contains a crushable nose with 10 stages of replaceable aluminum honeycomb cartridges. Two bridge rail designs were tested: one four-bolt design and one three-bolt design. The pendulum is 838 kg (1,847 lbs) and impacts the rail at a nominal velocity of 9,835 mm/sec (22 mi/h). The four-bolt rail experienced punching shear failure in two tests (designated P3 and P4). The three-bolt rail did not fail, although hairline cracks were visible in one of two tests (P5 and P7). A third three-bolt rail test was conducted using the previously tested, but undamaged rail (P6). Again, this rail did not fail, but hairline cracks were visible. Rail deflections and pendulum crush are listed in Table 14 for all five tests.

Table 14. Rail deflection and pendulum crush in the Texas T4 bridge rail tests.

Test No.	Design	Rail Deflection	Honeycomb Crush	Damage
P3	four-bolt	117 mm (4.6 inch)	417 mm (16.4 inch)	Punching shear failure
P4	four-bolt	51 mm (2.0 inch)	414 mm (16.3 inch)	Punching shear failure
P5	three-bolt	15 mm (0.6 inch)	439 mm (17.3 inch)	None
P6	three-bolt	33 mm (1.3 inch)	295 mm (11.6 inch)	Cracks
P7	three-bolt	30 mm (1.2 inch)	439 mm (17.3 inch)	Cracks

The honeycomb crush listed in Table 14 is for nine stages of the honeycomb, as reported in Buth.[12] It does not include the first stage, which is the 76-mm (3-inch) stage that impacts the bridge rail. In all tests, the first stage crushes nearly completely; thus, the developer suggests adding an additional 70 to 76 mm (2.8 to 3 inches) to the crush listed in Table 1 to get the total crush of all 10 honeycomb stages.

The measured deflections vary by a factor of 2.3 for the four-bolt design. The average rail deflection measured in tests P3 and P4 is 81.5 mm (3.21 inches), and the standard deviation is 43.1 mm (1.7 inches). Assuming a normal distribution, approximately 68 percent of all test results are expected to lie within 1 standard deviation of the mean, 95 percent within 2 standard deviations, and 99 percent within 3 standard deviations. Therefore 68 percent of all test results

are expected to lie between 38 and 125 mm (1.5 and 5 inches), 95 percent of all test results are expected to lie between 0 and 168 mm (0 and 6.1 inches) , and 99 percent of all test results are expected to lie between 0 and 211 mm (0 and 8.31 inches).

PARAMETRIC STUDIES

At the beginning of the computational effort discussed in this appendix, initial calculations conducted by the user correlated well with the measured deflections and damage modes of the three-bolt design, but not those of the four-bolt design. The four-bolt design calculations were stiff (less deflection and damage) relative to the test data. Therefore, the user reduced the mesh size (fewer elements) in order to improve the run time for parametric studies. This task was accomplished by removing the entire deck and fixing the nodes at the bottom of the parapet.

The developer performed a series of parametric studies to help understand and improve the correlations for the four-bolt design. Studies were conducted using both the original mesh with the full deck and the reduced mesh with the fixed parapet. The baseline impact velocity used was that measured in test P3, which is 9,555.6 mm/sec (376 inches/sec), 34.4 km/h (21.375 mi/h). The three-bolt design was not analyzed by the developer.

Parametric studies were conducted to examine three possible sources of excess stiffness:

- The concrete material properties.
- The steel reinforcement material properties.
- The pendulum spring material properties.

A spring element with a nonlinear force-deflection curve is used to represent nine crushable stages of the honeycomb. Hex elements and a honeycomb material model are used to represent the first stage of honeycomb that impacts the rail. The reduced finite element mesh is shown in Figure 194.

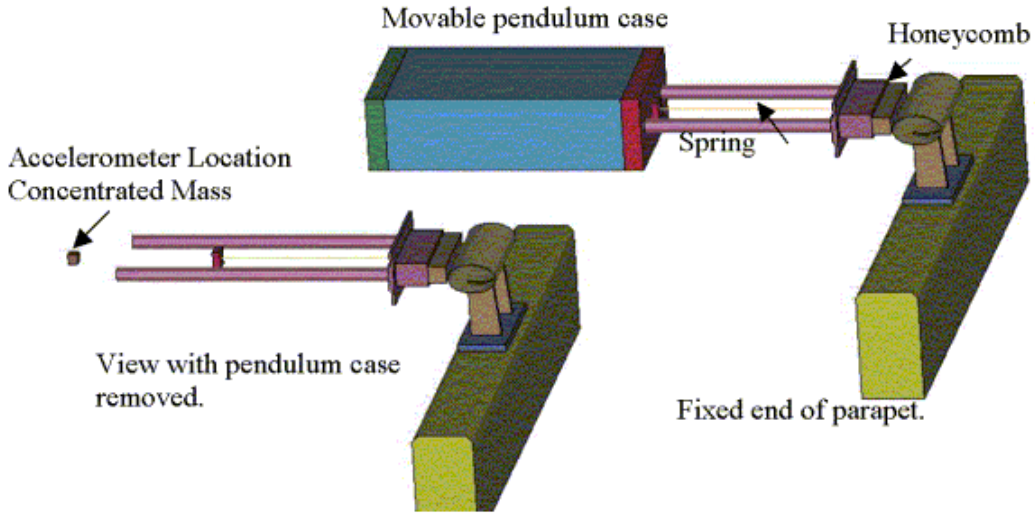

Figure 194. Finite element model of the pendulum, rail, and fixed end of parapet.

The studies indicate that adjustments in the steel reinforcement properties have little effect on the computed response. On the other hand, adjustments in both the concrete model properties and pendulum spring properties have significant effects on the computed response. The tradeoffs between adjustments in the properties of the concrete versus pendulum spring are discussed by the developer in the following sections.

Fixed Parapet Computational Results

Damage from the baseline property calculation is shown in Figure 195. Baseline properties are approximately those for 30.44 MPa (4,415 lbf/inch^2) concrete with 24 mm (0.94 inches) maximum aggregate size. Most parametric studies examine response for variations in fracture energy; thus, fracture energy values are reported throughout this chapter. The baseline fracture energies are G_{ft} = 0.074 N-mm with $G_{fs} = G_{ft}$ and $G_{fc} = 100\ G_{ft}$. Although the damage mode is similar to that observed in the tests, the damage is less severe. Rail deflection is approximately 10 mm (0.4 inches), which is substantially less than the 51 mm (2 inches) and 117 mm (4.6 inches) measured in the tests.

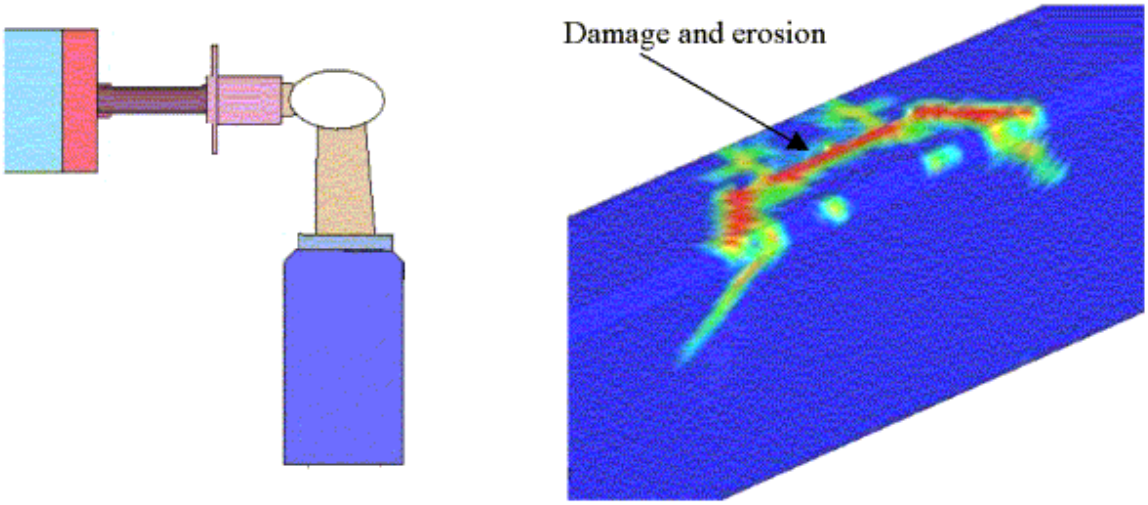

a. Impact of parapet. b. Damaged parapet.

Figure 195. Damage fringes calculated with baseline properties for a fixed end parapet.

Modified Concrete Property Studies. The first parametric studies were conducted on the concrete material properties. These calculations indicate that an overall reduction in concrete properties, for example, those of concrete in the 22 to 24 MPa (3,191 to 3,481 lbf/inch^2) range, would produce the measured deflection. However, 22 to 24 MPa (3,191 to 3,481 lbf/inch^2) is a much lower strength concrete than the 30.4 MPa (4,415 lbf/inch^2) used in the test. It is doubtful that the concrete used in the test structure could somehow be as low as 22 to 24 MPa (3,191 to 3,481 lbf/inch^2) when the reported value is 30.4 MPa (4,415 lbf/inch^2).

For example, as a lower bound case, the four-bolt calculation was run with approximate properties for 20 MPa (2,901 lbf/inch^2) concrete with 8 mm (0.3 inches) aggregate ($G_{ft} = G_{fs}$ =

0.041 N-mm and G_{fc} = 2.03). Recall that fracture energy and stiffness decrease with a reduction in concrete compressive strength. Fracture energy also decreases with a reduction in aggregate size. With these weak and brittle properties, the rail breaks through the concrete, with no rebound of the pendulum. Additional calculations were performed with 26 MPa (3,771 lbf/inch^2) concrete with fracture energies for 8 mm (0.3 inches) (G_{ft} = 0.049 N-mm) and 24 mm (0.94 inches) (G_{ft} = 0.066 N-mm) aggregate. Although damage was more extensive than calculated with the baseline properties, the calculated deflections of 27 mm (1.06 inches) and 14 mm (0.6 inches) are still less than measured. Also note that a 35 percent increase in tensile fracture energy due to aggregate size results in a computed decrease in deflection of nearly 50 percent (from 27 mm (1.06 inches) to 14 mm (0.6 inches)).

Energy Absorption Studies. The next parametric studies examined the amount of energy needed to deflect the rail 51 to 117 mm (2 to 4.6 inches) using 30.4 MPa (4,415 lbf/inch^2) concrete. The mass and impact velocity of the pendulum set the maximum amount of energy available to be absorbed by the pendulum and target rail. Crushing of the pendulum honeycomb and spring absorbs energy. As more energy is absorbed during pendulum crush, less energy is imparted to the rail target. Less rail energy results in less rail deflection.

The objective of these studies was to determine if it were possible to achieve the measured deflections using 30.44 MPa (4,415 lbf/inch^2) concrete if no energy were absorbed by the pendulum crush. These bounding calculations maximize the energy imparted to the rail by eliminating the energy absorbed by pendulum crush. These calculations allowed the author to determine the relationship between the energy absorbed by the rail and its subsequent damage and deflection. The boundary calculation also provided a rough estimate of the energy needed to computationally damage and deflect the structure in a manner consistent with that observed in the tests.

All energy absorption studies were conducted using a noncrushable pendulum model and the fixed end parapet model. The original finite element model of the pendulum was simplified by removing the moveable crushable nose of the pendulum (spring and honeycomb) and replacing it with elastic steel. The simplified pendulum has the dimensions of the first stage of honeycomb. The mass of the simplified pendulum is equal to that of the original pendulum (838 kg (1,847.5 lb)). Little or no internal energy is absorbed by the simplified pendulum model.

Computed rail deflections as a function of kinetic energy level are given in Table 15. Six calculations were performed at six different pendulum impact velocities, which correspond to six different pendulum initial kinetic energy levels. The kinetic energy levels are listed as a percentage of the maximum kinetic energy available from impact with an 838 kg (1,847.5 lb) pendulum at a velocity of 9,555.6 mm/sec.

Table 15. Rail deflection as a function of maximum kinetic energy available.

Kinetic Energy (%)	Rail Deflection
10	26 mm (1.02 inches)
15	42 mm (1.7 inches)
20	60 mm (2.4 inches)
25	95 mm (3.7 inches)
30	>163 mm (6.42 inches)
100	No rebound

Approximately 20 to 25 percent of the available kinetic energy is needed to deflect the rail between 51 and 117 mm (2 and 4.61 inches) (the measured values). At 30 percent kinetic energy, no rebound occurred by 100 msec (the duration of the calculation). Therefore, the deflection is probably infinite rather than 163 mm (6.42 inches). The deformed configuration of the structure for the 25 percent kinetic energy case is shown in Figure 196.

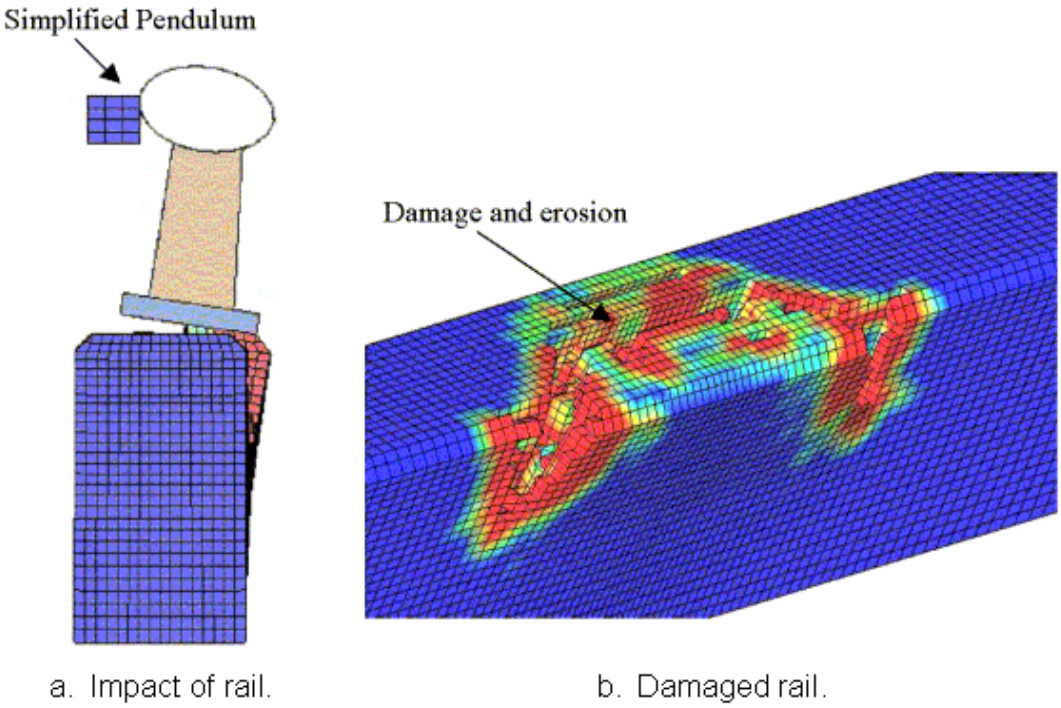

Figure 196. The deformed configuration and damage of the Texas T4 bridge rail (four-bolt design) from impact with the simplified pendulum model (without a crushable nose) at 25 percent maximum available kinetic energy is similar to that observed during the tests.

The significance of these calculations is that the majority of available kinetic energy is absorbed by crush of the pendulum and not by internal energy of the structure. Small changes in the amount of energy absorbed by pendulum crush result in large changes in the energy absorbed by the structure. For example, an 11 percent change in energy absorbed by the pendulum (from 90

to 80 percent) results in a 100 percent change in energy absorbed by the structure (from 10 to 20 percent). This level of change can make the difference between the structure appearing to be too stiff and the structure deflecting in the appropriate range. Therefore, accurate modeling of the crush and energy absorption of the pendulum spring and honeycomb is needed in order to get accurate delivery of energy to the target structure.

Review of the theoretical honeycomb cartridge configurations discussed in reference 12 confirms that most of the available kinetic energy is expected to be absorbed by crush of the pendulum, as is being calculated. The available kinetic energy is approximately 38,200 kN-mm, based on the pendulum mass and impact velocity. If the theoretical potential energy of crush is calculated, based on the total crush force of each honeycomb cartridge times the thickness of each cartridge, a total of 49,500 kN-mm is estimated. However, honeycomb typically crushes to about 75 percent strain, then stiffens dramatically, so the estimated crush energy is about equal to the available kinetic energy.

Fracture Energy Studies. Additional concrete material property studies were conducted with the noncrushable pendulum model. Unlike the previously discussed studies, which examined different strengths of concrete, these studies examine only 30.4 MPa (4,415 lbf/inch^2) concrete with possible modifications in baseline fracture energies.

Four calculations were conducted with 10 percent of available impact energy. In the first calculation, the fracture energy was reduced from the baseline value of G_{ft} = 0.072 N-mm to a low end value of G_{ft} = 0.040 N-mm. Rail deflection increased from 26 mm (1.02 inches) to about 35 mm (1.38 inches). In the other three calculations, the rate effect on the fracture energy was adjusted via the *repow* input parameter. This parameter scales the fracture energy in proportion to the theoretical increase in strength with strain rate, as discussed in the companion to this report Users Manual. The additional three calculations were conducted with the following parameters:

- *repow* = 0 and G_{ft} = 0.072 N-mm.
- *repow* = 0 and G_{ft} = 0.040 N-mm.
- *repow* = 0 and G_{ft} = 0.072 N-mm and $G_{fs} = 0.5G_{ft}$.

By default, *repow* = 1. With this value, if the rate effects formulation increases the strength by a factor of 3, the rate effects formulation will also increase the fracture energy by a factor of 3. If *repow* = 0, no increase in fracture energy is calculated; the input value is used independent of the strain rate.

Calculated deflections are 36 mm (1.42 inches), 68 mm (2.68 inches), and 40 mm (1.57 inches), respectively. The first additional calculation indicates that removing the rate effect from the baseline fracture energy moderately increases deflection from 26 mm (1.02 inches) to 36 mm (1.42 inches), similar to the effect of reducing G_{ft} from 0.072 to 0.040 N-mm. Reducing both *repow* and G_{ft} has a combined effect and moves the rail deflection into the desired range. The third addition calculation indicates that reducing G_{fs} from one to one-half of G_{ft} also has a small but noticeable effect on rail deflection.

These studies indicate that it is possible to achieve the measured deflection of 51 mm (2 inches) to 117 mm (4.61 inches) at 10 percent of available impact energy if the tensile fracture

energies—static and dynamic—are reduced below the current default baseline values. However, the values needed are not necessarily realistic. For example, the fracture energy G_{ft} = 0.072 N-mm is the approximate default fracture energy for 30.44 MPa (4,415 lbf/inch^2) concrete with 24-mm (0.94-inch) aggregate. The fracture energy G_{ft} = 0.040 N-mm is the approximate default for 20 MPa (2,901 lbf/inch^2) concrete with 8-mm (0.31-inch) aggregate. The default value for 30.44 MPa (4,415 lbf/inch^2) concrete with 8-mm (0.31-inch) aggregate is G_{ft} = 0.054 N-mm. These values agree with CEB tabulated values. Hence, use of G_{ft} = 0.040 N-mm for 30.44 MPa (4,415 lbf/inch^2) concrete is unusually brittle and outside the range of expected values.

In general, the developer recommends a rate effect on fracture energy equivalent to *repow* = 1, as do many experienced analysts. However, some analysts suggest no rate effect. Thus, it may be reasonable to allow *repow* to drop below a value of 1. In addition, although the fracture energy in tension is well documented, the fracture energy in shear is not well documented. It therefore seems reasonable to allow the fracture energy in shear to drop below the tensile baseline value as well.

Modified Spring Stiffness. It was previously concluded that the energy absorbed by crush of the spring and honeycomb models has a significant effect on computed response. Therefore, a series of parametric studies was conducted with an increase in spring stiffness. The spring is defined by a tabulated force versus deflection curve. The increase in stiffness is accomplished by scaling the tabulated deflection listing by a scale factor. The smaller the deflection scale factor, the larger the spring stiffness. For example, a scale factor on deflection of 80 percent results in an increase in spring stiffness of 125 percent (the reciprocal of 0.8).

Results from the baseline calculation, plus 10 additional calculations, are given in Table 16. Results are reported as a function of the scale factor applied to the spring deflection, as well as the input values used for *repow* and the ratio G_{fs}/G_{ft} (with G_{ft} = 0.074 N-mm). Results reported are approximate crush energy (absorbed by spring and honeycomb), rail deflection, and pendulum crush (of the spring plus honeycomb). The majority of the studies were conducted with the 60 percent deflection scale factor because, at the time, it was not known that only 9 of the 10 honeycomb stages were included in the documented crush measurements. Therefore, most calculations were conducted to achieve a computed crush of about 417 mm (16.4 inches), the documented value.

Table 16. Rail deflection, pendulum crush, and crush energy as a function of spring stiffness and concrete properties for the fixed end parapet model.

Spring Deflection Factor (%)	Stiffness Factor	Repow	G_{fs} / G_{ft}	Crush Energy (%)	Rail Deflection (mm)	Pendulum Crush (mm)
50	2.00	1	–	79	65	363
60	1.00	1	1	87	41	427
60	1.67	1	½	82	65	414
60	1.67	½	1	84	57	418
60	1.67	½	½	76	129	411
60	1.67	0	1	76	∞	424
60	1.67	0	½	68	∞	374
70	1.43	½	½	83	76	451
80	1.25	½	½	89	47	513
100	1.00	0	½	95	39	568
100	1.00	½	½	97	18	586
100	1.00	1	1	98	10	592

mm = 0.039 inch

One significant point is that as the spring stiffness increases (the applied deflection scale factor decreases), the energy absorbed by the pendulum spring and honeycomb decreases. This is the desired trend because it increases the amount of energy delivered to the structure, which increases rail deflection. In general, pendulum crush energy absorption in the 79 to 89 percent range produces computed rail deflections in agreement with measured deflections.

Stiffening of the spring also affects the calculated acceleration history. Calculated acceleration histories are given Figure 197. The calculated histories are plotted for the baseline calculation, as well as three stiffened spring calculations. The calculated trend observed is that as spring stiffness increases, the maximum deceleration increases, and the time to maximum deceleration decreases. In addition, as rail deflection increases, the "tail" on the initial triangular-shaped pulse also increases. In other words, the deceleration does not drop down to 0 as rapidly as it does with minimal rail deflection.

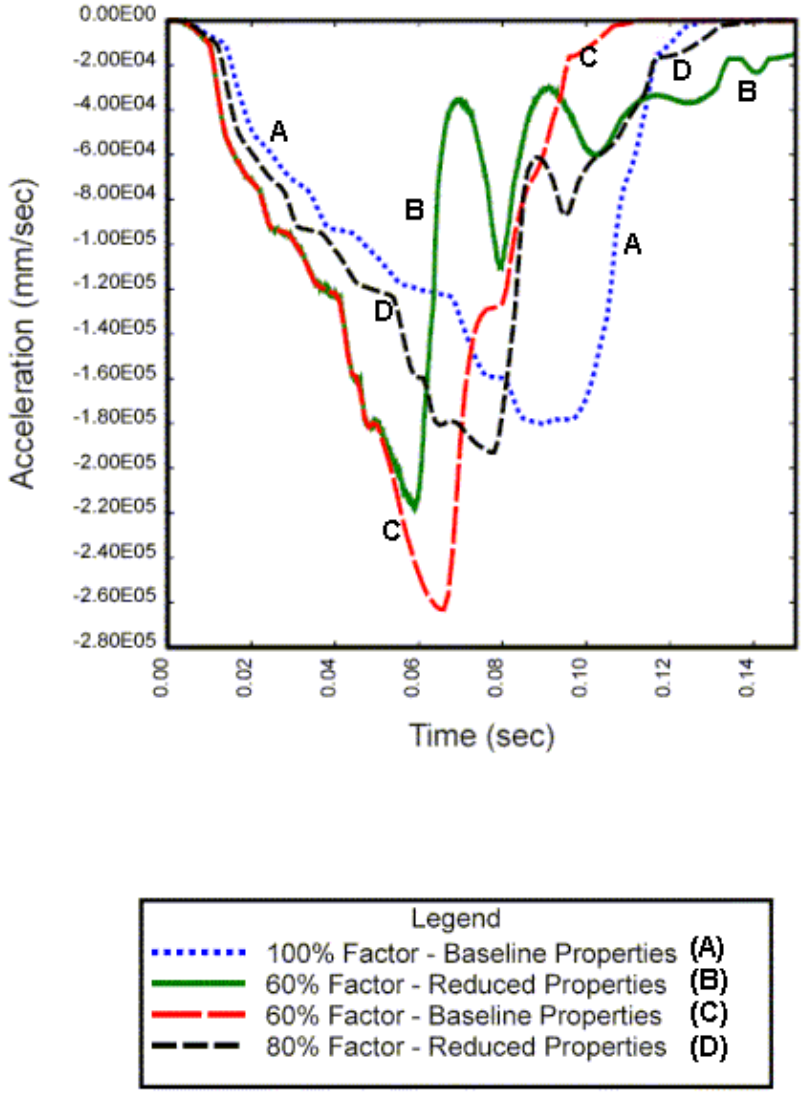

mm/sec = 0.039 inch/sec

Figure 197. Stiffening the spring increases the maximum deceleration and decreases the time at which the maximum deceleration occurs.

As an additional sensitivity study, one calculation was conducted at 9,835 m/sec (32,267 ft/sec) (35.4 km/h) (22 mi/h, the nominal impact velocity) rather than 9,556 m/sec (31,352 ft/sec) (34.45 km/h) (21.4 mi/h), the measured impact velocity). The calculation was conducted with a 60 percent scale factor on spring deflection (1.67 on spring stiffness), using baseline properties. The calculated deflection is 52 mm (2.05 inches) at 35.41 km/h (22 mi/h) compared with 41 mm (1.7 inches) at 34.45 km/h (21.4 mi/h). This is an increase in rail deflection of 27 percent for an increase in velocity of 2.9 percent.

The best correlation between the measured and calculated spring compression occurs for the 80 percent deflection scale factor case (1.25 on spring stiffness). Recall that the measured pendulum crush (all 10 stages) is just below 500 mm (19.7 inches). The computed compression of 513 mm (20.2 inches) is in reasonable agreement with this value. In addition, the 47 mm (1.9

inches) of deflection is also in reasonable agreement with the 51 mm (2 inches) of measured deflection reported for test P4. Figure 198 shows that the computed acceleration history is in good agreement with the P3 and P4 test histories throughout most of the measured response. This calculation was conducted with reduced properties ($G_{fs}/G_{ft} = 0.5$ and *repow* = 0.5).

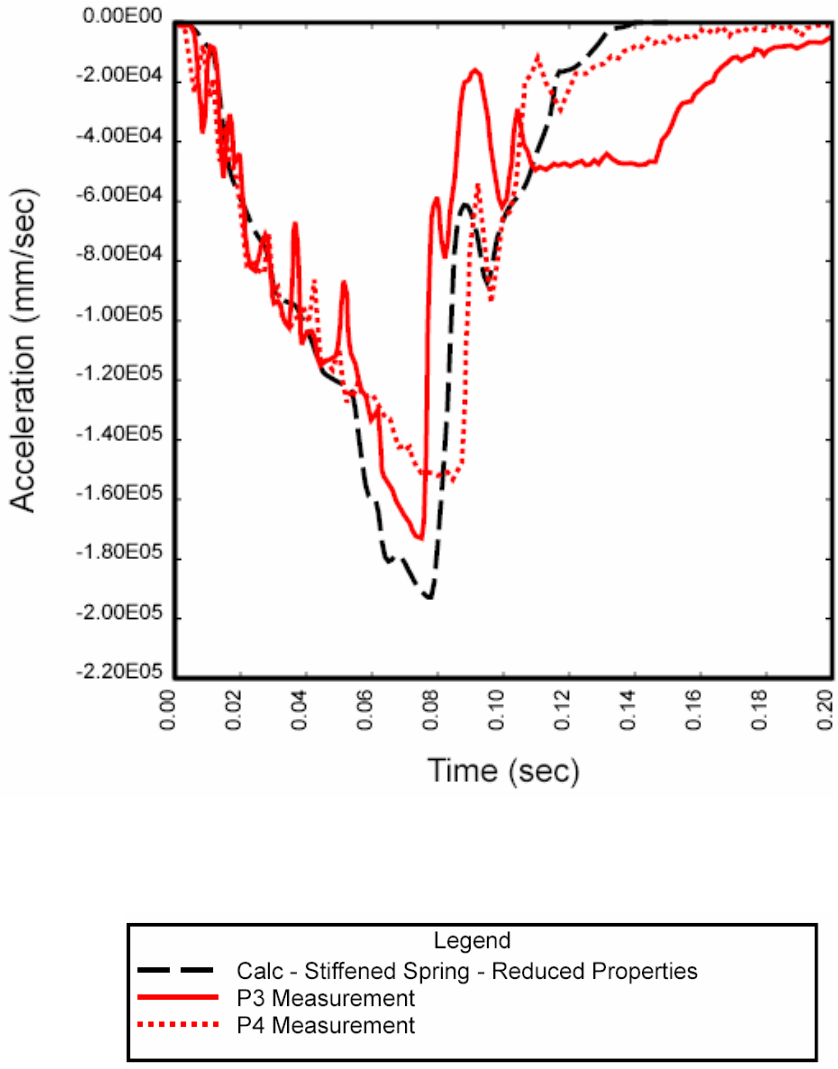

mm = 0.039 inch

Figure 198. Good comparison of measured and calculated acceleration histories for the reduced fixed parapet mesh (spring stiffened using 80 percent deflection scale factor).

Full Deck Computational Results

The bridge rail tested is mounted on top of a parapet, which is attached to a deck. All previously discussed calculations were conducted with the parapet fixed at the bottom edge, without inclusion of the deck. This was done to increase the runtime of the calculations so that parametric studies could be performed with reasonable turnaround time (overnight). Calculations discussed in this section were conducted with the deck modeled.

Comparisons With and Without Deck. To start, one calculation was conducted with the full deck mesh using baseline properties and original spring stiffness. The calculated rail deflection is 28 mm (1.1 inches) and the calculated spring compression is 578 mm (25.8 inches). This deflection is 280 percent larger than the 10 mm (0.4 inches) calculated with the fixed end condition previously reported in Table 16 using baseline properties and the original spring stiffness. Both models (full or reduced meshes) underpredict the measured deflections of 51 mm (2 inches) and 117 mm (4.6 inches).

The acceleration history for a second calculation conducted with the deck explicitly modeled is shown in Figure 199. The computed acceleration history is compared with both the P3 and P4 test data and with the corresponding calculation conducted with the fixed parapet end condition. The calculations were conducted with reduced properties (G_{fs}/G_{ft} = 0.5 and *repow* = 0.5) and with the spring stiffened with the 80 percent scale factor.

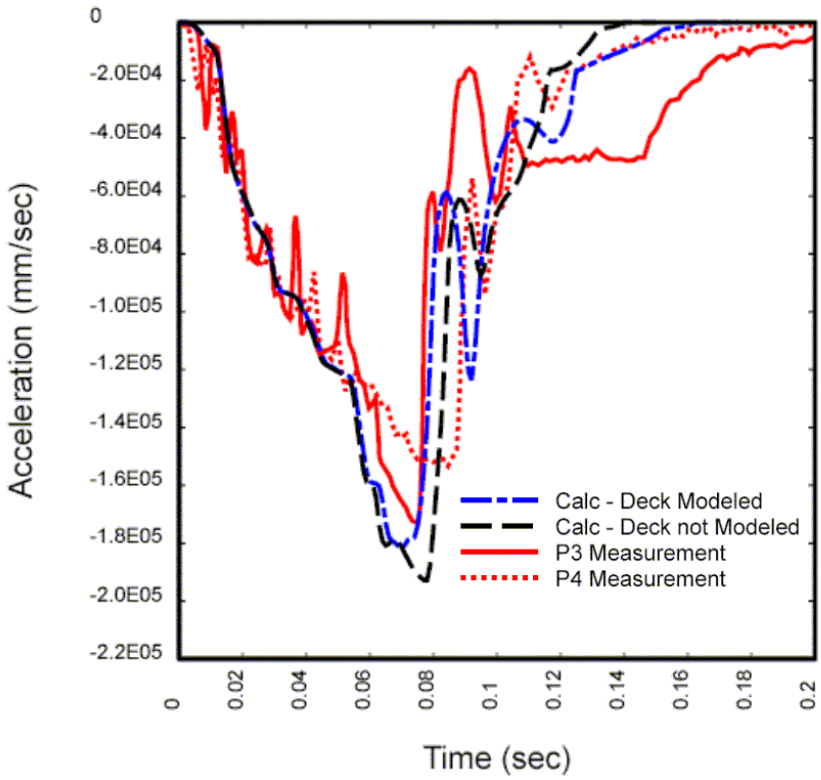

mm = 0.039 inch

Figure 199. Addition of the deck model improves correlations with the test data (spring stiffened using 80 percent deflection scale factor).

With the deck modeled, the calculated rail deflection is 87 mm (3.4 inches) and the calculated pendulum crush is 484 mm (19.1 inches). Without the deck modeled, the calculated rail deflection is 47 mm (1.9 inches) and the calculated pendulum crush is 513 mm (20.2 inches). Both calculations compare well with the measured P3 and P4 test results (51- and 117-mm (2- and 4.61-inch) deflection and 500-mm (19.7-inch) crush). However, the calculated accelerometer history with the deck modeled is in better agreement with the late time accelerometer measurements than that calculated with the fixed end condition. Hence, inclusion of the deck adds flexibility to the rail structure and improves correlation with the measured accelerometer records.

Note that the stiffness of the adjusted spring model is based on scaling the stiffness of the original nonlinear spring model. Additional adjustments to the spring might improve correlations if the spring is made more stiff at low deflection (below about 200-mm (7.87-inch) compression) and made less stiff at high deflection (above about 400-mm (15.7-inch) compression). Refer back to Figure 197 for the original spring stiffness modeled. This type of adjustment is discussed in subsequent sections.

Spring Stiffness Parameter Studies. Eleven calculations were run with the full deck mesh, as listed in Table 17. All were conducted at 9,555.6 mm/sec (21.375 mi/h). Three calculations were conducted with original spring stiffness (100 percent spring deflection scale factor), as provided by the user. The remainder of the calculations was calculated with a stiffened spring, using a 60 to 90 percent scale factor on the spring deflection.

Table 17. Rail deflection, pendulum crush, and crush energy as a function of spring stiffness and concrete properties for the full deck model.

Spring Deflection Factor (%)	Stiffness Factor	Repow	G_{fs} / G_{ft}	Crush Energy (%)	Rail Deflection (mm)	Pendulum Crush (mm)
60	1.67	1	1	76	75	413
65	1.54	½	½	74	∞	423
70	1.43	1	1	83	56	461
75	1.33	½	½	79	∞	464
80	1.25	½	½	89	87	484
80	1.25	1	1	86	44	499
90	1.11	½	½	85	57	530
90	1.11	1	1	90	33	541
100	1.00	0	½	83	∞	550
100	1.00	½	½	88	45	568
100	1.00	1	1	91	28	578

mm = 0.039 inch

Calculations conducted with a spring deflection scale factor of 80 percent are in best agreement with the measured pendulum crush of approximately 500 mm (19.7 inches). One of the two calculations was run with original baseline properties and the 80 percent scale factor on the spring deflection. The calculated rail deflection is 44 mm (1.73 inches) and the calculated spring compression is 499 mm (19.6 inches). These computed values compare well with measured

values of 51 mm (2 inches) of rail deflection and 500 mm (19.7 inches) of pendulum crush for test P4. The other calculation was run with reduced properties (G_{fs}/G_{ft} = 0.5 and *repow* = 0.5) and the 80 percent scale factor on the spring deflection. The calculated rail deflection is 87 mm (3.43 inches) and the calculated spring compression is 484 mm (19.1 inches). These computed values compare well with the average measured deflection and the 500 mm (19.7 inches) of pendulum crush for test P3. Hence, the baseline properties model the stiffer response associated with test P4, while the reduced properties (G_{fs}/G_{ft} = 0.5 and *repow* = 0.5) model the more flexible response associated with the average of test P3 and test P4.

Calculations conducted with original spring stiffness do not correlate as well with the test data as do the calculations with increased spring stiffness (80 percent scale factor on deflection). Using baseline properties, the computed rail deflection of 28 mm (1.1 inches) is lower than those measured in tests P3 and P4 (51 mm (2 inches) and 111 mm (4.4 inches), respectively). The computed pendulum crush is higher than measured (500 mm (19.7 inches) in both tests). Using reduced properties, the calculated rail deflection varies from 45 mm (1.8 inches) to infinity. The 45 mm (1.78 inches) of rail deflection is in agreement with the stiffer measured value (51 mm (2 inches)) of test P4. Property adjustments also could be made to obtain agreement with test P3 (112 mm (4.41 inches) of rail deflection). However, the calculated pendulum crush is still larger than the measured value. Hence, use of reduced concrete properties with original spring stiffness does not correlate well with all test measurements.

Results from Table 17 are plotted in Figure 200, along with the range in measured data. By examining the computed results in Table 17 and Figure 200, it is apparent that only one calculated rail deflection lies outside the three standard deviations range. This is the calculation conducted with *repow* reduced to 0 (which means that fracture energy is independent of rate effects) and G_{fs} / G_{ft} = 0.5. Although not shown in Table 17, the observed trends indicate that all calculations, regardless of spring deflection scale factor, would produce infinite deflection with *repow* = 0 and G_{fs} / G_{ft} = 0.5. This suggests that *repow* = 0 with G_{fs} / G_{ft} = 0.5 are not appropriate input parameter values. The response modeled is too brittle, at least for this example problem.

Only one calculated rail deflection lies outside the one standard deviation range, although it lies within the two standard deviations range. This is the calculation conducted with baseline properties and original spring stiffness. The calculated deflection of 28 mm (1.1 inches) is 26 percent lower than the one standard deviation value of 38 mm (1.5 inches). This suggests that baseline properties are on the stiff side if original spring stiffness is assumed, but they are adequate if reduced spring stiffness is assumed.

Damage fringes for two of the stiffened spring calculations (80 percent scale factor on deflection) are shown in Figures 201–204. The damage calculated with reduced properties (G_{fs}/G_{ft} = 0.5 and *repow* = 0.5) is more severe than that calculated with baseline properties. Both results are similar to the post-test damage previously shown in chapter 8 for tests P3 and P4.

Following this computational effort, data-to-data comparisons were made between the accelerometer records of bridge rail tests P3 through P7 with those of the rigid pole calibration tests. Comparisons were made for acceleration versus time, force versus deflection, energy absorbed versus deflection, and derived spring stiffness versus deflection. These comparisons indicated that the honeycomb in the calibration tests was less stiff than that in the bridge rail

tests; therefore, stiffening of the spring was warranted. Ultimately, a new stiffened spring model was setup by the user.

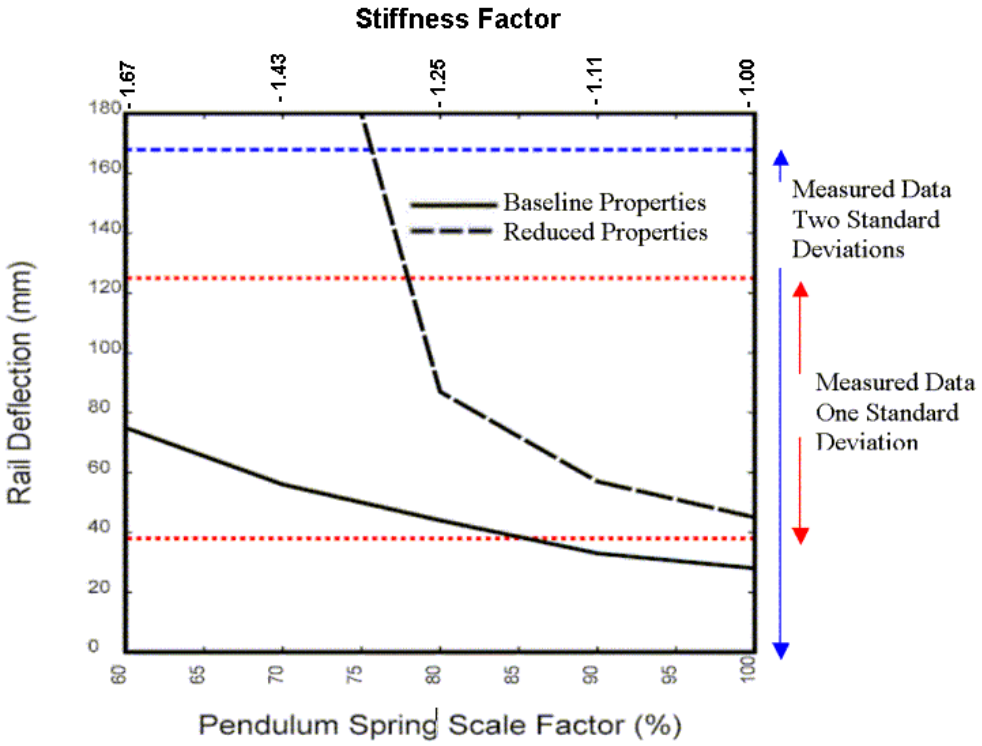

mm = 0.039 inch

Figure 200. All calculations run with baseline or slightly reduced properties (*repow* = 0.5 and $G_{fs} / G_{ft} = 0.5$) produce rail deflections within two standard deviations of the measured results.

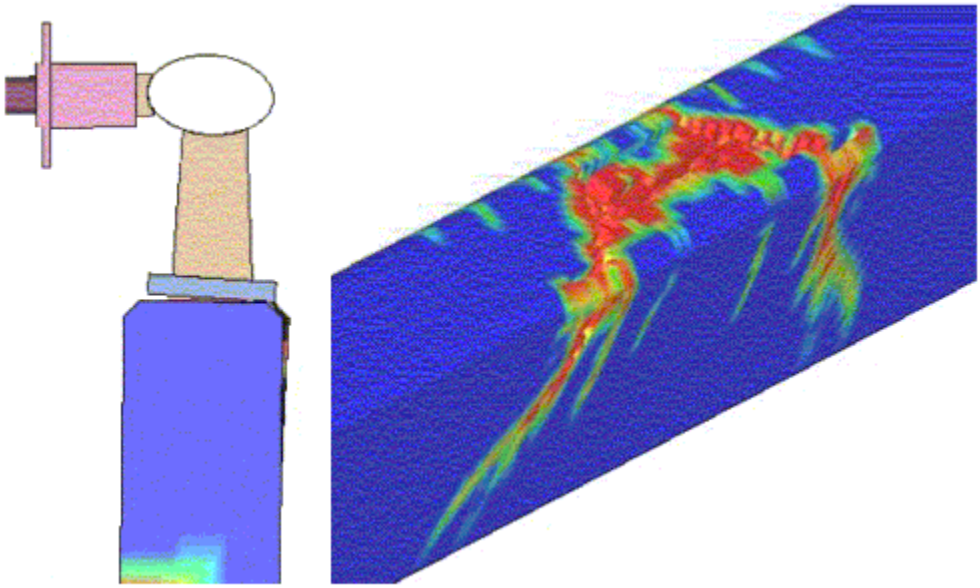

Figure 201. Deflection and damage calculated with baseline properties using a stiffened spring (80 percent displacement scale factor).

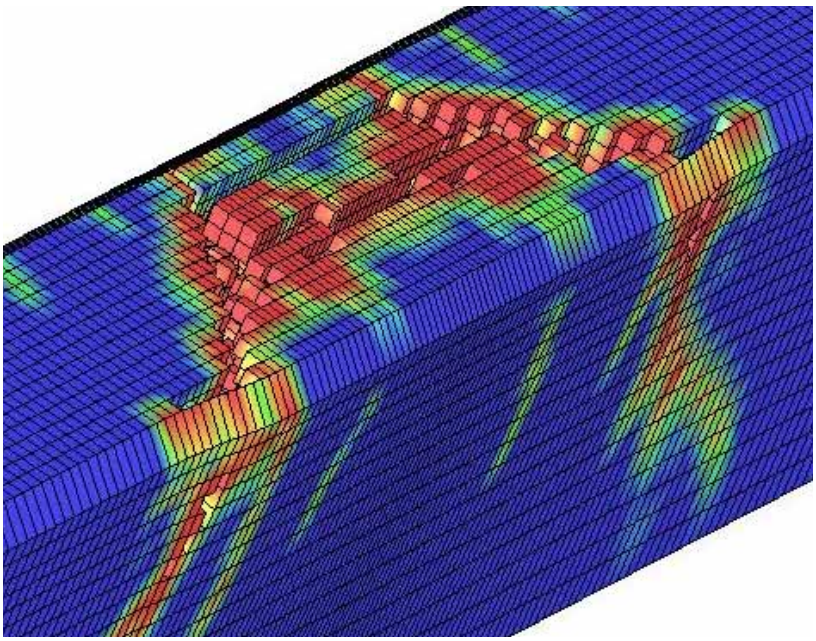

Figure 202. Closeup of damage calculated with baseline properties using a stiffened spring (80 percent displacement scale factor).

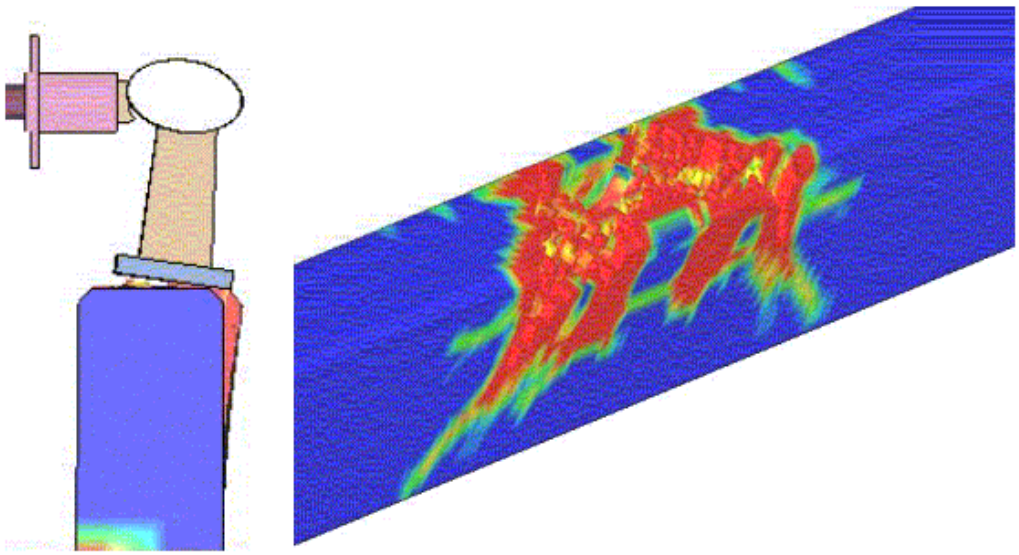

Figure 203. Deflection and damage calculated with slightly reduced properties using a stiffened spring (80 percent displacement scale factor).

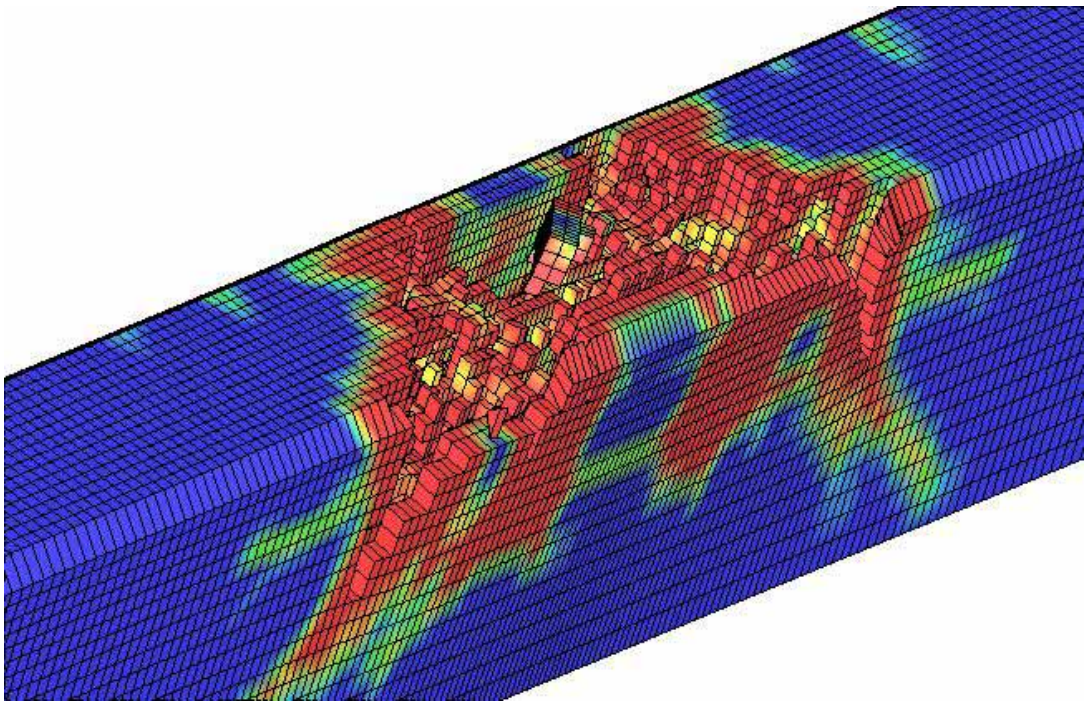

Figure 204. Closeup of damage calculated with slightly reduced properties using a stiffened spring (80 percent displacement scale factor).

Impact Velocity Parameter Study. Additional full deck mesh calculations were conducted at 9,835 mm/sec (35.41 km/h) (22 mi/h), the nominal impact velocity) rather than 9,555.6 mm/sec (34.4 km/h (21.4 mi/h), the measured impact velocity), as shown in Table 18 and plotted in Figure 205. This is an increase of roughly 1 km/h (0.62 mi/h). In general, the increase in velocity has a much stronger effect on the deflections computed with reduced properties than on the deflections produced with baseline properties. For the calculation with baseline spring and concrete properties, the deflection is 33 mm (1.3 inches) at 35.4 km/h (22 mi/h) 9,835 mm/sec compared with 28 mm (1.1 inches) at 9,555.6 mm/sec. This is an increase in rail deflection of 18 percent for an increase in velocity of 2.9 percent and an increase in kinetic energy of 5.9 percent. The 33-mm (1.3-inch) computed rail deflection is close to the 38-mm (1.5-inch) deflection associated with 1 standard deviation.

Table 18. Rail deflection, pendulum crush, and crush energy for calculations conducted with increased impact velocity (9,835 mm/sec) for the full deck model.

Spring Deflection Factor (%)	Stiffness Factor	Repow	G_{fs} / G_{ft}	Crush Energy (%)	Rail Deflection (mm)	Pendulum Crush (mm)
60	1.67	1	1	78	95	412
70	1.43	½	½	78	∞	451
80	1.25	1	1	89	54	510
85	1.18	½	½	83	107	510
90	1.11	½	½	86	216	544
100	1.00	½	½	91	62	574
100	1.00	1	1	96	33	589

mm = 0.039 inch

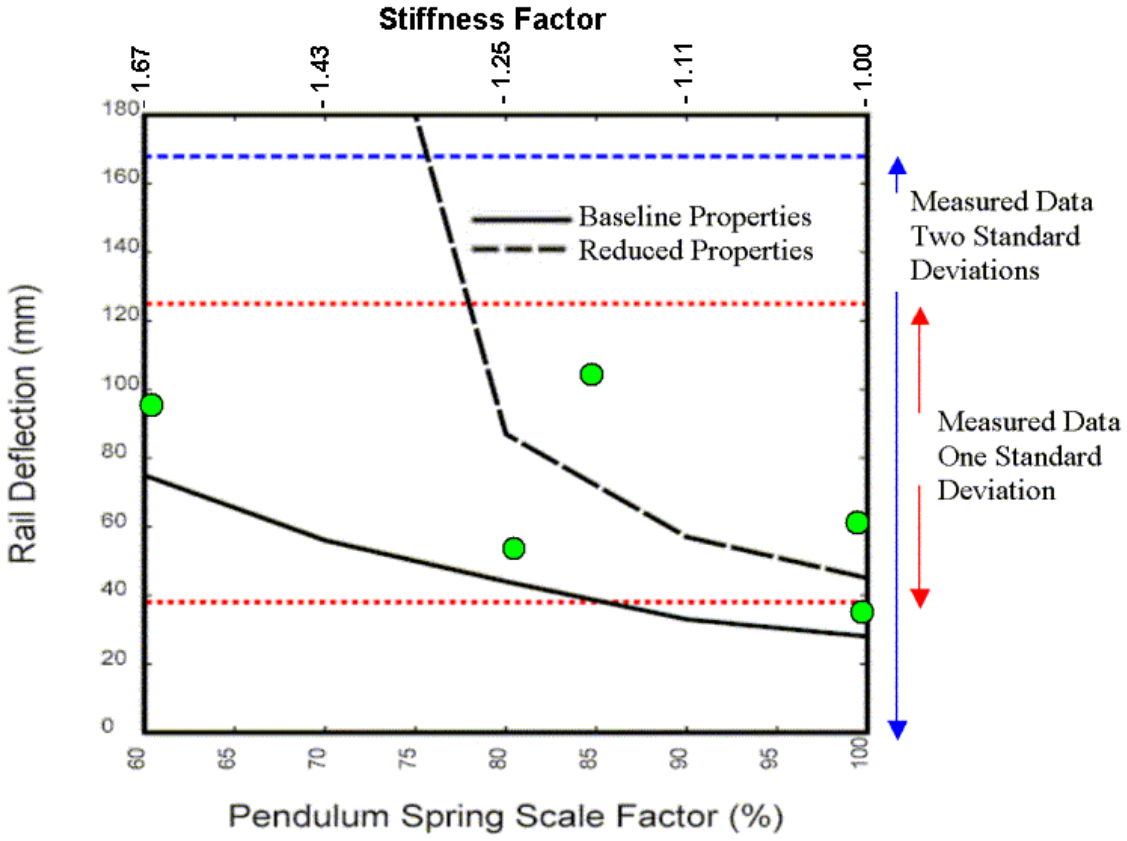

mm = 0.039 inch

Figure 205. Larger rail deflections are calculated at 9,835 mm/sec (large dots) compared with 9,556 mm/sec (solid and large dashed lines).

DECK TO PARAPET CONNECTION

One final study examined how the joint is modeled between the deck and parapet. In the test structure, the concrete in the deck is poured separately from the concrete in the parapet. Thus, a joint exists between the deck and parapet. In all calculations previously discussed, this joint is not modeled. Instead, a tied interface firmly connects the parapet to the deck (CONTACT_TIED_NODES_TO_SURFACE). The developer's experience is that this type of interface is more suitable for a deck and parapet that are poured at one time (without a joint), but it is much too strong for a joint. Therefore, two additional calculations were conducted with the joint explicitly modeled. This was accomplished by using an interface that allows concrete separation but not penetration (CONTACT_NODES_TO_SURFACE). The parapet will not disconnect from the deck because it is secured by steel reinforcement.

The two calculations were conducted with baseline and reduced properties, using the spring stiffened with the 80 percent scale factor. With baseline properties, the effect of modeling the joint is to increase the calculated deflection 9 percent from 44 mm (1.7 inches) to 48 mm (1.9

inches). The calculated pendulum crush is 502 mm (19.8 inches). Damage fringes are shown in Figure 206. The effect of including the joint is to eliminate damage at the base of the parapet where it connects to the deck. With reduced properties, inclusion of the joint increases the calculated rail deflection from 87 mm (3.4 inches) to infinity. The rail breaks completely through the concrete. Maximum separation between the deck and parapet is approximately 0.36 mm (0.01 inches), which is not visible to the eye.

The developer suggests that the calculations performed with the joint modeled are a better representation of the test structure than the calculations performed without the joint modeled. Both are bounding calculations. With a tied interface, the effect is to model no joint at all, as if the deck and parapet were one piece of continuously poured concrete. This calculation provides an upper bound on joint stiffness. With a separable interface, the effect is to model a joint with no tensile strength, as if there were no bonding of the paste from the parapet with that from the deck. This provides a lower bound on joint stiffness. In reality, slight bonding and tensile strength probably exist (but are much less than those of solid concrete). The developer's recommendation is to model joints with an interface that allows for separation but not penetration. More sophisticated approaches might include adding tensile strength to the contact surface or predamage to the concrete.

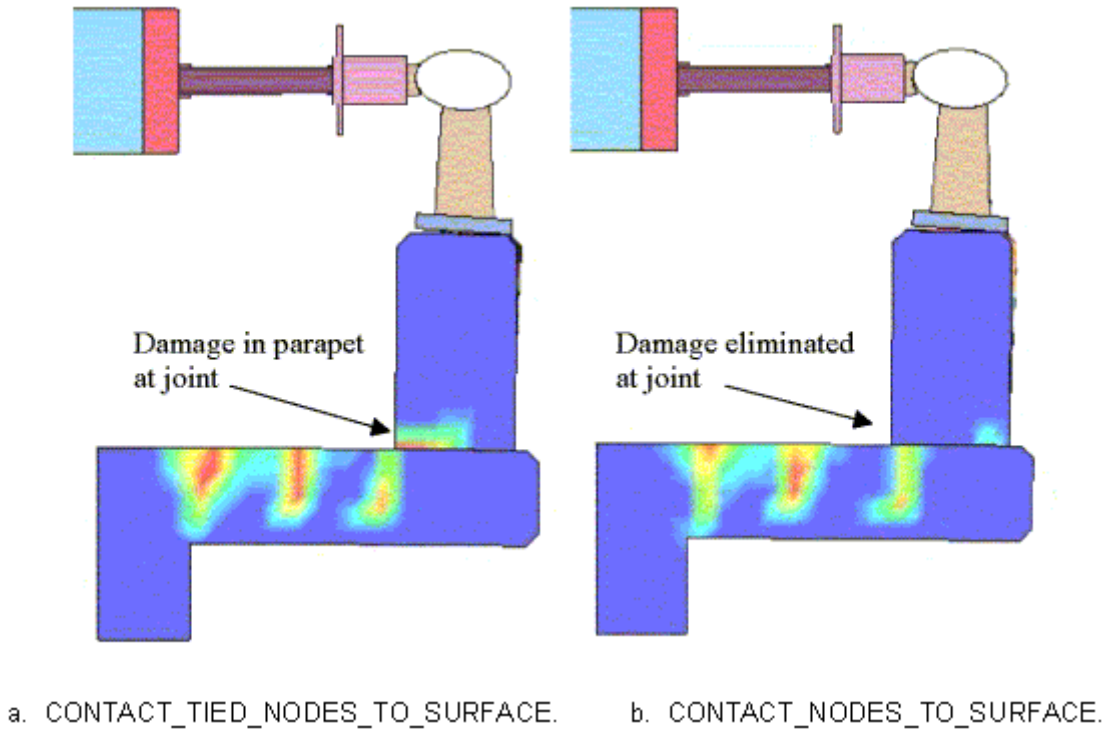

Figure 206. The tensile damage at the base of the parapet is eliminated if a flexible joint is modeled (80 percent displacement scale factor with baseline properties).

SUMMARY OF BRIDGE RAIL CALCULATIONS

All calculations conducted with the full deck mesh produce rail deflections that lie within two standard deviations of the measured rail deflections using either baseline (*repow* = 1.0 and G_{fs}/G_{ft} = 1.0) or slightly reduced (*repow* = 0.5 and G_{fs}/G_{ft} = 0.5) material properties for concrete. This is true regardless of whether the pendulum model is run with original spring stiffness or increased spring stiffness. However, the developer suggests that these calculations are overly stiff because the joint between the deck and parapet was not modeled.

Data-to-data comparisons (not shown) indicate that the pendulum crushing stiffness in the bridge rail tests is greater than that in the original calibration tests. Therefore, use of a stiffened spring model is warranted. The spring stiffened with an 80 percent deflection scale factor (1.25 stiffness factor) produces spring/honeycomb compressions in agreement with those in the tests. Therefore, the spring with 80 percent deflection scale was chosen as the appropriate spring stiffness. All full deck mesh calculations conducted with the stiffened spring (80 percent scale factor on displacement) produce rail deflections that lie within one standard deviation of the measured rail deflections using either baseline or slightly reduced material properties for concrete, whether or not the joint is modeled.

Without modeling the joint, the baseline properties tend to produce a response on the stiff side of the measured deflections, whereas the slightly reduced properties tend to produce a response closer to the mean measured deflection. Extremely reduced properties (*repow* = 0 and G_{fs}/G_{ft} = 0.5) produce infinite deflections, and therefore are not recommended for use.

With the joint modeled, more flexibility is added to the structure. The baseline properties produce a response close to that of test P4. The slightly reduced properties allow the bridge rail to break through the concrete parapet. The developer‘s recommendation is to leave the baseline properties modeled as currently implemented, but to make each user aware that slightly reduced properties (*repow* = 0.5 and G_{fs}/G_{ft} = 0.5) are an option that could be examined parametrically.

CHAPTER 12. REFERENCES

1. Hargrave, M.W. and D. Smith, "Using the Computer and DYNA3D to Save Lives," *Public Roads Magazine*, January/February 2001.

2. Livermore Software Technology Corporation (LSTC), LS-DYNA Keyword Users Manual (Nonlinear Dynamic Analyses of Structures in Three Dimensions), Version 960, Volume 1, 2001.

3. Murray, Y.D., "Modeling Rate Effects in Rock and Concrete," *Proceedings of the 8th International Symposium on Interaction of the Effects of Munitions with Structures*, Volume IA, Defense Special Weapons Agency, April 1997.

4. Murray, Y.D. and B.A. Lewis, *Numerical Simulation of Damage in Concrete*, APTEK technical report to the Defense Nuclear Agency, Contract No. DNA001-91-C-0075, Report No. DNA-TR-94-190, November 1995.

5. Schwer, L.E. and Y.D. Murray, "A Three-Invariant Smooth Cap Model with Mixed Hardening," *International Journal for Numerical and Analytical Methods in Geomechanics*, Vol. 18, pp. 657–688, 1994

6. Murray, Y.D., "Users Manual for LS-DYNA Concrete Material Model 159," Report No. FHWA-HRT-05-062, Federal Highway Administration, 2007.

7. CEB-FIP Model Code 1990, Comité Euro-International du Béton, Thomas Telford House, 1993.

8. D.C. Alberson, W.F. Williams, W.L. Menges, and R.R. Haug. *Testing and Evaluation of the Florida Jersey Safety Shaped Bridge Rail*, Research Report 9-8132-1. Texas Transportation Institute, College Station, TX, February 2004.

9. Bazant, Z.P. and J. Planas, *Fracture and Size Effect in Concrete and Other Quasi-brittle Materials*, CRC Press, ISBN 0-8493-8284-X, 1998.

10. Oldani, E., F. Orengo, C.A. Plaxico, and M.H. Ray, *Drop Tower Testing of Concrete Beams,* Worcester Polytechnic Institute Report submitted to APTEK, Inc., July 2003.

11. Bielenberg, B.W., R.K. Faller, J.D. Reid, J.C. Holloway, J.R. Rohde, and D.L. Sicking, "Impact Analysis of Three Reinforced Concrete Beam Specimens," Midwest Roadside Safety Facility, University of Nebraska, Report #TRP-03-130-03, submitted to APTEK, Inc., March 2003.

12. Buth, E., *NCHRP 350 Pendulum Test and Transition Connection Project*, Letter Report for Project 408930, Texas Transportation Institute, College Station, TX, August 2002.

13. Zimmer, R.A. and A.G. Arnold, *Calibration of the TTI 820 KG Pendulum*, Texas Transportation Institute Report 270687, College Station, TX, June 1997.

HRDS-04/05-07(1M)E